université PARIS-SACLAY

Thèse de doctorat

UNIVERSITÉ DE VERSAILLES ST-QUENTIN-EN-YVELINES

université PARIS-SACLAY

ULB FACULTÉ DES SCIENCES

UNIVERSITÉ LIBRE DE BRUXELLES

Effects of river delivery of nutrients and carbon on the biogeochemistry of the Arctic Ocean

Thèse de doctorat de l'Université Paris- Saclay et de l'Université Libre de Bruxelles préparée à l'Université Versailles Saint-Quentin en Yvelines

École doctorale n°129 Sciences de l'Environnement enˆIle-de-France (SEIF)

Spécialité de doctorat: Océan, atmosphère, climat et observations spatiales

Thèse présentée par

Jens Terhaar

Composition du Jury :

Philippe Bousquet Professeur, LSCE-IPSL, Gif-sur-Yvette	Président du jury
Tatiana Ilyina Professeur, Max-Planck-Institut für Meteorologie, Hamburg	Rapporteur
Nicolas Gruber Professeur, Eidgenössische Technische Hochschule Zürich	Rapporteur
Lei Chou Professeur, Université libre de Bruxelles	Examinateur
Leif Anderson Professeur, Göteborgs universitet	Examinateur
Laurent Bopp Professeur, École Normale Supérieure de Paris	Directeur de thèse
Pierre Regnier Professeur, Université libre de Bruxelles	Co-Directeur de thèse
James Orr Directeur de recherche, LSCE-IPSL, Gif-sur-Yvette	Responsable CEA

université PARIS-SACLAY
ÉCOLE DOCTORALE
Sciences de l'environnement d'île-de-France (SEIF)

Titre : Les effets du transport de carbone et sels nutritifs sur la biogéochimie de l'océan Arctique
Mots clés : Biogéochimie, océan Arctique, débit fluvial, changement climatique

Résumé : Malgré une faible superficie à l'échelle globale, les zones côtières océaniques représentent des zones clefs pour la production primaire des océans et de l'acidification, jouant ainsi un rôle important dans le cycle du carbone global. Ce sont des zones fortement influencées par les fleuves, en particulier en zone Arctique. Mais l'impact de ces apports fluviatiles pour l'Océan Arctique est encore largement inconnu en raison du faible nombre d'observations dû aux conditions hostiles qui règnent dans cette zone. Ce travail de thèse a pour objectif d'améliorer notre compréhension de l'influence des apports fluviatiles en carbone et nutriments pour l'Océan Arctique.
La première partie de ce travail de thèse a d'abord permis d'évaluer les performances de plusieurs versions du modèle biogéochimique océanique NEMO-PISCES dans l'Océan Arctique. En analysant les résultats du modèle pour des résolutions horizontales variables, j'ai pu montrer l'importance des apports latéraux pour l'inventaire de carbone anthropique de l'Océan Arctique. Ces résultats ont ensuite permis d'ajuster une méthode d'estimation du carbone anthropique à partir d'observations pour l'océan Arctique.
Dans la deuxième partie, une estimation des flux de carbone et de nutriments provenant de l'ensemble des fleuves arctiques a été construite à partir d'une série d'observations. En utilisant ces flux pour forcer le modèle biogéochimique, j'ai ainsi montré que les apports fluviatiles expliquent jusqu'à 24 % de la production primaire dans l'océan Arctique. Ces apports réduisent en même temps de 20% l'absorption de CO2 par l'océan et diminuent saisonnièrement l'acidification de l'océan en surface. Finalement, des simulations idéalisées m'ont permis de quantifier la sensibilité de la biogéochimie de l'océan Arctique aux changements futurs d'apport de carbone et de nutriments par les fleuves. Cette sensibilité est de faible amplitude à l'échelle de l'océan Arctique, mais très importante dans les zones côtières et à proximité de l'embouchure des fleuves.

Title : Effects of river delivery of nutrients and carbon on the biogeochemistry of the Arctic Ocean
Keywords : Biogeochemistry, Arctic Ocean, riverine delivery, climate change

Abstract : Coastal oceans play an important role in the carbon cycle and are hotspots of ocean primary production and ocean acidification. These coastal regions are strongly influenced by rivers, especially in the Arctic. Despite the importance of the riverine delivery of carbon and nutrients, their effect on the Arctic Ocean is still poorly understood due to hostile conditions and the consequently low number of observations. This thesis aims at improving our understanding of the influence of Arctic riverine delivery of carbon and nutrients by using ocean biogeochemical models.
The first part of the thesis evaluated the model skills of the ocean biogeochemical model NEMO-PISCES in the Arctic Ocean. By analyzing model results at different horizontal resolutions, the importance of lateral influx from the adjacent oceans for anthropogenic carbon cycle in the Arctic Ocean was demonstrated. These results were then used to adjust a previously published data-based estimate of anthropogenic carbon storage in the Arctic Ocean and the corresponding ocean acidification.
In the second part, a pan-Arctic observation-based dataset of riverine carbon and nutrient fluxes was created. This dataset was then used to force the ocean biogeochemical model and the river fluxes were quantified. River fluxes have been shown to sustain up to 24% of Arctic Ocean primary production, to reduce the air-sea CO2 uptake by 20%, and to reduce surface ocean acidification seasonally. Eventually, idealized simulations were made to quantify the sensitivity of the Arctic Ocean biogeochemistry to future changes in riverine delivery of carbon and nutrients. Sensitivities are of small magnitude on a pan-Arctic scale, importance in the coastal areas, and the dominant factor close to river mouths.

Université Paris-Saclay
Espace Technologique / Immeuble Discovery
Route de l'Orme aux Merisiers RD 128 / 91190 Saint-Aubin, France

Diese Arbeit widme ich meinen Großeltern Hedwig, Heinrich, Maria und Josef.

Acknowledgments

Firstly, I want to thank my PhD advisers James Orr, Laurent Bopp, and Pierre Regnier. All of you have contributed in your own personal way and without you this work would not have been possible.

James, you had more time for me than I could have expected from a primary supervisor. During this PhD, you assumed the responsibility of supervising my PhD, committed yourself to it, and fulfilled this role entirely. I will not forget the unique role that you had in this PhD. Furthermore, let me thank you for the endless time you have taken to improve my manuscripts, for teaching me ocean chemistry, for introducing my into Python Notebooks, and for your patience while teaching me how to become a good writer.

Laurent, thank you for your guidance, your enthusiasm, and your 'Yes We Can' mentality. You encouraged me to pursue a lot of different paths and embraced new ideas. At the same time you always managed to connect each part of this work to the overarching research question and thus helped me to focus on the big picture.

Pierre, thank you for challenging by asking the difficult questions. You pulled me out of my comfort zone, the ocean, and forced me to learn more about the riverine and coastal ecosystems. Although this meant a lot of extra work, your help made it much easier and eventually this additional knowledge has substantially improved this PhD and helped integrating my results into the broader picture of the land-ocean aquatic continuum.

Second I want to thank all the people I had the pleasure to collaborate with: Ronny Lauerwald, Toste Tanhua, Tim Stöven, Marion Gehlen, Lester Kwiatkowski, Timothée Bourgeois, Christian Ethé, and many others. Thanks a lot for your help and your patience with me. I want to thank Christian espacially, because without his helped I would not have been able to run only one simulation of the ocean biogeochemical model NEMO-PISCES. In addition, I want to thank the whole LSCE and all the people I met during my time as a PhD student. You all made my time much more enjoyable. A particularly thank you to Cathy, Sabina, and Olivier for all the great moments.

Thirdly, I want to thank the European Union for funding this PhD through the C-Cascades project. Moreover I want to thank all the great people in the C-Cascades project, especially our project manager Emily who helped me to find my way to the French administration and who helped me to organize my secondment in Brussels.

Last but not least, I want to thank my entire family. A big thank you to my parents who made it possible for me to study Physics in Heidelberg, Southampton, and Paris. Moreover I want to thank my wife for helping me through this PhD and for the greatest gift during our PhD: Our son Henri for whom she cared almost alone during the last months of this PhD. Thank you Christine!

Contents

List of figures

List of Tables

Chapter 1

Introduction

“ I don’t know why it should be me - I’m not a very clever horse. ”

The Magician’s Nephew, C.S. Lewis

Contents

1.1 Arctic Ocean - Hotspot of climate change

With climate change, global air temperatures are continuously increasing (Figure 1.1). The last four years were the hottest years since the beginning of the temperature record in 1880. In the Arctic, these temperature increases over the period 1979-–2014 are amplified by a factor of 2 to 3 [Cohen et al., 2014]. In the last three years, Arctic temperature anomalies were even amplified by 4–5 (Figure 1.1). This Arctic Amplification was already predicted at the end of the 19th century by Svante Arrhenius, a Swedish professor and winner of the Nobel prize for chemistry in 1903 [Arrhenius, 1896]. For the 21st century, multi-model studies project continuing Arctic Amplification with Arctic temperature increases being 1.9 times larger than global temperatures during the 21th century [Winton, 2006].

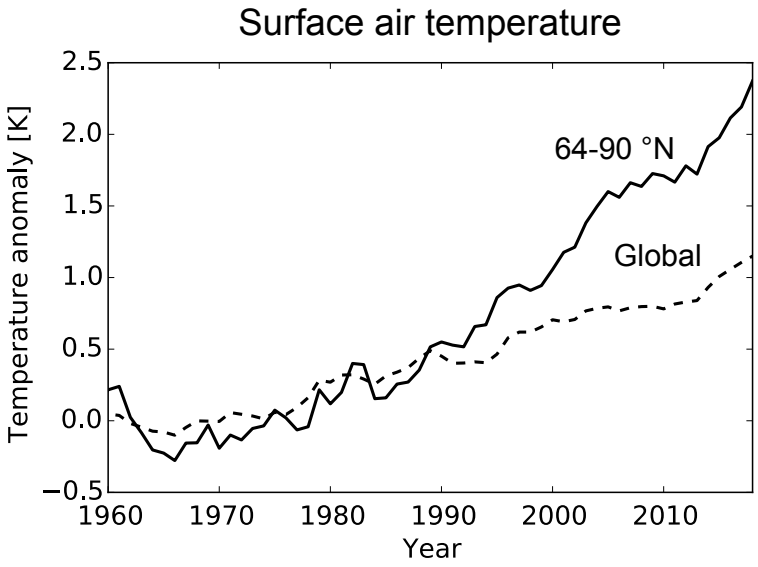

Figure 1.1 – Surface temperature anomalies relative to 1951-1980 average temperatures, based on the National Aeronautics and Space Administration Goddard Institute for Space Sciences (NASA GISS) temperature analysis (http://data.giss.nasa.gov/gistemp)

The main driver of this Arctic Amplification is the reduction in sea ice cover in the Arctic Ocean, which is well documented by satellite observation since the beginning of the observations in 1979. Average September sea ice has decreased from 1981 to 2010 by 13.3% per decade or about 86000 km^2 yr^{-1} [Serreze and Stroeve, 2015a]. The first ice-free summer in the Arctic Ocean is predicted by 2030 [Overland and Wang, 2013]. This reduction in sea ice cover reduces the Arctic Ocean surface albedo, the capacity of the earth surface to reflect solar radiation. The albedo of sea ice is relatively high (0.5–0.7), whereas the albedo of ocean water is lower ($\sim$ 0.06). Thus the decline of sea ice reduces the surface albedo of the Arctic Ocean, which hence leads to a consequent increase in uptake of solar radiation by the Arctic Ocean and an amplified temperature increase [Arrhenius, 1896]. This positive albedo feedback is accompanied, in smaller magnitude, by changes in cloud cover and increase in water vapor [Screen and Simmonds, 2010].

Both, the increase in temperature and the decline in sea ice cover, have cascading effects on the

biogeochemistry of the Arctic Ocean. For example, the decline in sea ice extent increases the light availability at the Arctic Ocean surface and prolongs the growing season of phytoplankton, the basis of the ocean's food web. Observations show, that primary production (PP) of phytoplankton has increased by 30% between 1998 and 2012 [Arrigo and van Dijken, 2015] and a multi-model average projects a continuing rise in PP within the next century [Vancoppenolle et al., 2013]. This increase in PP with climate change is opposite to the projected global decline in marine PP [Bopp et al., 2013].

During the process of PP, dissolved inorganic carbon (C_T) in the surface layers of the ocean is converted to organic carbon, which then partly sinks towards the ocean floor. This decrease in surface C_T by PP favors the additional uptake of atmospheric CO_2 [Bates et al., 2006]. While the efficiency of this biological carbon pump is uncertain in the Arctic Ocean, model studies suggest that globally 20% of all carbon used for PP is replaced by carbon from the atmosphere [Orr and Sarmiento, 1992]. The projected increase in Arctic Ocean PP was thus assumed to lead to increase to an increased uptake in the future [Bates et al., 2006]. More recently, Cai et al. [2010] and Manizza et al. [2019] argued that the positive effect of increased biological activity on the air-sea uptake might be offset (1) by a negative effect on the Arctic Ocean solubility pump, more specifically by a decrease in CO_2 solubility due to increased surface ocean temperature, and (2) by a decrease in ventilation of surface waters due to higher stratification from increased river runoff and sea ice melt. The decreased ventilation may also decrease upwelling of nutrient rich waters and thus even limit the postulated increase of the biological pump [Cai et al., 2010].

Although the Arctic Ocean stored only 2% of the anthropogenic CO_2 emitted to the atmosphere [Tanhua et al., 2009] and thus has a minor effect on climate change regulation, small differences in C_T can cause strong ocean acidification in the Arctic Ocean, to which it is specifically vulnerable [Steinacher et al., 2009]. Due to its low temperatures and the consequently high solubility of CO_2, the calcium carbonate saturation states of aragonite (Ω_{arag}) and calcite (Ω_{calc}) in the Arctic Ocean are lower than global average values [Orr et al., 2005; Steinacher et al., 2009]. With the uptake of anthropogenic carbon, the surface values of Ω_{arag} have decreased by 0.5 since the beginning of the industrialization [Steinacher et al., 2009]. In addition to surface acidification, the increased uptake of anthropogenic carbon from the atmosphere and its transport to the deeper ocean also lead to deep ocean acidification. Consequently, the aragonite saturation horizon (ASH), the depth at which waters become undersaturated towards aragonite, has risen by ~190 m in the last 250 years [Anderson et al., 2010]. Further uptake of anthropogenic carbon via increased air-sea CO_2 fluxes is projected to make the entire Arctic Ocean undersaturated towards aragonite at the end of the 21st century under the RCP8.5 scenario [Steinacher et al., 2009; Anderson et al., 2010]. As calcium carbonate minerals are necessary for many species in the ocean to form shells, the undersaturation of ocean waters towards these minerals will have important effects on the ecosystem of the Arctic Ocean [Gattuso and Hansson, 2011; Riebesell et al., 2013].

Opposite to most parts of the global ocean, the Arctic Ocean is largely impacted by rivers. River

runoff in the Arctic Ocean represents 11% of global ocean river runoff [Raymond et al., 2007], although the Arctic Ocean represents only 1% of the global ocean volume. Accordingly, riverine delivery of dissolved organic carbon (DOC) from Arctic rivers is 2.5 times larger than the DOC delivery from rivers of comparable size in temperate regions [Raymond et al., 2007]. This delivery of DOC is estimated to reduce the uptake of atmospheric CO_2 by 10% [Manizza et al., 2011]. Riverine delivery of carbon from rivers, also enhances ocean acidification in the Arctic Ocean. Regional seas, which are strongly influenced by riverine input, are already observed to be largely corrosive towards calcium carbonate minerals [Chierici and Fransson, 2009; Tremblay et al., 2015; Semiletov et al., 2016]. Together with carbon, rivers also provide important amounts of nutrients to the Arctic Ocean. These riverine nutrients are believed to drive 1-10% of the global Arctic Ocean PP [Le Fouest et al., 2013; Tremblay et al., 2015]. In nearshore regions, the relative contribution of riverine nutrients to the annual PP is estimated to reach ~40% [Tank et al., 2012a]. In the future, higher atmospheric temperatures in the Arctic will lead to thawing of old permafrost, perennial frozen ground, and the consequent liberation of old organic carbon, which will eventually enter the Arctic Ocean via rivers [Lawrence and Slater, 2005; Schuur et al., 2008]. This increased riverine delivery of carbon is amplified by a projected increase in river runoff as a consequence of increasing precipitation over the Arctic watersheds [Peterson et al., 2002; Lawrence and Slater, 2005; Nohara et al., 2006].

The combined effect of large temperature increases, reduction of sea ice, increases in PP, increased riverine runoff, increased riverine delivery of C_T, DOC, and nutrients, and large scale ocean acidification make the Arctic Ocean a hotspot of environmental change (Figure 1.2).

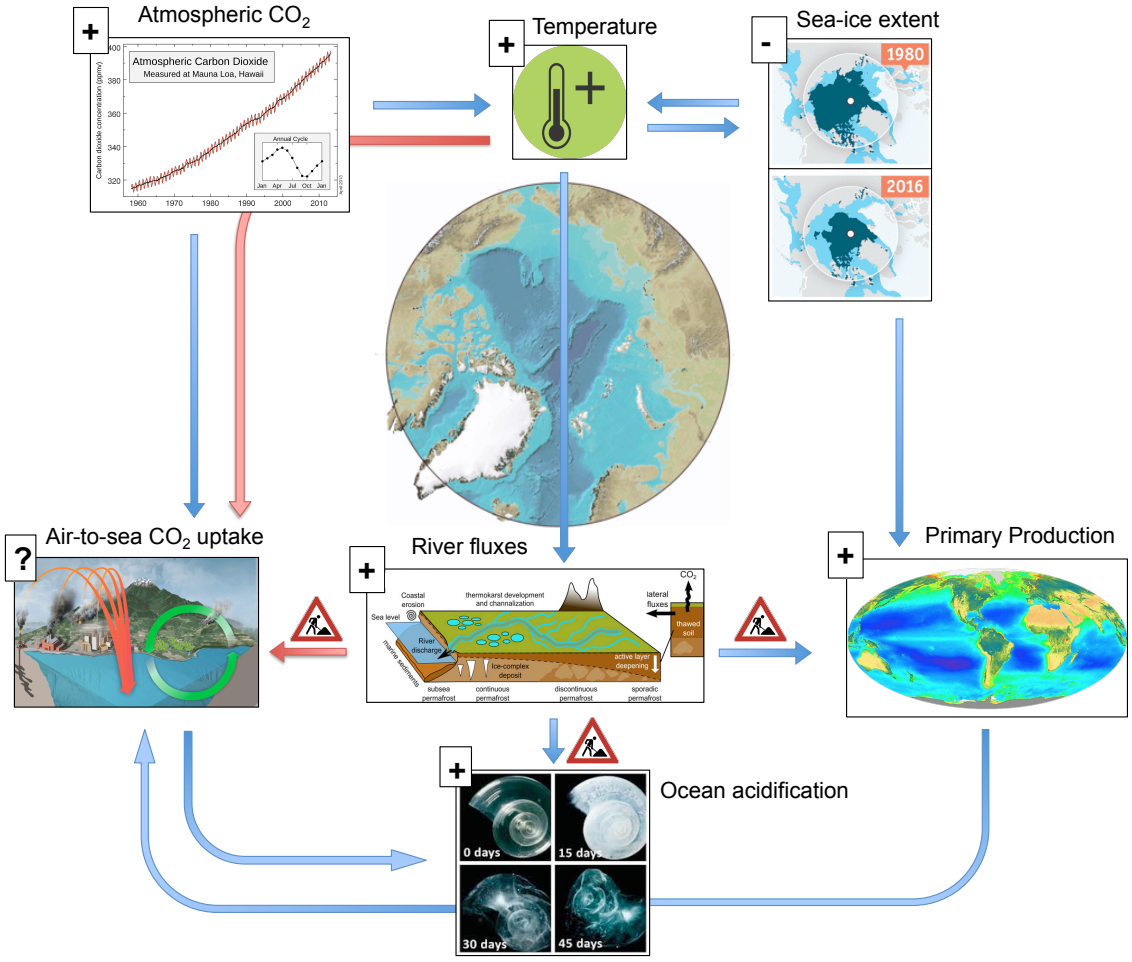

Figure 1.2 – Principal effects of climate change in the Arctic Ocean and their feedbacks (blue arrows: positive feedback; red arrows: negative feedback): Atmospheric CO_2 increase, temperature increase (ocean and atmosphere), reduced sea ice cover, changes in air-sea CO_2 flux, increased riverine discharge and increased riverine fluxes of carbon and nutrients, increased primary production, and enhanced ocean acidification. The processes that are analyzed in this thesis are marked by the 'work in progress' symbol.

1.2 Arctic Ocean

1.2.1 Geography

The Arctic Ocean is situated around the North Pole between Canada, the United States of America, Russia, Norway, and Greenland. With its length of ~4000 km and width of ~2400 km, the Arctic Ocean is the smallest of the five major ocean basins, representing only 4% of the global ocean area and 1% of the global ocean volume [Jakobsson, 2002]. The high area-to-volume ratio stems from the large Arctic shelf seas, which make up 53% of the Arctic Ocean area. These large shelf seas have a mean depth of 48–200 m and are generally divided into 7 regional seas: the Barents Sea, the Kara Sea, the Laptev Sea, the East-Siberian Sea, the Chukchi Sea, the Beaufort Sea, and the Canadian Arctic Archipelago (CAA). The remaining 47% of the Arctic Ocean area, the Central Arctic Ocean Basin, has a mean depth of 2748 m and is divided into the Eurasian and Amerasian basins, which themselves are divided into the Nansen and Amundsen basin in the Eurasian part, and the Makarov and Canada basin in the Amerasian part (Figure 1.3). The two principal basins are divided by the Lomonosov ridge, which rises ~3 km above the abyssal plain and thus reaches a mean water depth of about 1000 m.

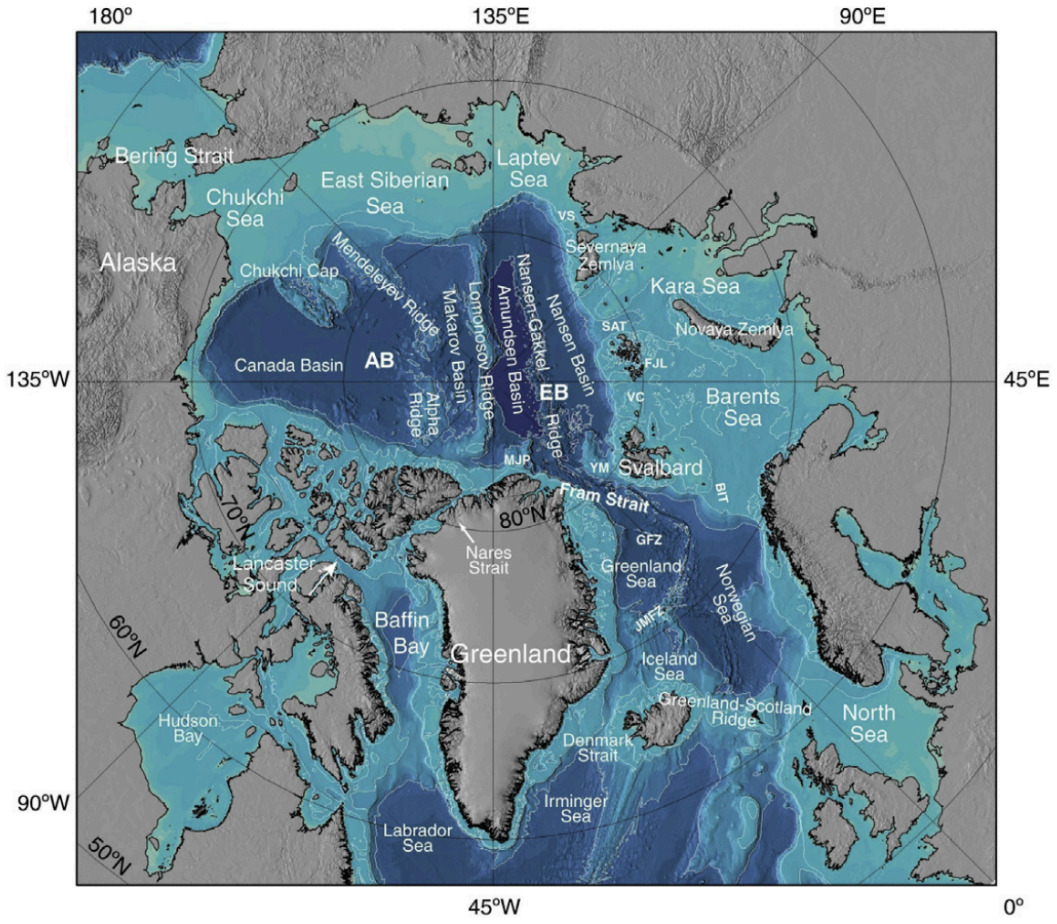

Figure 1.3 – Recent bathymetric map of the Arctic Mediterranean Sea based on Jakobsson et al. [2008]. (taken from Rudels [2015])

The Arctic Ocean is also called the "Arctic Mediterranean Sea", because it is almost entirely encircled by land (Figure 1.3). Thus its connection to the global ocean is limited to four narrow passages: (1) The Fram Strait, (2) the Barents Sea Opening, (3) the Barents Sea, (4) and the Canadian Arctic Archipelago (CAA). This limited exchange and the long Arctic coastlines lead to an important role of land-derived fluxes of water, carbon and nutrients for the Arctic Ocean physics and biogeochemistry. Despite its small size, 11% of the global river discharge drains into the Arctic Ocean [McClelland et al., 2012]. Out of this discharge, 70% comes from the six major Arctic rivers (Yenisey, Ob', Lena, Kolyma, Yukon, Mackenzie). On the Eurasian side, the Yenisey and Ob' drain into the Kara Sea, the Lena drains into the Laptev Sea, and the Kolyma into the East-Siberian Sea. On the Amerasian side, the Mackenzie river drains into the Beaufort Sea, while the Yukon drains into the North Pacific, with most of its runoff being transported via ocean currents through the Bering Strait into the Chukchi Sea.

1.2.2 Ocean Physics

1.2.2.1 Circulation

The circulation in the Arctic Ocean is dominated by lateral exchanges with the Atlantic and Pacific Oceans. The fate of Pacific waters (PW) and Atlantic Waters (AW) are presented separately.

From the Pacific ocean 0.8 ± 0.2 Sv (1 Sv = 10^6 m^3 s^{-1}) enter through the Bering Strait [Woodgate et al., 2010] (Table 1.1 and Figure 1.4). Given the average depth of ~ 50 m in the Bering Strait, the PW enter the Arctic Ocean only at the surface. This inflow has a significant seasonal signal. In summer, the water flow is stronger (1.2 Sv), warmer (>2 °C), and less saline (31.9 psu). In winter, it is weaker (0.4 Sv), colder (-1.9 °C), and more saline (33 psu) [Woodgate et al., 2005]. The inflowing waters from the Pacific Ocean account for one third of the Arctic Ocean heat influx [Woodgate et al., 2010], 30% of the Arctic Ocean freshwater influx [Serreze et al., 2006], and 25% of the nitrate influx [Torres-Valdés et al., 2013]. Within the Arctic Ocean, the PW divide, one part flowing along the North American coast towards the CAA while the other part flows along the Russian coast towards the East Siberian Sea. The horizontal extent of PW is limited by the position of the Transpolar drift, a wind driven surface current from the East-Siberian Sea towards the Fram Strait, and not by the bathymetry (e.g. the Lomonosov Ridge) [Steele et al., 2004]. Due to their low salinity and hence low density, the PW are vertically limited to the first 200 m by the more saline and dense AW [Coachman and Barnes, 1962]. Eventually, the PW leave the Arctic Ocean via the CAA and the Fram Strait into the Atlantic Ocean.

Compared to PW, the inflow of Atlantic water (AW) is ~17 times larger (14 Sv) and is separated into two branches (Figure 1.4). The main part of the water flux (12 Sv) enters the Arctic Ocean through the Fram Strait [Schauer et al., 2008; Rudels et al., 2008] along the eastern shelf slope off Spitzbergen. With a depth of 2600 m, the Fram Strait is the deepest passage into the Arctic Ocean. As a consequence of this depth, a large part of the inflowing AW current occurs below the surface

Table 1.1 – Net lateral transport of water in Sv (10^6 m^3 s^{-1}) across Arctic Ocean boundaries

	Observations	Sources
Fram Strait	-2.0 ± 2.7	Schauer et al. [2008]
	-1.7	Rudels et al. [2008]
Barents Sea	2.0	Skagseth et al. [2008]
	2.0	Smedsrud et al. [2010]
Bering Strait	0.8 ± 0.2	Woodgate et al. [2010]
CAA	-2.7 ± 0.2	Curry et al. [2014]

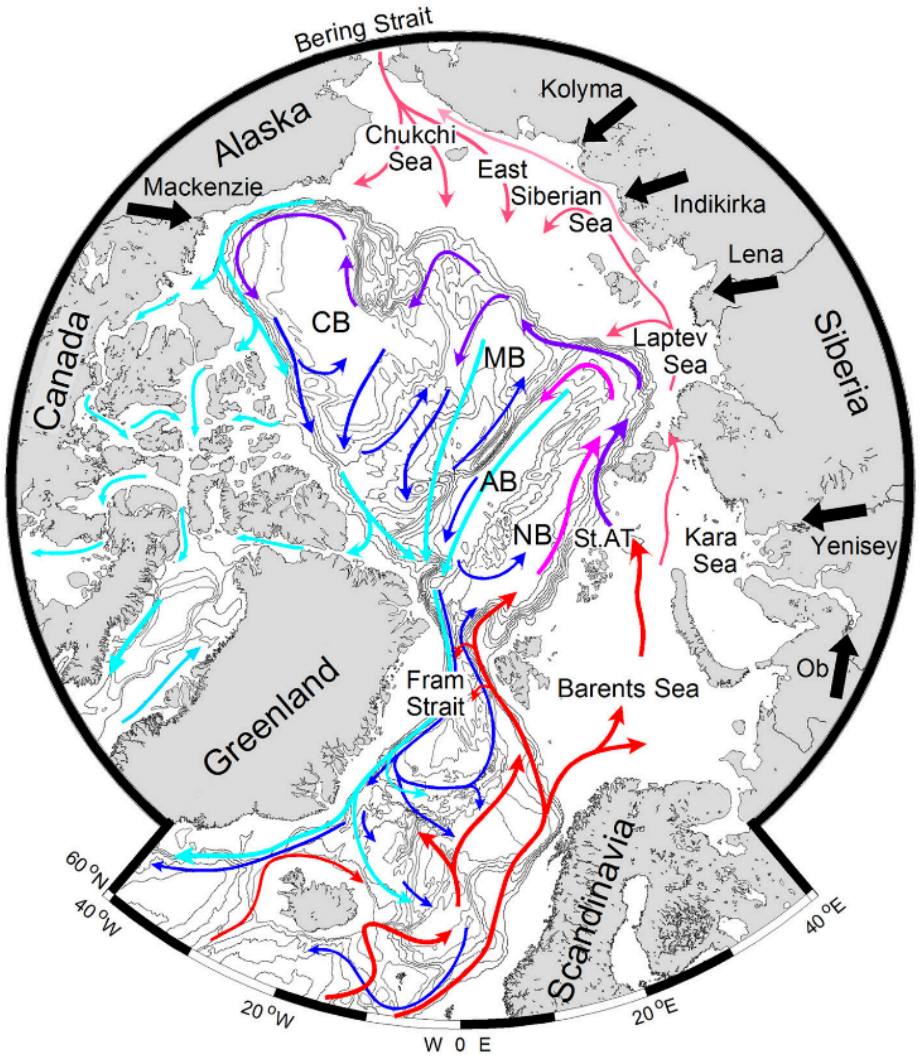

Figure 1.4 – Dominating Arctic Ocean currents with inflowing relative warms surface currents (red) and colder surface currents (light blue) together with intermediate and deep currents (burgundy and dark blue). Features of the Arctic Ocean are abbreviated as follows: Canadian Basin (CB), Makarov Basin (MB), Amundsen Basin (AB), Nansen Basin (NB) and St. Anna Trough (St.AT). (taken from Anderson and Macdonald [2015])

and these waters masses are thus not in contact with the cold air of the Arctic region and can conserve their warm temperature (>0 °C). After entering the Nansen basin, the Fram Strait current splits into two currents: One part returns directly into the Atlantic Ocean through recirculation within the Fram Strait, while the other current flows further north to supply the largest fraction of AW inside the Arctic Ocean [Beszczynska-Möller et al., 2011]. Next to the Fram Strait, the Barents Sea Opening (BSO) is the second gateway from the Atlantic Ocean into the Arctic Ocean. Around 2 Sv of water flow through this passage [Skagseth et al., 2008; Smedsrud et al., 2010]. As opposed to the Fram Strait, the Barents Sea Opening is on average only 230 m deep. Thus, the AW is in constant exchange with the atmosphere and cools from 6°C down below 0°C while flowing through the BSO [Smedsrud et al., 2010]. This decrease in temperature, accompanied by brine formation, leads to the formation of dense Arctic Ocean waters [Midttun, 1985; Gammelsrød et al., 2009]. These dense water masses flow through the St. Anna Through into the Nansen basin [Schauer et al., 2002], where they either sink down to depth between 1000 m and the ocean floor [Rudels et al., 1994] or mix with the current originating from the Fram Strait. These merged AW from the Fram Strait and the BSO form the Arctic Ocean Boundary Current (AOBC) [Rudels et al., 1999]. Vertically positioned between 500 m and 3000 m, the AOBC transports ~5 Sv along the continental slope of the Nansen basin, of which 3 Sv flow back to the Fram Strait and 2 Sv continue along the continental boundary towards the Eurasian basin [Woodgate et al., 2001]. This counter-clockwise circulation is typical for the Arctic Ocean and is also observed, with decreasing strength, in the Makarov and Canada basins [Schauer et al., 2002; Shimada et al., 2004]. Eventually, the AW leave the Arctic Ocean through the CAA and the Fram Strait along the eastern coast of Greenland. The combined flows of AW and PW yield a net outflow of 1.7–2.0 Sv in the Fram Strait [Schauer et al., 2008; Rudels et al., 2008] and 2.7 Sv through the CAA [Curry et al., 2014] compensated by a net inflow of ~2 Sv through the BSO [Skagseth et al., 2008; Smedsrud et al., 2010] and 0.8 ± 0.2 Sv through the Bering Strait [Woodgate et al., 2010]. The unbalanced budget highlights the scarcity of measurements and associated uncertainties in existing measurements.

1.2.2.2 Sea Ice

One of the most remarkable features of the Arctic Ocean is its sea ice cover. In pre-industrial conditions, the sea-ice extent ranged from $9 \times 10^6 \text{km}^2$ in September to $16 \times 10^6 \text{km}^2$ in March (Figure 1.5) [Gloersen et al., 1993]. The only year-round ice-free region in the Arctic Ocean is the Barents Sea, as it receives large quantities of heat from the inflowing AW [Smedsrud et al., 2010]. From 1953 to 2011, the sea ice extent is in constant decline (-0.44×10^6 km^2 decade^{-1}). This rate almost doubled in the second half of this period (1981–2010) to -0.86×10^6 km^2 decade^{-1} [Serreze and Stroeve, 2015a]. This decrease is mainly explained by a strong radiative forcing as a consequence of rising greenhouse gas concentrations in the atmosphere [Serreze et al., 2007; Notz and Stroeve, 2016]. While until recently the first ice-free summers were predicted by models to occur around

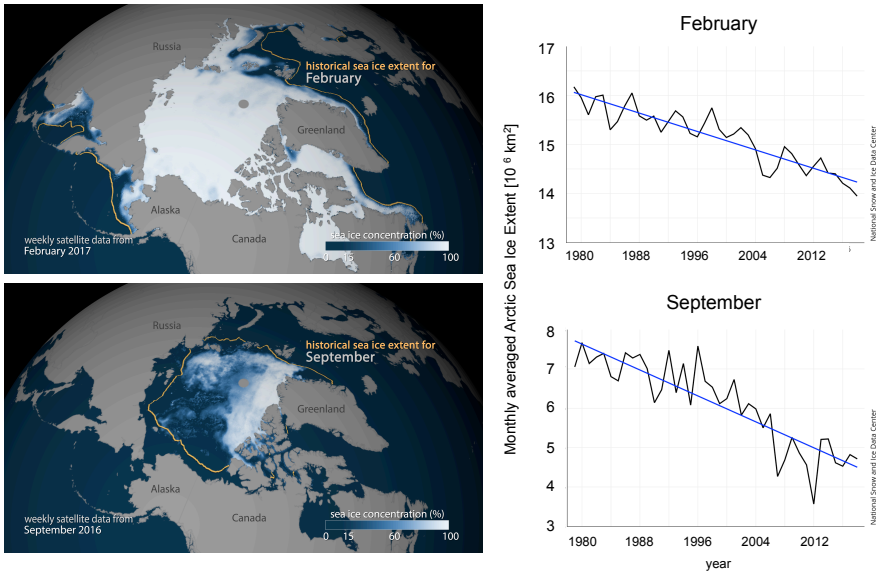

Figure 1.5 – Left: Weekly Arctic sea ice for the week of September 10, 2016, and February 12, 2017. Places where satellite-detected sea ice concentration was below 15% are colored dark blue. Places with 15% or more ice concentration are colored shades of lighter blue to white (100% ice covered). The gold line shows the historic (1981-2010) median extent for September (beginning of animation) and February (end). (taken from NOAA Climate.gov, Dan Pisut). Right: Time series of monthly Arctic Ocean sea ice extent from 1978 to 2018 in Februar and September (National Snow and Ice Data Center).

2070 [Boé et al., 2009], observations in the last years exhibited a faster reduction rate of Arctic sea ice extent, so that the first ice-free summer could occur as early as 2030 [Overland and Wang, 2013].

Sea ice strongly influences the Arctic Ocean circulation. The release of fresh water during sea ice melting periods leads to strong stratification, whereas brine rejection during sea ice formation leads to a deepening of the mixed layer. The sea ice also limits the impact of wind on the Arctic Ocean circulation and the upwelling of nutrient and carbon rich waters in the coastal seas [Mathis et al., 2012]. Apart from regulating the Arctic Ocean circulation, sea-ice confines air-sea gas exchanges and heat exchanges at the ocean surface and limits primary production by preventing light from entering the ocean.

1.2.3 Ocean Biogeochemistry

1.2.3.1 Carbon cycle

The ocean carbon cycle is part of the global carbon cycle, connected to the atmosphere via air-sea CO_2 exchange and to the terrestrial biosphere through river runoff. In the pre-industrial state, the global ocean received a net carbon riverine influx of 0.78 ± 0.41 Pg C yr^{-1}, which was compensated pre-industrial outgassing via the air-sea interface [Resplandy et al., 2018]. With climate change and increasing atmospheric CO_2, the ocean turned from a source of carbon for the atmosphere to a sink, taking up approximately 23% of the additional atmospheric carbon since the beginning

of the industrial revolution [Le Quéré et al., 2018]. While riverine carbon enters the ocean simply as a part of the freshwater flux, the air-sea CO_2 flux is a complicated gas exchange between the atmosphere and the ocean. It depends on the difference in partial pressure of CO_2 (pCO_2) between the ocean and the atmosphere, the wind speed, and the solubility of CO_2 in sea water. Generally the exchanges that happens on very small scales is determined from the bulk formula:

$$F = k\, s\, (pCO_2^{oc} - pCO_2^{atm}), \tag{1.1}$$

where k is the transfer velocity, s the solubility of CO_2 in sea water, and pCO_2^{oc} and pCO_2^{atm} are the partial pressures in the ocean and the atmosphere. The solubility of CO_2 in sea water increases towards lower temperature and salinity [Weiss, 1974]. The transfer velocity k mainly depends on wind speed at the surface and other minor factors including turbulent mixing, surface waves, bubbles, and molecular diffusion [Jähne and Haußecker, 1998]. Once inside the ocean, the dissolved CO_2 reacts with the water to form bicarbonate ion (HCO_3^-):

$$CO_2 + H_2O \Leftrightarrow H^+ + HCO_3^-, \tag{1.2}$$

Some of the released hydrogen ions will then react with carbonate ion (CO_3^{2-}) to form more HCO_3^-:

$$H^+ + CO_3^{2-} \Leftrightarrow HCO_3^-, \tag{1.3}$$

The sum of CO_2, HCO_3^-, and CO_3^{2-} is defined as total dissolved inorganic carbon (C_T).

In the Arctic Ocean, the carbon cycle is driven by lateral transport across its ocean boundaries, riverine inputs, air-sea exchange, and storage (Table 1.2). At present-day, the Arctic Ocean takes up 66–199 Tg C yr^{-1} of CO_2 from the atmosphere [Bates and Mathis, 2009]. Two thirds of the air-sea CO_2 uptake occurs in the Barents and Chukchi Seas, the two shelves that receive a net inflow from the adjacent oceans ("inflow" shelves) [Sakshaug, 2004; Bates and Mathis, 2009]. This high uptake in the "inflow" shelves is caused by cooling of inflowing waters and an associated increase in solubility of CO_2 and by a higher biological productivity sustained by the large supply of nutrients from the Atlantic and Pacific Oceans [Carmack and Wassmann, 2006]. In addition to the air-sea flux, 66 Tg C yr^{-1} is supplied by river fluxes, 41 Tg C yr^{-1} in the form of C_T [Tank et al., 2012c] and 25 Tg C yr^{-1} in the form of DOC [Holmes et al., 2012]. In contrast to the air-sea CO_2 flux, the riverine fluxes are mainly (81%) located in the "interior" Arctic Ocean shelves [Tank et al., 2012c], the shelves that are not adjacent to the Arctic or Pacific Ocean (Figure 1.4). To close the C_T budget in the Arctic Ocean, an equivalent amount of C_T (231 ± 49 Tg C yr^{-1}) leaves the Arctic Ocean laterally into the Atlantic Ocean via the Fram Strait and the CAA [MacGilchrist et al., 2014]. Although the carbon budget is usually closed by burial of organic matter in sediments, burial is almost negligible in the Arctic Ocean given the observed sedimentation rate of only a few millimeters per thousand years [Backman et al., 2004]. This small sedimentation rate is in line with the export production in the Arctic Ocean, which is one order of magnitude smaller than in the global ocean [Anderson et al., 2003; Honjo et al., 2010].

Table 1.2 – Arctic Ocean carbon budgets in Tg C yr^{-1}. Positive numbers represent fluxes into the AO.

	Present day	Anthropogenic	Preindustrial[a]
Net ocean transport	-231 ± 49[b]	~ 29[c]	~ -202
Land & river sources	66 ± 6[d]	0	65
Air-sea flux	133 ± 66[e]	~ 26[c]	~ 107
Storage	-55 ± 7[c]	-55 ± 7[c]	0
Sum	-88 ± 83	0	~ -30

[a] Calculated as the difference between present-day and anthropogenic component
[b] From MacGilchrist et al. [2014]
[c] Olsen et al. [2015]
[d] Tank et al. [2012c]; Holmes et al. [2012]
[e] Bates and Mathis [2009]

1.2.3.2 Anthropogenic carbon cycle

The natural carbon cycle in the ocean is perturbed as a consequence of increasing atmospheric CO_2 during the period of industrialization [Revelle and Suess, 1957]. Out of this additional C_{ant}, around one quarter was taken up by the global ocean so far [Le Quéré et al., 2015]. After being taken up from the atmosphere, this anthropogenic carbon (C_{ant}) is redistributed in the global ocean. Unfortunately, the large natural background of C_T makes it practically impossible to measure C_{ant} directly. Several attempts were made to estimate C_{ant}, such as using corrections for the biological effects [Gruber et al., 1996] or using the concurrent measures of transient tracers such as CFC-12 or SF_6 [Hall et al., 2002; Waugh et al., 2004]. Taking account a series of existing methods, the global C_{ant} inventory is estimated to be 155 ± 31 Pg C normalized to 2011 [Khatiwala et al., 2013]).

Out of this C_{ant}, ~2% are stored in the Arctic Ocean [Tanhua et al., 2009]. Given that the Arctic Ocean volume represents only 1% of the global ocean volume, the Arctic Ocean is a relatively strong sink of C_{ant}. This C_{ant} enters the Arctic Ocean via air-sea CO_2 flux and lateral flux from the Atlantic Ocean and Pacific Ocean. While direct estimates of the air-sea flux of C_{ant} in the Arctic Ocean do not exist, the lateral fluxes across the Arctic Ocean boundaries can be estimated by multiplying measured velocity fields along the boundaries with estimations of C_{ant} based on transient tracers. An inflow of 41 ± 8 Tg C yr^{-1} through the Barents Sea Opening [Jeansson et al., 2011] plus an inflow of 18 Tg C yr^{-1} in the Bering Strait [Olsen et al., 2015] minus an outflow of 1 ± 17 Tg C yr^{-1} through the Fram Strait [Jeansson et al., 2011; Stöven et al., 2016] and an outflow of 29 Tg C yr^{-1} through the CAA [Olsen et al., 2015] lead to a net lateral C_{ant} influx of 29 Tg C yr^{-1}. By combining this net lateral C_{ant} influx estimate with the estimated yearly storage rate of C_{ant} ($\sim$ 55 Tg C yr^{-1}), the yearly air-sea C_{ant} flux is estimated to be $\sim$ 26 Tg C yr^{-1} [Olsen et al., 2015]. This estimated

air-sea C_{ant} flux is slightly lower than the lateral inflow of C_{ant}. For different reasons, these estimates come with very large uncertainties: First, C_{ant} concentrations are data-based estimates and not direct measurements, second observations of transient tracers, on which C_{ant} estimates are based, were not taken at the same time as the velocity measurements, and third measurements are not taken continouusly and do not capture all possible variations in time.

1.2.3.3 Ocean acidification

As a consequence of C_{ant} uptake, the concentration of hydrogen ions in the ocean increases and the concentration of CO_3^{2-} decreases (Equations 1.2 and 1.3). This increase in hydrogen ion concentration corresponds to a decrease in pH on the total pH scale and a shift towards more acidic conditions [Orr et al., 2005]. This phenomenon is called ocean acidification and will affect the capability of calcifying organisms, such as reefs [Hoegh-Guldberg et al., 2007], plankton [Kawaguchi et al., 2013] or shellfish [Swiney et al., 2015], to form calcium carbonate. Eventually, cascading effects on the entire ocean ecosystem are expected [Gattuso and Hansson, 2011; Riebesell et al., 2013]. Ocean acidification can be measured in different ways, the most prominent among them are changes in pH and the calcium carbonate ($CaCO_3$) saturation state (Ω). The pH scale is a logarithmic scale of hydrogen ions ($pH = -\log_{10}[H^+]$) that describes the acidity (<7) or basicity (>7) of a liquid. Ω is a chemical measure that indicates supersaturation ($\Omega > 1$) or undersaturation ($\Omega < 1$) of $CaCO_3$. It is defined as the product of calcium ion concentration (Ca^{2+}) and CO_3^{2-} normalized by their apparent solubility product (K'_{sp}):

$$\Omega = \frac{[Ca^{2+}] \times [CO_3^{2-}]}{K'_{sp}}, \tag{1.4}$$

With reduced CO_3^{2-}, Ω is reduced and it becomes harder for calcifying organisms to form calcium carbonate $CaCO_3$:

$$Ca^{2+} + CO_3^{2-} \Leftrightarrow CaCO_3, \tag{1.5}$$

The definition of Ω implies that waters with $\Omega < 1$ are undersaturated with respect to calcium carbonate. In this case, the direction of equation 1.5 changes and and the prevailing environmental conditions can only lead to $CaCO_3$ dissolution. The dissolution of calcium carbonate under corrosive conditions was demonstrated in laboratory studies [Gattuso et al., 1998; Langdon et al., 2000] and also directly observed in the ocean (after a volcanic eruption that caused the temporary reduction of pH and Ω) (Figure 1.6) [Hall-Spencer et al., 2008]. Ω is usually defined with respect to the carbonate minerals calcite (Ω_{calc}) and aragonite (Ω_{arag}), which have the same chemical formula but a different crystal structure leading to different solubility (K'_{sp})

Since the beginning of the industrial revolution and the increased uptake of CO_2 from the atmosphere, the average global ocean pH has decreased from 8.2 to 8.1 [Doney et al., 2014] with a rate of -0.0018 ± 0.0004 yr^{-1} from 1991 to 2011 [Lauvset et al., 2015]. In the Arctic Ocean, the preindustrial surface pH was higher than the globally averaged surface pH, but the comparatively

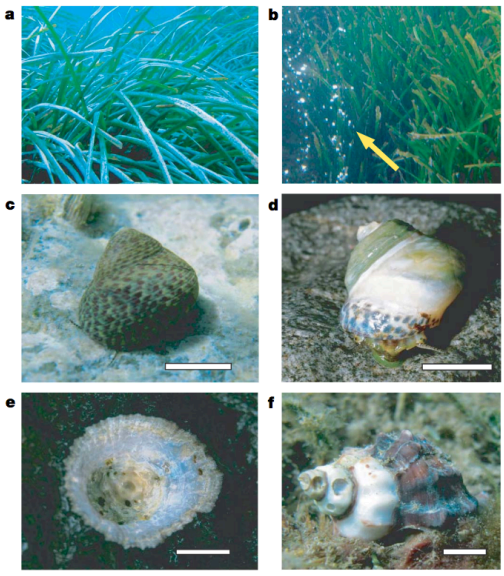

Figure 1.6 – **Dissolution of calcified organisms due to naturally acidified seawater. a,b,** *Posidonia oceanica* with heavy overgrowth of Corallinaceae at pH 8.2 (**a**) and lacking Corallinaceae at mean pH 7.6 (**b**); arrow indicates bubbles from the CO_2 vent field. **c,d,** Typical examples of *O. turbinata* with the periostracum intact at pH 8.2 (**c**) and with old parts of the periostracum removed at mean pH 7.3 (**d**). **e,f,** Live *P. caerulea* (**e**) and *H. trunculus* (**f**) showing severely eroded, pitted shells in areas of minimum pH 7.4. Scale bars represent 1 cm. (taken from Hall-Spencer et al. [2008])

stronger decrease in Arctic Ocean pH is expected to reverse this situation during the course of the 21st century [Steinacher et al., 2009]. Although the Arctic Ocean exhibits highest pH under pre-industrial conditions, Arctic Ocean Ω is smaller than global Ω. The positive effect of higher pH on Ω is compensated by low Arctic temperatures, which reduce the solubility of CO_3^{2-} and thus lower Ω concentrations below global surface ocean averages. Further, model studies suggest that the more soluble $CaCO_3$ mineral aragonite will become seasonally undersaturated in the surface layers of the Arctic Ocean within decades and that the entire Arctic Ocean will become undersaturated towards the end of the 21st century under the RCP8.5 scenario [Steinacher et al., 2009]. Already today, this undersaturation of Arctic waters is observed close to river mouths [Chierici and Fransson, 2009; Tremblay et al., 2015; Semiletov et al., 2016] and in subsurface waters in the Canada basin [Yamamoto-Kawai et al., 2009]. At the same time, ocean acidification is also occurring in the deep Arctic Ocean. While the deep Ocean is naturally undersaturated towards aragonite, the depth at which waters become undersaturated, the aragonite saturation horizon (ASH), is found at present-day at around 1900 m. During the last 250 years, its shoaling has been estimated to be 100–200 m. The deep, undersaturated Arctic Ocean waters are expected to rise further and to merge with the undersaturated surface waters towards the end of the 21st century [Steinacher et al., 2009; Anderson et al., 2010].

1.2.3.4 Primary Production

While ocean acidification is a direct effect of the increased atmospheric CO_2 levels, the Arctic Ocean biogeochemistry is also impacted by indirect effects from a changing climate. For instance, decreasing sea-ice and enhanced light availability led to an increase of PP by 30% in the Arctic Ocean from 1998 to 2012 [Arrigo and van Dijken, 2015].

Ocean PP describes synthesis of organic matter from inorganic carbon and nutrients by primary producers. The produced organic matter stands at the beginning of the ocean food chain and thus provides the source of energy for almost all life in the ocean. PP is limited by lights, phosphorus (P), nitrogen (N), silicon (Si), iron (Fe), or a combination of them. About two thirds of the produced organic matter is quickly remineralized in the euphotic layer by bacteria and zooplankton [Falkowski et al., 1998]. The remaining third sinks towards the ocean floor and only a small part ends up in the sediments. The total amount of global ocean PP is estimated to be 58 ± 7 Pg C yr^{-1} [Buitenhuis et al., 2013].

Out of the global ocean PP, 1% (433 ± 94 Tg C yr^{-1}) is occurring in the Arctic Ocean [Codispoti et al., 2013; Hill et al., 2013; Pabi et al., 2008]. Around half of the Arctic Ocean PP is located in the“inflow” shelves and half in the “interior” shelves [Arrigo and van Dijken, 2015](Figure 1.7). In the "inflow" shelves high PP appears to be mainly driven by inflowing nutrients from the Atlantic and Pacific Oceans [Codispoti et al., 2013; Popova et al., 2013; Walsh et al., 1989] and a relatively large open water area (not covered by sea ice) compared to the other shelves [Pabi et al., 2008]. In the “interior” shelves, nutrient supply is dominated by deep water upwelling at the shelf break [Carmack and Chapman, 2003] and riverine delivery of nutrients [Frey and McClelland, 2009]. Although these “interior” shelves exhibit the lowest coastal PP in the Arctic Ocean, their PP increased fastest due to their relatively large decline in sea ice cover in the last years [Arrigo and van Dijken, 2015].

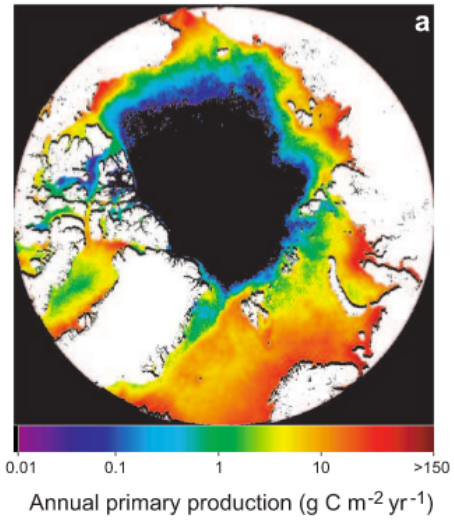

Figure 1.7 – Climatology (1998-–2006) for annual primary production. (taken from Pabi et al. [2008])

In contrast to the projected global negative trend of PP [Bopp et al., 2013], PP increased in the Arctic Ocean by 30% from 1998 to 2012 [Arrigo and van Dijken, 2015]. This change is mainly attributed to temperature increase, and shrinking sea-ice cover and a consequently longer growing season [Stammerjohn et al., 2012]. In the future, a Coupled Model Intercomparison Project Phase 5 (CMIP5) study using 11 climate models projects a further increase of Arctic Ocean PP by 58 ± 105 Tg C yr^{-1} [Vancoppenolle et al., 2013]. The large uncertainty of these projections reflects the ongoing debate about the future development of PP in the Arctic Ocean. For instance, it is not yet clear if upwelling of deep water will be suppressed by more fresh water input from melting sea ice and increasing river runoff [Tremblay et al., 2008] or if larger ice-free areas will increase the wind-ocean interaction and thus increase the mixed layer and enhance nutrient supply [Tremblay et al., 2011]. In addition, the change in riverine delivery of nutrients with increasing river runoff and thawing permafrost (Section 1.3.2) and its consequences on the coastal PP remain unclear.

1.3 Arctic rivers

1.3.1 River runoff

Comparatively to any other part of the global ocean, the Arctic Ocean is the region where river discharge plays the most important role for the physical and biogeochemical functioning. The Arctic watersheds cover 15% of global terrestrial landmass and rivers draining into the Arctic Ocean represent 11% of the global river discharge and ~ 20% of the fresh water input into the Arctic Ocean [McClelland et al., 2012]. About 70% of this Arctic river discharge comes from the six major rivers in the Arctic (Yenisey, Ob', Lena, Kolyma, Yukon, Mackenzie). Together, their watersheds cover 53% of pan-Arctic watershed area and extend south down to roughly 45°N (Figure 1.8). Since the first records of Arctic river discharge in 1939, a constant increase in freshwater fluxes has been observed. In the main Eurasian rivers (Yenisey, Lena, Ob', Pechora, Kolyma, and Severnaya Dvina), the runoff increased by 7% from 1936 to 1999, corresponding to an average increase rate of 2 km^3 yr^{-1} [Peterson et al., 2002; McClelland et al., 2004]. This rate has increased over the observed period up to 5.6 km^3 yr^{-1} averaged over the last 36 years of the 20^{th} only [McClelland et al., 2006]. Different to the Eurasian rivers, the North American river discharge decreased by 10% from 1964 to 2003 [Déry and Wood, 2005]. In recent years (1989–2007), this trend reverted and an increase of 15% has been reported for this shorter period [Déry et al., 2009]. A further rise of pan-Arctic river discharge by 16–35% during the next century is expected as a result of increasing precipitation, thawing permafrost, and changing vegetation [Peterson et al., 2002; Lawrence and Slater, 2005; Nohara et al., 2006]. Increased river discharge is expected to lead to a dillution of coastal waters and a stronger stratification of the Arctic Ocean surface waters. Possible consequences for the Arctic Ocean biogeochemistry include enhanced ocean acidification due to the dilution of ocean water [Yamamoto-Kawai et al., 2009; Semiletov et al., 2016; Bates et al., 2009], a reduced uptake of

atmospheric CO_2 and a reduced PP due to the stronger stratification [Cai et al., 2010].

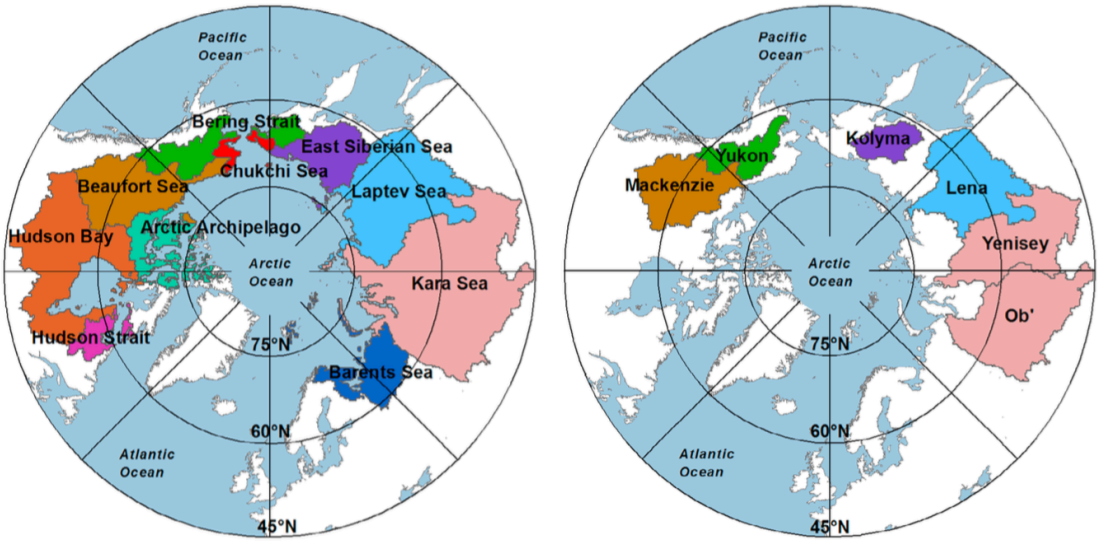

Figure 1.8 – (left) The 10 major sea basins of the Arctic Ocean. Note that the Bering Strait and Chukchi sea basins span the North American and Eurasian landmasses. (right) The six PARTNERS watersheds. The color of each watershed is identical to the sea basin within which it lies. (taken from Tank et al. [2012c])

1.3.2 Carbon and nutrient fluxes

The Arctic rivers do not only deliver freshwater into the Arctic Ocean, but also carbon and nutrients. About 13–15% of global riverine C_T drains into the Arctic Ocean [Tank et al., 2012c] and the quantity of dissolved DOC fluxes from Arctic rivers is ~2.5 times higher than the DOC delivery from temperate rivers of similar watershed size and runoff [Raymond et al., 2007]. These high carbon fluxes affect the Arctic Ocean biogeochemistry in several ways. For example, the remineralization of riverine DOC fluxes increases pCO_2 in the surface layers of the Arctic Ocean and leads locally to outgassing of CO_2 [Anderson et al., 2009]. On the pan-Arctic scale, riverine DOC flux is estimated to reduce the uptake of atmospheric CO_2 by 10% [Manizza et al., 2011]. The increase in pCO_2 due to the mineralization of riverine DOC fluxes also enhance ocean acidification in coastal areas [Semiletov et al., 2016]. In addition to DOC fluxes, ocean acidification is also enhanced by land-derived C_T and total alkalinity (A_T) fluxes [Chierici and Fransson, 2009; Bates et al., 2009]. In Arctic rivers, the A_T:C_T ratios of 0.7–0.9 [Tank et al., 2012c] are lower than typical open ocean A_T:C_T ratios of 1.1–1.2 and thus reduce this ratio in coastal areas and thereby enhance acidification. In addition to these effects from carbon fluxes, riverine nutrient fluxes also impact Arctic Ocean biogeochemistry and are estimated to sustain 1–10% of Arctic Ocean PP [Letscher et al., 2013; Le Fouest et al., 2013, 2015, 2018]. This increase in PP due to riverine nutrients reduces surface ocean C_T and hence surface ocean acidification, whereas the remineralization of the produced organic matter at the bottom of the shelf increases C_T and enhances bottom shelf ocean acidification [Bates et al., 2005; Anderson et al., 2011b].

Despite the importance of river fluxes of carbon and nutrients for the Arctic Ocean biogeochemistry, measurements of carbon and nutrient fluxes from Arctic rivers remained scarce until the beginning of the 21st century [Bring and Destouni, 2009] and in the case of nitrogen flux measurements "grossly in error" [Holmes et al., 2000, 2001]. In 2002, the Pan-Arctic River Transport of Nutrients, Organic Matter, and Suspended Sediments project (PARTNERS) was launched as the first initiative to coordinate measurements of carbon and nutrients concentrations in the six largest Arctic rivers. These measurements captured the full seasonal cycle for the six largest rivers (Figure 1.8) [McClelland et al., 2008]. The PARTNERS project was later embedded into the Arctic Great River Observatory (ArcticGRO), which is still in operation (https://arcticgreatrivers.org/). Based on watershed characteristics, the C_T (30 Tg C yr^{-1}) and DOC (18 Tg C yr^{-1}) fluxes from the six largest rivers were extrapolated to all Arctic rivers, yielding a pan-Arctic riverine C_T flux of 57 ± 10 Tg C yr^{-1} [Tank et al., 2012c] and a pan-Arctic riverine DOC flux of 38 Tg C yr^{-1} [Manizza et al., 2009]. A pan-Arctic extrapolation of nutrient fluxes does not exist yet, but Holmes et al. [2012] provide a first estimate by upscaling the fluxes from the six largest rivers to the other rivers assuming that the average yields for the unmonitored rivers are the same as for the monitored rivers. Note that not all Arctic rivers drain into the Arctic Ocean, leading to an important distinction between Arctic river fluxes and river fluxes into the Arctic Ocean.

Arctic river fluxes have strongly changed in the past and they are estimated to change further during the 21st century. For example, the pan-Arctic DOC river fluxes are estimated to have increased by 0.037 Tg C yr^{-2} over the 20th century using a biogeochemical process model [Kicklighter et al., 2013]. A further increase during the 21st is simulated as a result of the decline in near-surface permafrost extent from 10.5 million km^2 to 1.0 million km^2 in 2100 [Stendel and Christensen, 2002; Lawrence and Slater, 2005] and advancing tree lines [Harsch et al., 2009]. The ongoing decrease in permafrost cover is also stimulating weathering of the underlying bedrock and, hence, led to a rise in A_T fluxes over the last 35 years by 185% and 134% for the Yenisei and Ob, respectively [Drake et al., 2018]. Further increase in weathering and associated increase of A_T and C_T fluxes is projected for the 21st century [Beaulieu et al., 2012]. As opposed to riverine carbon fluxes, projections of nutrient fluxes exist only locally. For instance, in the West-Siberian watersheds, increases in concentrations of dissolved organic nitrogen (DON) (32–53%), total dissolved nitrogen (TDN) (30–50%) and total dissolved phosphate (TDP) (29–47%) have been simulated [Frey et al., 2007]. Given the importance of river fluxes for the present-day biogeochemistry of the Arctic Ocean, future changes of these fluxes might have a significant influence on projections of NPP, air-to-sea CO_2 fluxes, and ocean acidification.

1.4 Ocean-biogeochemical modeling in the Arctic Ocean

Ocean models present a useful tool to improve the understanding of the ocean's circulation and the biogeochemistry. They allow to make projections, sensitivity studies, and to constrain uncertainties. Models are especially valuable in the Arctic Ocean, where observations are scarce due to the Arctic's hostile environment, e.g. polar winter, very low temperatures, and ice cover.

Depending on the scientific question, the Arctic Ocean biogeochemistry is simulated by models of different complexity and resolution, ranging from simple box models [Anderson et al., 1998; Luo et al., 2016], over earth-system models [Steinacher et al., 2009; Vancoppenolle et al., 2013], to local high-resolution models [Popova et al., 2013; Le Fouest et al., 2015; Manizza et al., 2019]. Despite important progress in the last years, modeling of the Arctic Ocean remains a challenge, due to the Arctic Ocean's large and shallow shelf seas, its sea-ice, its small-scale deep water formation, its narrow scale boundary currents, and the small passages that connect the Arctic Ocean to the global ocean. Moreover, the scarcity of data against which the models could be evaluated makes the situation even more complicated.

1.4.1 Ocean-biogeochemical models

Ocean general circulation models (OGCM) coupled to a sea ice model and a biogeochemical models can be used to simulate the Arctic Ocean circulation and biogeochemistry. The OGCM simulates the ocean circulation, temperature, and salinity based on the Navier-Stokes equations and the equation of state. The coupled sea ice model simulate the horizontal extent, and the thickness of the sea ice as well as its advection by wind and surface currents. Lastly the biogeochemical model simulates the spatio-temporal distribution of the main components of the ocean chemistry, such as C_T, A_T, and inorganic nutrients, and biology, such as phytoplankton, zooplankton, and organic matter. The components of the biogeochemical model are moved by advection, diffusion, and sinking and have internal sources and sinks, such as the consumption of carbon and nutrients during simulated primary production and the consequent production of organic matter. In addition C_T and oxygen are exchanged with the atmosphere via air-sea CO_2 flux.

Dependent on the scientific question, the complexity and resolution of the model change. For exampled, Manizza et al. [2009] used an OGCM coupled to a single tracer model to estimate the fate of riverine DOC in the Arctic Ocean. In a next step, Manizza et al. [2011] increased the model complexity by adding five more tracers (C_T, A_T, PO_4, dissolved organic phosphorus (DOP), and dissolved O_2) to calculate surface pCO_2 and assess the influence of the riverine DOC fluxes on the air-sea CO_2 exchange. Lastly, Manizza et al. [2013] included PP in the model to estimate the changes of air-sea CO_2 fluxes from 1996 to 2007 as realistic as possible. This stepwise increase of model complexity demonstrates that, depending on the scientific question, highest model complexity does not necessarily provide the best results.

The above presented model studies focused on past or present conditions, allowing the OGCM

to be forced with historic climate conditions, such as reanalyses of sea surface temperature and surface winds. As opposed to simulations focusing on the past or present-day Arctic Ocean, future simulations covering the 21st century and beyond are generally coupled to an atmospheric general circulation model (AGCM), which simulates the future climate. However, the computation of the atmospheric and the ocean dynamics at the century scale is not yet computationally feasible with a high resolution model. Thus for relatively long-term projections, one has to resort to models using a relatively coarse resolution. As an example, Steinacher et al. [2009] used the coupled climate–carbon cycle model NCAR CSM1.4-carbon at a relatively coarse resolution (0.8–3.6°) to make projections of ocean acidification, e.g. Ω_{arag}, until the end of the 21st century. The same model was later used to estimate the long-term decline of Ω_{arag} in the Arctic Ocean until 2500 and the (ir-)reversibility of these changes even if CO_2 were stopped in 2100 [Frölicher and Joos, 2010]. The trade-off of using coarse resolution models is that small scale ocean processes might be wrongly simulated. For instance, coarse resolution models simulate a lower rate of deep Arctic Ocean acidification [Ciais et al., 2013] as the expected rise based on data-based C_{ant} [Anderson et al., 2010].

Despite the importance of the river fluxes for the ocean biogeochemistry (Section 1.3.2), they are often only implemented partly [Manizza et al., 2011, 2013; Le Fouest et al., 2013, 2015] or not at all [Steinacher et al., 2009; Frölicher and Joos, 2010; Popova et al., 2013; Ilyina et al., 2013; Tjiputra et al., 2013; Manizza et al., 2019]. While this has little influence on the global ocean, it may substantially influence model results in the Arctic Ocean. For example, a set of five different models simulate very different NPP in the Arctic Ocean, mainly due to large differences in light and nutrient availability [Popova et al., 2012] and projections of Arctic NPP range from a simulated decrease in Arctic NPP of 21% to a simulated increase of NPP of 39% [Vancoppenolle et al., 2013]. One reason for the difference in nutrient availability across the models is the different external forcing, including river fluxes.

1.4.2 Coupled Model Intercomparison Project (CMIP)

In addition to single model studies, the Coupled Model Intercomparison Project (CMIP) coordinated by the World Climate Research Program (WCRP) represents the largest coordinated climate model project. The results of the CMIP simulations are an essential part of the Intergovernmental Panel on Climate Change (IPCC) assessment report. The latest published simulations (CMIP5) were made available in February 2013 and include results from 20 climate modeling groups around the world. These climate models are comprised of coupled atmospheric, ocean, land surface, and sea ice models. The simulations made by these models include historical reanalyses, projections following different CO_2 concentration pathways, and idealized simulations. Due to limited computational capacities, the ocean components of these climate models have typically coarse horizontal resolutions ($\sim 1°$), which cannot capture the small scale features of the Arctic Ocean

bathymetry.

Despite these limitations, CMIP5 type simulations were used in several instances to improve our understanding of the Arctic Ocean. For instance, Vancoppenolle et al. [2013] compared the output of 11 Earth-System Models and find an increase in PP of 58 ± 105 Tg C yr^{-1} during the 21^{st} century (Figure 1.9c). The large uncertainty highlights the differences between model results and their difficulty to make robust projections in the Arctic Ocean. Similarly projections of future ocean acidification were made by calculating Ω_{arag} from 11 different CMIP5 models [Ciais et al., 2013] and results show that polar regions, especially the Arctic Ocean, are the first ones to become undersaturated with respect to calcium carbonate (Figure 1.9). Although these simulations give a first general idea, they do not simulate the measured local extremes in low surface ocean Ω_{arag} [Chierici and Fransson, 2009; Semiletov et al., 2016] and the data-based projected rise of the ASH in the Arctic Ocean by 2100 [Anderson et al., 2010]. While model resolution certainly plays a role for the differences between model results and observational studies, the rudimentary or non-exisiting implementation of river fluxes in these models may be another important cause for differences in simulated Ω_{arag} and PP.

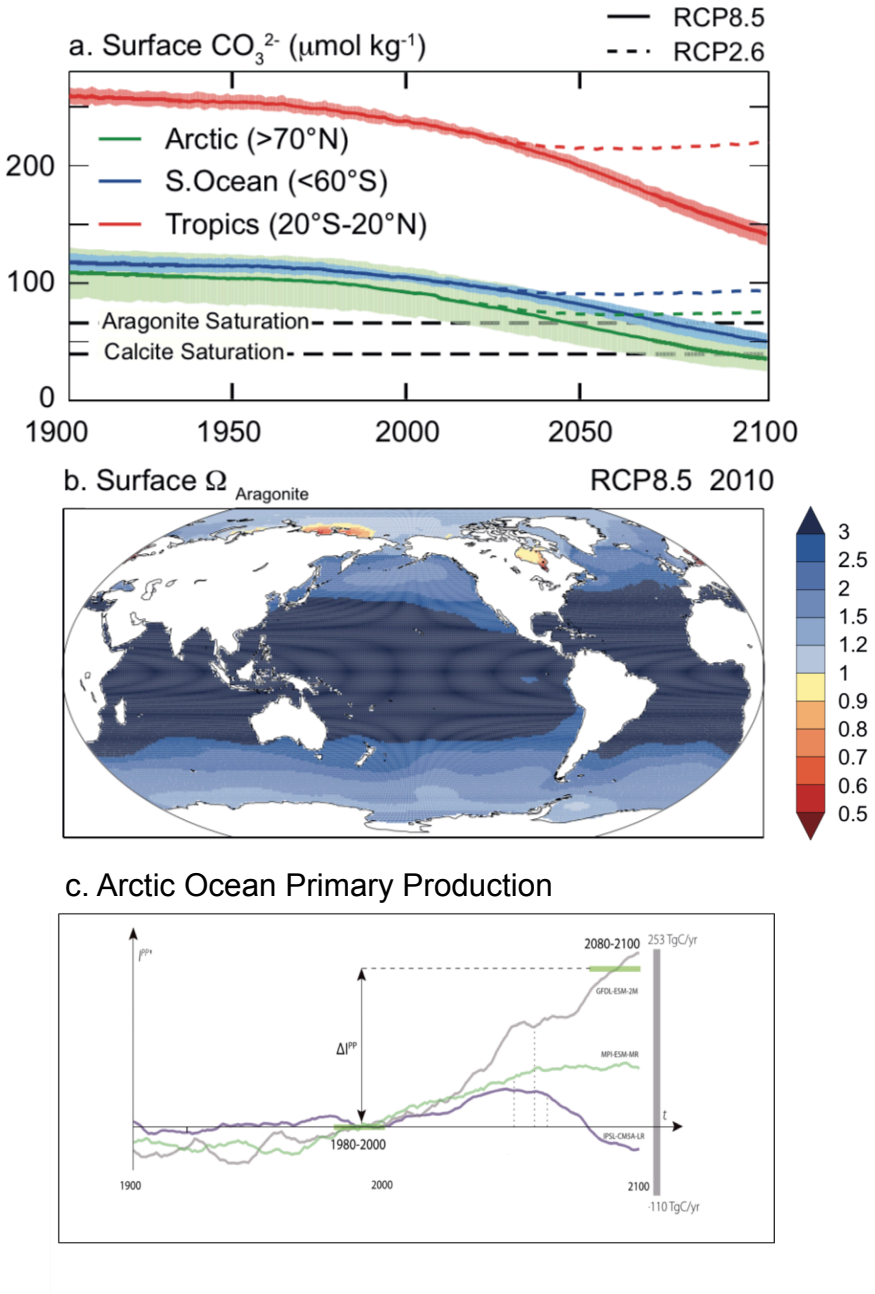

Figure 1.9 – Projected aragonite saturation state from 11 CMIP5 Earth System Models under RCP8.5 scenario: (a) time series of surface carbonate ion concentration shown as the mean (solid line) and range of models (filled), given as area-weighted averages over the Arctic Ocean (green), the tropical oceans (red), and the Southern Ocean (blue); and (b) maps of the median model's surface Ω_A in 2010. (c) Typical evolution of Arctic Ocean PP anomalies (Tg C yr^{-1}) over 1900–2100 (with respect to the 1980–2000 mean, 20 year running mean) from three selected CMIP5 models. (adapted from Ciais et al. [2013] and Vancoppenolle et al. [2013])

1.5 Open scientific questions

Despite the observed impact of river fluxes on the Arctic Ocean biogeochemistry [Semiletov et al., 2016; Tremblay et al., 2015; Anderson et al., 2011b; Chierici and Fransson, 2009], assessments on their effects at the pan-Arctic scale remain limited and uncertain [Manizza et al., 2011; Tank et al., 2012a; Le Fouest et al., 2015]. Moreover, ocean biogeochemical models often only account for land-derived fluxes in a very simplified way or not at all. In the future river fluxes in the high latitudes are projected to increase and their impact on the Arctic Ocean biogeochemistry might thus become even more prominent.

In this thesis, I aim at quantifying the influence of riverine fluxes of carbon and nutrients on the Arctic Ocean biogeochemistry under present-day conditions and in the future, thereby closing important gaps in the understanding of the Arctic Ocean biogeochemistry (Figure 1.2 and 1.10). To establish a baseline against the river fluxes can be evaluated, I will first estimate ongoing changes in the Arctic Ocean biogeochemistry due to the increasing uptake of anthropogenic carbon from the atmosphere

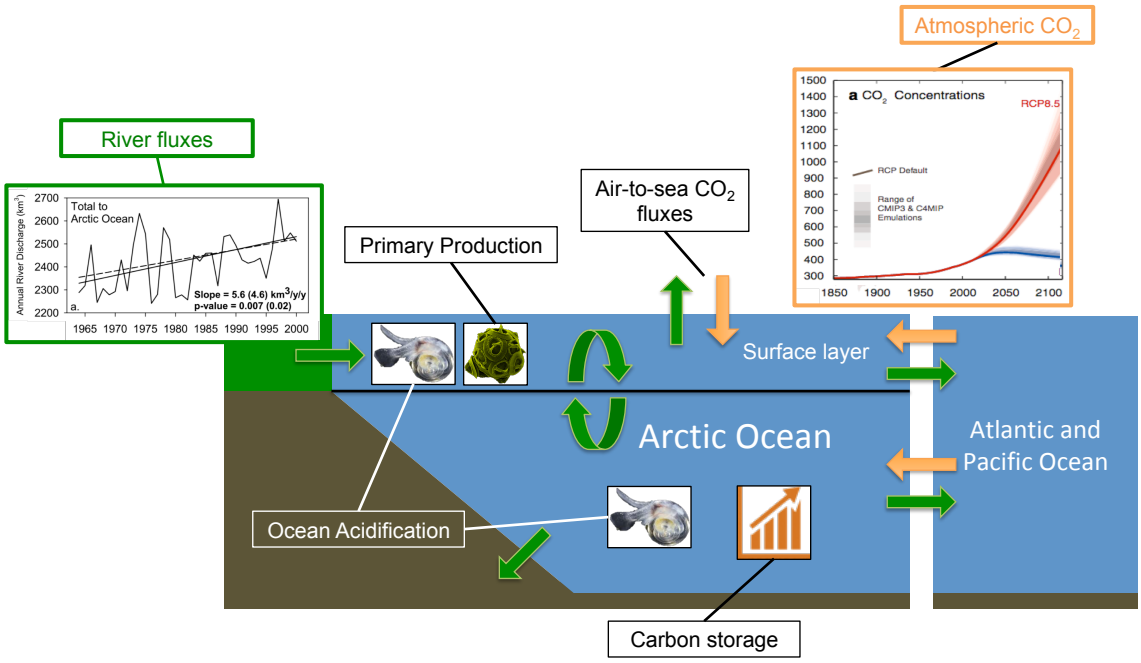

Figure 1.10 – Scheme of the Arctic Ocean, the fluxes of anthropogenic carbon taken up from the atmosphere (orange) and the carbon and nutrient fluxes from rivers (green). All of these fluxes influence the Arctic Ocean biogeochemistry, in particular ocean acidification, PP, and air-sea CO_2 fluxes. The chapters 3 and 4 aim at improving the understanding of the orange fluxes and their effects, while chapter 5 and 6 aim at quantifying the importance of river fluxes for the present-day and in the future.

To improve the knowledge about the influence on riverine fluxes of carbon and nutrients, I will try to answer the following research questions in this thesis:

- How does model resolution affect the result in the Arctic Ocean, and which resolution is needed to simulate the Arctic Ocean circulation and biogeochemistry?

- What controls the carbon and nutrient cycles in the Arctic Ocean, and can we establish a baseline against which we can evaluate past and future changes?

- How much carbon did the Arctic Ocean take up in the past and how much may it take up in the future, what is the effect on ocean acidification?

- Can we extrapolate the PARTNERS/ArcticGRO observations of riverine fluxes on a pan-Arctic grid to create a consistent forcing set of Arctic Ocean river fluxes for ocean models?

- To which extent do these fluxes affect the present-day Arctic Ocean biogeochemistry?

  - How much of the Arctic Ocean PP is driven by riverine delivery of nutrients?

  - What impact do C_T and DOC river fluxes have on the air-sea CO_2 flux of the Arctic Ocean?

  - What are the effects of river fluxes on ocean acidification, directly via their influence on the carbon cycle (C_T, A_T, and DOC fluxes) and indirectly via riverine sustained primary production?

- Will changes in Arctic river fluxes significantly affect the future Arctic Ocean biogeochemistry?

  - Will changes in riverine delivery with climate change significantly contribute to changes in Arctic Ocean PP?

  - Will the Arctic Ocean become a source of CO_2 to the atmosphere?

  - How much do rivers contribute to the increase of C_T in the Arctic Ocean?

  - Will ocean acidification be enhanced or reduced with increasing riverine delivery of carbon and nutrients?

To answer these questions, I will:

1. Use the ocean circulation model 'Nucleus for European Modeling of the Ocean (NEMO) [Madec et al., 2015] coupled to the biogeochemical model 'Pelagic Interactions Scheme for Carbon and Ecosystem Studies' (PISCES) [Aumont et al., 2015] to constrain the anthropogenic carbon budget in the Arctic Ocean and to quantify ongoing changes in its carbon cycle through quantification of the C_{ant} inventory.

2. Use the same simulations to evaluate and improve a data-based method, which estimates C_{ant} using observations of CFC concentrations.

3. Create a pan-Arctic dataset of riverine fluxes of carbon and nutrients from observations and use it to force the NEMO-PISCES model. Next, I will quantify the effects of riverine inputs on the Arctic Ocean biogeochemistry by comparing model results using the created dataset to simulations with no riverine input.

4. Make idealized simulations to quantify the sensitivity of the Arctic Ocean biogeochemistry to increased Arctic riverine delivery of carbon and nutrients.

1.6 Summary

- Arctic amplification makes the Arctic Ocean a hotspot of climate change
- The Arctic Ocean is already experiencing major changes, like increasing temperature, decreasing sea ice cover, increasing acidification, and increasing primary production
- Riverine runoff and fluxes of carbon and nutrients in the Arctic Ocean are more important than in other basins of the global ocean
- With climate change, the carbon and nutrient fluxes from Arctic rivers are predicted to increase further during the next century
- The influence of these riverine fluxes on the Arctic Ocean biogeochemistry at present-day and in the future is not well understood yet
- As observations in the Arctic Ocean are sparse, ocean models are are a useful tool to understand the Arctic Ocean circulation and biogeochemistry
- Many ocean models include no or rudimentary representations of the carbon and nutrient fluxes from Arctic rivers
- This thesis aims at improving the representation of Arctic rivers in models and the ocean-biogeochemical model NEMO-PISCES will be used to quantify the effect of riverine delivery on the Arctic Ocean biogeochemistry today and in the future

Chapter 2

Methods

“ Sometimes it is the people no one can imagine anything of who do the things no one can imagine. ”

Alan Turing

Contents

2.1 Introduction

The objective of this thesis is to quantify the impacts of riverine delivery of carbon and nutrients on the Arctic Ocean biogeochemistry. In a region where observations are scarce, modeling was chosen as the adequate tool to address this task. More specifically, the Nucleus for European Modelling of the Ocean (NEMO) modeling framework with the DRAKKAR configurations was used in this thesis. This work was executed thanks to the supercomputer of the Institut du développement et des ressources en informatique scientifique (IDRIS).

2.2 NEMO modeling framework

The NEMO modeling framework is made up by three core engines: (1) The ocean circulation and thermodynamics 'Océan PArallélisé' (OPA) [Madec et al., 2015], (2) the 'Louvain-la-Neuve sea Ice Model' (LIM) [Fichefet and Maqueda, 1997], (3) and the passive tracer model 'Tracer in the Ocean Paradigm' (TOP), which includes the 'Pelagic Interactions Scheme for Carbon and Ecosystem Studies' (PISCES) biogeochemical model [Aumont et al., 2015]. This framework is developed by five European institutions: the *Euro-Mediterranean Center on Climate Change* (CMCC) in Italy, the *Centre national de la recherche scientifique* (CNRS) and *Mercator Océan* in France,and the *Met Office* and *Natural Environment Research Council* (NERC) in the United Kingdom. The model code is freely available under CeCILL free software license at https://www.nemo-ocean.eu/.

2.2.1 Ocean circulation component OPA

The ocean model OPA simulates the circulation and thermodynamics of the ocean [Madec, 2008]. The three-dimensional motion of a fluid is best described by the Navier-Stokes equations. Within these equations the fluid **U** depends on the density, which is calculated from simulated temperature and salinity by the equation of state.

To transform the equations in a numerically solvable shape, six assumptions are made:

- *Spherical earth approximation*: the earth surface is supposed to be a perfect sphere, so that gravity force is parallel to the earth's radius
- *Thin-shell approximation*: the ocean depth (0–11 km) is neglected with respect to the earth's radius (6371 km)
- *Incompressibility hypothesis*: The density of a fluid is constant over time, thus the divergence of the velocity vector is assumed to be zero
- *Turbulent closure hypothesis*: the effects of small-scale turbulent fluxes are expressed in terms of large-scale features (mean flow quantities)

- *Boussinesq hypothesis*: density variations affect the flow only by their contribution to the buoyancy force
- *Hydrostatic hypothesis*: the vertical pressure gradient is compensated by the buoyancy force

Using the six hypothesis above, the state of the system can be described by the momentum equation, the hydrostatic equilibrium, the incompressibility equation, the heat and salt conservation equations, and the equation of state. In these equations, the vector velocity **U** is defined along a three dimensional set of unit vectors (**i**,**j**,**k**). These unit vectors are orientated, so that **k** is parallel to the earth's radius and **i** and **j** are both orthogonal to **k** and thus span the geopotential surfaces. Consequently the velocity can be divided into a horizontal velocity $\mathbf{U}_\mathrm{h}$ and a vertical velocity $\omega\mathbf{k}$, along the vertical component **k** of the vector set:

$$\frac{\partial \mathbf{U}_h}{\partial t} = [(\nabla \times \mathbf{U}) \times \mathbf{U} + \frac{1}{2}\nabla(\mathbf{U}^2)]_h - f\mathbf{k} \times \mathbf{U}_h - \frac{1}{\rho_0}\nabla_h p + \mathbf{D}^\mathbf{U} + \mathbf{F}^\mathbf{U}, \tag{2.1}$$

$$\frac{\partial p}{\partial z} = -\rho g, \tag{2.2}$$

$$\nabla \cdot \mathbf{U} = 0, \tag{2.3}$$

$$\frac{\partial T}{\partial t} = -\nabla \cdot (T\mathbf{U}) + D^T + F^T, \tag{2.4}$$

$$\frac{\partial S}{\partial t} = -\nabla \cdot (S\mathbf{U}) + D^S + F^S, \tag{2.5}$$

$$\rho = \rho(T, S, p), \tag{2.6}$$

where ∇ is the generalized derivative vector operator in (**i**,**j**,**k**) directions, t is the time, z is the vertical coordinate, ρ is the *in situ* density, p the pressure, $f = 2\Omega\mathbf{k}$ is the Coriolis force (where Ω is the Earth's angular velocity vector), and g is the gravitational acceleration. $\mathrm{D^U}$, $\mathrm{D^T}$ and $\mathrm{D^S}$ are the parameterizations of small-scale physics for momentum, temperature and salinity, and $\mathrm{F^U}$, $\mathrm{F^T}$ and $\mathrm{F^S}$ surface forcing terms.

2.2.1.1 Discretization

Space is divided into grid cells (Figure 2.2). The properties of the grid cell ($\mathrm{T}, \mathrm{S}, p, \rho$) are defined in the center of the grid cell, whereas the vector velocities (u, v, w) are defined orthogonal to each face of the grid cell, with u and v being parallel to the horizontal vector components **i** and **j**, and w parallel to the vertical vector component **k** [Mesinger and Arakawa, 1976]. In general, the size of each grid cell varies with the chosen model configuration. Only the heights of the surface and bottom ocean grid cell are variable. At the surface ocean, the height of the grid cell changes with

the divergence or convergence of water. For the deepest grid cell, a partial step bathymetry is used, meaning that the depth of this deepest grid cell is adapted to represent the bathymetry in the best possible way (Figure 2.1).

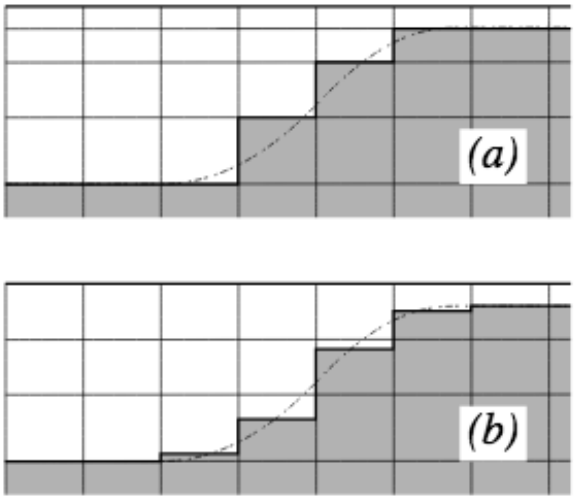

Figure 2.1 – Depth of the deepest grid cell when using gull step bathymetry (a) and partial step bathymetry (b). The line indicates the true bathymetry. (taken from Madec et al. [2015])

Ocean model grids for the NEMO modeling framework are developed and maintained by the international DRAKKAR project[1]. The series of provided grids is called ORCA and described by Barnier et al. [2006a]. In this thesis, four different ORCA grids with different nominal resolutions are used: ORCA2 (2°), ORCA1 (1°), ORCA05 (0.5°), and ORCA025 (0.25°). All ORCA grids are tripolar to avoid a singularity at the geographical North Pole [Madec and Imbard, 1996], meaning they have one pole on the greographical South Pole and two poles placed over North America and Asia. Consequently, the grid is progressively distorted into ellipses north of 20°N, while it remains a normal mercator grid south of 20°N (Figure 2.2). The distortion leads to an increase of the model resolution in the Arctic Ocean, yielding an average grid length in the Arctic of 120 km (ORCA2), 60 km (ORCA1), 29 km (ORCA05), and 14 km (ORCA025). The vertical column is divided into 45 levels for ORCA2, ORCA05 and ORCA025, and 75 levels for ORCA1. The vertical size of the grid cells increases with depth from 6 m (1 m in ORCA1) at the surface to 250 m in the deepest grid cell. The global bathymetry map is derived from three different sources: (1) the 2-minute ETOPO2 bathymetry map from the National Geophysical Data Center, applied over most of the ocean [Smith and Sandwell, 1997]; (2) the IBCAO bathymetric data, applied in the Arctic[Jakobsson et al., 2000a]; and (3) the BEDMAP bathymetric data, applied south of 72°S [Lythe and Vaughan, 2001]. ORCA2 and ORCA05 are used in chapter 3, ORCA1 is used in chapter 6, and ORCA025 is used in chapters 3, 4, and 5.

To calculate the temporal evolution of the model variables, time is divided into discrete time steps t. The evolution with time is calculated using the leapfrog scheme [Mesinger and Arakawa,

[1] https://www.drakkar-ocean.eu/

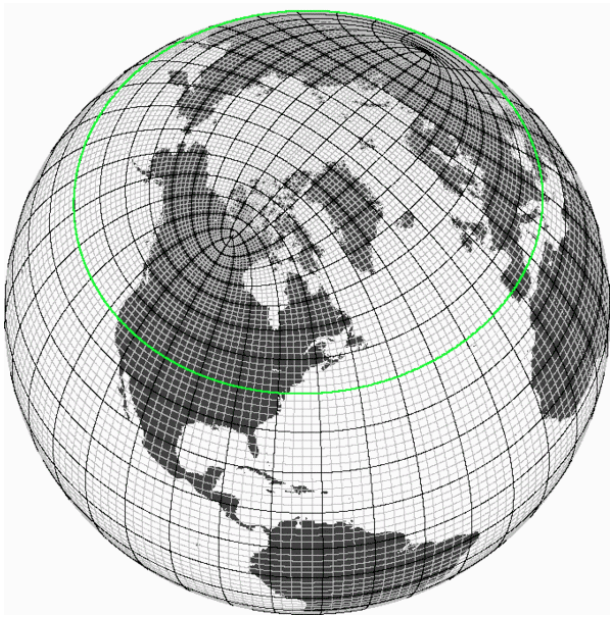

Figure 2.2 – Tripolar grid, as used by all ORCA model configurations. North of the green line the model grid differs from a regular geographic grid with a single north pole (taken from https://www.geomar.de/en/research/fb1/fb1-tm/ocean-models/)

1976], which is computational efficient and reaches second-order accuracy with only one evaluation of the right-hand side of an equation. To reduce the dissipation of high frequency motion, the scheme is used in association with the Robert-Asselin filter [Robert, 1966; Asselin, 1972]. The diffusive part of the movement is calculated using a simpler forward time differencing scheme. The lateral isopycnal diffusion and viscosity coefficients were chosen depending on the resolution (Table 3.2). For ORCA2 and ORCA1, a Laplacian viscosity operator was used, whereas a bi-Laplacian operator was used for ORCA05 and ORCA025. To simulate the effect of eddies on the mean advective transport in the two coarser resolution configurations, the eddy parameterization scheme of Gent and McWilliams [1990] was applied with eddy diffusion coefficients indicated in Table 3.2. For the tracer advection of salinity and temperature a Total Variance Dissipation scheme (TVD) is applied [Zalesak, 1979].

Table 2.1 – Selected physical coefficients and parameters for ORCA2, ORCA05, and ORCA025.

Configuration	Lateral diffusivity	Lateral viscosity	Eddy parameterization
ORCA2[a]	2000 $m^2\ s^{-1}$	4×10^4 m^2 s^{-1} [b]	2000 m^2 s^{-1}
ORCA1	1000 $m^2\ s^{-1}$	2×10^4 m^2 s^{-1} [b]	1000 m^2 s^{-1}
ORCA05	600 $m^2\ s^{-1}$	-4×10^{11} m^2 s^{-1}	1000 m^2 s^{-1}
ORCA025	300 $m^2\ s^{-1}$	-1.5×10^{11} m^2 s^{-1}	none

[a] Lateral diffusivity and viscosity coefficients decrease towards the poles proportional to the grid size.
[b] reduced to 2100 m^2 s^{-1} in the tropics (except along Western boundaries)

2.2.2 Sea Ice model LIM

The sea ice model LIM includes thermodynamics, dynamics, advection, ridging and rafting. The original code was written by Fichefet and Maqueda [1997]. Later, it was coupled to OPA and called LIM2 [Timmermann et al., 2005]. LIM2 simulates one layer of snow and two layers of ice. The newest version of the model, LIM3, includes an elastic–viscous–plastic rheology, several categories of ice thickness and multi-layer halo-thermodynamics [Vancoppenolle et al., 2009]. In both versions, the sea ice growth is determined by the energy budget at the lower end of the ice layer in contact with the ocean and at the upper end, which is in contact with the atmosphere. The ice is advected by an ice-drift velocity. This velocity is calculated by a momentum balance including the wind and the ocean currents. The ice-model is coupled to OPA every 5 time steps, which is three times per day given the time step used by OPA. It is not only the ocean that affects the sea ice by heat and currents, but also the sea ice that affects the ocean model by fresh water input from sea ice melting or brine rejection during ice formation. During ice melting fresh water is released and the salinity is reduced. This leads to lighter surface water and higher stratification in the Arctic. In this study we use the version LIM2 in chapter 3, 4 and 6, and LIM3 in chapter 5.

2.2.3 Biogeochemical model PISCES

The biogeochemical model PISCES simulates the carbon and nutrient cycles, and the lower trophic levels of the marine ecosystem, namely phytoplankton, microzooplankton and mesozooplankton [Aumont et al., 2015]. The inorganic carbonate system in PISCES consists of C_{T} and A_{T}. These tracers are transported by advection and diffusion and follow the ocean currents simulated by OPA. In addition these tracers have internal sources and sinks, e.g. C_{T} is reduced by PP and increases with the remineralization of organic matter. The simulated inorganic nutrients are nitrogen (N), phosphorus (P), iron (Fe), and silicon (Si) (Figure 2.3).

PISCES simulates the consumption of nutrients by two types of phytoplankton, nanophytoplankton and diatoms. This primary production is limited by light and nutrients. In both types of phytoplankton, the ratio of oxygen, carbon, nitrogen, and phosphorus is held constant at the Redfield ratio O:C:N:P=165:122:16:1 [Takahashi et al., 1985; Körtzinger et al., 2001], while the Fe:C and Chl:C ratios, and in the case of diatoms also the Si:C ratio, are prognostically predicted. The production rate of phytoplankton is calculated by:

$$\mu = \mu_{max}\left(1 - e^{\left(\frac{\alpha^{\mathrm{P}}(\frac{Chl}{\mathrm{C}})\mathrm{PAR}}{\mu \mathrm{L}_{lim}}\right)}\right)\mathrm{L}_{lim}, \tag{2.7}$$

with μ_{max} being the maximal growth rate based on the temperature, α^{P} being the slope of the PI (photosynthesis-irradiance) curve, $\frac{Chl}{\mathrm{C}}^{\mathrm{P}}$ being the chlorophyll-carbon ratio, PAR (Photosynthetic Actic radiation) being a constant fraction of the total shortwave radiative flux at the sea surface (set to 0.43) , and L_{lim} being the the nutrient limitation term. The nutrient limitation terms for N,

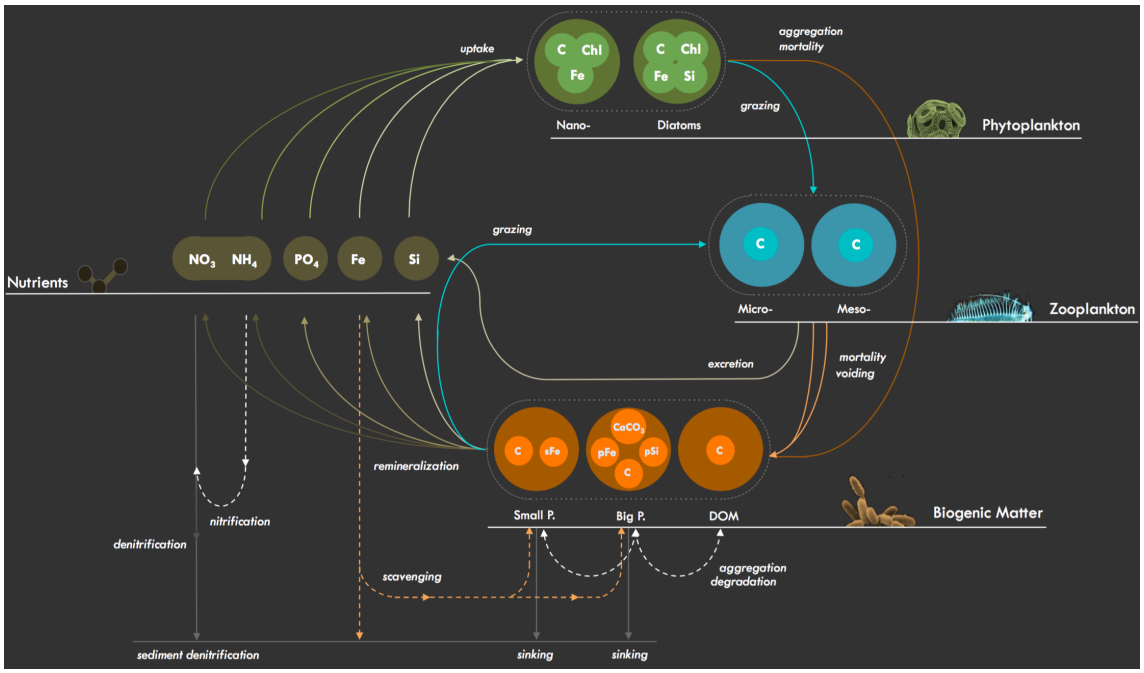

Figure 2.3 – Architecture of PISCES. This figure only shows the ecosystem model omitting thus oxygen and the carbonate system. The elements which are explicitly modeled are indicated in the left corner of each box. (adapted from Aumont [2012])

P, Fe, and Si (only for diatoms) are all calculated based on the Michaelis-Menten ratio [Michaelis and Menten, 1913]. The smallest of these so calculated limitation terms is the one that is limiting and is thus used for the calculation of primary production.

The produced phytoplankton is then either consumed by the micro- and meso-zooplankton or aggregates as biogenic matter. The zooplankton is assumed to have the same Redfield ratio as the phytoplankton. The same Redfield ratio also applies for the three non-living compartments of organic matter: Dissolved organic carbon (DOC), small particulate organic carbon (POC), and big particulate organic carbon (GOC). Conversely, the silicon, iron, and calcite pools in the particles are explicitly modeled. These non-living particles sink towards the ocean floor. While the particles sink, they are continuously remineralized. The ones that reach the ocean floor are buried in the ocean sediments depending on the burial efficiency.

The burial flux of organic matter in the sediments depends directly on the flux of particular organic matter that sinks towards the ocean floor (Figure 2.4). Part of this flux is buried, and the remaining part of organic matter is assumed to be remineralized in the sediments and is reinjected into the ocean in its inorganic form. The relative amount of organic matter that is buried is determined by the burial efficiency (E_{burial}). In PISCES-v1 [Aumont and Bopp, 2006], used in chapters 3, 4, and 5, the burial efficiency is calculated in a way that globally integrated external nutrient input ($\int Nut_{ext}$) equals the globally integrated nutrient flux in form of organic matter into

the sediments ($\int \mathrm{F_{OM}}$):

$$\mathrm{E}_{burial} = \frac{\int \mathrm{N}ut_{ext}}{\int \mathrm{F_{OM}}}. \tag{2.8}$$

In PISCES-v2 [Aumont et al., 2015], used in chapter 6, the burial efficiency is explicitly calculated based on findings from Dunne et al. [2007]:

$$\mathrm{E}_{burial} = \frac{0.53 \times \mathrm{F}_{\mathrm{OM}}^2}{(7.0 + \mathrm{F_{OM}})^2}. \tag{2.9}$$

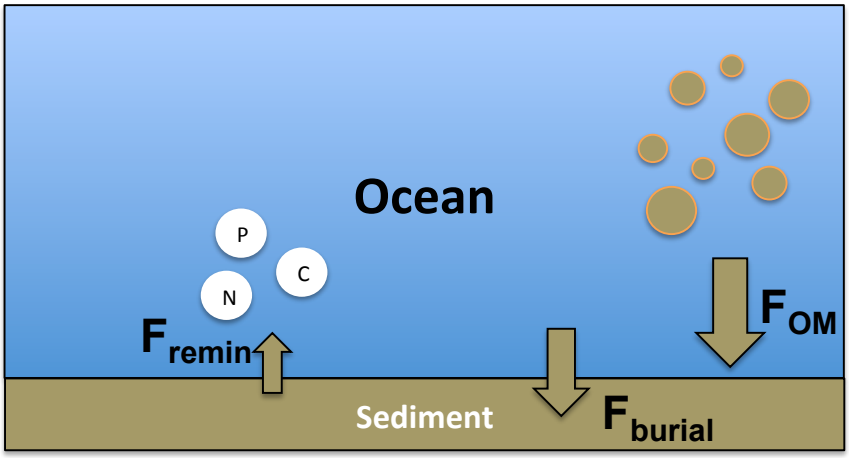

Figure 2.4 – Scheme of burial fluxes in PISCES

In this thesis the standard versions of PISCES-v1 and PISCES-v2 were used and only boundary conditions were changed. Detailed descriptions and applied parameters for all processes can be found in the corresponding references [Aumont and Bopp, 2006; Aumont et al., 2015].

2.2.3.1 Boundary conditions

At the ocean surface, carbon in the form of CO_2 and oxygen are exchanged with the atmosphere via air-sea gas exchange following [Wanninkhof, 1992]:

$$\mathrm{F}_{\mathrm{CO_2}} = \alpha k \Delta p\mathrm{CO_2}, \tag{2.10}$$

$$k = 0.30 u_w^2 \sqrt{\frac{660}{\mathrm{S}c}} (1 - \mathrm{I}), \tag{2.11}$$

with α being the solubility of CO_2 according to [Weiss, 1974], $\Delta p\mathrm{CO_2}$ being the difference in partial pressure between the atmosphere and the ocean, k being the gas transfer coefficient, u_w being the wind speed at 10 m, Sc being the Schmidt number, and I being the fractional sea ice cover. No air-sea exchange is allowed where the ocean surface is fully covered by ice.

In addition to air-sea CO_2 exchange, C_T is supplied to the ocean via riverine influx. As opposed to carbon, nutrients are supplied to the ocean via atmospheric deposition, river discharge, iron

mobilization from sediments, iron from hydrothermalism, and iron from sea ice. The river input of carbon and nutrients is described in further detail in Section 2.3.

2.2.3.2 Atmospheric forcing

The atmospheric forcing sets used in this thesis are the DRAKKAR Forcing Set DFS4.2 and DFS4.4 [Brodeau et al., 2010]. DFS4.2 uses ERA40 [Uppala et al., 2005] and covers 35 years (1958-2002). DFS4.4 covers the 10 year (2003–2012) using ERA-interim [Dee et al., 2011]. Both dataset thus cover 55 years in total. These datasets provide meteorological variables for the air-sea fluxes in the model: i- and j-component of the 10 m air velocity, 2 m air temperature, 2 m specific humidity, incoming long wave radiation, incoming short wave radiation, total precipitation (liquid + solid). The data is provided in 6 hour time steps.

2.3 Simulations

In this thesis, two kind of simulations are used: Hindcast simulations and sensitivity tests. Hindcast simulations simulate a historical period and results can be used to evaluate the model against observations, to simulate regions where observations are sparse, or to understand underlying mechanisms. As opposed to hindcast simulations, sensitivity tests are idealized simulations and do not represent a historical period. They are mainly used in climate studies to calculate the sensitivity of a system or a process to changes in forcing conditions. For instance, Friedlingstein et al. [2003] quantified the ocean and land uptake capacity of carbon per increase in atmospheric CO_2. In this thesis, I followed the same idea, but I calculated the sensitivity of PP, ocean acidification, air-sea CO_2 flux, and carbon storage to changes of riverine fluxes of carbon and nutrients.

2.3.1 Biogeochemical simulations

2.3.1.1 Hindcast simulations

In the biogeochemical hindcast simulations in this thesis, the global ocean physics and biogeochemistry is simulated for the period from 1870–2012 using the NEMO-PISCES version from Aumont and Bopp [2006]. The atmospheric forcing in this model is the DFS4.2 from 1958–2001 and DFS4.4 from 2002–2012. For the period from 1870–1957, the same 55 years of atmospheric forcing were continuously looped. Atmospheric CO_2 concentrations from 1870 to 2012 are taken from [Le Quéré et al., 2018]. The physics of the model were initialized with a 50-year spin-up using ORCA05. The initial conditions for PISCES, and the atmospheric and riverine forcing are detailed in Table 2.2.

As computational time is limited, the simulation were run on the ORCA05 grid from 1870–1957. At the end of year 1957, the simulated fields are extrapolated on the grids of ORCA2 and ORCA025

(Figure 2.5). Thus, the period from 1958–2012 is simulated with the three resolutions to compare the effect of model resolution.

The standard version of these simulations uses the riverine input for C_T and DOC based on the Global Erosion model [Ludwig et al., 1996]. Total alkalinity in rivers is assumed to be equal to C_T and nutrients are computed based on total riverine carbon (C_T+DOC) using the ratios C : N : P : Si : Fe = $320 : 16 : 1 : 53.3 : 3.64 \times 10^{-3}$ (C:N from Meybeck [1982], N:P from Takahashi et al. [1985], C:Fe

Table 2.2 – Initial conditions, atmospheric forcing and riverine forcing for the NEMO-PISCES hindcast simulations

Initial conditions	
Temperature	WOA[1] 1998 Levitus et al. [1998]
Salinity	WOA 1998 Levitus et al. [1998]
NO_3, PO_4, Si, O_2	WOA 2001 [Conkright et al., 2002]
DOC, Fe	2000 years spin-up with ORCA2 [Aumont and Bopp, 2006]
C_T, Alkalinity	GLODAPv1[2] [Key et al., 2004]
Atmospheric forcing	
Wind at 10 m	DFS[3] [Brodeau et al., 2010]
2 m specific humidity	DFS [Brodeau et al., 2010]
2 m air temperature	DFS [Brodeau et al., 2010]
Solar radiation	DFS [Brodeau et al., 2010]
Precipitation	DFS [Brodeau et al., 2010]
Iron deposition	Tegen and Fung [1995]
Arctic riverine forcing	
Runoff	Dai and Trenberth [2002]
Nutrients	Chap. 3 and 4: derived from GEM[4] [Ludwig et al., 1996]
	Chap. 5: derived from observations [Holmes et al., 2012]
	Chap. 6: derived from GN2[5] [Mayorga et al., 2010]
C_T	Chap. 3, 4, and 6: derived from GEM [Ludwig et al., 1996]
	Chap. 5: derived from observations [Tank et al., 2012c]
DOC	Chap. 3 and 4: derived from GEM [Ludwig et al., 1996]
	Chap. 5: derived from observations [Holmes et al., 2012]
	Chap. 6: derived from GN2 [Mayorga et al., 2010]

[1] WOA (World Ocean Atlas)

[2] GLODAPv1 (GLobal Ocean Data Analysis Product version 1)

[3] DFS (Drakkar Forcing Set)

[4] GEM (Global Erosion Model)

[5] GN2 (Global News 2)

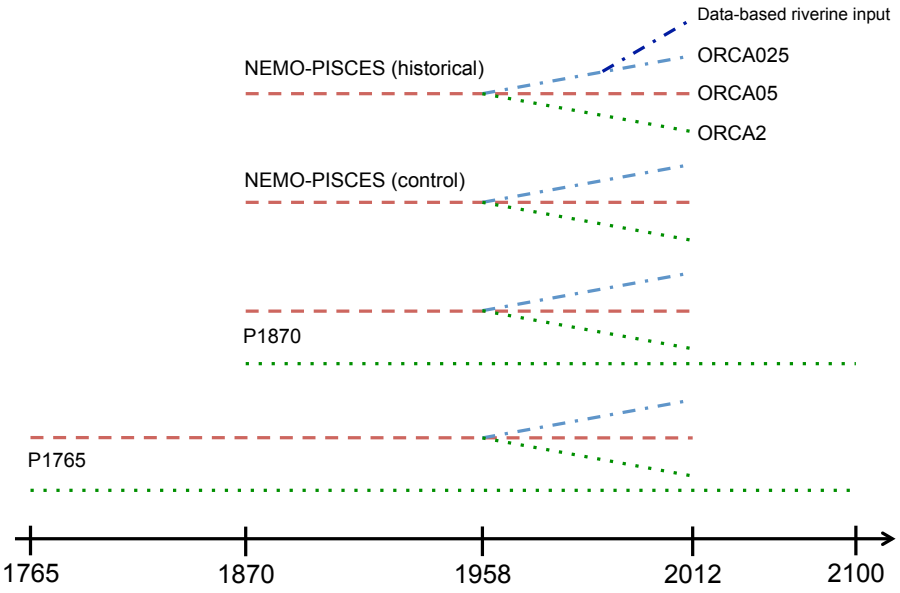

Figure 2.5 – Simulation strategy for standard historical and future simulations for ORCA2 (dotted green), ORCA05 (dashed red), and ORCA025 (dash-dotted light blue). The simulation from 1990 to 2010 with data-based riverine input is shown in as a dash-dotted dark blue line.

from de Baar and de Jong [2001], and C:Si from Tréguer et al. [1995]). In addition to this standard version we simulated the period from 1990 to 2010 with a riverine forcing file, which is based on observations of C_T, DOC, and nutrients from PARTNERS and ArcticGRO [Holmes et al., 2012; Tank et al., 2012c]. To quantify the impact of this data-based riverine input, we simulated the same 21 years with riverine delivery of C_T, DOC, and nutrients set to zero.

2.3.1.2 Sensitivity tests

The sensitivity tests are a set of five 75-year simulations using PISCESv2 [Aumont et al., 2015]: (1) a preindustrial control simulation with a constant atmospheric CO_2 fixed at 284.7 ppm (1850) having constant riverine input as prescribed above; (2) a simulation just like the control simulation except that atmospheric CO_2 is increased by 1% per year; (3) a simulation just like (2) except that the riverine flux of DOC is also increased by 1% per year; (4) a simulation just like (3) except that the flux of riverine C_T is also increased by 1% per year; and (5) a simulation just like (4) except that the flux of riverine nutrients is also increased by 1% increase per year.

At the beginning of all simulations, the river inputs into the Arctic Ocean for DOC, dissolved inorganic nitrogen (DIN), dissolved organic nitrogen (DON), total dissolved inorganic phosphorus (P_T), dissolved organic phosphorus (DOP), and silicon (Si_T) are derived from mean annual fluxes from the Global NEWS 2 model (GN2) [Mayorga et al., 2010] and C_T fluxes are derived from mean annual fluxes from the Global Erosion Model (GEM) [Ludwig et al., 1996]. GN2 is a composite of independent submodels for dissolved inorganic, dissolved organic, and particulate C, N, and P, as well as dissolved silicon. For consistency between submodels, a unified formulation was adapted

for dissolved elements. To estimate annual riverine exports of DOC and nutrients, all submodels use hydrological and physical factors, hydrography, and basin characteristics. The GN2 models consider both, natural processes and anthropogenic activities. GEM establishes a relationship between C_T yield and hydroclimatic and geomorphological factors from 60 different river basins for four different climatic zones. These relationships are then applied to all rivers around the world, dependent on their respective the climatic zone. In the sensitivity simulations, contemporary annual river fluxes from GEM's C_T (R_{C_T}) and GN2's DOC (R_{DOC}), DIN and DON (R_N), P_T and DOP (R_P), and Si (R_{Si}) and associated discharge are used to calculate riverine concentrations of carbon and nutrients. These concentrations are then multiplied with the monthly river discharge from Dai and Trenberth [2002] used in NEMO to calculate the respective riverine fluxes.

Due to the long simulation period (5 × 75 years), we had to make these simulations on the rather coarse ORCA1 configuration with 75 depth levels. The same DFS atmospheric forcing that was used in the hindcast simulations (Section 2.3.1.1) was looped.

2.3.2 Perturbation Simulations

Due to computational costs, the NEMO-PISCES simulations start in 1870, similar to the widely applied starting date 1850 in CMIP5 simulations. This late starting date leads to an underestimation of C_{ant} in the global by ~30% in 1995 [Bronselaer et al., 2017]. To account for this underestimation in our model, two simulations with the more efficient single-tracer perturbation approach were made [Sarmiento et al., 1992], rather than using the full PISCES biogeochemical model (24 tracers). One perturbation simulation starts in 1765 (P1765) and another one in 1870 (P1870). The difference of both simulations amounts to the underestimation of C_{ant} in the PISCES simulations from 1870 to 2012.

This perturbation approach avoids the computationally intensive standard CO_2 system calculations by only accounting for the perturbation (C_{ant}), assuming it is independent of the natural carbon cycle. By focusing only on anthropogenic carbon, this approach exploits a linear relationship between the anthropogenic change in oceanic pCO_2 [µatm] and its ratio with the ocean's corresponding change in C_T (C_{ant}):

$$\frac{\delta pCO_{2_o}}{C_{ant}} = z_0 + z_1 \delta pCO_{2_o}, \tag{2.12}$$

where δpCO_{2_o} is the perturbation in oceanic pCO_2 and the coefficients z_0 and z_1 are each quadratic functions of temperature [°C],

$$z_0 = a_0 + a_1 T + a_2 T^2 \tag{2.13}$$

$$z_1 = b_0 + b_1 T + b_2 T^2. \tag{2.14}$$

In the model, Eq. (3.1) was rearranged to solve for surface-ocean δpCO_{2_o} in terms of C_{ant} [Sarmiento et al., 1992, Eq. (11)], as needed to compute the air-sea flux [Sarmiento et al., 1992, Eq. (2)]. One

set of coefficients ($a_0, a_1, a_2, b_0, b_1, b_2$) was derived for our reference atmospheric xCO_2 in 1765; another set was derived for our reference atmospheric xCO_2 in 1870. In the air-sea flux equation, the atmospheric xCO_2 was corrected for humidity and atmospheric pressure to convert to $pCO_{2\text{atm}}$. The atmospheric xCO_2 history for 1765–1869 is from Meinshausen et al. [2017], while the history for 1870 and beyond is the same as used in the NEMO-PISCES simulations [Le Quéré et al., 2018].

The original approach [Sarmiento et al., 1992] was updated to use the equilibrium constants recommended for best practices [Dickson et al., 2007] and to cover a perturbation of up to 280 ppm. The relative error introduced by approximating the perturbation to the ocean CO_2 system equilibria with Eq. (3.1) remains less than ±0.3% across the global ocean's observed temperature range when $\delta pCO_2^{oc} < 280$ ppm.

Equivalent to the PISCES simulations, the perturbations simulations were made using ORCA05 from 1765 to 1957 (Figure 2.5). In 1958, the results from ORCA05 were extrapolated on the grids of ORCA2 and ORCA025. The simulations were continued in each of the three configurations during 1958 to 2012. In addition, a full only ORCA2 simulation was made from 1765 to 2100.

2.3.3 CFC-12 simulations

CFC-12 is a purely anthropogenic tracer, a sparingly soluble gas whose concentration began to increase in the atmosphere in the early 1930's, part of which has been transferred to the ocean via air-sea gas exchange. Its uptake and redistribution in the ocean has been simulated following OCMIP-2 protocols [Dutay et al., 2002]. The CFC-12 flux (F_{CFC}) at the air-sea interface was calculated as follows:

$$F_{CFC} = k_w(\alpha_{CFC}\ pCFC - C_s)(1 - I), \tag{2.15}$$

where k_w is the gas-transfer velocity (piston velocity) in m s^{-1} [Wanninkhof, 1992], pCFC the atmospheric partial pressure of CFC-12 in atm from the reconstructed atmospheric history by Bullister [2015], C_s is the sea surface concentration of CFC-12 (mol m^{-3}), α_{CFC} is the solubility of CFC-12 (mol m^{-3}atm^{-1}) from Warner and Weiss [1985], and I is the model's fractional sea-ice cover. Once in the ocean, CFC-12 is an inert tracer that is distributed by advection and diffusion; it has no internal sources and sinks. Many high-precision measurements of CFC-12 are available throughout the ocean, in sharp contrast to C_{ant} which cannot be measured directly.

Similar to the PISCES simulations, CFC-12 was simulated using ORCA05 until 1957. In 1958 the results were extrapolated on the ORCA2 and ORCA025 grids and the simulation was continued with all three configurations separately.

2.4 Transient Time Distribution (TTD)

Unfortunately, C_{ant} can not be directly measured in the ocean, due to the large background of C_T. Nevertheless, different methods exist to estimate C_{ant} in the ocean [Khatiwala et al., 2013]. In this thesis, the Transient Time Distribution (TTD) is used. The TTD approximates the invasion of C_{ant} into the interior ocean by observations of transient-tracers such as CFC-12, He/Tri, and SF_6 [Hall et al., 2002; Waugh et al., 2004]. By using surface boundary conditions of the respective tracer and subsurface measurements of the tracer concentration, temperature, and salinity, the mean age of the water parcel can be determined by the TTD. The mean age is then used in combination with the atmospheric C_{ant} history to estimate the C_{ant} concentration in the respective water parcel.

In this thesis, the TTD was applied following Hall et al. [2002] and Waugh et al. [2004]. The concentration of a tracer c(r,t) was calculated at any point r and any time t using the following equation:

$$c_r(t) = \int_0^\infty c_0(t-t')\mathrm{G}_r(t')dt' \tag{2.16}$$

with $c_0(t-t')$ being the tracers atmospheric concentration at time t' and G(r,t) being a Green's function. To evaluate the TTD method as it is usually applied, we used in this study the commonly applied inverse Gaussian as our Green's function [Waugh et al., 2004, 2006; Tanhua et al., 2009; Olsen et al., 2010]:

$$\mathrm{G}_r(t) = \sqrt{\frac{\Gamma^3}{4\pi\Delta^2 t^3}} exp\left(\frac{-\Gamma(t-\Gamma)^2}{4\Delta^2 t}\right) \tag{2.17}$$

where Δ represents the width of the TTD, Γ the mean age of the water sample, and t the transit time. The ratio of Δ and Γ determines the repartition of advection and diffusion in the water parcel, with Δ/Γ <1 indicating a larger advective part. A typically applied Δ/Γ ratio of 1.0 was used [Waugh et al., 2006; Tanhua et al., 2009]. In addition TTD method was tested for a range of different Δ/Γ ratios. To calculate the partial pressure of CO_2 in the ocean, the matlab version of the routine CO2SYS [van Heuven et al., 2011] was used with the dissociation constants from Millero et al. [2002] and Dickson [1990]. The solubility of CFC-12 was calculated following Warner and Weiss [1985].

When partial pressure of CFC-12 (pCFC-12) in ocean water was found to be supersaturated with respect to the current atmospheric pCFC-12, the age of the water parcel cannot be determined and therefore the TTD method cannot be applied. Oceanic pCFC-12 can surpass the atmospheric pCFC-12 the latter is slightly decreasing in the last years. When comparing C_{ant} calculated by the TTD method to directly simulated C_{ant}, we thus consequently masked out areas where oceanic pCFC-12 is above atmospheric pCFC-12.

2.5 Observations and data products

In the scope of this thesis measurements and data products were used to evaluate the model results, to develop a new river flux dataset for Arctic rivers, or to estimate future C_{ant} and Ω_{arag} in the Arctic Ocean.

2.5.1 CFC-12 observational data

Model simulations were evaluated indirectly by comparing simulated to observed CFC-12. CFC-12 was chosen to evaluate the model, because it is an anthropogenic, passive, conservative, and inert tracer, and in contrast to anthropogenic carbon, it is directly measurable.

The CFC-12 observations used in this study come from two trans-Arctic cruises: the 1994 Arctic Ocean Section (AOS94) [Jones et al., 2007] and the Beringia 2005 expedition [Anderson et al., 2011c] (Figure 3.1). AOS94 started on 24 July and finished on 1 September and CFC-12 measurements were made at 39 stations. That section starts in the Bering Strait, enters the Canada basin adjacent to the Mendeleev ridge, continues to the Makarov basin, and ends at the boundary of the Nansen basin and the Barents Sea. The Beringia expedition started on 19 August and ended on 25 September 2005. It started off the coast of Alaska, went through the Canada and Makarov basins, crossed the Lomonosov ridge, and its last CFC-12 station was taken on the Gakkel ridge. These two cruises were chosen among other cruises because of their geographically similar placement and because they cross large parts of the Arctic, including almost all four major basins.

2.5.2 Data-based estimates of anthropogenic carbon

Simulated C_{ant} was compared to data-based estimates from Tanhua et al. [2009] for the year 2005 and from the gridded database GLODAPv2 for the year 2002 [Lauvset et al., 2016], both based on the TTD approach.

2.5.3 C_T, A_T, and nutrients

Simulated C_T, A_T, and nutrients (DIN, P_T, and Si_T) were compared to the discrete version of the GLODAPv2 database [Olsen et al., 2016] and the mapped climatology derived from the discrete data [Lauvset et al., 2016]. The GLODAPv2 database contains observations from 724 cruises in the global ocean, out of which 116 cruises are in the Arctic and Nordic Seas (> 65°N). This dataset also includes the AOS94 and Beringia 2005 cruises.

2.5.4 Net Primary Production

Simulated NPP was compared to two data-based products of vertically derived NPP [Hill et al., 2013; Arrigo and van Dijken, 2015]. Both data-based products use satellite observation of ocean color from the Sea-viewing Wide Field-of-view Sensor (SeaWiFS) and the Moderate Resolution

Imaging Spectroradiometer (MODIS) Aqua. From the observed ocean color data, chlorophyll *a* can be derived by algorithms that were calibrated with *in situ* data. While Arrigo and van Dijken [2015] use solely the satellite derived estimates, Hill et al. [2013] added *in situ* measurements of chlorophyll *a* to better account for sub surface maxima of chlorophyll *a*.

2.5.4.1 Air-to-sea CO_2 flux

Simulated air-to-sea CO_2 flux was compared to Bates and Mathis [2009] and sources within and to annual-mean air-to-sea flux estimates of total CO_2 from 1997 to 2013 derived with self-organizing pCO_2 maps that exploit 1.6 million observed data points [Yasunaka et al., 2016].

2.5.5 Temperature and salinity

Temperature and salinity measurements were taken from three sources: (1) The gridded version of the database GLODAPv2, (2) the discrete version of GLODAPv2, (3) and measurements from AOS94 and Beringia 2005.

2.5.6 Sea ice cover

Simulated sea-ice cover was compared to observations by the U.S. National Snow and Ice Data Center [Walsh et al., 2015]. Until 1979, the data is based on historical sources, such as ship observations, and since 1979 the data is based on satellite observations.

2.5.7 River fluxes of carbon and nutrients

Concentrations of DOC, DIN, DON, P_T, DOP, and Si_T and the derived fluxes from the international Pan-Arctic River Transport of Nutrients, Organic Matter, and Suspended Sediments program (PARTNERS) and its successor, the Arctic Great Rivers Observatory (ArcticGRO) [McClelland et al., 2008] were used in this thesis. The data was collected in a coordinated effort in the six largest Arctic rivers and covered the full seasonal cycles of riverine carbon and nutrient fluxes [Holmes et al., 2012; Tank et al., 2012c].

2.6 Summary

- The ocean model NEMO and the biogeochemichal model PISCES are the main tools of this thesis
- Three types of simulations were used in this thesis: hindcast simulations, perturbations simulations, and sensitivity tests.
- Hindcast simulations with NEMO-PISCES were made at three different resolutions (2°, 0.5°, 0.25°) between 1870 and 2012
- These hindcast simulations were made with historical and pre-industrial atmospheric CO_2 levels to calculate the anthropogenic perturbation
- The computational less expensive perturbation approach was used to correct the NEMO-PISCES simulations for the late starting date and to evaluate the Arctic Ocean data-based C_{ant} estimates by the TTD method
- Different riverine input fluxes were used in the NEMO-PISCES simulations: one based on a C_T river flux model (hindcast simulations), one based on a set of models for organic matter and nutrients (sensitivity tests)
- Using the highest model resolution (0.25°), the period from 1990 to 2010 in the hindcast simulations was re-run with observation-based riverine fluxes and with zero riverine fluxes to quantify the effect of these fluxes on the Arctic Ocean biogeochemistry
- Idealized NEMO-PISCES simulations with steadily increasing riverine input were made to quantify the sensitivity of the Arctic Ocean biogeochemistry (primary production, air-sea CO_2 flux, and acidification) to changing riverine fluxes

Chapter 3

Model constraints on the anthropogenic carbon budget of the Arctic Ocean

“ Success consists of going from failure to failure without loss of enthusiasm. ”

Sir Winston Churchill

Contents

3.1 Preamble

Before analyzing the influence of riverine input of carbon and nutrient on the Arctic Ocean biogeochemistry, the capability of NEMO-PISCES to simulate the Arctic Ocean needs to be evaluated. In this chapter, global ocean hindcast simulations of NEMO-PISCES at three different resolutions (ORCA2, ORCA05, and ORCA025) are used to simulate the uptake of C_{ant} in the Arctic Ocean.

The simulated temperature, salinity, circulation, CFC-12 concentrations, and C_{ant} are compared to observations and data-based estimates (in the case of C_{ant}). The understanding of the model performance allows us to decide on the simulation strategy in the following chapters and provides an important element for the interpretation of the following results.

At the same time, these simulations are much more than a simple tool to understand the performance of NEMO-PISCES at different resolutions. They allow to better constrain the data-based estimates of the C_{ant} budget in the Arctic Ocean. While the present day C_{ant} inventory is relatively well constrained by data-based estimates by Tanhua et al. [2009] (2.5–3.3 Pg C in 2005), the lateral exchanges with the other oceans and the air-sea C_{ant} flux have still large uncertainties [Olsen et al., 2015]. In this chapter, the model results will be used to better constrain the budget, the lateral fluxes, and the air-sea CO_2 flux.

The Arctic Ocean C_{ant} storage accounts for only 2% of the global ocean C_{ant} inventory and has an almost negligible effect on climate change mitigation. Nevertheless, an increase of the Arctic Ocean C_{ant} inventory has immediate effects on the Arctic Ocean acidification. This relative small perturbation of the natural carbon inventory in the Arctic Ocean is projected by the NCAR model to lead to seasonal undersaturated surface waters towards Ω_{arag} within a few decades [Steinacher et al., 2009]. At the end of the century, the entire water column is projected to be undersaturated [Steinacher et al., 2009; Anderson et al., 2010]. Thus, the Arctic Ocean will experience some of the earliest and most intense impacts of ocean acidification under twenty-first century atmospheric CO_2 levels. By constraining the Arctic Ocean C_{ant} budget, the simulations will be used to improve our understanding of future Arctic Ocean acidification.

3.2 Accepted article for publication in *Biogeosciences*

J. Terhaar[1], J. C. Orr[1], M. Gehlen[1], C. Ethé[2], and L. Bopp[3]

[1]Laboratoire des Sciences du Climat et de l'Environnement, LSCE/IPSL, CEA-CNRS-UVSQ, Université Paris-Saclay, 91191 Gif-sur-Yvette, France

[2]Institut Pierre et Simon Laplace, 4 Place Jussieu, 75005 Paris, France

[3]LMD/IPSL, Ecole Normale Supérieure / PSL Research University, CNRS, Ecole Polytechnique, Sorbonne Université, Paris, France

3.2.1 Abstract

The Arctic Ocean is projected to experience not only amplified climate change but also amplified ocean acidification. Modeling future acidification depends on our ability to simulate baseline conditions and changes over the industrial era. Such centennial-scale changes require a global model to account for exchange between the Arctic and surrounding regions. Yet the coarse resolution of typical global models may poorly resolve that exchange as well as critical features of Arctic Ocean circulation. Here we assess how simulations of Arctic Ocean storage of anthropogenic carbon (C_{ant}), the main driver of open-ocean acidification, differ when moving from coarse to eddy-admitting resolution in a global ocean circulation-biogeochemistry model (NEMO-PISCES). The Arctic's regional storage of C_{ant} is enhanced as model resolution increases. While the coarse-resolution model configuration ORCA2 (2°) stores 2.0 Pg C in the Arctic Ocean between 1765 and 2005, the eddy-admitting versions ORCA05 and ORCA025 (1/2° and 1/4°) store 2.4 and 2.6 Pg C. The difference in inventory between model resolutions that is accounted for is only from their divergence after 1958, when ORCA2 and ORCA025 were initialized with output from the intermediate resolution ORCA05. The difference would have been larger had all model resolutions been initialized in 1765 as was ORCA05. The ORCA025 Arctic C_{ant} storage estimate of 2.6 Pg C should be considered a lower limit because that model generally underestimates observed CFC-12 concentrations. It reinforces the lower limit from a previous data-based approach (2.5 to 3.3 Pg C). Independent of model resolution, there was roughly three times as much C_{ant} that entered the Arctic Ocean through lateral transport than via the flux of CO_2 across the air-sea interface. Wider comparison to nine earth system models that participated in the Coupled Model Intercomparison Project Phase 5 (CMIP5) reveals much larger diversity of stored C_{ant} and lateral transport. Only the CMIP5 models with higher lateral transport obtain C_{ant} inventories that are close to the data-based estimates. Increasing resolution also enhances acidification, e.g., with greater shoaling of the Arctic's average depth of the aragonite saturation horizon during 1960–2012, from 50 m in ORCA2 to 210 m in ORCA025. Even higher model resolution would likely further improve such estimates but its prohibitive costs also call for other more practical avenues for improvement, e.g., through

model nesting, addition of coastal processes, and refinement of subgrid-scale parameterizations.

3.2.1.1 Introduction

The Arctic is experiencing amplified ocean acidification [Steinacher et al., 2009] and amplified climate change [Bekryaev et al., 2010], both of which may affect the marine ecosystem [Gattuso and Hansson, 2011]. The main driver of the ongoing acidification of the open ocean is the increase in atmospheric CO_2 during the industrial era and the ensuing uptake of anthropogenic carbon from the atmosphere. Although this absorbed anthropogenic carbon cannot be measured directly, being dominated by the natural component, it has been estimated from other oceanographic data.

For instance, Gruber et al. [1996] developed the $\Delta C^\star$ method, building on seminal studies [Brewer, 1978; Chen and Millero, 1979] and their criticism [Broecker et al., 1985] as well as large new global data sets with improved CO_2 system measurements. That back-calculation method first calculates the total dissolved inorganic carbon (C_T) at equilibrium with atmosphere before the water parcel is subducted. The preformed C_T is then corrected for changes due to biological activity, as estimated from measurements of dissolved oxygen, total alkalinity (A_T), and nutrients, after which an estimate of preindustrial carbon is removed, finally yielding $\Delta C^\star$. Yet the $\Delta C^\star$ method's assumption of a constant air-sea CO_2 disequilibrium appears problematic in the high latitudes [Orr et al., 2001].

A second approach approximates the invasion of anthropogenic CO_2 into the interior ocean by a Transient Time Distribution (TTD) method, itself constrained by observations of transient-tracers such as CFC-12 or SF_6 [Hall et al., 2002; Waugh et al., 2004]. A third approach uses a Green's function instead of a TTD while also exploiting multiple transient tracers to assess the ocean's temporally changing distribution of anthropogenic carbon [Khatiwala et al., 2009]. A comparison of these methods suggests that by 2010 the ocean had absorbed 155 ± 31 Pg C of anthropogenic carbon, around one-third of all emitted anthropogenic carbon [Khatiwala et al., 2013]

Less attention has been paid to anthropogenic carbon storage in the Arctic. Sabine et al. [2004] estimated that the Arctic Ocean had absorbed 4.9 Pg C by 1994. Yet without estimates for anthropogenic carbon in the Arctic itself, Sabine et al. scaled the Arctic inventory to be 5% of their $\Delta C^\star$-based estimate for global anthropogenic carbon storage, assuming the same Arctic:Global ocean ratio as in the global gridded distribution of observed CFC-12 [Willey et al., 2004]. More recently, Tanhua et al. [2009] used Arctic observations of CFC-11, CFC-12, and SF_6 and the TTD approach, revising the former Arctic anthropogenic carbon storage estimate downward to a range of 2.5 to 3.3 Pg C for year 2005. With that estimate, they emphasized that while the Arctic Ocean represents only 1% of the global ocean volume, it stores 2% of the global ocean's anthropogenic carbon. Although these numbers are relatively small, Arctic concentrations of anthropogenic C_T must be relatively large, thus driving enhanced acidification in the Arctic Ocean. No other approaches have been used in the Arctic.

To provide an alternate approach to estimate anthropogenic carbon in the Arctic and to assess its budget and the mechanisms that control it, one could make carbon cycle simulations over the industrial era with a coupled ocean circulation-biogeochemical model. A global-scale model configuration would be needed to account for the Arctic in the context of the global carbon cycle, while avoiding artefacts from lateral boundary conditions that must be imposed in regional models. Yet typical ocean general circulation models have coarse resolution, which may be insufficient to adequately represent Arctic Ocean bathymetry, shelf, slopes, and ridges, all of which affect Arctic Ocean circulation [Rudels et al., 1994].

The bathymetry of the Arctic Ocean differs from that in other oceans in part because of the preponderance of shelf seas, comprising 53% of the total surface area [Jakobsson, 2002] (Figure 3.1). The remaining 47% of its surface area covers 95% of the total volume of the Arctic Ocean, split across four deep basins: the Nansen basin, the Amundsen basin, the Makarov basin, and the Canadian basin. Water masses enter these deep basins via (1) deep inflow from the Atlantic through the Fram Strait into the Nansen basin, (2) inflow from the Barents Sea that sinks into the Nansen basin through the St. Anna Trough, as cooling increases density, and (3) transport from density flows along the continental shelves that are driven by brine rejection from sea-ice formation [Jones et al., 1995]. These three local transfers are difficult to resolve in coarse-resolution models, e.g., local density flows necessitate much higher resolution [Proshutinsky et al., 2016]. Model resolution also affects the simulated interior circulation of the Arctic Ocean by its connection to the global ocean circulation via four relatively narrow and shallow passages: (1) the Canadian Archipelago, (2) the Fram Strait, (3) the Barents Sea Opening, and (4) the Bering Strait [Aksenov et al., 2016]. Lateral exchange of water, carbon, and nutrients across these sections also affects Arctic Ocean primary production and acidification [Popova et al., 2013; Luo et al., 2016].

Here our aim is to use a three-dimensional model to help refine the estimate of the total anthropogenic carbon in the Arctic Ocean while assessing the dominant pathways by which anthropogenic carbon enters the Arctic Ocean and the importance of that lateral input relative to the air-sea flux. Three simulations made at increasingly higher lateral grid resolution are aimed at assessing the extent to which the coarse resolution used by typical global ocean models may need to be improved to adequately estimate storage of anthropogenic carbon in the Arctic Ocean and associated ocean acidification.

3.2.2 Methods

Multiple global simulations were made to assess C_{ant} in the ocean. Simulations were made with a state-of-the-art ocean circulation-biogeochemical model at three resolutions over the industrial period since the mid-19th century, i.e., as typical of recent model comparison efforts. Longer simulations were also made at the same resolutions with a less costly (and less precise) perturbation approach to correct for the missing anthropogenic carbon given that the actual industrial era

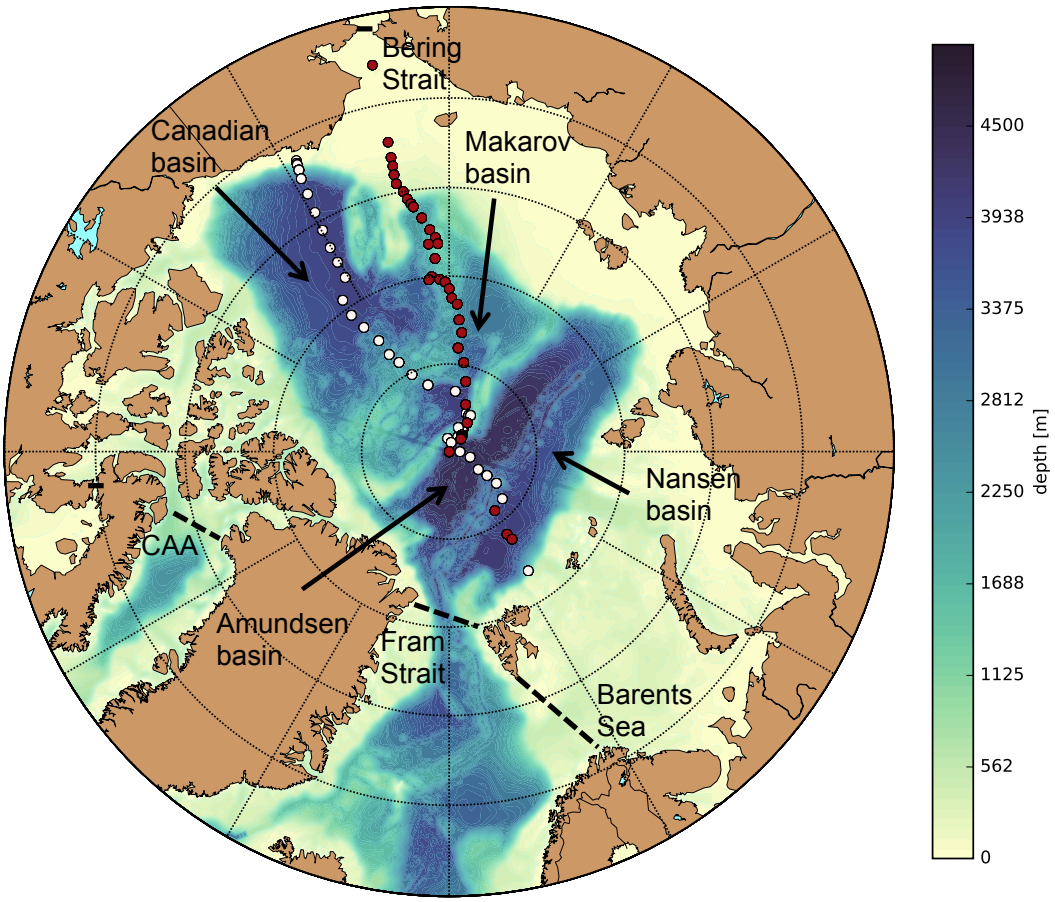

Figure 3.1 – CFC-12 stations along the AOS94 (red) and Beringia 2005 expeditions (white). Other colors indicate the bathymetry of the Arctic Ocean, while the four dashed black lines show the boundaries of the Arctic Ocean domain used in this study.

began about a century earlier (mid-18th century). The highest resolution configuration used an unprecedented lateral grid spacing for such long, global, biogeochemical simulations, although its cost meant its effect could be assessed only over 1958–2012.

3.2.2.1 Models

For our study, we used the global ocean circulation model NEMO-v3.2 (Nucleus for European Modeling of the Ocean - version 3.2). The NEMO model has three parts: (1) the ocean dynamics and thermodynamics model OPA [Madec, 2008], (2) the sea-ice model LIM [Vancoppenolle et al., 2009], and (3) the passive tracer module TOP. This physical model is coupled via TOP to version 1 of PISCES (Pelagic Interactions Scheme for Carbon and Ecosystem Studies) [Aumont and Bopp, 2006]. For this study we used NEMO at three resolutions: a laminar 2° configuration (ORCA2) typical of coarse-resolution ocean models [Madec et al., 1998], which does not resolve eddies; an intermediate 0.5° configuration (ORCA05) that just begins to allow eddies to appear spontaneously [Bourgeois et al., 2016]; and a higher-resolution, eddy admitting version, i.e., 0.25° configuration

Table 3.1 – Arctic Ocean grid size and basin volumes as a function of model resolution.

Configuration	Horizontal grid (km)			Volume (10^6 km^3)				
					Basin			
	Mean	Min	Max	Arctic	Nansen	Amundsen	Makarov	Canada
ORCA2	120.8	63.3	180.5	14.3	2.8	3.2	2.2	4.7
ORCA05	29.0	9.4	41.3	13.3	2.6	2.7	1.9	4.9
ORCA025	14.4	3.2	20.5	13.3	2.3	2.9	1.8	5.0

(ORCA025), which is still not eddy resolving [Barnier et al., 2006b]. The highest resolution simulation is referred to as ORCA025-G70 in the DRAKKAR ensemble.

All three configurations have a tripolar, curvilinear horizontal grid. One grid pole (singularity) is located at the geographical South Pole while the conventional North-Pole grid singularity over the Arctic Ocean has been replaced by two grid singularities, both displaced over land, one over Canada and the other over Russia [Madec and Imbard, 1996], thereby saving computational costs and avoiding numerical artefacts. From 90°S to 20°N, the grid is a normal Mercator grid; north of 20°N, it is distorted into ellipses to create the two northern singularities [Barnier et al., 2006b; Madec, 2008]. The grid size changes depending on resolution and location (Table 3.1). The mean horizontal grid size in the Arctic Ocean (average length of the 4 horizontal edges of surface grid cells in the Arctic Ocean) is 121 km in ORCA2, 29 km in ORCA05, and 14 km in ORCA025. The smallest horizontal grid size in the Arctic is 63 km in ORCA2, 9 km in ORCA05, and 3 km in ORCA025.

Vertically, all three model configurations have the same discretization, where the full-depth water column is divided into 46 levels whose thicknesses vary from 6 m (top level) to 249 m (level 45), but the latter can reach up to 498 m, being extended into level 46 as a function of the bathymetry (partial steps). For its bathymetry, the ocean model relies on the 2-minute bathymetry file ETOPO2 from the National Geophysical Data Center, which is based on satellite derived data [Smith and Sandwell, 1997] except for the highest latitudes: the IBCAO bathymetric data is used in the Arctic [Jakobsson et al., 2000b] and BEDMAP bathymetric data is used for the Southern Ocean south of 72°S [Lythe and Vaughan, 2001]. To interpolate the bathymetry on the model grid, the median of all data points in one model grid cell was computed. NEMO uses the partial-step approach for the model to better match the observed topography. In this approach, the bathymetry of the model is not tied directly to the bottom edge of the deepest ocean grid level, which varies with latitude and longitude; rather, the deepest ocean grid level for each column of grid cells is partially filled in to better match the observed ocean bathymetry [Barnier et al., 2006b].

The lateral isopycnal diffusion and viscosity coefficients were chosen depending on the resolution (Table 3.2). In ORCA2, a Laplacian viscosity operator was used, whereas a bi-Laplacian

Table 3.2 – Selected physical coefficients and parameters for ORCA2, ORCA05, and ORCA025.

Configuration	Lateral diffusivity	Lateral viscosity	Eddy parameterization
ORCA2[a]	2000 $m^2\ s^{-1}$	4×10^4 m^2 s^{-1} [b]	2000 m^2 s^{-1}
ORCA05	600 $m^2\ s^{-1}$	-4×10^{11} m^2 s^{-1}	1000 m^2 s^{-1}
ORCA025	300 $m^2\ s^{-1}$	-1.5×10^{11} m^2 s^{-1}	none

[a] Lateral diffusivity and viscosity coefficients decrease towards the poles proportional to the grid size.
[b] reduced to 2100 m^2 s^{-1} in the tropics (except along Western boundaries)

operator was used in ORCA05 and ORCA025. To simulate the effect of eddies on the mean advective transport in the two coarser resolution configurations, the eddy parameterization scheme of Gent and McWilliams [1990] was applied with eddy diffusion coefficients indicated in Table 3.2. Vertically, the same eddy viscosity (1.2×10^{-4} m^2 s^{-1}) and diffusivity coefficients (1.2×10^{-5} m^2 s^{-1}) were used in all three resolutions.

The biogeochemical model PISCES [Aumont and Bopp, 2006] includes four plankton functional types: two phytoplankton (nanophytoplankton and diatoms) and two zooplankton (micro- and meso-zooplankton). The growth of phytoplankton is limited by the availability of five nutrients: nitrate, ammonium, total dissolved inorganic phosphorus P_T, total dissolved silicon Si_T, and iron. The nanophytoplankton and diatoms are distinguished by their need for all nutrients, with only diatoms requiring silicon. While the Fe:C and Chl:C ratios of both phytoplankton groups as well as the Si:C ratio of diatoms are predicted prognostically by PISCES, the remaining macronutrient ratios are held constant at C:N:P = 122:16:1 [Takahashi et al., 1985]. The same ratio holds for nonliving compartments: dissolved organic matter (DOM) and both small and large sinking particles, which differ in their sinking velocity. In PISCES, nutrients are supplied by three external pathways: atmospheric dust deposition, river delivery, and sediment mobilization of iron. Dust deposition was taken from a simulation by Tegen and Fung [1995]. River discharge of C_T and dissolved organic carbon (DOC) is based on the Global Erosion Model (GEM) by Ludwig et al. [1998]. Riverine DOC was assumed to be entirely labile, being instantaneously transformed into C_T as soon as it enters the ocean. River delivery of the other four nutrients (Fe, N, P, and Si) were calculated from riverine C_T delivery, assuming constant ratios of C:N:P:Si:Fe = $320:16:1:53.3:3.64 \times 10^{-3}$ [Meybeck, 1982]. For sediment mobilization, the dissolved iron input was parameterized as 1 µmol Fe m^{-2} day^{-1} for depths shallower than 386 m and decreases exponentially with depth following Moore et al. [2004].

3.2.2.2 Biogeochemical simulations

For initial conditions, we used observational climatologies for temperature and salinity combined from three sources [Barnier et al., 2006b], for dissolved oxygen and nutrients (nitrate, P_T, and Si_T) from the 2001 World Ocean Atlas [Conkright et al., 2002], and for preindustrial C_T and A_T from the observation-based Global Data Analysis Product (GLODAP) [Key et al., 2004]. As comparable observational climatologies for DOC and iron are lacking, those variables were initialized from output of a 3000-year spin up of an ORCA2 simulation including PISCES. Other tracers have short recycling times and were thus initialized with globally uniform constants.

For physical boundary conditions, all simulations were forced with the same DRAKKAR Forcing Set (DFS) constructed originally by Brodeau et al. [2010] and routinely updated. This historical reanalysis-based forcing data set provides surface air temperature and humidity at 2 m, wind fields at 10 m, shortwave and longwave radiation, and the net surface freshwater flux (evaporation minus precipitation). It covers 55 years, including 1958–2001 from version 4.2 and 2002–2012 from version 4.4.

A 50-year spin up was first made from rest in the ORCA05 NEMO-PISCES model (coupled circulation-biogeochemistry), after initializing the model variables with the above-mentioned fields. The resulting simulated physical and biogeochemical fields were then used to initialize the ORCA05 NEMO-PISCES simulations in 1870, and that model was subsequently integrated over 1870–1957. Since no atmospheric reanalysis is available during that period, we simply looped the DRAKKAR Forcing Set. Then at the beginning of 1958, the ORCA05 simulated fields were interpolated to the ORCA2 and ORCA025 grids, and simulations were continued in each of the three configurations from 1958 to 2012. We refer to these simulations as B1870-ORCA2, B1870-ORCA05, and B1870-ORCA025 (Table 3.3), where the first letter refers to the type of simulation (B for biogeochemical), the following four numbers refer to the initialization year, and the remainder refers to the resolution used over 1958–2012.

The initialization of the ORCA2 and ORCA025 models in 1958 with interpolated fields from ORCA05 introduces an error in the results from B1870-ORCA2 and B1870-ORCA025. To estimate this branching error in the low resolution model, we also made a simulation using ORCA2 from 1870 to 2012 (referred to as B1870-ORCA2*) and compared it to B1870-ORCA2 (initialized in 1958 with output from ORCA05). This strategy was not possible for ORCA025, because running ORCA025 with PISCES over 1870–2012 is too costly.

For each member of this "B" class of simulations, we actually made two types of runs, historical and control, both forced with the same reanalysis fields. Those two runs differ only in their atmospheric CO_2 concentrations. The control simulations were forced with the preindustrial CO_2 concentration of 287 ppm in the atmosphere over the entire period from 1870 to 2012. The historical simulations were forced with yearly averaged historical atmospheric CO_2 concentrations reconstructed from ice cores and atmospheric records over 1870 to 2012 starting at the same ref-

Table 3.3 – Set of simulations

Name	Resolution	
	Before 1958	After 1958
Biogeochemical		
B1870-ORCA2	ORCA05	ORCA2
-ORCA05	ORCA05	ORCA05
-ORCA025	ORCA05	ORCA025
-ORCA2*	ORCA2	ORCA2
Perturbation		
P1870-ORCA2	ORCA05	ORCA2
-ORCA05	ORCA05	ORCA05
-ORCA025	ORCA05	ORCA025
-ORCA2*	ORCA2	ORCA2
P1765-ORCA2	ORCA05	ORCA2
-ORCA05	ORCA05	ORCA05
-ORCA025	ORCA05	ORCA025
-ORCA2*	ORCA2	ORCA2

erence of 287 ppm [Le Quéré et al., 2015]. Making both the control and the historical runs for each of the B class of simulations and taking the difference automatically corrects for model drift. That difference is defined as the anthropogenic component.

3.2.2.3 C_{ant} perturbation simulations

Because of computational limitations, it was necessary to start the anthropogenic CO_2 perturbation of our reference ORCA05-PISCES simulation in 1870 as opposed to the traditional earlier reference of 1765 [Sarmiento et al., 1992], a more realistic approximation of the start of the industrial-era CO_2 increase. A similar compromise was adopted for CMIP5 [Taylor et al., 2012]. During that missing 105 years, atmospheric xCO_2 increased from 278 to 287 ppm, a 9 ppm difference that seems small relative to today's total perturbation with atmospheric xCO_2 now above 400 ppm. However, Bronselaer et al. [2017] estimated that global ocean uptake of C_{ant} in 1995 is actually underestimated by ~30% (29 Pg C) for simulations that reference the natural preindustrial state to 1850 rather than 1765. The cause is partly due to ocean carbon uptake during the missing 1765–1850 period, but mostly it is due to the higher preindustrial reference for atmospheric xCO_2 that results in the air-sea flux of C_{ant} being underestimated throughout the entire simulation. Unfortu-

nately, we cannot use Bronselaer et al.'s results to correct our biogeochemical simulations because they do not include the Arctic Ocean in their global data-based assessment. Furthermore, their reference date in the mid 19th century is 20 years earlier than ours.

Instead, to correct for the late starting date of our biogeochemical simulations, we made additional simulations using the more efficient single-tracer perturbation approach [Sarmiento et al., 1992] rather than the full PISCES biogeochemical model (24 tracers). To account for the missing carbon, we added the difference between two perturbation simulations, denoted as P rather than B, one starting in 1765 (P1765) and the other starting in 1870 (P1870). For consistency, we applied the same initialization strategy as for the biogeochemical simulations, i.e. using ORCA05 until the end of 1957 with that output serving as the initial fields for subsequent 1958–2012 simulations in all three configurations. The naming convention for the "P" class of simulations is like that for the "B" class (indicated by the first letter). The difference is that in each P simulation there is only one tracer and one run for each (no need for a control and a historical run). However initializing a set of P simulations in 1765 as well as in 1870 implies twice the number of simulations (Table 3.3). The difference in C_{ant} between P1765 and P1870 simulations was later added as a late-start correction to the biogeochemical simulations (B1870), for each resolution separately.

The perturbation approach of Sarmiento et al. [1992] avoids the computationally intensive standard CO_2 system calculations by accounting for only the perturbation (C_{ant}), assuming it is independent of the natural carbon cycle. By focusing only on anthropogenic carbon, this approach exploits a linear relationship between the anthropogenic change in surface-ocean pCO_2 [µatm] and its ratio with the corresponding change in surface-ocean dissolved inorganic carbon (δC_T):

$$\frac{\delta pCO_{2_o}}{\delta C_T} = z_0 + z_1 \delta pCO_{2_o}, \tag{3.1}$$

where δpCO_{2_o} is the perturbation in surface-ocean pCO_2 and the coefficients z_0 and z_1 are each quadratic functions of surface temperature [°C],

$$z_0 = a_0 + a_1 T + a_2 T^2 \tag{3.2}$$

$$z_1 = b_0 + b_1 T + b_2 T^2. \tag{3.3}$$

In the model, Eq. (3.1) was rearranged to solve for δpCO_{2_o} in terms of δC_T [Sarmiento et al., 1992, Eq. (11)], as needed to compute the air-sea flux [Sarmiento et al., 1992, Eq. (2)]. In the air-sea flux equation, the atmospheric xCO_2 was corrected for humidity and atmospheric pressure to convert to $pCO_{2_{atm}}$, which thus varies spatially while atmospheric xCO_2 does not (in the model). The atmospheric xCO_2 history for 1765–1869 is from Meinshausen et al. [2017], while the history for 1870 and beyond is the same as used in the NEMO-PISCES simulations. One set of coefficients was derived for our reference atmospheric xCO_2 in 1765; another set was derived for our reference atmospheric xCO_2 in 1870 (Table 3.4). The original approach was only updated to use the equilibrium constants recommended for best practices [Dickson et al., 2007] and to cover a perturbation of up to 280 ppm (see Supplement). The relative uncertainty introduced by approximating the

Table 3.4 – Fitted parameters in Eqs. 2 and 3 for the perturbation simulations P1765 and P1870.

Parameter	P1765	P1870
a_0	1.7481	1.8302
a_1	-3.2813 $\times 10^{-2}$	-3.4631 $\times 10^{-2}$
a_2	4.1855 $\times 10^{-4}$	4.3614 $\times 10^{-4}$
b_0	3.9615 $\times 10^{-3}$	4.0105 $\times 10^{-3}$
b_1	-7.3733 $\times 10^{-5}$	-7.3386 $\times 10^{-5}$
b_2	5.4759 $\times 10^{-7}$	5.1199 $\times 10^{-7}$

perturbation to the ocean CO_2 system equilibria with Eq. (3.1) remains less than ±0.3% across the global ocean's observed temperature range when $\delta pCO_2^{oc} < 280$ ppm.

The Arctic C_{ant} inventory in 2012 simulated by the perturbation approach (P1870-ORCA2*) underestimates that simulated by the full biogeochemical approach (B1870-ORCA2*) by 3% (Appendix A). The corresponding underestimation by P1765-ORCA2* is expected to be similar. The similar bias of P1765-ORCA2* and P1870-ORCA2* means that the bias in their difference is probably much less than 3%. The same holds for P1765-ORCA2 vs. P1870-ORCA2. Thus using their difference to correct for the late start of B1870-ORCA2 is not only practical but also sufficiently accurate for our purposes. In contrast, not correcting B1870-ORCA2 for its late starting date would lead to a 19% underestimation of its Arctic C_{ant} inventory for the full industrial era.

In practice, to make the late-start correction, at each grid cell we added the time-varying difference in C_{ant} between the two perturbation simulations (P1765 – P1870) to the C_{ant} simulated with B1870 for each resolution separately. From here on, we refer only to these corrected biogeochemical simulations, denoting them as ORCA2, ORCA05, ORCA025, and ORCA2*.

3.2.2.4 CFC-12 simulation

CFC-12 is a purely anthropogenic tracer, a sparingly soluble gas whose concentration began to increase in the atmosphere in the early 1930's, part of which has been transferred to the ocean via air-sea gas exchange. Its uptake and redistribution in the ocean has been simulated following OCMIP-2 protocols [Dutay et al., 2002]. The CFC-12 flux (F_{CFC}) at the air-sea interface was calculated as follows:

$$F_{CFC} = k_w(\alpha_{CFC}\ pCFC - C_s)(1 - I), \tag{3.4}$$

where k_w is the gas-transfer velocity (piston velocity) in m s^{-1} [Wanninkhof, 1992], pCFC is the atmospheric partial pressure of CFC-12 from the reconstructed atmospheric history by Bullister [2015], C_s is the sea surface concentration of CFC-12 (mol m^{-3}), α_{CFC} is the solubility of CFC-12 (mol m^{-3}atm^{-1}) from Warner and Weiss [1985], and I is the model's fractional sea-ice cover. Once

in the ocean, CFC-12 is an inert tracer that is distributed by advection and diffusion; it has no internal sources and sinks. Many high-precision measurements of CFC-12 are available throughout the ocean, in sharp contrast to C_{ant} which cannot be measured directly.

As for the other simulations, those for CFC-12 were made using ORCA05 until 1957, at which point those results were interpolated to the ORCA2 and ORCA025 grids. The ORCA05 CFC-12 simulation began in 1932. From 1958 to 2012, CFC-12 was simulated for each resolution separately.

3.2.2.5 Arctic Ocean

To assess the anthropogenic carbon budget in the Arctic Ocean, we adopt the regional domain defined by Bates and Mathis [2009] delineated in Fig. 3.1. That domain's lateral boundaries and the volume of water contained within them vary slightly among the three model versions due to their different resolutions and bathymetries (Table 3.1). The signature of these different volumes is also apparent in the integrated quantity of anthropogenic carbon that is stored in the Arctic in 1958, although the fields for all three models are based on the same 1957 field from the ORCA05 model (Fig. 3.2).

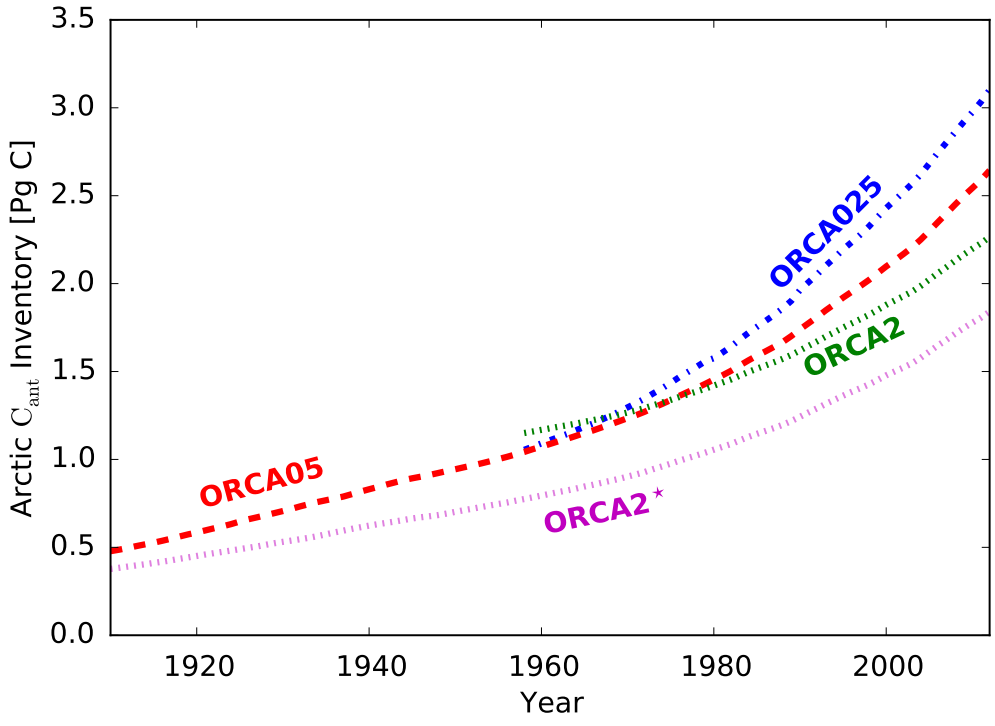

Figure 3.2 – Arctic Ocean C_{ant} inventory for ORCA2, ORCA05, ORCA025, and ORCA2*. The discontinuity for ORCA2 in 1958 is due to its larger total volume of water when integrated across the Arctic domain (Table 3.1).

3.2.2.6 Transport across boundaries

Transects are defined (Fig. 3.1) along the four boundaries as consistently as possible for the three resolutions. Water transport across each of the four boundaries is calculated for each model configuration by using monthly average water velocities at each boundary grid cell along a transect multiplied by the corresponding area of the face of the grid cell through which the water flows. For boundaries defined by a row of cells (Fram Strait, Canadian Arctic Archipelago [CAA], and Bering Strait), the transport is calculated across the northern face of each cell. Conversely, for the jagged boundary of the Barents Sea Opening, transport is calculated at the northern and eastern faces of each cell and the two transports are summed. For each transect, transport across all of its cells are summed to obtain the transect's monthly net transport.

For the C_{ant} transport, we do the same but also multiply the water transport at the boundary between two grid cells with their volume-weighted monthly-average concentration. This multiplication of monthly means introduces an error into the transport calculations owing to neglect of shorter term variability. To elucidate that error, we sum results from those monthly calculations across all four sections, integrate them over time from 1960 to 2012, and compare that to the net transport of C_{ant} into the Arctic Ocean implied by the inventory change minus the cumulative air-sea flux over the same time period. The inventory of C_{ant} is the total mass of C_{ant} inside the Arctic Ocean at a given time, while the cumulative flux is the time-integrated air-sea flux of anthropogenic CO_2 over the Arctic Ocean since the beginning of the simulation. The difference between these two spatially integrated values is the reference value for the net lateral flux into the Arctic Ocean to which is compared the less exact total lateral flux of anthropogenic carbon computed from monthly mean velocity and concentration fields integrated over time. The relative error for transport of C_{ant} across all the separate boundaries introduced by the monthly average calculations is 28% for ORCA2, 7% for ORCA05, and 3% for ORCA025. This error applies neither to the C_{ant} inventory, nor to the cumulative C_{ant} air-sea flux or the lateral C_{ant} fluxes, which are all calculated online, i.e., during the simulations.

3.2.2.7 CFC-12 observational data

Model simulations were evaluated indirectly by comparing simulated to observed CFC-12. We choose CFC-12 to evaluate the model, because it is an anthropogenic, passive, conservative, and inert tracer, and in contrast to anthropogenic carbon, it is directly measurable. The CFC-12 atmospheric concentration increased from zero in the 1930s to its peak in the 2000s, since declining as a result of the Montreal protocol. Thus CFC-12 is a transient tracer similar to anthropogenic carbon but for which there exist extensive direct measurements, all carried out with high precision during WOCE (World Ocean Circulation Experiment) and CLIVAR (Climate and Ocean - Variability, Predictability and Change) era. Nowadays, ocean models are often evaluated with CFC-11 or CFC-12, especially those destined to be used to assess anthropogenic carbon uptake [Dutay et al.,

2002; Orr et al., 2017].

The CFC-12 observations used in this study come from two trans-Arctic cruises: the 1994 Arctic Ocean Section (AOS94) [Jones et al., 2007] and the Beringia 2005 expedition [Anderson et al., 2011a] (Fig. 3.1). AOS94 started on 24 July and was completed on 1 September, during which CFC-12 measurements were made at 39 stations. That section began in the Bering Strait, entered the Canada basin adjacent to Mendeleev ridge, continued to the Makarov basin, and ended at the boundary of the Nansen basin and the Barents Sea. The Beringia expedition started on 19 August and ended on 25 September 2005. It began off the coast of Alaska, went through the Canada and Makarov basins, crossed the Lomonosov ridge, and its last CFC-12 station was taken on the Gakkel ridge. These two cruises were chosen from among others because they cross large parts of the Arctic, including almost all four major basins.

3.2.2.8 Data-based estimates of anthropogenic carbon

Our simulated C_{ant} was compared to data-based estimates from Tanhua et al. [2009] for the year 2005 and from GLODAPv2 for the year 2002 [Lauvset et al., 2016], both based on the TTD approach.

3.2.3 Results

3.2.3.1 Lateral water fluxes

The lateral water flux across each of the four Arctic boundaries is a fundamental reference for the simulated physical transport, especially given our goal to construct a budget that includes lateral transport of passive tracers. Results for lateral water transport in the three model resolutions may be grouped into two classes: coarse resolution and higher resolutions. In ORCA2, water enters the Arctic Ocean from Barents Sea and the Bering Strait (2.1 Sv split evenly), with 86% of that total leaving the Arctic via the Fram Strait and the remaining 14% flowing out via the CAA (Table 3.2.3.1). Conversely, outflow through the CAA is seven times larger for ORCA05 and nine times larger for ORCA025, being fueled by 26 to 46% more inflow via the Bering Strait and 110 to 170% more inflow via the Barents Sea. Outflow via the Fram Strait is 1.76 Sv in ORCA2, 1.42–1.75 Sv in ORCA05, and 1.46–1.80 Sv in ORCA025, depending on the time period (Table 3.2.3.1).

Relative to the observed CAA outflow of 2.7 Sv [Curry et al., 2014; Straneo and Saucier, 2008], only ORCA05 and ORCA025 simulate similar results. In contrast, ORCA2's simulated CAA outflow is about one ninth of that observed. Likewise, its inflow via the Barents Sea is half of that observed, while the two higher resolution simulations have Barents Sea inflows that are 20% and 40% larger than observed. Yet for inflow through the Bering Strait, it is ORCA2 that is closest to the observed estimate, overestimating it by 30%, while ORCA05 and ORCA025 overestimate it by 60% and 90%. Thus too much Pacific water appears to be entering the Arctic Ocean. All resolutions underestimate the central observational estimate for the Fram Strait outflow by ~12% but still easily fall within the large associated uncertainty range.

Table 3.5 – Lateral transport of water and C_{ant} across Arctic Ocean boundaries. Simulated values are calculated for the same time period as observations.

	Model configuration			Observations	Year	Sources
	ORCA2	ORCA05	ORCA025			
Lateral water transport (Sv)						
Fram Strait	-1.76	-1.75	-1.80	-2.0 ± 2.7	1997–2006	Schauer et al. [2008]
	-1.76	-1.42	-1.46	-1.7	1980–2005	Rudels et al. [2008]
Barents Sea	1.20	2.50	2.77	2.0	2003–2005	Skagseth et al. [2008]
	1.04	2.42	2.78	2.0	1997–2007	Smedsrud et al. [2010]
Bering Strait	1.02	1.29	1.49	0.8 ± 0.2	1991–2007	Woodgate et al. [2010]
CAA	-0.29	-2.00	-2.59	-2.7 ± 0.2	2004–2013	Curry et al. [2014]
Sum	-0.12	-0.16	-0.18			
	Model configuration			Observations	Year	Sources
	ORCA2	ORCA05	ORCA025			
Lateral C_{ant} fluxes (Tg C yr^{-1})						
Fram Strait	-17	-12	-8	-1 ± 17	2002	Jeansson et al. [2011]
	-17	-7	5	-12	2012	Stöven et al. [2016]
Barents Sea	16	43	50	41 ± 8	2002	Jeansson et al. [2011]
Bering Strait	18	22	27	18	2000-2010[a]	Olsen et al. [2015]
CAA	-5	-28	-36	-29	2000-2010[a]	Olsen et al. [2015]
Sum	18	29	38	29	2000-2010[a]	Olsen et al. [2015]

[a]Year or period impossible to identify exactly as C_{ant} and velocity measurements are not from the same year.

Summing up, the net water transport across all four boundaries is not zero. A net Arctic outflow between 0.12 and 0.17 Sv is found for the three model resolutions owing to river inflow and precipitation as well as artefacts caused by using monthly averages. In contrast, when the observed water transport estimates at all four boundaries are summed up, there is a net outflow of 1.9 Sv, more than ten times larger. This strong net outflow is also much larger than freshwater input from rivers of 0.08 Sv [McClelland et al., 2006] and precipitation of 0.12 Sv [Yang, 1999]. It can only be explained by uncertainties in the data-based estimates of water transport, which are at least ±2.7 Sv for the net transport based on the limited uncertainties available for transport across the individual boundaries (Table 3.2.3.1). The excessive central observational estimated for the net outflow might be explained by a data-based estimate for the Barents Sea inflow that is too weak combined with a data-based estimate for the Fram Strait outflow that is too strong, a possibility that is consistent with results from the higher resolution models ORCA05 and ORCA025.

3.2.3.2 Sea ice

Because sea-ice cover affects the air-sea CO_2 flux and hence anthropogenic carbon concentrations in the ocean, we compare the modeled sea-ice cover to that observed by the U.S. National Snow

and Ice Data Center [Walsh et al., 2015]. Yearly averages of sea-ice extent agree within 2% between the observations and models. Only in summer are simulated sea-ice concentrations slightly too high (by 0.25–0.5 $\times$ 10^6 km^3, e.g. 5%). Despite this overall agreement in integrated sea-ice extent, regionally differences are larger. During winter (Fig. 3.3), all three model configurations slightly overestimate the sea-ice extent northeast of Iceland and north of the Labrador Sea, while the simulated sea-ice extent in the Barents Sea and the Bering Strait are similar to observations. During summer, the simulated sea-ice extent resembles that observed in the western Arctic particularly near the Pacific, but all model resolutions slightly overestimate sea-ice extent in the Nordic Seas, north of the Barents Sea, the Kara Sea, and the Laptev Sea. This overestimation should reduce air-sea CO_2 fluxes locally in these regions. Overall, the close model-data agreement for sea-ice extent in terms of the total amount, its trend and seasonal coverage, as well as regional coverage in winter contrasts with the tendency of the models to overpredict sea-ice cover in summer in the highest latitudes of the eastern Arctic.

3.2.3.3 Atlantic water

In the Arctic Ocean, water temperature is used to help identify water masses, with values above 0°C typically coming from the Atlantic Ocean [Woodgate, 2013]. The observed temperature along the 1994 and 2005 sections (Fig. 3.4) indicates that Atlantic Water (AW) is found between 200 and 1000 m, penetrating laterally below the strongly stratified Arctic Ocean surface waters. In ORCA025, this AW layer is deeper and more diffuse, lying between 500 and 1500 m, thus leading to a cold bias around 500 m and a warm bias around 1000 m. The Beringia station at the boundary between the Barents Sea and the Nansen basin indicates AW lies between 200 m (2.5°C) and the seafloor at 1000 m (0°C). Conversely in the same location in ORCA025, model temperatures remain above 1.5°C throughout the water column. That lower maximum temperature and weaker vertical gradient suggests that when ORCA025's Atlantic water enters the Arctic Ocean through the Barents Sea it is too diffuse, being well mixed throughout the water column. Weaker maxima in ORCA025's simulated temperature relative to observations are also found further west in the Canada basin along both sections. There observed temperatures reach maxima of 1.1°C, while its simulated maxima reach only 0.5°C.

The two lower resolutions represent lateral invasion of AW less successfully than does ORCA025. Both simulations show water with temperatures higher than 0°C only at the southern end of the Nansen basin. Vertically, these water masses are situated around 400 m for ORCA2 and between 200 and 1300 m for ORCA05.

3.2.3.4 CFC-12

Simulated CFC-12 was compared among the three resolutions and with observations, focusing first on basin-scale tendencies based on vertical profiles of the distance-weighted means along

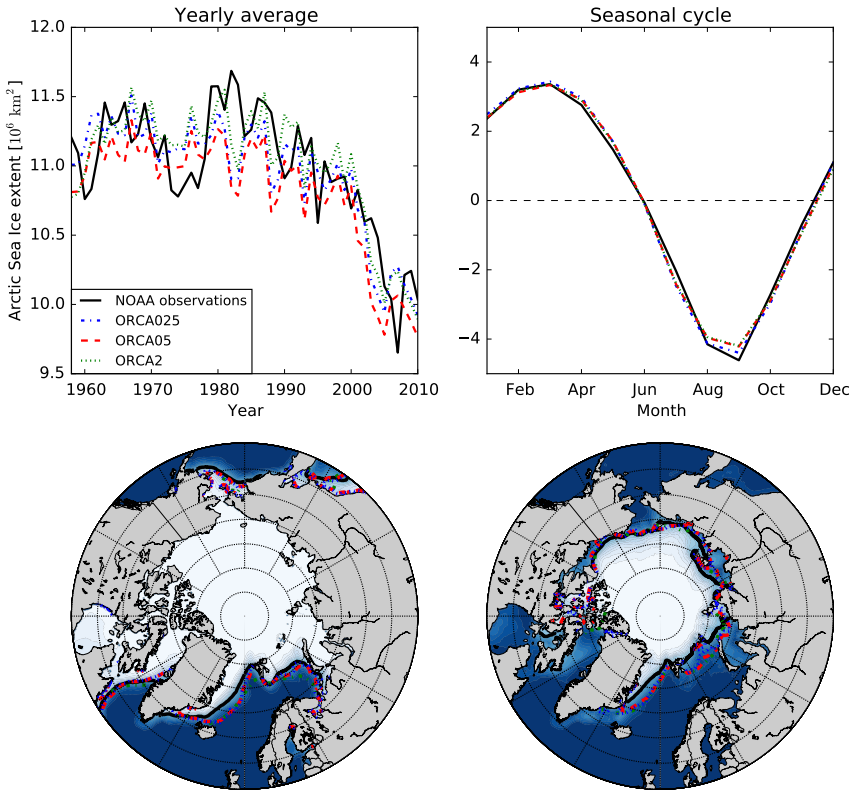

Figure 3.3 – Sea-ice extent (top) and sea-ice concentration (bottom) over the Arctic from 1960 to 2012 comparing microwave-based observations from NOAA (black) to simulated results from ORCA2 (green dots), ORCA05 (red dashes), and ORCA025 (blue dot-dash). Shown are the yearly averages (top left), the average (climatological) seasonal cycle over 1958–2010 (top right), and the average sea-ice extent in winter (December, January, February) (bottom left) and summer (July, August, September) (bottom right). The lines on the maps show the 50% sea-ice cover for the three model resolutions and the observations, while the color indicates the observed sea-ice concentration.

the Beringia 2005 section (Fig. 3.5). This comparison reveals that among resolutions, simulated CFC-12 concentrations differ most between 400 and 1900 m; conversely, above and below that intermediate zone, simulated average profiles are nearly insensitive to resolution. In that intermediate zone and above, simulated concentrations are also generally lower than observed. The only exception is the top 100 m in the Canada basin where all resolutions overestimate observed concentrations by 10%. Between 200 and 400 m, all resolutions underestimate observations by ~50%. Below 400 m, the ORCA2 CFC-12 concentrations decline quickly to zero by ~1000 m, while the ORCA05 and ORCA025 concentrations continue to increase, both being 15% greater at 900 m than at 400 m. Below that depth, the ORCA05 concentrations decline quickly reaching zero at 1350 m, while ORCA025 concentrations remain above 1 pmol kg^{-1} until 1400 m. Between 1100 and

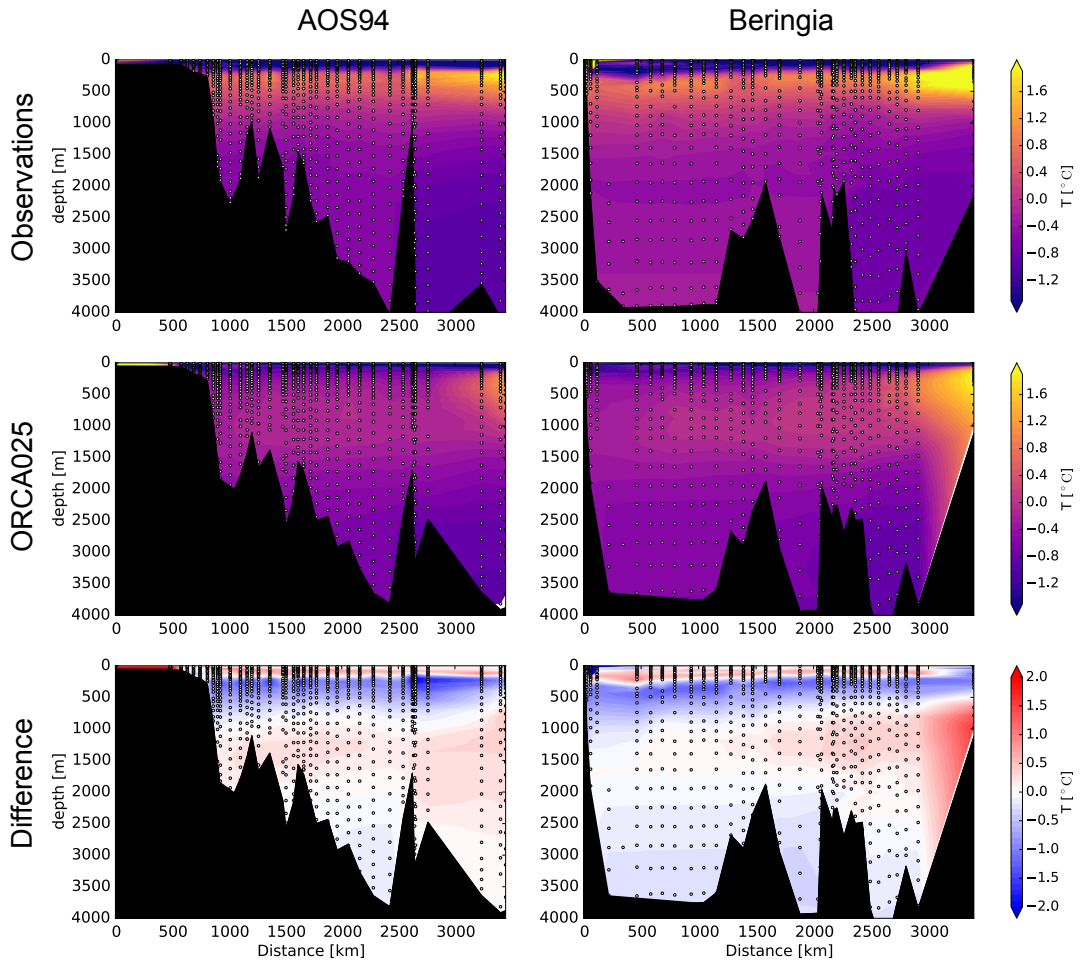

Figure 3.4 – Temperature along the 1994 Arctic Ocean Section (AOS94) cruise (left) and the Beringia/HOTRAX 2005 section (right), both trans-Arctic transects (Fig. 3.1). The observations (top) are compared to simulated results from ORCA025 averaged over summer of the respective year (middle). The model-data difference is shown at the bottom.

1500 m, average CFC-12 concentrations along the Beringia section in ORCA025 are larger than observed by up to ~10% at 1300 m. This overestimation of CFC-12 by ORCA025 reaches up to 40% in the Canada and Makarov basins. Below 1900 m, the simulated concentrations are essentially zero, while the observations are slightly higher (0.12 pmol kg^{-1}). For comparison, the reported detection limit for CFC-12 for the Beringia 2005 expedition is 0.02 pmol kg^{-1} [Anderson et al., 2011a].

Given the closer overall agreement of the ORCA025 simulated CFC-12 to the observations, let us now focus on its evaluation along the 1994 and 2005 sections (Fig. 3.6). On the Atlantic end of the Beringia 2005 section, where water enters the Nansen basin from the Barents Sea, the water column in ORCA025 appears too well mixed, having CFC-12 concentrations that remain above 2.0 pmol kg^{-1}. Conversely, observed CFC-12 is less uniform, varying from 2.8 pmol kg^{-1} at the surface to 1.3 pmol kg^{-1} in bottom waters at 1000 m, thereby indicating greater stratification. Sim-

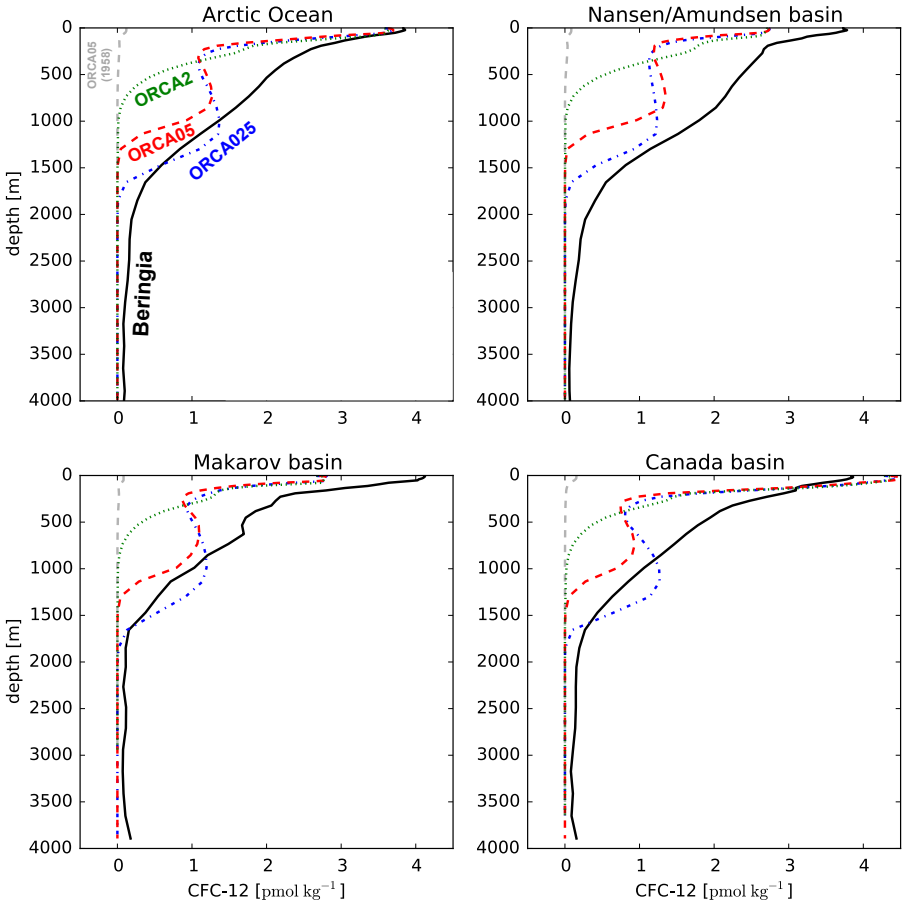

Figure 3.5 – Profiles of observed CFC-12 (black solid) and simulated CFC-12 in ORCA2 (green dots), ORCA05 (red dashes), and ORCA025 (blue dot-dash) along the Beringia 2005 section. Shown are distance-weighted means across that entire section (top left) as well as over that section covering the Nansen and Amundsen basins (top right), the Makarov basin (bottom left), and the Canada basin (bottom right). In light grey is the ORCA05 vertical profile in 1958, the branching point for the other two resolutions.

ilar contrast in stratification was deduced from modeled and observed temperature profiles at the same location (Sect. 3.2.3.3). On the other side of the Arctic in the Canada basin, there are observed local chimneys of CFC-12 where concentrations remain at about 2.0 pmol kg^{-1} from near the surface down to 1000 m, particularly along the 1994 section. These chimneys suggest localized mixing that is only barely apparent in ORCA025 (Fig. 3.6). Such localized features are absent at lower resolution. The CFC-12 inventories were also calculated along the two sections, integrated over depth and distance (Table 3.6). Depending on the expedition, ORCA025 underestimates the observed CFC-12 section inventories by 13–18%, ORCA05 by 36–38%, and ORCA2 by 47–61%.

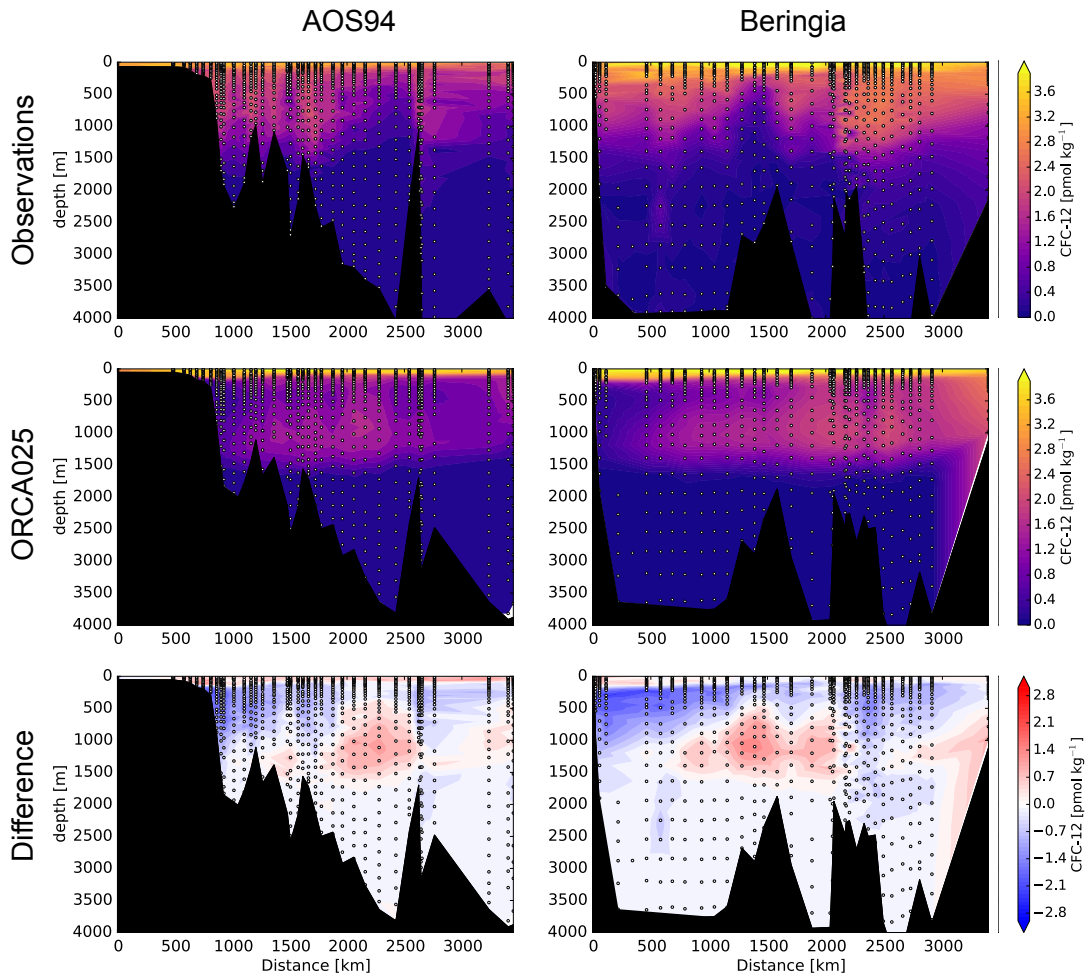

Figure 3.6 – CFC-12 concentrations along the AOS94 section (left) and the Beringia section (right) for the observations (top), the simulated summer means in ORCA025 (middle), and the model – data difference (bottom).

3.2.3.5 Anthropogenic carbon inventories and concentrations

Simulated global ocean C_{ant} inventories are 152 Pg C in ORCA2, 146 Pg C in ORCA05, and 148 Pg C in ORCA025 in 2008, after accounting for corrections for the earlier starting date of 1765 using our perturbation simulations (P1765–P1870). The correction is similar for each resolution, e.g. 24–25 Pg C in 1995, and is consistent with our biogeochemical model simulation strategy (all three resolutions initialized with the ORCA05 output in 1958). Furthermore, these model-based corrections fall within the 29 ± 5 Pg C correction calculated for the same 1765–1995 period with a data-based approach [Bronselaer et al., 2017]. For the 1765–2008 period, the data-based global C_{ant} inventory estimate from [Khatiwala et al., 2009] is 140 ± 24 Pg C, the range of which encompasses the results from all three model resolutions.

In the Arctic Ocean, the corrected modeled C_{ant} inventories range from 1.9 to 2.5 Pg C in 2002

Table 3.6 – Along-section CFC-12 inventories [μmol m^{-1}] integrated over depth and distance along the AOS94 and Beringia 2005 sections vs. co-located results in ORCA2, ORCA05, and ORCA025.

	AOS94	Beringia 2005
Observations	5.5	9.4
ORCA2	2.9	3.7
ORCA05	3.5	5.8
ORCA025	4.8	7.7

and from 2.0 to 2.6 Pg C in 2005, in each case with the low from ORCA2 and the high from ORCA025 (Table 3.7 and Fig. 3.2). These simulated basinwide Arctic Ocean C_{ant} inventories were compared to the TTD-based estimates of anthropogenic carbon from (1) the GLODAPv2 assessment [Lauvset et al., 2016] normalized to the year 2002 and (2) the Tanhua et al. [2009] assessment normalized to 2005. The data-based assessment from GLODAPv2 suggests that 2.9 Pg C of anthropogenic carbon was stored in the Arctic Ocean in 2002, while that from Tanhua et al. suggests that 2.5–3.3 Pg C was stored there in 2005. In 2002, the upper limit of the modeled C_{ant} inventory range remains 0.4 Pg C lower than the GLODAPv2 data-based estimate, but the ORCA025 result in 2005 falls within the data-based uncertainty range of Tanhua et al. [2009]. As for the global estimates, the modeled Arctic Ocean C_{ant} inventories include corrections for the late starting date of the biogeochemical simulations. This correction is 0.4 Pg C in 2005 for each of the three resolutions (Table 3.7).

The differences in basinwide inventory estimates were further studied by comparing vertical profiles of C_{ant} from the models to those from the GLODAPv2 data-based estimates (Fig. 3.7). Surface concentrations in ORCA05 and ORCA025 are up ~35% larger (+12 μmol kg^{-1}) than the data-based estimate, whereas the ORCA2 concentration is ~22% larger (+7 μmol kg^{-1}). By 150 m, the simulated concentrations in all resolutions have dropped below the data-based estimates and remain so, except for ORCA025, down to the ocean bottom. Data-model differences are largest at 400 m, with all resolutions underestimating data-based C_{ant} estimates by up to ~28% (9 μmol kg^{-1}). Below that depth, results from the three resolutions differ more. The C_{ant} concentration in ORCA2 decreases monotonically reaching 11 μmol kg^{-1} at 1000 m and essentially zero by 2300 m. The vertical penetration of C_{ant} in ORCA2* (the simulation without branching from ORCA05 in 1958) is shallower, reaching zero by 1400 m. In ORCA05, C_{ant} concentrations decrease slowly to 19 μmol kg^{-1} at 1000 m, below which they decline rapidly, reaching zero at 2300 m. Only in ORCA025 do C_{ant} concentrations increase again below 400 m, reaching a local maximum at 900 m, an increase that causes the ORCA025 results to exceed data-based estimates by up to 2 μmol kg^{-1} (~11%) at 1100 m. A similar maximum and excess are also seen in the CFC-12 profile for ORCA025 as is the minimum around 400 m (Fig. 3.5). Below 1500 m, the ORCA025 C_{ant} concentrations decline quickly, essentially reaching zero at 2300 m. Conversely, data-based C_{ant} concentrations remain roughly constant at 6 μmol kg^{-1} down to the seafloor. Thus the largest vertically integrated

Table 3.7 – Total inventory, its change during 1960–2012, cumulative air-sea flux, and lateral flux of C_{ant} in Pg C

	Model configuration		
	ORCA2	ORCA05	ORCA025
C_{ant} inventory[a]			
C_{ant} in 2002[b]	1.90 (1.47)	2.25 (1.81)	2.49 (2.06)
C_{ant} in 2005[c]	1.99 (1.56)	2.37 (1.96)	2.64 (2.21)
Inventory change (1960-2012)			
Total Arctic	1.08	1.55	1.98
Nansen Basin	0.14	0.33	0.30
Amundsen Basin	0.13	0.28	0.34
Makarov Basin	0.15	0.21	0.33
Canada Basin	0.31	0.36	0.61
Cumulative fluxes (1960-2012)			
Air-Sea flux	0.29	0.43	0.48
Lateral flux of C_{ant}[d]	0.79	1.13	1.50
Fram Strait	-0.74	-0.40	-0.06
Barents Sea	0.79	1.75	1.98
Bering Strait	0.74	0.89	1.03
CAA	-0.22	-1.20	-1.50
Summed lateral flux	0.57	1.05	1.45

[a] Numbers in brackets show the uncorrected value (starting date 1870).
[b] Data-based inventory in 2002: 2.95 Pg C (GLODAPv2)
[c] Data-based inventory in 2005: 3.03 Pg C (2.5-3.3) [Tanhua et al., 2009]
[d] omputed as inventory change minus cumulative air-sea flux

differences between ORCA025 and data-based estimates are found in the deep Arctic Ocean below 1600 m.

3.2.3.6 Anthropogenic carbon budget

For the budget of C_{ant}, we focused on the final decades over which the model resolutions differed (Tables 3.2.3.1 and 3.7). During 1960 to 2012, the C_{ant} inventory in ORCA025 increased by 1.98 Pg C, 80% of which is stored in the four major Arctic Ocean basins: the Nansen Basin (0.30 Pg C), the Amundsen Basin (0.34 Pg C), the Makarov Basin (0.33 Pg C) and the Canada Basin (0.61 Pg C). Although the Canada Basin C_{ant} inventory increased most, its volume is larger so that its average C_{ant} concentration increased less than in the other basins (Fig. 3.7). Out of the total inventory stored in the Arctic Ocean during that time, only about one-fourth (0.48 Pg C) entered the Arctic Ocean via air-sea flux, most of which was transferred from atmosphere through the surface

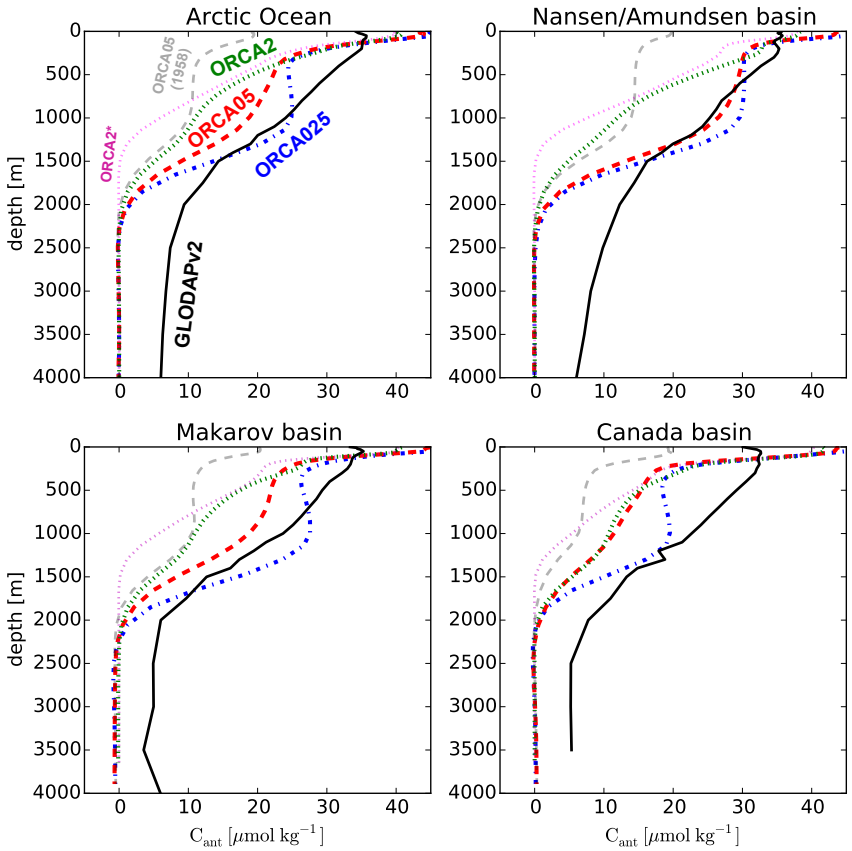

Figure 3.7 – Area-weighted basinwide average vertical profiles of C_{ant} concentration in 2002 for GLODAPv2 data-based estimates (black solid), ORCA2 (green dots), ORCA05 (red dashes) and ORCA025 (blue dot-dash) over the entire Arctic (top left) as well as over the Nansen and Amundsen basins (top right), the Makarov basin (bottom left), and the Canada basin (bottom right). Ocean corrected for the starting year by the perturbation approach simulations. Also shown is the ORCA05 profile in 1958 (dashed, light grey), the branching point for the other two resolutions, and the ORCA2* profile (magenta dots).

of the Barents Sea (Fig. 3.8). The remaining 75% (1.50 Pg C) entered the Arctic Ocean via lateral transport. This net lateral influx is the sum of the fluxes (1) from the Atlantic to the Barents Sea (1.98 Pg C), (2) from the Pacific through the Bering Strait (1.03 Pg C), (3) to the Atlantic via the Fram Strait (-0.06 Pg C), and (4) to the Atlantic via the CAA (-1.50 Pg C). Summed up, the net lateral inflow of anthropogenic carbon across the four boundaries is 1.45 Pg C. This lateral flux computed from monthly mean C_{ant} concentrations and flow fields is 0.05 Pg C (~3%) smaller than the lateral flux computed from the change in inventory minus the cumulative air-sea flux (Fig. 3.8). Within the Arctic, coastal regions typically exhibit net lateral losses, while the deep basins exhibit net lateral gain. The largest lateral loss occurs in the Barents Sea, where the cumulative air-sea flux of C_{ant} is also largest.

The budget of C_{ant} changes notably with resolution. Higher resolution results in more simu-

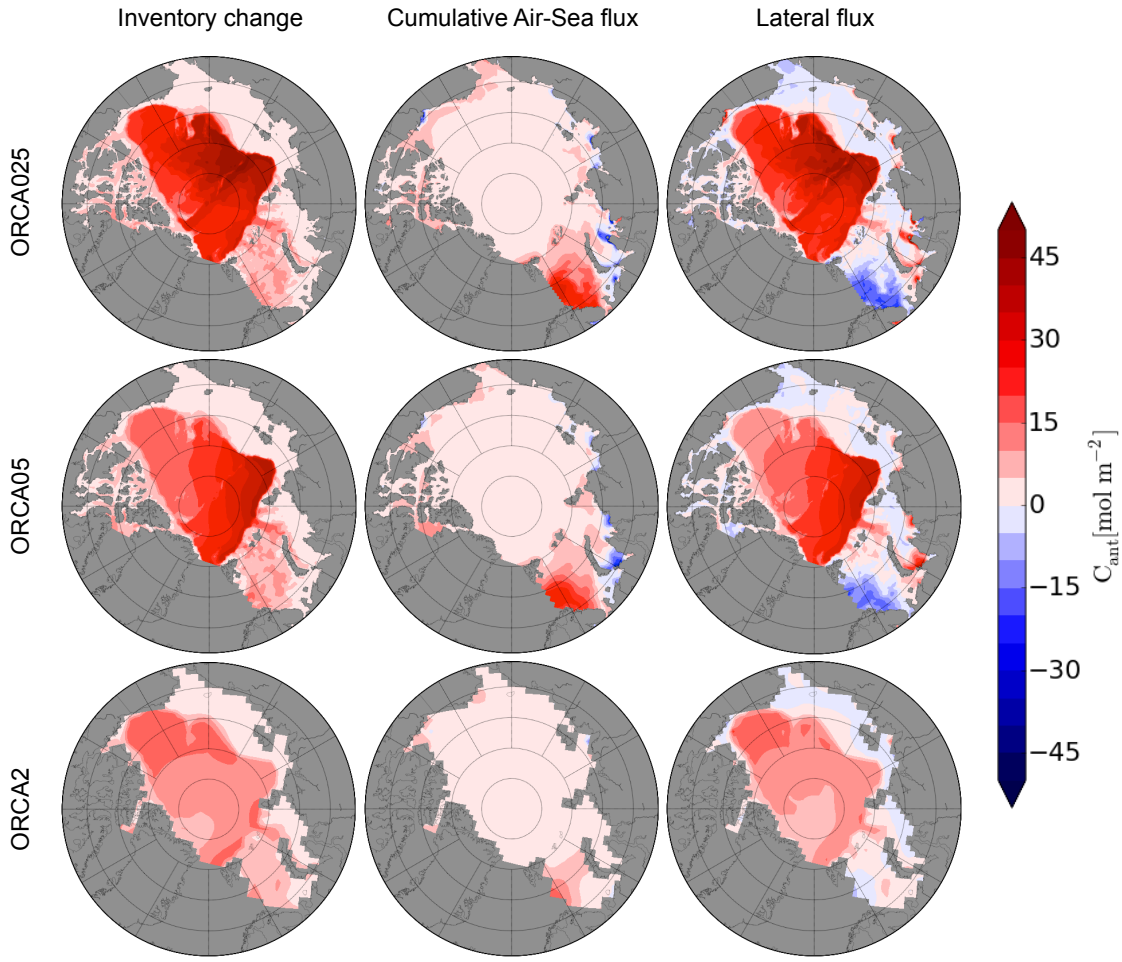

Figure 3.8 – Inventory change (left), cumulative air-sea flux (middle), and the lateral flux calculated as the inventory change minus the cumulative air-sea flux (right) of C_{ant} over 1960–2012 for ORCA025 (top), ORCA05 (center), and ORCA2 (bottom).

lated C_{ant} being stored in the Arctic region, with increases in both the cumulative air-sea flux and lateral transport. The C_{ant} inventory change from 1960 to 2012 nearly doubles with the resolution increase between ORCA2 and ORCA025 (from 1.08 to 1.98 Pg C). Out of that additional C_{ant}, 93% is found between 300 and 2200 m with the maximum being located at 1140 m. The remaining 7% is located in the upper 300 m (Fig. 3.7). Resolution also affects regional partitioning of C_{ant} (Figs. 3.7 and 3.8). When refining resolution from ORCA2 to ORCA05, the Arctic Ocean C_{ant} inventory increases by 0.47 Pg C, 72% of which occurs in the Eurasian basins: the Nansen basin (0.19 Pg C) and Amundsen basin (0.15 Pg C). Another 23% of that increase occurs in the Amerasian basins: the Makarov basin (0.06 Pg C) and Canada basin (0.05 Pg C). Coastal regions account for only 5% of the total inventory increase. In contrast, the subsequent resolution enhancement between ORCA05 and ORCA025 results in little increase in inventory in the Eurasian basins (0.03 Pg C) but much more in the Amerasian basins (0.37 Pg C).

As resolution is refined between ORCA2 and ORCA025, the Arctic C_{ant} inventory increases as a result of a 66% increase in the air-sea flux (+0.19 Pg C) and a 90% increase in the lateral flux

(+0.71 Pg C). Thus the relative contribution of the lateral flux increases from 73 to 76%. Changing model resolution also affects the pathways by which C_{ant} enters the Arctic Ocean (Table 3.2.3.1). The most prominent change occurs in the CAA. From ORCA2 to ORCA025, the net outflow of C_{ant} through the CAA increases sevenfold (from -0.22 to -1.50 Pg C). Other notable changes include (1) the net outflow through the Fram Strait declining 12-fold from -0.74 to -0.06 Pg C, (2) the inflow through the Barents Sea increasing by 150% (from 0.79 to 1.98 Pg C), and (3) the inflow of C_{ant} through the Bering Strait increasing by 39% (from 0.74 to 1.03 Pg C).

3.2.4 Discussion

3.2.4.1 CFC-12

The simulated CFC-12 in ORCA025 underestimates observed concentrations between 100 and 1100 m, slightly overestimates them on average between 1100 and 1500 m, and again underestimates the low observed concentrations below 1500 m. The temperature sections suggest that excess simulated CFC-12 between 1100 and 1500 m is due to a vertical displacement of inflowing Atlantic water, which descends too deeply into the Arctic (Fig. 3.4). Such vertical displacement would indeed reduce simulated CFC-12 concentrations above 1000 m and enhance them between 1100 and 1500 m. Yet the underestimation of integrated CFC-12 mass above 1100 m is larger than the overestimation below 1100 m. Thus vertical displacement of Atlantic water cannot provide a full explanation. Simulated CFC-12 concentrations above 1100 m could also be too low because ventilation of subsurface waters is too weak, an hypothesis that is consistent with the simulated vertical gradients in both temperature and CFC-12 that are too strong between 100 and 1100 m.

3.2.4.2 Anthropogenic carbon

Vertical profiles of C_{ant} and CFC-12 are similar. Above 1000 m, ORCA025 underestimates data-based estimates of C_{ant} as well as observed CFC-12 owing to weak ventilation in the model. Between 1000 and 1500 m, simulated C_{ant} and CFC-12 in ORCA025 exhibit local maxima, which make them on average slightly higher than data-based and observed concentrations. These local maxima can be explained by the simulated Atlantic water masses, rich in both tracers, being too deep. However, the slight overestimation between 1000 and 1500 m is much smaller than the underestimation between 200 and 1000 m. Below 2000 m, simulated C_{ant} largely underestimates data-based estimates. The low simulated C_{ant} stems from too little deep-water formation in the model as indicated by the absence of simulated CFC-12 below 2000 m, an absence that contrasts with the observed CFC-12 concentrations that remain detectable all the way down to the ocean floor (Fig. 3.5).

A second reason for the low simulated Arctic C_{ant} inventory in ORCA025 is that it was initialized with ORCA05 results in 1958. Had ORCA025 been initialized in 1765, which was not computationally feasible, its simulated inventory would be larger, given that both C_{ant} and CFC-12 storage for

ORCA025 are larger than those for ORCA05 over 1958–2012. That hypothesis is consistent with our finding that ORCA2* (complete simulation at 2° without branching from the 0.5°configuration) takes up less C_{ant} than does ORCA2 (0.5° until 1958 then 2° afterwards), which is in line with ORCA2 taking up less C_{ant} and CFC-12 than ORCA05 (Figs. 3.2, 3.5, and 3.7). The initialization of ORCA2 with ORCA05 output in 1958 mainly affects C_{ant} storage between 1000 and 2000 m, the same depth range over which differences in simulated CFC-12 concentrations are largest between ORCA2 and ORCA05. Nevertheless that 1958 initialization has little effect on subsequent changes in C_{ant} storage, cumulative lateral flux, and air-sea flux (Fig. 3.9). Rather it is the changes before 1958 that dominate the difference between ORCA2 and ORCA2*.

All our model configurations underestimate C_{ant} concentrations in the deep waters of the Arctic Ocean based on the CFC-12 model evaluation. The same conclusion is drawn from comparing simulated to data-based estimates of C_{ant}. However, results from different data-based approaches to estimate C_{ant} can differ substantially in the deep ocean [e.g. Vázquez-Rodríguez et al., 2009]. Furthermore, the TTD approach typically produces the highest values in deep waters due to its assumption of constant air-sea disequilibrium [Khatiwala et al., 2013]. Hence applying other data-based approaches to assess the Arctic Ocean inventory of C_{ant} inventory would eventually help to further constrain uncertainties.

3.2.4.3 Lateral flux

In our model, about three-fourths of the net total mass of C_{ant} that accumulates in the Arctic Ocean enters laterally from the Atlantic and Pacific Oceans, independent of model resolution. Our simulated lateral fluxes of C_{ant} in ORCA025 were compared to data-based estimates from studies that multiply data-based C_{ant} concentrations (TTD estimates) along the Arctic boundaries by corresponding observation-based estimates of water transport.

The simulated lateral transport of C_{ant} in ORCA025 generally agrees with data-based estimates within their large uncertainties. These uncertainties result from uncertainties in data-based estimates of C_{ant} and from uncertainties in observational constraints on water flow, which also varies interannually [Jeansson et al., 2011]. For the Fram Strait, Jeansson et al. [2011] estimated a net C_{ant} outflux (from the Arctic) of 1 ± 17 Tg C yr^{-1} in 2002, while for 2012 Stöven et al. [2016] estimate an outflux of 12 Tg C yr^{-1} without indicating uncertainties. For the same years, ORCA025 simulates a net outflux of 8 Tg C yr^{-1} in 2002 but a net influx (to the Arctic) of 5 Tg C yr^{-1} in 2012. Both model and data-based estimates vary greatly between 2002 and 2012. Across the Barents Sea Opening, there is a consistent net influx from the Atlantic to the Arctic Ocean, i.e., 41 ± 8 Tg C yr^{-1} in 2002 for the data-based estimate [Jeansson et al., 2011] and 50 Tg C yr^{-1} for ORCA025 in the same year.

More recently, Olsen et al. [2015] added data-based estimates of lateral fluxes of C_{ant} across the two other major Arctic Ocean boundaries, completing the set of four boundaries that define the perimeter. They estimate a C_{ant} influx of ~18 Tg C yr^{-1} from the Pacific through the Bering Strait

and a C_{ant} outflux through the CAA of ~29 Tg C yr^{-1}, both for the 2000s. For the same time period, ORCA025 simulates 50% more inflow through the Bering Strait (~27 Tg C yr^{-1}) and 24% more outflow through the CAA (~36 Tg C yr^{-1}). The larger Bering-Strait C_{ant} influx in ORCA025 is consistent with its overestimated Bering-Strait water inflow (Table 3.2.3.1, Section 3.2.3.1). Integrating over all four lateral boundaries, Olsen et al. found a total net C_{ant} influx of ~29 Tg C yr^{-1}, which is 24% less than that simulated in ORCA025 averaged over 2000–2010 (~38 Tg C yr^{-1}). Olsen et al. did not provide uncertainties, but the uncertainty of their net lateral flux estimate is at least ±18 Tg C yr^{-1} based on the data-based transport estimates at the two other Arctic boundary sections where uncertainties are available (Table 3.2.3.1).

Weighing in at about one-fourth of the lateral flux is the simulated air-sea flux of C_{ant} in ORCA025 of 10 Tg C yr^{-1} when both are averaged over 2000–2010. That simulated estimate is only about 40% of the data-based estimate of 26 Tg C yr^{-1} from Olsen et al. [2015]. Although no uncertainty is provided with that data-based air-sea flux estimate, it too must be at least ±18 Tg C yr^{-1} given that it is calculated as the difference between the data-based storage estimate [Tanhua et al., 2009] and Olsen et al.'s data-based net lateral flux. The simulated air-sea flux of C_{ant} falls within that assigned uncertainty range for the data-based estimate. In any case, both the model and data-based estimates suggest that the air-sea flux of C_{ant} is not the dominant contributor to the anthropogenic carbon budget of the Arctic Ocean, respectively representing 21 and 47% of the total C_{ant} input averaged over 2000–2010. For both, the lateral flux dominates.

3.2.4.4 Model Resolution

Basin inventories of simulated anthropogenic carbon differ between model configurations because of how resolution affects their volume, bathymetry, circulation patterns, and source waters. Much of the water in the Nansen and Amundsen basins has entered laterally from the Atlantic Ocean through the Fram Strait and the Barents Sea [Jones et al., 1995]. Water inflow through the Barents Sea increases by 150% when moving from ORCA2 to ORCA05 but only by 20% more between ORCA05 and ORCA025. Water inflow in those two higher resolution models is also closer to observational estimates. Along with the increase in water inflow, higher resolution also increases the lateral influx of C_{ant}. Yet despite this increase in the C_{ant} lateral influx, the air-sea C_{ant} flux into the Arctic Ocean also increases with resolution. This finding can be explained by two mechanisms: (1) higher resolution increases the influx of C_{ant} through the Fram Strait, which mainly occurs in subsurface currents and thus does not greatly affect surface C_{ant} concentrations nor air-sea exchanges of C_{ant}, and (2) higher resolution enhances deep-water formation, mainly in the Barents Sea, which reduces surface C_{ant} and thus enhances the air-to-sea flux of C_{ant}. Although the air-sea flux of C_{ant} increases slightly, the larger lateral water fluxes in ORCA05 and ORCA025 mainly explain their higher C_{ant} concentrations in the Nansen and Amundsen basins. Some of this inflowing water continues to flow further along the slope, across the Lomonosov ridge into the Makarov

basin, and then across the Mendeleev ridge into the Canada basin. Yet how well models simulate that flow path depends on lateral resolution. Between ORCA2 and ORCA05, C_{ant} inventories increase by 16% in the Canada basin (+0.05 Pg C) and by 40% the Makarov basin (+0.06 Pg C). But between ORCA05 to ORCA025, increases are two to five times greater: +0.25 Pg C in the Canada basin and +0.12 Pg C in the Makarov basin (Sect. 3.2.3.6). The change from ORCA2 to ORCA05 mainly seems to improve lateral exchanges with adjacent oceans, while the change from ORCA05 to ORCA025 improves interior Arctic Ocean circulation.

As the increase from ORCA05 to ORCA025 stems from finer, more realistic representation of lateral transport within the Arctic, it would appear that eddying ocean models may be needed to adequately simulate the interior circulation in terms of its effect on C_{ant} storage in the Arctic Ocean. In the Canada basin, such lateral inflow may not be the only source of C_{ant}. Another major source appears to come from density flows along the continental slope, driven by brine rejection from sea-ice formation over the continental shelves [Jones et al., 1995]. A signature of this source in the observed sections may be the chimneys of constant CFC-12 concentration from the surface to about 1000 m in the Canada basin, features for which only ORCA025 exhibits any such indication, albeit faint. To adequately model lateral exchanges of C_{ant} in the Arctic Ocean, at least a resolution comparable to that used in ORCA05 may be needed, while resolutions comparable to that in ORCA025 or above may well be required to begin to capture the effects from density flows along the slope. As a consequence of the deficient representation of these density flows, we would expect to see an increase in C_{ant} when using even higher resolution.

Improved modeled circulation from higher model resolution has also been shown to be critical to improve simulated anthropogenic tracers in the Southern Ocean [Lachkar et al., 2007] and simulated oxygen concentrations in the tropical Atlantic [Duteil et al., 2014].

3.2.4.5 CMIP5 comparison

For wider perspective, we compared results from our forced NEMO-PISCES simulations to those from nine ocean biogeochemical models that were coupled within different earth system modeling frameworks as part of CMIP5 (Fig. 3.9). When the CMIP5 models are compared to the data-based estimate of the C_{ant} inventory, only the MIROC-ESM with its inventory of 2.7 Pg C falls within the data-based uncertainty estimate (2.5 to 3.3 Pg C in 2005). The next closest CMIP5 models are NorESM1-ME and HadGEM2-ES, which fall below the lower limit of the data-based range by 0.1 and 0.5 Pg C. Then come the MPI-ESM and GFDL-ESM models with their C_{ant} inventories in 2005 that are 0.9 to 1.5 Pg C lower than the lower limit. The lowest CMIP5 estimates are from both versions of the IPSL model whose inventories reach only ~20% of the data-based range. Adjusting all the CMIP5-model Arctic inventories upward by ~0.4 Pg C to account for their late start date in 1850, as we did for our three simulations, would place two of them (MIROC-ESM and NorESM1-ME) above the lower boundary of the data-based uncertainty estimate, and another

(HadGEM2-ES) just 0.1 Pg C below this lower boundary. Lateral fluxes over 1958–2012 also vary between CMIP5 models, from an outflow of 0.3 Pg C in the IPSL-CM5A-LR model and an inflow of 1.1 Pg C in the MIROC-ESM model. Only the first three CMIP5 models mentioned above exhibit large net inflow of C_{ant} into the Arctic basin (between 0.7 and 1.1 Pg C during 1960–2012), a condition that appears necessary to allow a model to approach the estimated data-based inventory range. Indeed, the six other CMIP5 models have lower lateral fluxes (-0.5 to 0.5 Pg C) and simulate low C_{ant} storage in 2005.

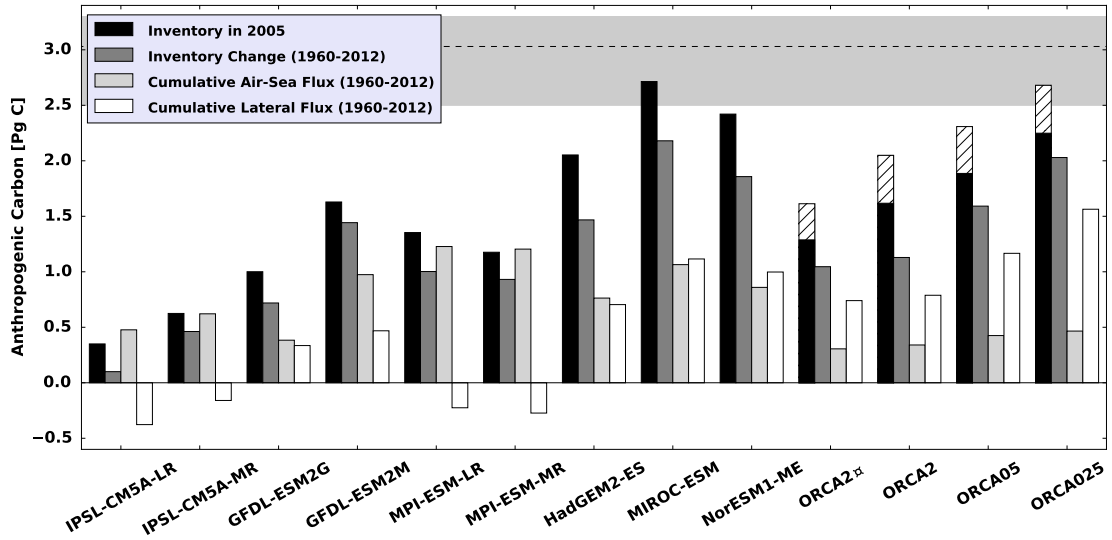

Figure 3.9 – Comparison of results for the Arctic Ocean from ORCA2, ORCA05, ORCA025, and ORCA2* and the nine Earth System Models that participated in CMIP5. Shown are the C_{ant} inventory in 2005 (black), the C_{ant} inventory change (dark grey) between 1960 and 2012, the corresponding cumulative air-sea flux of C_{ant} (light grey), and the cumulative lateral flux of C_{ant} (white). Also indicated are the data-based estimate from Tanhua et al. [2009] (dashed black line) along with its associated uncertainty range (grey background). The inventory correction for the late starting date for our forced simulations is indicated as striped bars.

What is perhaps most surprising are the large differences between our forced ORCA2* model and the IPSL-CM5A-LR and IPSL-CM5A-MR ESMs. All three of those models use the same coarse-resolution ocean model, although both ESMs rely on an earlier version with a different vertical resolution (31 instead of 46 vertical levels). The contrast in vertical resolution may explain part of the large difference in inventories (1.3 Pg C for our forced version that is not corrected for the late starting date vs. 0.3–0.6 Pg C for the two coupled versions) but the forcing could also play a role. Lateral resolution is not the only factor when aiming to provide realistic simulations of C_{ant} storage and lateral transport in the Arctic. Sensitivity studies testing other potentially critical factors are merited.

3.2.4.6 Effect on aragonite saturation state

Given that simulated C_{ant} is affected by lateral model resolution, so must be simulated ocean acidification. The aragonite saturation state (Ω_A) was computed for each resolution from the historical run's C_T, A_T, T, S, P_T, and Si_T, after correcting C_T and A_T for drift based on the control run. The higher concentrations of C_{ant} in the ORCA05 and ORCA025 simulations reduces Ω_A between 1960 and 2012 by more than twice as much as found with ORCA2 during the same period (Fig. 3.10). These differences translate into different rates of shoaling for the aragonite saturation horizon (ASH), i.e., the depth where $\Omega_A = 1$. During 1960–2012, the ASH shoals by ~50 m in ORCA2, while it shoals by ~150 m in ORCA05 and ~210 m in ORCA025. Thus model resolution also affects the time at which waters become undersaturated with respect to aragonite with higher resolution producing greater shoaling.

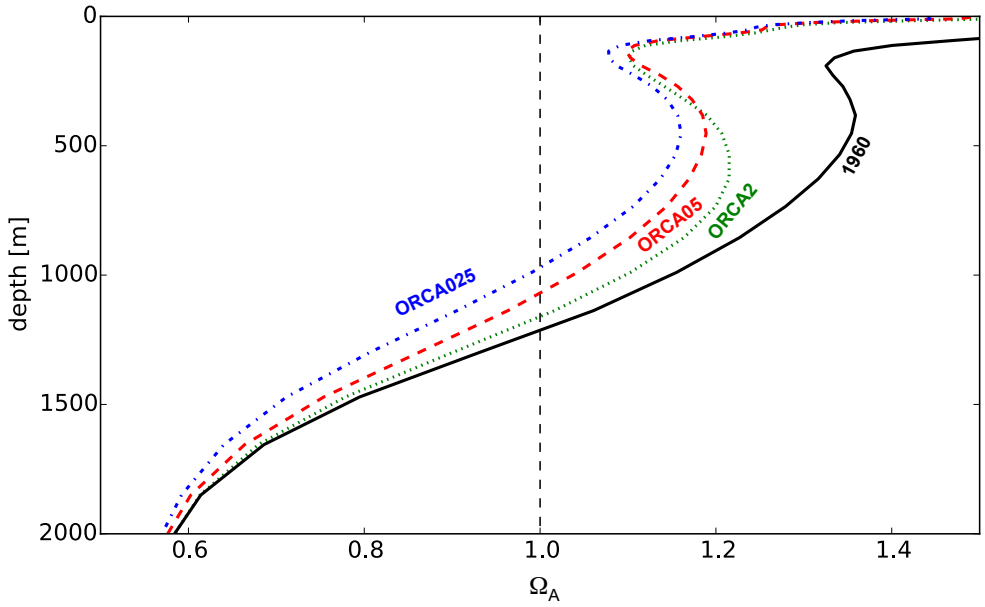

Figure 3.10 – Profiles of Ω_A for ORCA05 in 1960 (black solid) as well as ORCA2 (green dots), ORCA05 (red dashes), and ORCA025 (blue dot-dash) in 2012. The vertical black dashed line indicates the chemical threshold where $\Omega_A = 1$. Where that vertical line intersects the other curves indicates the depth of the ASH.

Although basinwide mean surface Ω_A does not differ among resolutions, there are regional differences such as over the Siberian shelf (Fig. 3.11). The minimum Ω_A in that region reaches 0.9 in ORCA2, while it drops to 0.3 in ORCA05 and 0.1 in ORCA025. That lower value in ORCA025 is more like that observed, e.g., down to 0.01 in the Laptev Sea [Semiletov et al., 2016]. As these lows in Ω_A are extremely local, they cannot be expected to be captured in coarse-resolution models such as ORCA2. Higher resolution models are needed in the Arctic to assess local extremes not only in terms of ocean acidification but also other biogeochemical variables.

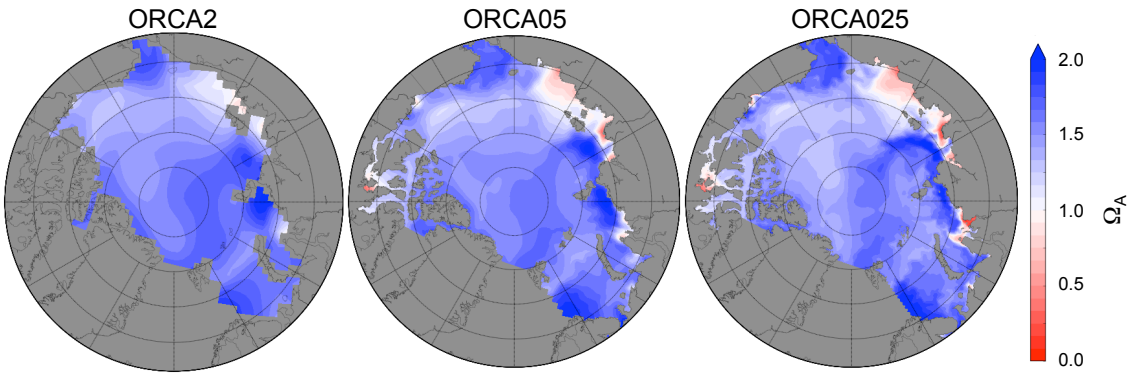

Figure 3.11 – Surface Ω_A for ORCA2, ORCA05 and ORCA025 (left to right) in August 2012.

3.2.5 Conclusions

Global-ocean biogeochemical model simulations typically have coarse resolution and tend to underestimate the mass of C_{ant} stored in the Arctic Ocean. Our sensitivity tests suggest that more realistic results are offered by higher resolution model configurations that begin to explicitly resolve ocean eddies. Our high-resolution model simulates an Arctic C_{ant} inventory of 2.6 Pg C in 2005, falling within the uncertainty from the data-based estimates (2.5–3.3 Pg C). That model estimate should be considered a lower bound because it generally underestimates CFC-12 concentrations. Thus it essentially confirms the lower bound from the data-based estimates, which are based on CFC-12 derived C_{ant} concentrations that are not without uncertainties, particularly in the deep Arctic Ocean where measured CFC-12 concentrations are small. The high-resolution model would have simulated a higher Arctic C_{ant} inventory had computational resources been available to use it throughout the entire industrial era rather than initializing it in 1958 with results from the intermediate resolution model (ORCA05), in which the penetration of CFC-12 and C_{ant} into Arctic intermediate waters is weaker. The largest source of differences in C_{ant} inventory between resolutions is due to the increasing ventilation of intermediate waters as model resolution is refined, as revealed by CFC-12 and C_{ant} model-data comparison. The highest resolution model, ORCA025, still underestimates the C_{ant} data-based estimates at around 400 m and slightly overestimates them at around 1300 m. The deeper overestimate appears due to excessive penetration of C_{ant}-rich Atlantic water. The shallower underestimate may be partly due to inadequate representation of ventilation of intermediate waters via down-slope flows that are driven by brine formation over the Arctic's enormous continental shelf, a transport process that is notoriously difficult to represent in z-coordinate models, especially at lower resolution.

Our forced ocean simulations suggest that Arctic Ocean storage of C_{ant} is driven mostly by net lateral inflow, the total input of which is about three times that from the air-sea flux. That 3:1 ratio varies little with resolution because both the lateral flux and the air-sea flux increase as resolution is refined. The lateral flux is typically less dominant in the CMIP5 models but its magnitude varies greatly as does its ratio relative to the air-sea flux. Some CMIP5 models even simulate net lat-

eral outflow of C_{ant}, but those models also simulate unrealistically low C_{ant} inventories. The only CMIP5 models that succeed in reaching the lower limit of the data-based C_{ant} inventory range are those that have a large net lateral input. Unfortunately, the causes of the CMIP5 model differences remain unclear as is often the case when comparing models having many differences. Most of the CMIP5 models appear to not have been evaluated in terms of their ability to simulate realistic lateral water transport at the boundaries of the Arctic Ocean, which is fundamental to simulating realistic C_{ant} but may be problematic given their coarse resolution. The next phase of CMIP is ongoing and includes CFC-12 and related transient transient tracers, which will help weigh simulated results for C_{ant}.

As the mass of simulated anthropogenic carbon in the Arctic Ocean increases with resolution, so does the simulated acidification. For instance, during 1960–2012, the average ASH in the Arctic shoals four times faster in ORCA025 than in ORCA2. Higher resolution is also needed to capture local extremes. Despite these benefits, the higher computational costs of making centennial-scale, high-resolution, biogeochemical ocean simulations remain prohibitive. More practical in the short term would be to assess effects from less-costly model improvements, including heightened vertical resolution, subgrid-scale parameterizations, and adjustments to model parameters for viscosity and slip conditions. For such regional studies, nested models would offer the advantage of focused higher resolution while still avoiding adverse effects from imposed lateral boundary conditions. These efforts along with including more coastal ocean processes in global models should eventually lead to greater prognostic skill and more reliable projections not only for the Arctic Ocean but for regional seas and the coastal ocean in general.

3.2.6 Appendix A: Perturbation vs. full biogeochemical approach

To assess the reliability of the perturbation approach, we compared its results from the coarse-resolution ocean model over 1870–2012 (P1870-ORCA2*), i.e., without branching from ORCA05, to those from the analogous full biogeochemical simulation (B1870-ORCA2*). Globally, the simulated C_{ant} inventory with the perturbation approach in 2012 is 2% larger than that with the full biogeochemical approach (Table **??**). These differences are mainly located in the top 200 m (Fig. 3.12) of the tropics and Southern Ocean (Fig. 3.13), where regional inventories of C_{ant} from the perturbation approach overestimate those from the full approach by up to 3%. Those two regions are also the ones that store most of the anthropogenic carbon. Conversely, in the Arctic, the perturbation approach underestimates the 2012 C_{ant} inventory of the full approach by 3% because of its deficit between 200 and 600 m, the depth zone that is directly affected by Atlantic inflow (Sect. 3.2.3.3). Overall, these differences are small, thus supporting our use of the more efficient perturbation approach to correct for the late start date of the full biogeochemical simulations.

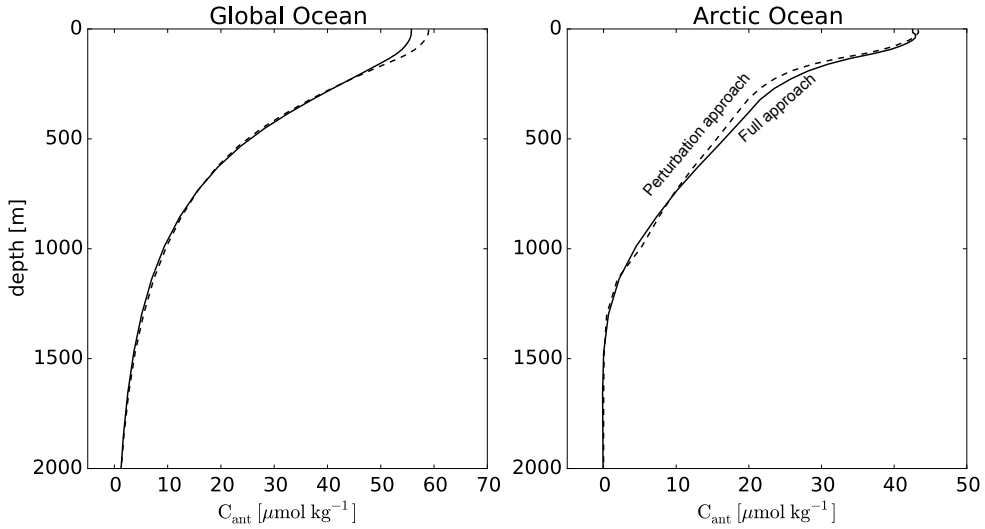

Figure 3.12 – Mean vertical profiles of C_{ant} for the global ocean (left) and the Arctic Ocean (right) in 2012 for the full biogeochemical approach (B1870-ORCA2*) (solid) and the perturbation approach (P1870-ORCA2*) (dashed).

These differences, although small, merit an explanation. The perturbation approach is regionally biased because its preindustrial reference state is assumed to be everywhere in equilibrium with the atmosphere (Sect. 3.2.2.3). Hence its results will differ from the full approach, which allows for disequilibrium between preindustrial atmospheric and oceanic pCO_2. For example, with the full approach, simulated surface-ocean pCO_2 in the tropics and Southern Ocean generally exceeds atmospheric pCO_2 under preindustrial conditions, a supersaturation that is also seen with ocean inversions for the same regions [Gruber et al., 2009]. So by assuming equilibrium and not accounting for this supersaturation, the perturbation approach relies on a buffer capacity that is too high. That is, when its preindustrial surface-ocean pCO_2 reference is too low, its corresponding

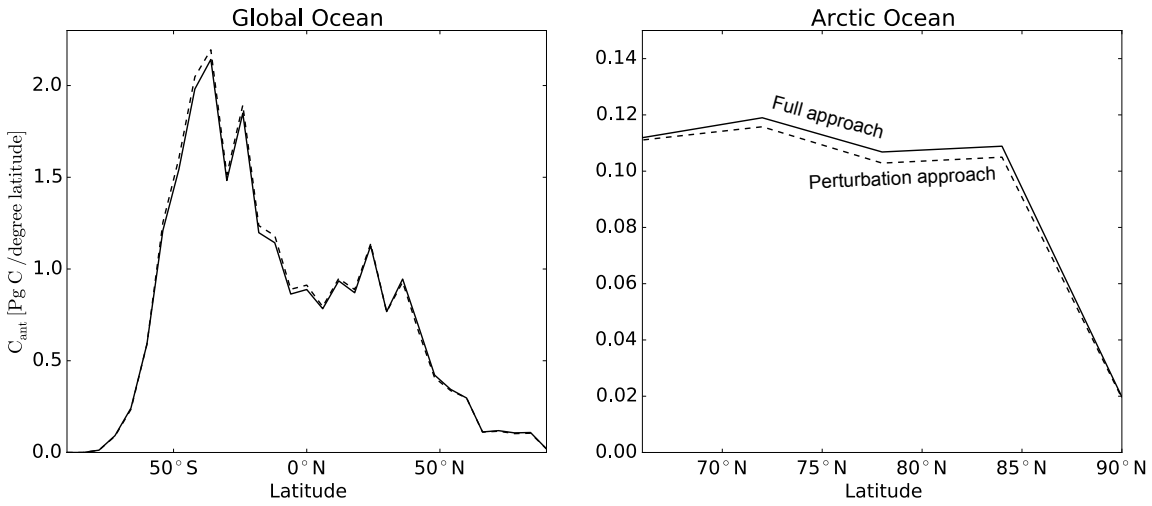

Figure 3.13 – Zonal integral of vertically integrated C_{ant} per degree of latitude in 2012 for the global ocean (left) and the Arctic Ocean (right) using the full biogeochemical approach (B1870-ORCA2*) (solid) and the perturbation approach (P1870-ORCA2*) (dashed)

carbonate ion concentration is too high and thus so must be its buffer capacity, i.e., its chemical capacity to absorb C_{ant}.

In contrast, in the North Atlantic, surface-ocean pCO_2 is generally undersaturated in the full approach under preindustrial conditions (B1870-ORCA2* in 1870), as it is in ocean inversions [Gruber et al., 2009]. By not accounting for this undersaturation, the perturbation approach overestimates the preindustrial surface ocean pCO_2 and thus underestimates the corresponding reference carbonate ion concentration, buffer capacity, and uptake of C_{ant} relative to the full approach. The growing influence of this underestimated uptake in the North Atlantic can be seen as its waters invade the Arctic during the course of the simulation (Fig. 3.14). That lateral invasion overwhelms the small but opposite tendency early in the perturbation simulation to overestimate Arctic C_{ant} uptake, an artefact of the perturbation approach's preindustrial reference state not accounting for local impacts from riverine inputs. Conversely, in the full approach with PISCES, riverine inputs typically lower the carbonate ion concentration and buffer capacity of shelf seas.

Despite its simplifications, the perturbation approach differs little from the full approach in terms of basinwide results. With it, we can envision garnering sufficient computational resources to soon make a global C_{ant} simulation at high resolution (ORCA025) over the full industrial era without branching it off from a lower resolution model along the way. That should in turn allow us to help further refine limits for C_{ant} uptake and storage in the Arctic as well as other regions. With the full biogeochemical approach, such would not be feasible for years to come.

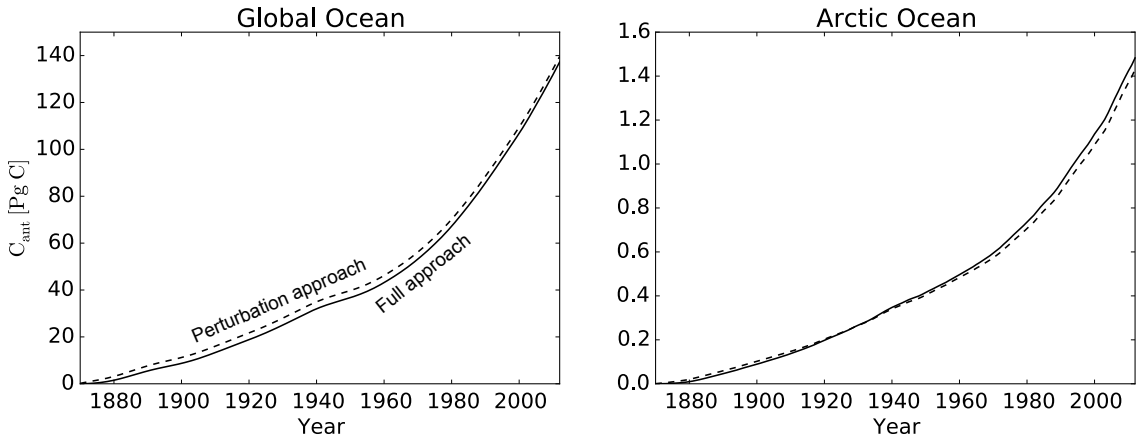

Figure 3.14 – Arctic Ocean C_{ant} inventory in the global ocean (left) and the Arctic Ocean (right) for the full biogeochemical approach (B1870-ORCA2*) (solid) and the perturbation approach (P1870-ORCA2*) (dashed).

3.3 Summary

- The simulated C_{ant} inventory of 2.6 Pg C in 2005 using NEMO-PISCES with a high horizontal resolution (ORCA025) is within the uncertainty range of the data-based estimate
- Around three quarters of this C_{ant} inventory have entered the Arctic Ocean via lateral transport from the Atlantic and Pacific Ocean. This calls for an improved observation system at the Arctic Ocean boundaries and more attention to boundary fluxes in ocean and climate models.
- The comparison between simulated and observed CFC-12 reveal that ORCA025 represents the general circulation well, but underestimates ventilation of surface waters and deep-water formation
- The comparison between simulated and data-based C_{ant} reveal local differences in the deep Arctic Ocean, which call for an evaluation of the data-based estimate.
- Average surface acidification is independent of resolution, but higher resolution allows to resolve extreme local ocean acidification in the coastal seas
- Higher resolution improves deep-water formation and thus leads to a faster shoaling of the aragonite saturation horizon
- Given their coarse resolution, results for C_{ant} from CMIP5 models in the Arctic Ocean diverge largely and should be treated with appropriate caution.

Chapter 4

Constrained estimates of anthropogenic carbon and future acidification in the Arctic Ocean

"Men and nature must work hand in hand. The throwing out of balance of the resources of nature throws out of balance also the lives of men"

Franklin Delano Roosevelt

Contents

4.1 Preamble

The results of the previous chapter demonstrated that a small change of C_{ant} in the deep Arctic Ocean leads to important changes in the depth of the aragonite saturation horizon (ASH). The intrusion of C_{ant} in the past is used to make estimates of the future shoaling of the ASH [Anderson et al., 2010].

In the Arctic Ocean, the only method that has been applied to estimate C_{ant} based on observations is the TTD method [Tanhua et al., 2009]. The results of the previous chapter suggest, that the data-based estimate by the Transient Time Distribution (TTD) method might overestimate C_{ant} in the deep Arctic Ocean. To test this hypothesis, an evaluation of the TTD method is necessary.

The TTD method was previously evaluated in the global ocean by Waugh et al. [2006]. They used an ocean-biogeochemical model (CSIRO GCM) and applied the TTD method to simulated CFC-12 concentrations. The so-obtained estimate of C_{ant} was then compared to directly simulated C_{ant}. Their evaluation demonstrated the globally good performance of the TTD method, but showed that C_{ant} in the Southern Ocean is overestimated by ~60%. Due to low data coverage, the TTD was not used in that region so the method was not evaluated there.

Increased data availability led a multiple use of the TTD in the Arctic Ocean during the last years [Tanhua et al., 2009; Jeansson et al., 2011; Stöven et al., 2016], which makes an evaluation important. In this chapter, we use the high-resolution configuration of NEMO (ORCA025), which was shown in the last chapter to reproduce observed sea ice, observed lateral fluxes of water, and C_{ant} in the Arctic Ocean relatively well. More precisely, we used simulated CFC-12 concentrations and C_{ant} concentrations from the perturbation simulations to evaluate the existing C_{ant} data-based estimate by Tanhua et al. [2009].

For the simplistic scenario where climate remains constant, the evaluated TTD was used to make future projections of C_{ant} following Anderson et al. [2010]. These idealized data-based projections of C_{ant} were then used to project future acidification of the Arctic Ocean.

4.2 Article in preparation for publication in *Geophysical Research Letters*

J. Terhaar[1,2], T. Tanhua[3], T. Stöven[3], J. C. Orr[1], and L. Bopp[4]

[1]Laboratoire des Sciences du Climat et de l'Environnement, LSCE/IPSL, CEA-CNRS-UVSQ, Université Paris-Saclay, 91191 Gif-sur-Yvette, France

[2]Biogeochemistry and Earth System Modelling, Department of Geoscience, Environment and Society, Université Libre de Bruxelles, Belgium

[3]GEOMAR Helmholtz Centre for Ocean Research Kiel, Kiel, Germany

[4]LMD/IPSL, Ecole Normale Supérieure / PSL Research University, CNRS, Ecole Polytechnique, Sorbonne Université, Paris, France

4.2.1 Abstract

The Arctic Ocean is the most vulnerable region to ocean acidification, a process that is mainly driven by the uptake of anthropogenic carbon (C_{ant}). Although C_{ant} cannot be measured directly, it can be estimated using methods such as the transient time distribution (TTD) approach, which characterizes the ventilation of water masses by using tracers, like CFC-11 and CFC-12. Here, we evaluate the TTD method in the Arctic Ocean with an eddying ocean model. When applied to simulated CFC-12 concentrations, the TTD underestimates directly simulated C_{ant} concentrations by up to 12%, caused by supersaturated C_{ant} and undersaturated CFC-12 in regions of deep-water formation in the Arctic Ocean. Adjusting the observation-based C_{ant} concentrations in the Arctic Ocean for this bias increases the previously published data-based estimate of the C_{ant} inventory by 8% to 3.3 ± 0.3 Pg C normalized to year 2005. By applying the adjusted TTD to future atmospheric CO_2 levels, we estimate that the entire Arctic Ocean will be undersaturated with respect to aragonite between 2080 and 2150 if atmospheric CO_2 rises above 450–540 ppm.

4.2.2 Introduction

The high-latitude oceans, and in particular the Arctic Ocean, have been shown to be most vulnerable to open ocean acidification owing to their low natural saturation states with respect to $CaCO_3$, particularly aragonite [Orr et al., 2005; Steinacher et al., 2009]. The Arctic Ocean's surface waters are already partly undersaturated with respect to aragonite [Chierici and Fransson, 2009; Semiletov et al., 2016] and are projected to become entirely undersaturated in 2080 under the SRES A2 scenario [Steinacher et al., 2009]. This undersaturation in surface waters distinguishes the Arctic Ocean from the global ocean, where undersaturation generally only occurs in deeper waters. In the deep Arctic Ocean, the depth at which waters change from supersaturated with respect to

aragonite to undersaturated, the aragonite saturation horizon (ASH), is located at around 1900 m [Anderson et al., 2010]. Over the 21st century, a coupled carbon-climate model projects a slight shoaling of the deep ASH (~100 m) and a large deepening of the undersaturated waters at the surface, leading to a merge of the deep ASH and the undersaturated surface waters at ~1800 m at the end of the 21st century following the SRES A2 scenario [Steinacher et al., 2009]. As opposed to this model projection, a data-based approach using the TTD method estimates a stronger shoaling of the deep ASH (~900 m) and consequently a merge of this deep ASH and the undersaturated waters from the surface at ~1000 m [Anderson et al., 2010].

The main driver of this acidification of the open ocean is the increase in atmospheric CO_2 during the industrial era and the resulting uptake of anthropogenic carbon (C_{ant}) from the atmosphere. Although this absorbed C_{ant} cannot be measured directly, it has been estimated from other oceanographic data by various methods, such as the transit-time distribution (TTD) method [Waugh et al., 2006; Khatiwala et al., 2013]. For instance, the Inverse Gaussian (IG)-TTD method, a specific solution of the TTD framework, constrains the invasion of C_{ant} into the interior ocean by observations of transient-tracers such as CFC-12, tritium helium combinations ($^3H/^3He$), and SF_6 [Hall et al., 2002; Waugh et al., 2004]. By using surface boundary conditions of the chosen tracer (e.g., CFC-12) and subsurface measurements of the same tracer, temperature (T), and salinity (S), the mean age of the water parcel can be determined by the IG-TTD. This mean age is then used in combination with the atmospheric CO_2 history to estimate the C_{ant} concentration in the respective water parcel.

The TTD method was first applied through the ocean by Waugh et al. [2006], who estimated a global C_{ant} uptake by the ocean of 134 Pg C in 1994. Due to sparse tracer observations, Waugh et al. [2006] could not apply the TTD method in the Arctic Ocean. With more tracer observations available, Tanhua et al. [2009] applied the TTD method in the Arctic Ocean and obtained a C_{ant} inventory estimate of 3.0 (2.5–3.3) Pg C normalized to 2005. Based on the C_{ant} concentration estimates from Tanhua et al. [2009], the shoaling of the ASH in the Arctic Ocean during the industrial period was estimated to be ~190 m on average [Anderson et al., 2010].

The performance of such data-based methods can be evaluated by ocean circulation models. For the evaluation, the TTD method can be applied to simulated CFC-12 concentrations to obtain C_{ant}. This C_{ant} concentration based on simulated CFC-12 can be compared to the directly simulated C_{ant} ('reference' C_{ant}). A first evaluation by Waugh et al. [2006] showed that the C_{ant} that was derived from simulated CFC-12 is similar to the 'reference' C_{ant} in all ocean regions, but the Southern Ocean. In the Southern Ocean, water masses with low CFC-12 and C_{ant} concentrations are upwelled to the surface and subducted after ~4 months [Weiss et al., 1979]. While this short surface residence time is sufficient for normal gases, such as CFC-12, to get into equilibrium with atmospheric concentrations, C_{ant} only reaches its equilibrium within ~8 month on average in today's oceans as the carbonate ion content in the surface ocean needs to adjust to increasing CO_2 levels [Broecker and Peng, 1974]. By assuming that both C_{ant} and CFC-12 are in perfect equi-

librium with the atmosphere, the TTD method systematically overestimates C_{ant} in the Southern Ocean [Matear et al., 2003; Waugh et al., 2006].

Similarly to the Southern Ocean, a difference in surface saturation of C_{ant} and CFC-12 in the Arctic Ocean is believed to cause a bias in C_{ant} estimates from the TTD method, although the magnitude and direction of this bias remains unknown [Tanhua et al., 2009]. In this study, we aim at evaluating the TTD method in the Arctic Ocean with an ocean model and, if possible, at adjusting the data-based estimate of C_{ant} [Tanhua et al., 2009]. In a last step, we will use the adjusted TTD and apply it to future atmospheric CO_2 levels to estimate how ocean acidification is expected to develop in the absence of any change other than the rise in atmospheric CO_2 following Anderson et al. [2010].

4.2.3 Methods

4.2.3.1 Arctic Ocean and its water masses

The boundaries of the Arctic Ocean were defined as in Bates et al. [2009] at the Fram Strait, the Barents Sea Opening, the Bering Strait, and the Canadian Arctic Archipelago (between Smith Sound and Baffin Bay).

The water masses in the Arctic Ocean were defined as follows (Table S1): the Pacific Water (PW) was divided into Summer Pacific Water (SPW), characterized by temperatures between -1.0°C and 0.4°C and salinity ranging from 31 to 33 [Woodgate et al., 2010; Bourgain et al., 2013; Steele et al., 2004], and Winter Pacific Water (WPW) characterized by temperatures below -1.4°C and salinity higher than 32.4 [Pickart et al., 2005]. Water from the Atlantic Ocean splits into two branches. The first branch enters the Arctic Ocean through the Fram Strait at intermediate depths and is generally warmer than 0°C and saltier than 34 [Woodgate, 2013]. Being disconnected from the surface it conserves its characteristics and is called Atlantic Water (AW) hereafter. The second branch enters the Arctic Ocean through the Barents Sea Opening. Being mainly located at the surface, it cools down to values below 0°C and increases its salinity above 34.6 by brine rejection. Consequently the density of this water mass increases and enters the deep Arctic Ocean basins through the St Anna Trough [Gammelsrød et al., 2009; Schauer et al., 2002; Smedsrud et al., 2013]. Water masses from this second Atlantic branch are named 'Barents Sea Water' (BSW) hereafter.

4.2.3.2 Ocean model

In this study, we used the global ocean circulation model NEMO-v3.2 (Nucleus for European Modeling of the Ocean - version 3.2) [Madec, 2008] with a single-tracer perturbation approach to calculate C_{ant} [Sarmiento et al., 1992; Lachkar et al., 2007; Palmiéri et al., 2015]. This approach is computationally less expensive than a full biogeochemical model and allows running the model at high resolution (nominal horizontal resolution of 0.25°). The atmospheric CO_2 concentration for the years 1765–1869 were taken from Meinshausen et al. [2017] and for the years 1870–2012

from Le Quéré et al. [2015]. To calculate pCO_2 in the ocean at every time step, the perturbation approach exploits a tight relationship between the anthropogenic perturbation of the partial pressure of CO_2 (referred to as δpCO_2) and total dissolved inorganic carbon (C_T) at the ocean surface. This relationship is solely based on surface ocean temperature and assumes constant alkalinity (2300 µmol kg^{-1}) and salinity (35) [Sarmiento et al., 1992]. Once inside the ocean C_{ant} was treated as a passive tracer with no internal sources minuses sinks. Despite these approximations, the simulated Arctic Ocean C_{ant} inventory by the perturbation approach agrees within 3% with the C_{ant} inventory simulated by the more costly full biogeochemical approach [Terhaar et al., 2018]. Similarly to C_{ant}, CFC-12 was calculated as an inert tracer following the OCMIP-2 protocol by Dutay et al. [2002]. The atmospheric boundary conditions of CFC-12 were taken from Bullister [2015]. Because of limited computational resources, we used the model on a nominal resolution of 0.5° (ORCA05) from 1765 to 1957 and only increased the nominal resolution to 0.25° (ORCA025) for the period from 1958 to 2012.

4.2.3.3 TTD calculation

The transient time distribution was applied following Hall et al. [2002] and Waugh et al. [2004]. The concentration of a tracer c(r,t) was calculated at any point r and any time t (in years) using the following equation:

$$c(r,t) = \int_0^\infty c_0(t-t')\mathrm{G}_r(t')\,dt', \tag{4.1}$$

where $c_0(t-t')$ is the tracer's atmospheric concentration at time t' (number of years before year t) and $G_r(t')$ is the commonly applied inverse Gaussian of the Green's function [e.g. Waugh et al., 2004, 2006; Tanhua et al., 2009; Olsen et al., 2010]. For every water parcel r, $G_r(t')$ is expressed as

$$\mathrm{G}_r(t') = \sqrt{\frac{\Gamma^3}{4\pi\Delta^2 t'^3}}\,exp\left(\frac{-\Gamma(t'-\Gamma)^2}{4\Delta^2 t'}\right), \tag{4.2}$$

where Δ represents the width of the TTD, Γ the mean age of the water sample, and t' the transit time. The ratio of Δ and Γ determines the repartition of advection and diffusion in the water parcel, with Δ / Γ < 1 indicating a larger advective than diffusive share. Here we used the typically applied Δ / Γ ratio of 1.0 [Waugh et al., 2006; Tanhua et al., 2009] as our standard case but also made a series of calculations over a range of Δ / Γ ratios (Supplement S1). To calculate the partial pressure of CO_2 in the ocean (pCO_2), the MATLAB version of the routine CO2SYS was used [van Heuven et al., 2011], with the K1 and K2 dissociation constants from Millero et al. [2002] and the acid dissociation constant from Dickson [1990]. The solubility of CFC-12 was calculated following Warner and Weiss [1985].

Where the partial pressure of surface ocean CFC-12 (pCFC-12) is supersaturated with respect to the current atmospheric pCFC-12, the TTD method cannot be applied. Oceanic pCFC-12 can

surpass atmospheric *p*CFC-12 because of the decreasing concentrations of CFC-12 in the atmosphere. When comparing C_{ant} calculated by the TTD method to directly simulated C_{ant}, we thus masked out areas where ocean *p*CFC-12 is above atmospheric *p*CFC-12. By doing so, 6.5% of the Arctic Ocean C_{ant} inventory was masked out (Section 4.2.3.4).

4.2.3.4 Evaluation of TTD

To evaluate the TTD method, we applied it to simulated CFC-12 and temperature from the summer of 2005, the time the TTD estimate from Tanhua et al. [2009] was normalized to. This C_{ant} is termed C_{ant}^{TTD}. To reproduce the assumptions that we made for the perturbation simulations, the total alkalinity was fixed to 2300 µmol kg^{-1}, the salinity was fixed to 35, and the atmospheric boundary conditions for CO_2 and CFC-12 were the same as these used in the perturbation approach. The TTD method was evaluated separately for SPW, WPW, AW, and BSW.

The evaluation of the TTD method was not possible in some parts of the Arctic Ocean due to our simulation strategy of initialization of all variables in ORCA025 in 1958 with results from ORCA05. As a consequence of the change in resolution, the invasion of C_{ant}^{NEMO} is to a large part (1765–1958) simulated with ORCA05, whereas the invasion of CFC-12 is mainly simulated with ORCA025 due to the relatively short atmospheric history of CFC-12. While this late initialization of ORCA025 poses no problem for the evaluation of the TTD method in relatively young water masses, it flaws the evaluation of the TTD for older water masses, especially in regions where the circulation in ORCA05 differs largely from ORCA025. The largest difference between ORCA05 and ORCA025 is the depth of vertical penetration of surface waters, which increases from 1300 m in ORCA05 to 1800 m in ORCA025 [Terhaar et al., 2018]. Thus, CFC-12 is relatively more abundant below 1300 m then C_{ant}^{NEMO} and the TTD method cannot be evaluated there.

Furthermore, the evaluation can only be performed in regions where the model represents the Arctic Ocean circulation sufficiently well. Terhaar et al. [2018] showed that the model represents the Arctic Ocean circulation in most parts of the Arctic Ocean above 1300 m relatively well, but simulated AW does not reach the western end of the Canada basin. As a consequence, simulated CFC-12 concentrations in this region are close to zero and well below observed concentrations [Tanhua et al., 2009]. Thus an evaluation of the TTD method in western end of the Canada basin is also not possible.

4.2.3.5 Correction of C_{ant}

The data-based C_{ant} was corrected based on the results from the TTD evaluation (Section 4.2.4). Although an evaluation was only possible in a restricted number of regions of the Arctic Ocean (Section 4.2.3.4), correction factors for all four dominant water masses in the Arctic Ocean could be identified. With these corrrection factors the data-based C_{ant} concentrations in the Arctic Ocean from Tanhua et al. [2009] were adjusted dependent on the water mass analysis (Table S1).

Simplified, water masses between 250 and 800 m across the Arctic Ocean were mainly identified as AW [Smethie et al., 2000] and water masses below 800 m mainly as WPW [Aagaard et al., 1981; Swift et al., 1997] and BSW [Jones et al., 1995; Jones, 2001; Smedsrud et al., 2013].

4.2.3.6 Projections of C_{ant}

Coarse-resolution models tend to underestimate the uptake of C_{ant} in the Arctic Ocean and the consequent rise of the deep ASH [Terhaar et al., 2018]. As high-resolution simulations with ocean-biogeochemical models until 2100 are computationally infeasible, C_{ant} estimates over the 21st century based on the TTD's assessement of the circulation in the last decades can provide complementary information to climate models.

Following Anderson et al. [2010], the TTD approach was used to estimate C_{ant} along the Beringia 2005 section over the 21st century [Anderson et al., 2011c]. The TTD was estimated based on observed CFC-12, temperature, and salinity. The alkalinity of each water sample was determined from the measured salinity with the salinity-alkalinity relationship for the Arctic Ocean from MacGilchrist et al. [2014]. The obtained TTD was then applied 13 times between 2014 and 2107 using atmospheric CO_2 from the four Representative Concentration Pathways RCP2.6, RCP4.5, RCP6.0, and RCP8.5 [Meinshausen et al., 2011]. The obtained C_{ant} concentrations were adjusted based on the correction factors that were obtained from the TTD evaluation (Section 4.2.4).

These TTD-based estimates implicitly assume no physical changes and are based on a tracer that has invaded the ocean over decades and not over centuries as C_{ant}. To test if the accuracy of the TTD method changes when being applied to a tracer with a longer atmospheric history, we also simulated CFC-12 and C_{ant} over 1765–2100 with the computationally efficient, coarse-resolution version of the model (ORCA2). The simulated CFC-12 concentration in 2005 was then used to derive the TTD. This TTD was then applied to atmospheric CO_2 levels over 1765–2005 and over 1765–2100 (S3). Despite the considerable longer atmospheric history of C_{ant} in 2100, the relative error of the TTD estimated C_{ant} remains almost the same. Although ORCA2 does not simulate the Arctic Ocean circulation nearly as well as ORCA025 [Terhaar et al., 2018], the results hold the whole range of observed CFC-12 concentrations and thus all different meanages. These results suggest that the TTD obtained from present-day CFC-12 can be used to estimate C_{ant} uptake over 1765–2100 in the absence of any change other than the rise in atmospheric CO_2.

4.2.3.7 Calculation of Ω_{arag} and undersaturation index

The aragonite saturation state Ω_A was calculated using mocsy routines [Orr and Epitalon, 2015] with dissociation constants recommended for best practices [Dickson et al., 2007]. Uncertainties of Ω_A resulting from potential errors on the chemical constants were estimated with routines from Orr et al. [2018]. Due to the idealized nature of our future estimates, we neglected uncertainties in the input variables (C_T, total alkalinity [A_T],...).

For present-day, Ω_A was calculated based on observed temperature, salinity, C_T, A_T, total dissolved inorganic phosphorus (P_T), total dissolved silicon (Si_T), and depth along the Beringia 2005 section. To estimate preindustrial Ω_A, the adjusted C_{ant} estimate was subtracted from the measured C_T concentration to obtain preindustrial C_T, thus assuming that the other variables did not change over the industrial period. For estimates of Ω_A over the 21st century, the additional estimated C_{ant} since 2005 was added to C_T measurements taken in 2005, also neglecting changes in all other variables.

To quantify the volume of the whole Arctic Ocean that is undersaturated with respect to aragonite, we introduce an Ω_A undersaturation index (UI). UI is defined as the fraction of the Arctic Ocean volume where $\Omega_A < 1$. Here, UI was calculated along the Beringia 2005 section, assuming that calculated Ω_A at every measurement point along the section is representative for its surrounding area.

4.2.4 Evaluation of TTD method in the Arctic Ocean

In the Arctic Ocean, our model simulates a total C_{ant}^{NEMO} (C_{ant} directly simulated by NEMO) inventory of 2.5 Pg C in 2005. This simulated inventory is at the lower end of the uncertainty range of the data-based estimate from Tanhua et al. [2009] (2.5 – 3.3 Pg C in 2005). The relatively low C_{ant}^{NEMO} inventory compared to the data-based estimates can be explained by too little horizontal extent of Atlantic Waters at intermediate depths and insufficient deep-water formation in the model [Terhaar et al., 2018]. Masking out cells with ocean pCFC-12 above atmospheric pCFC-12 reduces the C_{ant}^{NEMO} inventory to 2.31 Pg C in 2005. In comparison, the C_{ant}^{TTD} (C_{ant} calculated from CFC-12, T, and S simulated by NEMO) in the Arctic Ocean is 2.23 Pg C in 2005, 3% below the 'reference' C_{ant}^{NEMO} inventory.

This difference between C_{ant}^{TTD} and C_{ant}^{NEMO} had likely been larger if we had also used ORCA025 before 1958 and not the coarser model configuration ORCA05 that simulates less storage of C_{ant} [Terhaar et al., 2018]. Indeed, when evaluating the TTD method in younger waters that are almost not impacted by the change in resolution in 1958, we find that the calculated C_{ant}^{TTD} underestimates the 'reference' C_{ant}^{NEMO} by $7 \pm 2\%$ (2.5 ± 0.9 µmol kg^{-1}) in SPW, by $12 \pm 3\%$ (4.9 ± 1.3 µmol kg^{-1}) in WPW , by $4 \pm 2\%$ (1.1 ± 0.6 µmol kg^{-1}) in AW, and by $12 \pm 2\%$ (5.0 ± 1.1 µmol kg^{-1}) in BSW.

These underestimations of C_{ant}^{TTD} can be explained by the saturation of surface ocean δpCO_2 and pCFC-12 during deep-water formation in the Arctic Ocean (Figure 4.2). Contrary to the TTD's assumption of perfect equilibrium of δpCO_2 and pCFC-12 between the atmosphere and the surface ocean, we find that during deep-water formation, simulated δpCO_2 at the ocean surface is higher than atmospheric δpCO_2 (supersaturation) whereas surface ocean pCFC-12 is lower than atmospheric pCFC-12 (undersaturation). This disequilibrium in δpCO_2 and pCFC-12 between the surface ocean and the atmosphere can be attributed to the rapid heat loss of inflowing PW and AW [Midttun, 1985; Kaltin and Anderson, 2005]. This heat loss causes ocean surface δpCO_2 to

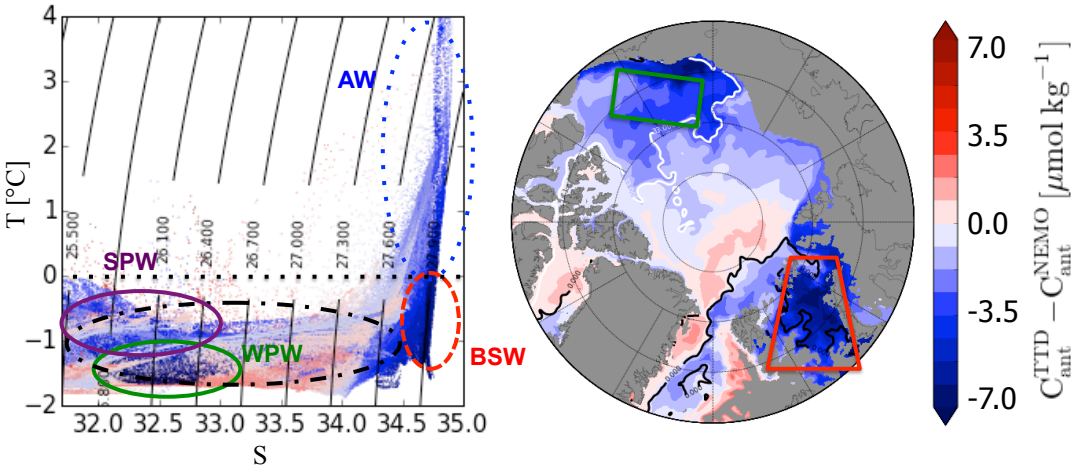

Figure 4.1 – Left panel: Difference between C_{ant}^{TTD} and C_{ant}^{NEMO} in the top 160 m as a function of simulated temperature and salinity. Colored circles indicate BSW (red dashed), AW (blue dotted), SPW (magenta solid), WPW (green solid), and remaining waters close to the surface (black dash dotted). Right panel: Mapped difference (C_{ant}^{TTD}–C_{ant}^{NEMO}) at 112 m. Contour lines are shown for S = 33 (white) and T = 0°C (black). The two regions over which averages are shown in Figure 4.2 are roughly outlined in green (Chukchi Sea) and in red (Barents Sea)

increase and ocean surface pCFC-12 to decline, because cold water can hold less C_{ant} and more CFC-12. The short surface residence time of waters in the Chukchi and Barents Sea [Loeng, 1991; Spall, 2007] prevents δpCO_2 and pCFC-12 to reach the equilibrium with the atmosphere before being subducted. By assuming both δpCO_2 and pCFC-12 to be in equilibrium with the atmosphere, the TTD thus underestimates C_{ant} in waters formed in the Chukchi and Barents Seas.

While these underestimations are well visible in the Chukchi and Barents Seas, they become smaller when these water masses mix with other water masses (Figure 4.1). The largest underestimations of C_{ant}^{TTD} were found in WPW, indicated by the isohaline at S=33, at the shelf break of the Chukchi Sea and in the BSW indicated by the 0°C isotherm (Figure 4.1). Once the BSW enters the Nansen basin and mixes with AW, the underestimation is reduced. This mixing can be identified in the model by the decrease in temperature gradient in simulated AW along the shelf-break of the Nansen basin and is well documented by observations [Schauer et al., 2002; Gammelsrød et al., 2009].

The calculated underestimations of C_{ant} are likely a lower limit for two reasons. First, the perturbation approach has been shown to underestimate C_{ant} in the Arctic Ocean [Terhaar et al., 2018]. A higher 'reference' C_{ant}^{NEMO} would hence lead to a larger underestimation of C_{ant} by the TTD method. Second, Smith et al. [2011] suggest that the Δ / Γ ratio (Equation 4.2) in the Arctic Ocean should be lower than the here used 1.0. If we had used a Δ / Γ ratio below 1.0, C_{ant}^{TTD} in the WPW and BSW would have been smaller (Figure S1 and S2) and the calculated correction factors would have been even higher.

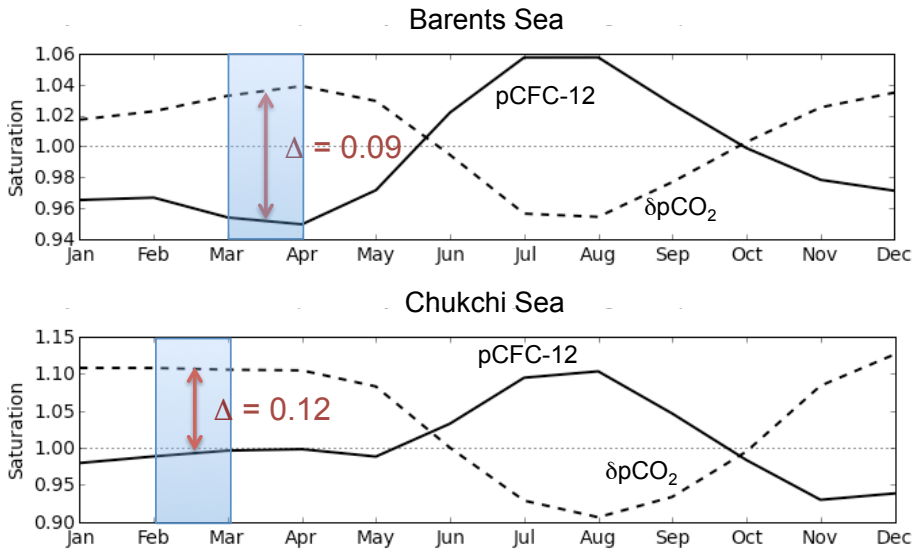

Figure 4.2 – Seasonal cycle of simulated δpCO_2 and pCFC-12 saturation averaged over the Barents Sea and Chukchi Sea in 2005. The saturation of surface ocean δpCO_2 and pCFC-12 are normalized by their respective atmospheric partial pressure in 2005 (100.6 ppm and 544.9 ppt). The shaded blue area indicates the period of deep-water formation and the red arrow the difference in saturation between δpCO_2 and simulated pCFC-12. The dashed horizontal line indicates the air-sea equilibrium

4.2.5 Correction of data-based estimate of C_{ant} in the Arctic Ocean

We adjust the data-based estimate from Tanhua et al. [2009] using the relative underestimation of the TTD method per water mass as a correcting factor: +4% (AW), +12% (WPW and BSW), and +7% in SPW (Section 4.2.4). By adjusting the TTD-based C_{ant} concentrations, the Arctic Ocean C_{ant} inventory increases from 3.0 to 3.3 Pg C in 2005 and the uncertainty range increases from 2.5–3.3 to 3.0–3.6 Pg C. The lower bar of the uncertainty range is increased by 0.2 Pg C more than the upper bar, because it previously included a potential bias caused by the difference in saturation of δpCO_2 and pCFC-12 [Tanhua et al., 2009] as found in the Southern Ocean [Waugh et al., 2006]. Here, we have quantified the direction and magnitude of this bias and could therefore reduce the uncertainty range.

4.2.6 Arctic Ocean acidification

Using the data-based C_{ant}^{obs} estimate from Tanhua et al. [2009], Anderson et al. [2010] calculated the spatially averaged deep ocean ASH in 2005 (1890 m) along the Beringia 2005 section and the corresponding shoaling of the latter since 1765 (190 m). Here, we update these estimates of the ASH using the adjusted C_{ant} estimate and we further explore the spatially resolved ASH estimate along the same section. Uncertainties in this section refer only to uncertainties in the dissociation constants. The mean deep ASH is found between 1700 and 2210 m, in agreement with Anderson et al. [2010]. Further we find a strong horizontal variability of this deep ocean ASH along the section (Figure 4.3). The deepest ASH is detected at the continental rise next to the Beaufort Sea between

2150 and 2730 m and the shallowest ASH is located only 500 km further along the section in the center of the Canada basin between 1320 and 1880 m. As opposed to the average depth of the ASH, the calculated average shoaling of the latter during industrialization of 280 m is 47% larger than estimated by Anderson et al. [2010] when using the corrected C_{ant} estimate. The shoaling of the ASH varies from 80 m in the southern part of the Canada basin to 490 m in the center of the Canada basin and 460 m in the northern part of the Nansen basin.

Following Anderson et al. [2010], we further estimate Ω_A changes over the 21st century caused solely by the increase in C_T. More specifically, we applied the obtained TTD to projected atmospheric CO_2 concentrations under the four RCPs to estimate C_{ant} along the Beringia section and the corresponding development of the undersaturation index (UI) (Section 4.2.3.7) (Figure 4.3). From 2005 to 2037, the UI follows the same trajectory under all four RCPs, rising from 39–50% to 45–64%, but diverges afterwards. Under RCP2.6, the UI rises slowly to 63–78% in 2096 and remains constant thereafter. Under the three remaining RCP's, the UI rises at different rates to above 90% in 2107, reaching 82–98% under RCP4.5, 94–100% under RCP6.0, and 99–100% under RCP8.5.

These idealized TTD-based estimates were further compared to simulated changes in Ω_A using the NCAR CSM1.4 climate-carbon model [Steinacher et al., 2009]. In their study, the change of Ω_A during the 21st century is simulated under the Special Report on Emissions Scenarios (SRES) B1 and A2, scenarios that are similar to RCP2.6 and RCP8.5. At the end of the 21st century, Steinacher et al. [2009] find the entire water column in the Arctic Ocean to be undersaturated towards aragonite when following the A2 scenario, but not when following the B1 scenario. Subsequently, they estimate the atmospheric CO_2 threshold at which the entire Arctic Ocean water column would become undersaturated towards aragonite to be 765 ppm, the atmospheric CO_2 reached at the end of the 21st century under the A2 scenario. Similarly, we also find that atmospheric CO_2 levels from RCP8.5 lead to an entirely undersaturated water column at the end of the 21st century (Figure 4.3) and that atmospheric CO_2 levels under RCP2.6 do not. In addition to Steinacher et al. [2009], we also exploit the two intermediate pathways RCP4.5 and RCP6.0. Under both pathways, the Arctic Ocean becomes entirely undersaturated, with an UI of 94–100% in 2107 under RCP6.0 and an UI of 93–99% in 2150 under RCP4.5. Therefore, the threshold at which the entire Arctic Ocean water column would become undersaturated towards aragonite is not found at 765 ppm, but well below between 450 ppm (atmospheric CO_2 in 2150 following RCP2.6) and 540 ppm (atmospheric CO_2 in 2150 following RCP4.5). This threshold of 450–540 ppm would already be reached between 2031 and 2051 if we kept following the RCP8.5 trajectory. However, even under RCP8.5, the undersaturation of the entire Arctic Ocean would not occur before 2080, due to the long ventilation time of surface water with high pCO_2.

As opposed to model studies [Steinacher et al., 2009; Steiner et al., 2013], our results also suggest that Arctic Ocean acidification during the 21st century is largely driven by a rise of the deep ASH and not by the deepening of undersaturated water from the surface. Ocean models that rely on coarse resolution models such as the one used by Steinacher et al. [2009] have been shown to

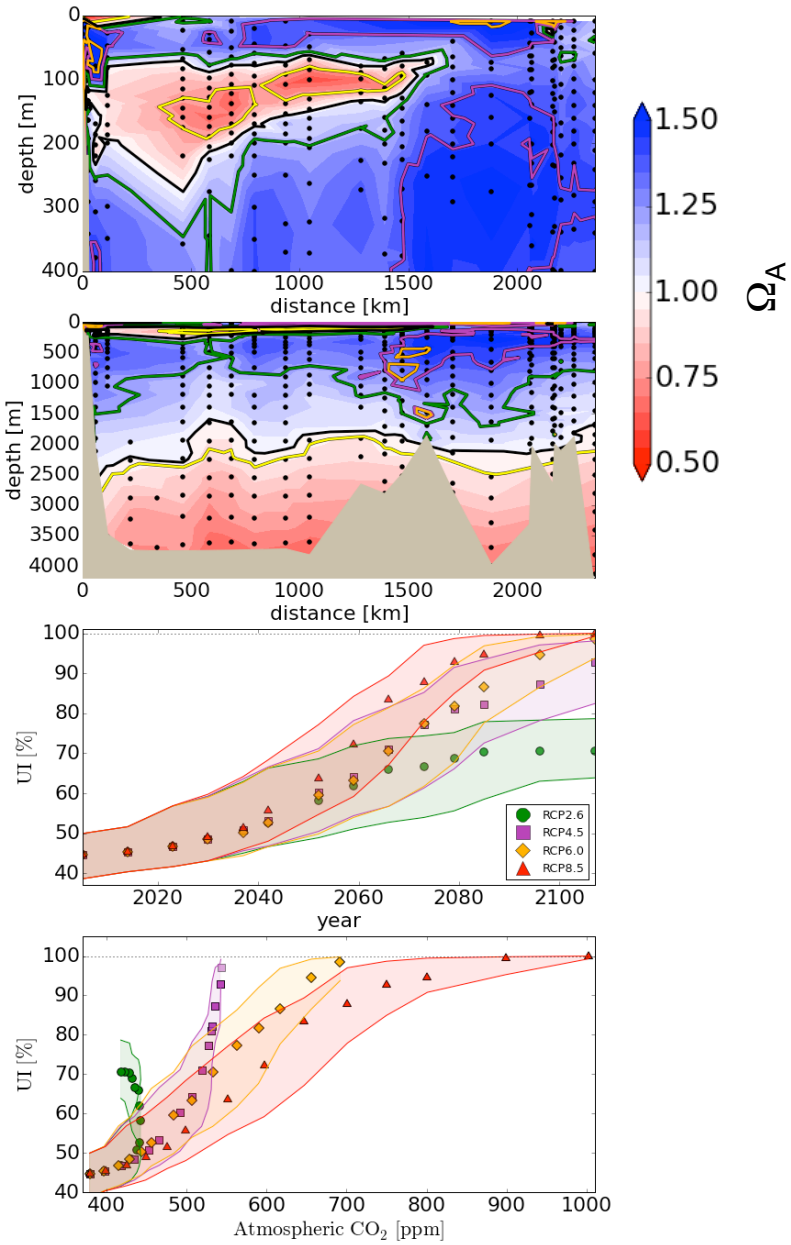

Figure 4.3 – Observed Ω_A at present-day conditions along the Beringia 2005 section for the first 400 m (top) and the whole depth range (upper middle). The ASH is marked for present day conditions (black), preindustrial conditions (yellow), and for 2107 following RCP2.6 (green), RCP4.5 (magenta), and RCP6.0 (orange). In addition projections of the UI for the four RCP's depending on the year (lower middle) and the atmospheric CO_2 concentrations (bottom). The light mark for RCP4.5 represents the year 2150. The shadowed area represents the uncertainty range based on uncertainties in the carbonate system constants.

inadequately represent the lateral transport and storage of C_{ant} in the Arctic Ocean [Terhaar et al., 2018]. This insufficient simulated storage of C_{ant} might explain why the simulated shoaling of the deep ASH is smaller than the TTD-based estimate.

Meanwhile, the TTD-based estimates of C_{ant} and acidification for the 21th century are highly idealized, because they implicitly assume that climate and circulation patterns do not change when estimating future invasion of C_{ant}. As opposed to this assumption, the Arctic Ocean is already experiencing large changes in sea surface temperature [Serreze and Barry, 2011], sea ice extent [Serreze and Stroeve, 2015b], and primary production [Arrigo and van Dijken, 2015], all of which influence the uptake of C_{ant} and the associated ocean acidification. For example, the combined effect of increased ocean temperature and dilution of C_T and A_T due to sea ice melt is projected to enhance the decline in Ω_A close to the surface. However, this effect has been shown to be of second order in comparison to the uptake of C_{ant} uptake [Steinacher et al., 2009]. Furthermore, decreasing sea ice cover and increasing temperatures are expected to alter the Arctic Ocean circulation and the associated advection of C_{ant} into the deep Arctic Ocean. Using the ocean—sea ice—atmosphere coupled model HiGEM under a 4 × preindustrial CO_2 scenario, Lique et al. [2018] find intensified deep water convection in the Eurasian basin with climate change as a consequence of increased brine rejection. Indications for this projected increase in Arctic Ocean deep-water formation were already observed, such as the increased contribution of Arctic waters to deep water masses in the Nordic Seas [Langehaug and Falck, 2012; Somavilla et al., 2013]. An increased Arctic deep convection would further enhance the uptake of C_{ant} and thus enhance deep ocean acidification and the rise of the deep ASH. These studies suggest that climate change will lead to a stronger decrease of Ω_A in the Arctic Ocean than estimated by the TTD. The idealized TTD-based estimates of future changes of Arctic Ocean Ω_A should therefore be regarded as a lower limit.

4.2.7 Conclusion

The model-based evaluation of the TTD method demonstrated that the method underestimates C_{ant} concentrations in the Arctic Ocean by 0–12%. This underestimation could be attributed to a bias in the TTD method towards too low estimates of C_{ant} concentration in water masses formed at the Arctic Ocean surface. These too low estimates of C_{ant} are caused by the methods assumption of perfect equilibrium of δpCO_2 and pCFC-12 between the surface ocean and the atmosphere. Contrary to this assumption, the ocean circulation model demonstrated supersaturation of δpCO_2 and undersaturation of pCFC-12, which causes the observed bias in the TTD method. By adjusting the C_{ant} inventory from Tanhua et al. [2009] for this bias, the latter augments from from 3.0 (2.5-3.3) Pg C to 3.3 (3.0-3.6) Pg C normalized to 2005.

When applying the TTD method to future atmospheric CO_2 concentrations, we find that an entirely undersaturated Arctic Ocean towards aragonite will occur if atmospheric CO_2 concentrations exceed 450 and 540 ppm, at ~200–300 ppm less than previously thought [Steinacher et al.,

2009]. Consequently, a completely undersaturated Arctic can only be avoided under RCP2.6. The time at which the Arctic Ocean will become undersaturated towards aragonite varies with the RCP. For example, under RCP8.5 ("business as usual") the threshold of 450–540 ppm will be reached between 2031 and 2051, but the Arctic Ocean will not become undersaturated before 2080 due to the water ventilation time from the surface to the deeper ocean.

4.2.8 Supplementary Material

The supplementary information includes three parts: An analysis of the effect of changing $\frac{\Delta}{\Gamma}$ in the Green's function of the TTD method (Text S1), a detailed description of the water mass analysis (Text S2), and an evaluation of the application of the TTD to future atmospheric CO_2 levels (Text S3).

4.2.8.1 Text S1: Varying $\frac{\Delta}{\Gamma}$

Although the TTD is generally applied with a $\frac{\Delta}{\Gamma}$ ratio of 1.0 [Tanhua et al., 2009; Stöven et al., 2016], studies using different tracers suggest that this $\frac{\Delta}{\Gamma}$ should be lower in surface waters [Smith et al., 2011]. To understand the effect of a changing $\frac{\Delta}{\Gamma}$, we applied the TTD method with $\frac{\Delta}{\Gamma}$ from 0.1 to 2.0, in steps of 0.1. The effect of a changing $\frac{\Delta}{\Gamma}$ depends on the water mass. In some parts of the ocean, $\frac{\Delta}{\Gamma} > 1.0$, increases the estimate of C_{ant}, in others it decreases the latter. The inverse is valid for $\frac{\Delta}{\Gamma} < 1.0$. We show results at various depths for $\frac{\Delta}{\Gamma} = 0.1$ and $\frac{\Delta}{\Gamma} = 2.0$, as the effect is most pronounced at the extremes (Figures 4.4), 4.5, 4.6, and 4.7)

Younger water masses, those that are close to the surface or recently ventilated, exhibit a C_{ant} increase with an increasing $\frac{\Delta}{\Gamma}$ and decreases with an decreasing $\frac{\Delta}{\Gamma}$. Applying a $\frac{\Delta}{\Gamma} < 1$ in waters close to the surface, as suggested by Smith et al. [2011], would increase the underestimation further. Even if we use a $\frac{\Delta}{\Gamma}$=2.0, the TTD still underestimates the reference C_{ant}^{NEMO} (Figure 4.5). The underestimation of the reference C_{ant}^{NEMO} is thus consistant across all $\frac{\Delta}{\Gamma}$ in young waters. Conversely in older water, the decreasing $\frac{\Delta}{\Gamma}$ augments the Cant estimate in older waters enough to bring them in accordance with the directly simulated C_{ant}^{NEMO}. Nevertheless there is no study to our knowledge that suggest a lower $\frac{\Delta}{\Gamma}$ in older waters. Thus the underestimation of Cant in older waters can also clearly be attributed to the difference in surface saturation.

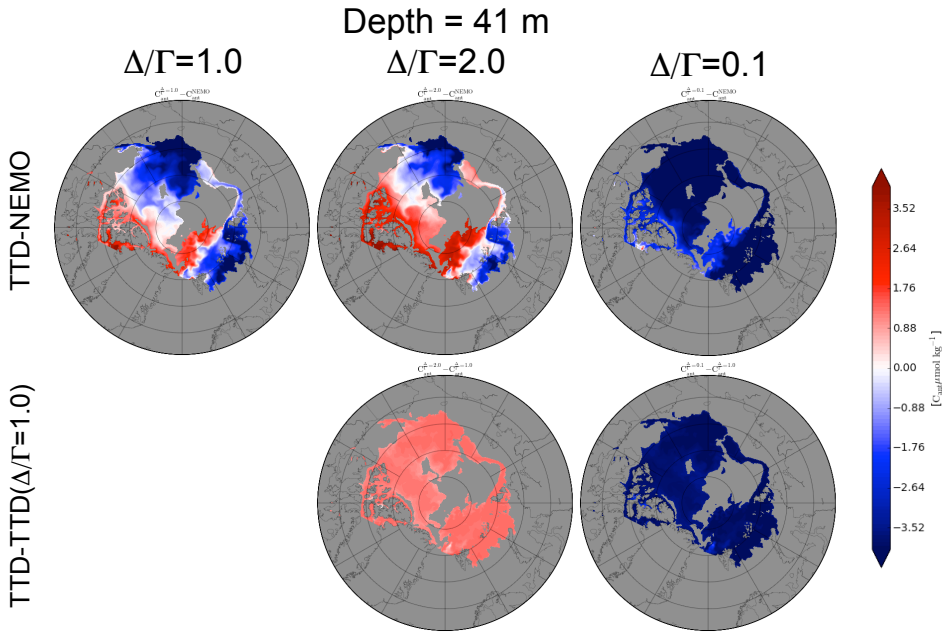

Figure 4.4 – Differences between TTD calculated C_{ant} and C_{ant}^{NEMO} at 41 m depth (upper line) for $\frac{\Delta}{\Gamma} = 1.0$, $\frac{\Delta}{\Gamma} = 2.0$, and $\frac{\Delta}{\Gamma} = 0.1$ (left to right). Below the respective differences to $\frac{\Delta}{\Gamma} = 1.0$ are shown.

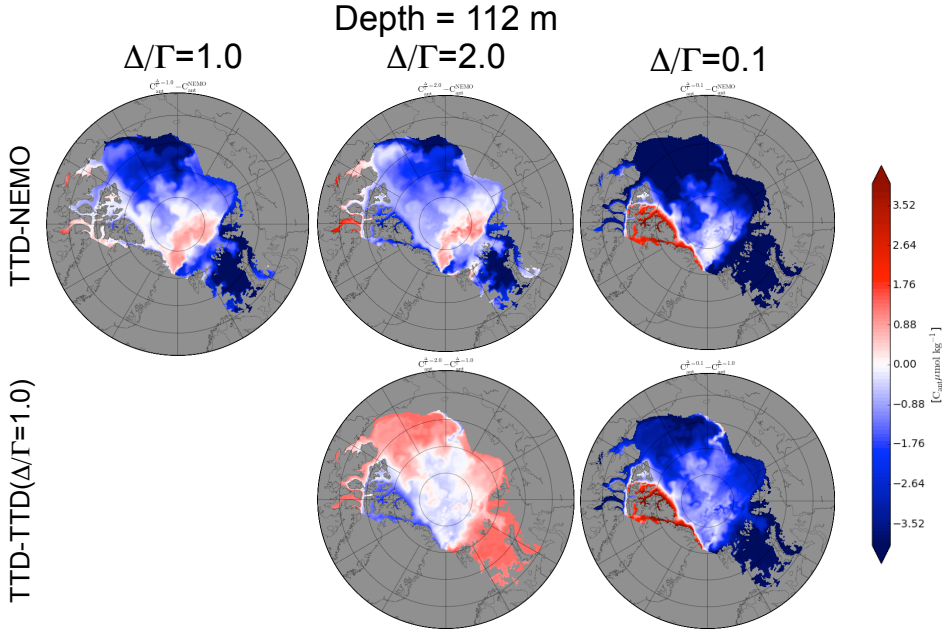

Figure 4.5 – Differences between TTD calculated C_{ant} and C_{ant}^{NEMO} at 112 m depth (upper line) for $\frac{\Delta}{\Gamma} = 1.0$, $\frac{\Delta}{\Gamma} = 2.0$, and $\frac{\Delta}{\Gamma} = 0.1$ (left to right). Below the respective differences to $\frac{\Delta}{\Gamma} = 1.0$ are shown.

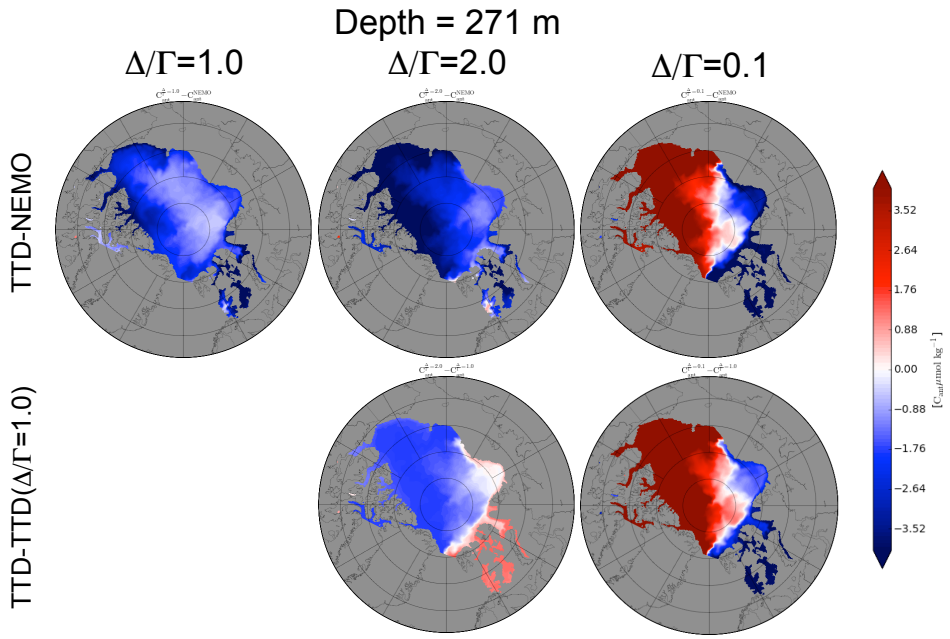

Figure 4.6 – Differences between TTD calculated C_{ant} and C_{ant}^{NEMO} at 271 m depth (upper line) for $\frac{\Delta}{\Gamma} = 1.0$, $\frac{\Delta}{\Gamma} = 2.0$, and $\frac{\Delta}{\Gamma} = 0.1$ (left to right). Below the respective differences to $\frac{\Delta}{\Gamma} = 1.0$ are shown.

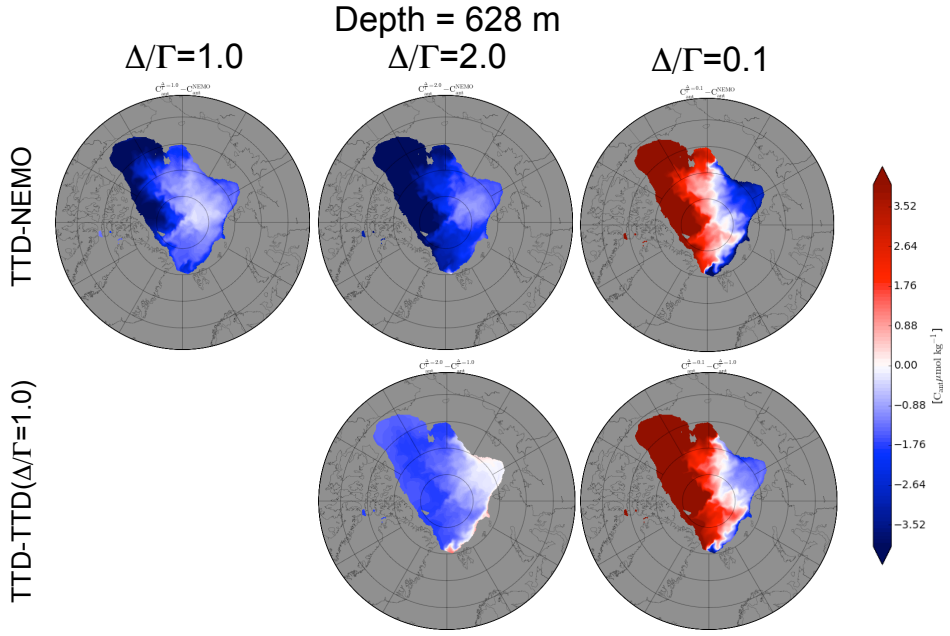

Figure 4.7 – Differences between TTD calculated C_{ant} and C_{ant}^{NEMO} at 628 m depth (upper line) for $\frac{\Delta}{\Gamma} = 1.0$, $\frac{\Delta}{\Gamma} = 2.0$, and $\frac{\Delta}{\Gamma} = 0.1$ (left to right). Below the respective differences to $\frac{\Delta}{\Gamma} = 1.0$ are shown.

4.2.8.2 Text S2: Water mass analysis

Here, we provide a detailed description of the water mass analysis and the correction factors useded in the paper for Summer Pacific Waters (SPW), Winter Pacific Waters (WPW), Atlantic Waters (AW), Barents Sea Waters (BSW), and surface waters (SW). References are provided in the main manuscript.

Table 4.1 – Water mass analysis and corresponding correction factors

	SPW	WPW	AW	BSW	SW
T [C°]	>-1	<-1	>0	<0	/
S [psu]	31-33	32.4-33	>34	>34.6	/
Depth [m]	50–100	50–500	50–ocean floor	50–ocean floor	0–300
Longitude	/	90E–180E & 90W–180W	/	/	/
Latitude	/	<85	/	/	/
Correction factor	1.07	1.12	1.04	1.12	1.0
Number of data points	54	228	3175	3127	3139

4.2.8.3 Text S3: Using the TTD method for projections of C_{ant}

The TTD is based on CFC-12, which have an atmospheric history of ~70 years. When we apply the TTD method for projections of C_{ant} uptake at the end of the 21st century, we apply it to a tracer (C_{ant}), which has an atmospheric history of ~330 years. Here, we test if the relatively short atmospheric history of CFC's is long enough to sufficiently describe the Arctic Ocean circulation and if it thus can be used to calculate future concentrations of C_{ant}.

For this test we calculate the TTD based on simulated CFC-12 in 2005. We then apply the so obtained TTD to the atmospheric C_{ant} history until 2005 and until 2100. The so obtained C_{ant}^{TTD} is then evaluated against the respective directly simulated C_{ant}^{NEMO} reference. If the relative error between C_{ant}^{TTD} and C_{ant}^{NEMO} is the same in 2005 and 2100, the TTD can be used for projections of C_{ant} over the 21st century. To simulate C_{ant}^{NEMO} over 1765–2100, the computationally less expensive ORCA2 configuration with a nominal resolution of 2°) has to be used instead of the computational too expensive ORCA025 configuration. Accordingly CFC-12 was also simulated using ORCA2.

Using ORCA2, the total Arctic Ocean C_{ant}^{TTD} inventory is 1.43 Pg C in 2005 and 5.8 Pg C in 2100. In comparison the C_{ant}^{NEMO} is 1.39 Pg C in 2005 and 5.6 Pg C in 2100. In both years, the C_{ant}^{TTD} consistently overestimates the C_{ant}^{NEMO} reference by 3%. Although the total relative difference between the C_{ant}^{TTD} and C_{ant}^{NEMO} inventory does not change with time, a slight relative increase in C_{ant}^{TTD} with time can be detected for the surface values when comparing grid point by grid for both years (Figure 4.8). When fitting a linear trend to the C_{ant}^{TTD} vs C_{ant}^{NEMO} plot, we find slopes of 1.07 in 2005 and 1.09 in 2100, indicating that the overestimation of C_{ant} by the TTD method is increasing by 2% from

2005 to 2100. This increase in surface ocean C_{ant}^{TTD} has little impact on the total C_{ant}^{TTD} inventory as the surface ocean cells represent a smaller volume than the deeper cells. Furthermore, the vertically integrated relative difference between C_{ant}^{TTD} and C_{ant}^{NEMO} in 2005 and 2100 exhibit the same horizontal pattern with minor differences north of Greenland and in the Beaufort Sea.

This detected overestimation of C_{ant}^{NEMO} is opposite to ORCA025, where C_{ant}^{TTD} is smaller then C_{ant}^{NEMO}. Due to a too weak horizontal circulation in ORCA2 compared to observations [Terhaar et al., 2018], the residence time of water at the Arctic Ocean increases and the partial pressure has more time to get in equilibrium with the atmosphere.

Overall, the relative error in C_{ant}^{TTD} when applying the TTD derived from CFC-12 concentrations in 2005 to atmospheric CO_2 levels in 2100 is approximately the same as for the C_{ant}^{TTD} in 2005. Thus the TTD from observed CFC-12 in 2005 can be applied to atmospheric CO_2 levels throughout the 21^{st} century.

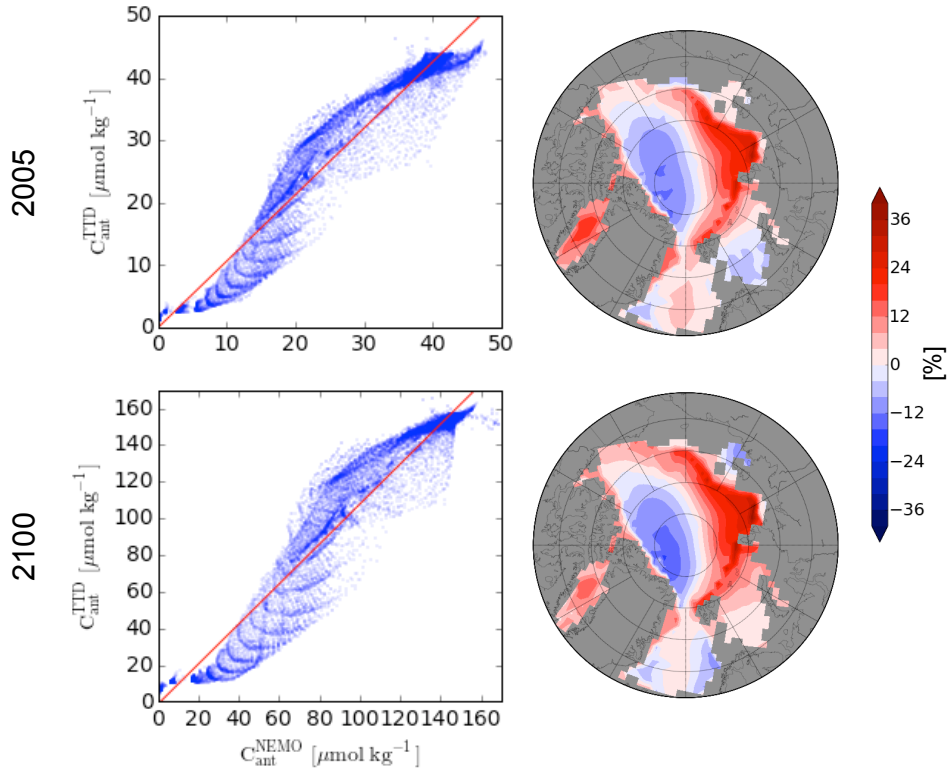

Figure 4.8 – Point-by-point comparison between C_{ant}^{TTD} and C_{ant}^{NEMO} for 2005 (top left) and 2100 (bottom left) with the respective linear fit (red line) and relative difference [%] between vertical integrated C_{ant}^{TTD} and C_{ant}^{NEMO} in 2005 (top right) and in 2100 (bottom right).

4.3 Summary

- The evaluation showed that the TTD method underestimates the C_{ant} inventory by ~7.5% in the Arctic Ocean, leading to new best estimate of 3.3 (3.0–3.6) Pg C normalized to 2005
- This underestimation stems almost exclusively from the underestimation of C_{ant} by up to 12% in waters formed at the Arctic Ocean surface
- This underestimation can be explained by rapid cooling of waters flowing into the Arctic Ocean and associated changes in solubility, which lead to an oversaturation of CFC-12 and an underestimation of C_{ant} at the moment of deep water formation
- Projections of ocean acidification in the Arctic Ocean suggest that the entire Arctic Ocean becomes undersaturated if atmospheric CO_2 reaches 450–540 ppm
- Although this threshold will be reached between 2031 and 2051 if we keep following the RCP8.5 trajectory, the entire undersaturation will not occur before the end of the century as the waters with high C_{ant} has to be transported to the deeper ocean
- The increase of the data-based C_{ant} inventory enlarges the difference with the simulated C_{ant} inventory in ORCA025. The difference is most important in the deep Arctic Ocean, which shows important shortcomings of the model regarding the deep water formation.
- The models shortcomings in deep-water formation do not pose a major problem for the river analyses in the following two chapters, but should nevertheless receive increased attention during the development of NEMO-LIM, so that deep water convection can be improved in future versions of the model.

Chapter 5

Pan-Arctic extrapolation of data-based riverine carbon and nutrient fluxes and their impact on the Arctic Ocean biogeochemistry

" I think that I was slightly naive. I thought that if I showed people the beauty of the Arctic and the beauty of the polar bears that they would care so much that they would stand up and try to make a change. "

Lewis Gordon Pugh

Contents

5.1 Preamble

Based on the comparison of NEMO-PISCES at different resolutions, the highest available resolution of the model (ORCA025) was used in this chapter to test the influence of Arctic river fluxes on the Arctic Ocean biogeochemistry.

To evaluate the effect of riverine fluxes with NEMO-PISCES, a horizontally resolved dataset of carbon and nutrient fluxes is needed to force the model. So far, the standard configurations of ocean-biogeochemical models used either no river fluxes of carbon and nutrients at all [Ilyina et al., 2013; Tjiputra et al., 2013]or river flux estimates from land-surface models [Aumont et al., 2015].

A different option to the use of land-surface models for the calculation of riverine fluxes for all Arctic rivers, is the extrapolation of data-based river fluxes on the pan-Arctic scale. So far, only data-based riverine DOC fluxes were extrapolated on a horizontally resolved grid and used to force ocean models [Manizza et al., 2009]. In this chapter, recent observations [Tank et al., 2012c; Holmes et al., 2012] are extrapolated based on watershed characteristics, like permafrost coverage, annual runoff, or the carbonate index.

This new dataset is then used to force NEMO-PISCES with the ORCA025 configuration. The aim of this study is to evaluate the model performance when using the new data-based riverine flux forcing set, and to quantify the impact of riverine fluxes of carbon and nutrients on key biogeochemical processes, such as net primary production, air-to-sea CO_2 fluxes, and ocean acidification. To clearly isolate the effect of riverine fluxes, a second simulation without river fluxes was made.

5.2 Article in preparation for publication in *Global Biogeochemical Cycles*

J. Terhaar[1,2], R. Lauerwald[2], P. Regnier[2], and L. Bopp[3]

[1]Laboratoire des Sciences du Climat et de l'Environnement, LSCE/IPSL, CEA-CNRS-UVSQ, Université Paris-Saclay, 91191 Gif-sur-Yvette, France

[2]Biogeochemistry and Earth System Modelling, Department of Geoscience, Environment and Society, Université Libre de Bruxelles, Belgium

[3]LMD/IPSL, Ecole Normale Supérieure / PSL Research University, CNRS, Ecole Polytechnique, Sorbonne Université, Paris, France

5.2.1 Abstract

Despite the large influence of river fluxes of carbon and nutrients in the coastal regions, the absolute amount of these fluxes and their effect on the ocean biogeochemistry remain uncertain. The importance of riverine fluxes is expected to be disproportional high in the Arctic Ocean, as it receives 11% of the global river discharge despite representing only 1% of the global ocean volume. In this study, we construct for the first time an observation-based, monthly, pan-Arctic riverine forcing data set that includes riverine fluxes of dissolved inorganic carbon (C_T), dissolved organic carbon (DOC), carbonate alkalinity (A_C), dissolved inorganic nitrogen (DIN), dissolved organic nitrogen (DON), total dissolved phosphorous (TDP), and dissolved silica (Si_T). When using this data set to force a high-resolution ocean biogeochemical model, we find that riverine nutrient fluxes sustain 13–19% of the basinwide integrated net primary production (NPP) in the Arctic Ocean. Furthermore, the combined effect of riverine delivery of carbon and nutrients increases the aragonite saturation state in summer basinwieder by 8% and locally by up to 50%, mainly driven by a reduction of surface C_T during the phytoplankton bloom. Despite this reduction of surface C_T by riverine driven NPP, outgassing of remineralized riverine DOC in the coastal regions leads to a reduction of the Arctic Ocean air-sea CO_2 uptake by 17%. The here presented estimates exceed earlier estimates of the influence of riverine carbon and nutrient fluxes on the Arctic Ocean biogeochemistry because of higher simulated recycling rate of riverine nutrients in the Arctic Ocean and higher lability of riverine DOC and DON.

Coastal regions have been shown to be an important component of the global carbon cycle [Cai, 2011; Bauer et al., 2013; Regnier et al., 2013b; Bourgeois et al., 2016], to contribute disproportionally strong to global ocean primary production [Cloern et al., 2014], and to be hotspots of ocean acidification [Semiletov et al., 2016; Chierici and Fransson, 2009] and deoxygenation [Breitburg et al., 2018]. Although river fluxes of carbon and nutrients are believed to be one of the

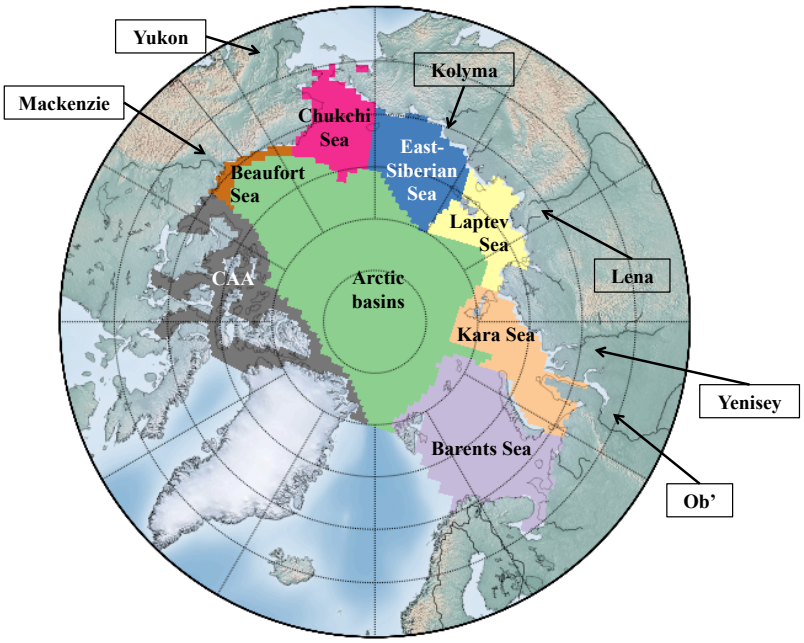

Figure 5.1 – Regional seas and the six major rivers of the Arctic

principal drivers of these processes, the quantity of these fluxes and their relative influence on the coastal ocean biogeochemistry are still uncertain.

The largest influence of river fluxes can be expected in the Arctic Ocean. Although this part of the ocean only represents 1% of the global ocean volume, it receives around 11% of global river discharge [McClelland et al., 2012] and 13–15% of global riverine C_T fluxes [Tank et al., 2012c]. Furthermore, riverine DOC fluxes in Arctic rivers is 2.5 times higher than DOC fluxes from temperate rivers of similar size driven by exceptionally high DOC concentrations in Arctic rivers from carbon rich soils and peatlands [Raymond et al., 2007]. Among Arctic rivers, the six largest rivers alone (Yenisei, Ob, Lena, Kolyma, Yukon, and Mackenzie) (Figure 6.1) account for ~69% of the total Arctic river runoff [Tank et al., 2012c; Fekete et al., 2002] and for 53% of the Arctic riverine C_T flux [Tank et al., 2012c].

The large delivery of carbon has been shown to directly affect the Arctic Ocean biogeochemistry. For example, the remineralization of large amounts of riverine DOC in the coastal Arctic Ocean leads to an increase of the partial pressure of CO_2 (pCO_2), which is locally large enough to drive outgassing of CO_2 from the ocean to the atmosphere [Anderson et al., 2009; Humborg et al., 2017]. On a pan-Arctic scale, decomposition of riverine DOC has been estimated to decrease the uptake of atmospheric CO_2 by ~10% [Manizza et al., 2011]. Further, degradation of riverine DOC and the following increase in C_T has also been shown to drive coastal ocean acidification, leading to observed aragonite saturation states (Ω_A) close to zero in the Laptev Sea [Semiletov et al., 2016]. Low Ω_A are also found close to the mouths of rivers with small DOC fluxes, like the Mackenzie [Chierici and Fransson, 2009]. In these cases, low riverine concentrations of C_T and total alkalinity (A_T) dilute calcium carbonate concentrations in coastal surface waters and hence reduce Ω_A.

In addition to riverine carbon, riverine delivery of nutrients influences the Arctic Ocean biogeochemistry via enhanced net primary production (NPP). Le Fouest et al. [2013] estimated 1% of the new primary production (PP) to be sustained by riverine DIN delivery by assuming a constant C:N:P:Si ratio of 112:14:1:26 for phytoplankton production and assuming that every mole of riverine DIN is consumed by new PP. Further, Tank et al. [2012a] accounted in addition for riverine DON fluxes by using an exponantially decaying tracer for riverine DON in an ocean circulation model and estimate that riverine DIN and DON fluxes together sustain 3% of Arctic new PP. By assuming typical recycling rates of N in the Arctic Ocean surface layers (0.5–3.2) [Smith et al., 1997; Tremblay et al., 2006; Garneau et al., 2007], Tank et al. [2012c] estimate riverine DIN and DON to sustain up to 4% of Arctic Ocean NPP. Recently, Le Fouest et al. [2015] explicitly simulated the recycling of riverine nutrients using an ocean-biogeochemical model and increased the estimate of riverine DIN and DON sustained NPP to 9%. This estimate may well be a lower limit, as recent observations suggest that 62–76% of riverine DON is transformed to DIN on the shelves within months [Thibodeau et al., 2017], 4 to 5 times more than the 15% that Le Fouest et al. [2015] assumed to be biodegradable.

Despite the importance of riverine fluxes of carbon and nutrients, observations of theses fluxes were for a long time scarce and partly of poor quality [Holmes et al., 2000, 2001]. To establish a consistent riverine flux estimate of carbon and nutrients for the Arctic, the international Arctic Great Rivers Observatory (ArcticGRO) program (successor of the PARTNERS program) [McClelland et al., 2008] collected in a coordinated effort biogeochemical data in the six largest Arctic rivers and covered the full seasonal cycles of riverine carbon and nutrient fluxes [Holmes et al., 2012; Tank et al., 2012c]. These measurements were extrapolated to obtain pan-Arctic river fluxes of C_T [Tank et al., 2012c], DOC [Manizza et al., 2009; Holmes et al., 2012], and DIN [Tank et al., 2012a; Le Fouest et al., 2013]. The complexity of these extrapolations ranges from a simple areal yields weighted extrapolation [Tank et al., 2012a; Le Fouest et al., 2013; Holmes et al., 2012] over an extrapolation based on catchment properties per region [Tank et al., 2012c] to an extrapolation per river catchment [Manizza et al., 2009]. This extrapolation per river catchment and the creation of a gridded map of riverine fluxes in the Arctic Ocean only exist for DOC. In the absence of a gridded product for nutrient fluxes to the Arctic Ocean, some of the above mentioned model studies estimated the riverine DON flux from pan-Arctic DOC flux estimates assuming a DOC:DON ratio of 50:1 [Tank et al., 2012a] or 40:1 [Le Fouest et al., 2015]. Other ocean modeling studies that include riverine fluxes of DIC, DOC, DIN, DIN, and TDP [Bourgeois et al., 2016; Terhaar et al., 2018] opted for a simulated riverine forcing by land-surface models to force their simulations, such as the Global NEWS2 (GN2) models [Mayorga et al., 2010] or the Global Erosion Model (GEM) [Ludwig et al., 1996].

In this study, we use the ArcticGRO observations to create the first consistent, data-based, monthly, pan-Arctic map of river fluxes, including C_T, DOC, A_C, DIN, DON, TDP, and Si_T. We then use this file to force the ocean biogeochemical model NEMO-PISCES with a high-resolution

configuration to simulate the present-day Arctic Ocean biogeochemistry, including air-sea CO_2 fluxes, ocean acidification, and NPP. To quantify the influence of riverine delivery of carbon and nutrients, we repeated the simulations with zero riverine delivery of carbon and nutrients.

5.2.2 Methods

5.2.2.1 Arctic regions

The Fram Strait, the Barents Sea Opening, the Bering Strait, and the Baffin Bay were defined as the Arctic Ocean boundaries. The Arctic coastal seas were defined as all areas where the bathymetry is shallower than 500 m (Figure 6.1). All areas with a bathymetry above 500 m were defined as the central Arctic Ocean.

5.2.2.2 Pan-Arctic extrapolation of ArcticGRO river flux measurements

We derived a new forcing file of monthly river fluxes of alkalinity (here assumed to represent entirely A_C), C_T and DOC, DIN and DON, TDP, and Si_T. This dataset is consistent with the monthly data of coastal river discharge from Dai and Trenberth [2002]. To do so, the flux estimates from the six big Arctic rivers from the ArcticGRO data set [Holmes et al., 2012; Tank et al., 2012c] were extrapolated to all river watersheds draining to coastal stretches North of 60°N latitude. First, the annual fluxes were spatially extrapolated (Section 5.2.2.3) to assure an optimized estimate with regard to the total annual fluxes. Then, the annual fluxes were redistributed over the seasonal cycle by using an empirical approach (Section 5.2.2.4)

5.2.2.3 Spatial extrapolation of annual fluxes

The delineations of river basins from the STN30p river network data set was used [Vörösmarty et al., 2000]. To identify potential predictors of the average annual fluxes of carbon and nutrients to the coast, a variety of catchment properties from available geodata were calculated (Table 6.2 and Figure 5.2). The first four of the catchment properties listed in Table 6.2 were already used by Tank et al. [2012c] to extrapolate riverine C_T fluxes. In addition, average soil properties and lake cover per river basins were computed as potential predictors for dissolved organic matter and nutrients fluxes [Behrendt and Opitz, 1999; Humborg et al., 2008; Ludwig et al., 1996] (Figure 5.2).

Multiple linear regression was applied to set-up statistical models to extrapolate the annual river fluxes of the different carbon and nutrient species. For each of the carbon and nutrient species, the four predictors which best explain the differences between the six big Arctic rivers, i.e. which gave the lowest root mean squared error (RMSE) between observed and predicted fluxes, were identified (Table 5.2). Like Tank et al. [2012c], a statistical model for C_T fluxes was found based on the Carbonate Index after Dürr et al. [2005], the areal extend of permafrost, the glacial coverage, and the annual runoff. The regression coefficients in this study deviate only slightly

Table 5.1 – Catchment properties used in regressions and their source.

Parameters	Data sources
Carbonate Index for lithology	Dürr et al. [2005]
Areal extend of continuous permafrost	Brown et al. [1997]
Glacial cover	World Glacier Inventory (http://nsidc.org/data/g01130.html)
Annual runoff (for regression equation)	Average observed runoff from ArcticGRO data
Lake cover	Global Lake and wetland data base [Lehner and Döll, 2004]
Topsoil organic carbon content (Topsoil C_{org})	Harmonized World Soil Data base (HWSD)
Topsoil clay content	Nachtergaele et al. [2010]

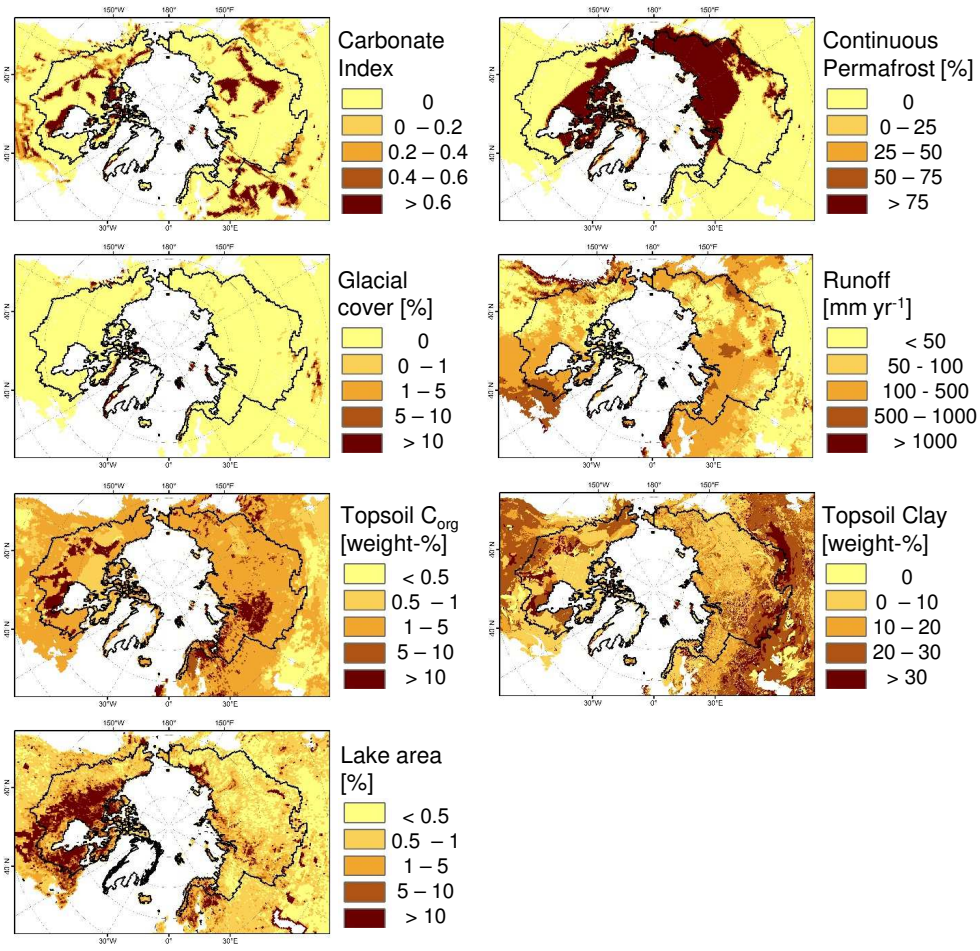

Figure 5.2 – Maps of catchment properties used in regressions.

from those calculated by Tank et al. [2012c], as different delineations of river basins are used in both studies. For A_C, a statistical model with the same set of predictors was fitted.

While observed annual runoff was used to fit the regression, the runoff data set from Fekete et al. [2002] was used to extrapolate C_T and A_C exports to all Boreal to Artic rivers on the Northern Hemisphere. In order to obtain fluvial C_T and A_C fluxes which are consistent with the river dis-

charge used as forcing data [Dai and Trenberth, 2002], C_T concentrations and A_C were calculated by dividing the extrapolated annual fluxes by the annual runoff after Fekete et al. [2002]. These concentrations were then multiplied with the river discharge from Dai and Trenberth [2002].

For DOC and dissolved nutrients, multiple linear regression was used to set up statistical models for the concentrations (Table 5.2). For DOC, DON, DIN, and TDP, the retained predictors were the areal extent of permafrost, the areal proportion of lakes, as well as the average clay and organic carbon contents of the topsoil. Lake cover and permafrost extent had in each case a negative impact, due to the negative effect of permafrost on organic carbon and nutrient leaching, and due to an increased residence time through lakes, which increase the retention and/or loss of carbon and nutrients within the inland water network. Topsoil clay content has a negative effect on DOC, DON and TDP fluxes, which can be explained by the adsorption of organic matter and phosphate on clay minerals [Lauerwald et al., 2012]. For DIN, which is dominated by NO_3, adsorption is not statistically important. In our regression, clay content has a positive effect on DIN fluxes, which may indicate that more organic N is already oxidized in the soils, and thus nitrogen leaches from the soil rather in its inorganic form. Finally, to avoid unreasonable numbers for extrapolated carbon and nutrient concentrations, the maximum and minimum flux weighted annual concentrations from the ArcticGRO-data were imposed on our extrapolation (Table 5.3).

5.2.2.4 Seasonal extrapolation

In a next step, the average monthly fluxes were estimated based on the empirical relationship between the relative seasonal variation in matter fluxes and in river discharge.:

$$F_{monthly} = F_{annual}\ a_1 \left(\frac{Q_{monthly}}{Q_{annual}}\right)^{a_2}, \tag{5.1}$$

with $F_{monthly}$ and F_{annual} being the monthly and annual flux, $Q_{monthly}$ and Q_{annual} being the monthly and annual discharge, and a_1 and a_2 being the fitted parameters (Table 5.4). Only for DIN, the position of each month in the seasonal cycle was used as an additional predictor:

$$F_{monthly} = F_{annual}\ a_1 \left(\frac{Q_{monthly}}{Q_{annual}}\right)^{a_2} b_1\ \sin\left(\frac{b_2 + month}{6}\pi\right), \tag{5.2}$$

with b_1 and b_2 being additional fitting parameters (Table 5.4). For species other than DIN, no statistically significant ($p<0.05$) fit for this part of the equation could be obtained. A negative a_2 indicates a dilution effect, i.e. decreasing concentrations with increasing discharge. This dilution is often observed for inorganic species with high concentrations in the ground water, like A_C and Si_T (Figure 5.3). Conversely, a positive a_2 indicates a flushing effect, i.e. increasing concentrations with discharge. This flushing effect is often observed for dissolved organic matter. To avoid unrealistic A_C to C_T ratios, we derived minimum and maximum observed ratios from the ArcticGRO data and imposed them on our monthly estimates of A_C. The minimum and maximum possible A_C ($\mu eq\ L^{-1}$) to C_T ($\mu mol\ L^{-1}$) ratios were thus defined as 0.24 and 1.07, respectively. Finally, to obtain the best possible forcing data set of fluvial matter fluxes to coastal waters, the monthly

Table 5.2 – Results for the multiple-linear regressions for annual fluxes and concentrations.

Predicted variable	Intercept	Predictors							R^2	RMSE
		Carbonate index [%]	Permafrost [%]	Glacial coverage [%]	Runoff [cm yr^{-1}]	Lake coverage [%]	Topsoil C_{org} [%]	Topsoil Clay [%]		
Inorganic carbon fluxes										
C_T [g C m^{-2} yr^{-1}]	1.513	0.059	-0.014	2.207	0.046	-	-	-	0.92	0.37
A_C [g $CaCO_3$ m^{-2} yr^{-1}]	4.494	0.280	-0.061	8.359	0.221	-	-	-	0.93	1.34
Concentrations of DOC and nutrients										
DOC [mg C L^{-3}]	17.143	-	-0.050	-	-	-1.375	1.142	-0.544	0.92	0.54
DON [µg N L^{-3}]	442.922	-	-1.668	-	-	-34.171	21.609	-11.720	0.88	18.94
DIN [µg N L^{-3}]	65.030	-	-0.869	-	-	-16.840	12.850	3.865	0.96	9.78
TDP [µg P L^{-3}]	19.330	-	-0.211	-	-	-5.941	5.647	-0.171	0.94	2.69
Si_T [mg Si L^{-3}]	3.660	-0.027	-0.009	0.217	-	-0.144	-	-	0.86	0.22

Table 5.3 – Maximum concentration of annual fluxes. All values in mg L^{-1}. A_C is in mg $CaCO_3$ L^{-1}.

Species	Min	Max
C_T	6.82	22.54
A_C	21.0	84.7
DOC	4.36	10.79
DON	0.10	0.29
DIN	0.05	0.22
TDP	0.008	0.046
Si_T	1.84	4.12

Table 5.4 – Parameters for the statistical model of seasonality in fluvial matter fluxes (Eqs. 5.1 & 5.2). The RMSE is unitless like the predicted variables, which give the proportion of the monthly flux relative to the average annual flux.

	a_1	a_2	b_1	b_2	RMSE
C_T	1.074	0.6221	-	-	0.1950
A_C	1.0678	0.8023	-	-	0.2141
DOC	0.79379	1.23824	-	-	0.4301
DON	0.83105	1.18158	-	-	0.4696
DIN	1.02323	0.7842	0.49375	0.67591	0.4356
TDP	0.85018	1.12083	-	-	0.3833
Si_T	1.03644	0.69412	-	-	0.3149

concentrations from the ArcticGRO data were used to calculate monthly fluxes for the six big Arctic rivers. Thus the extrapolated concentrations were only used for the remaining rivers. The final forcing file is provided on a regular 1° grid.

5.2.2.5 Ocean biogeochemical model NEMO-PISCES

To analyze the effect of the riverine delivery of carbon and nutrients on the Arctic Ocean biogeochemistry, we used the version 3.2 of the ocean modeling framework 'Nucleus for European Modelling of the Ocean' (NEMO). This framework includes the ocean dynamics part OPA [Madec, 2008], the version 2 of the Louvain-La-Neuve sea Ice Model LIM [Fichefet and Maqueda, 1997], and the 'Tracers in the Ocean Paradigm (TOP)' that models the oceanic tracer transport. TOP allows the coupling of NEMO to the 'Pelagic Interaction Scheme for Carbon and Ecosystem Studies' (PISCES) biogeochemical model [Aumont and Bopp, 2006].

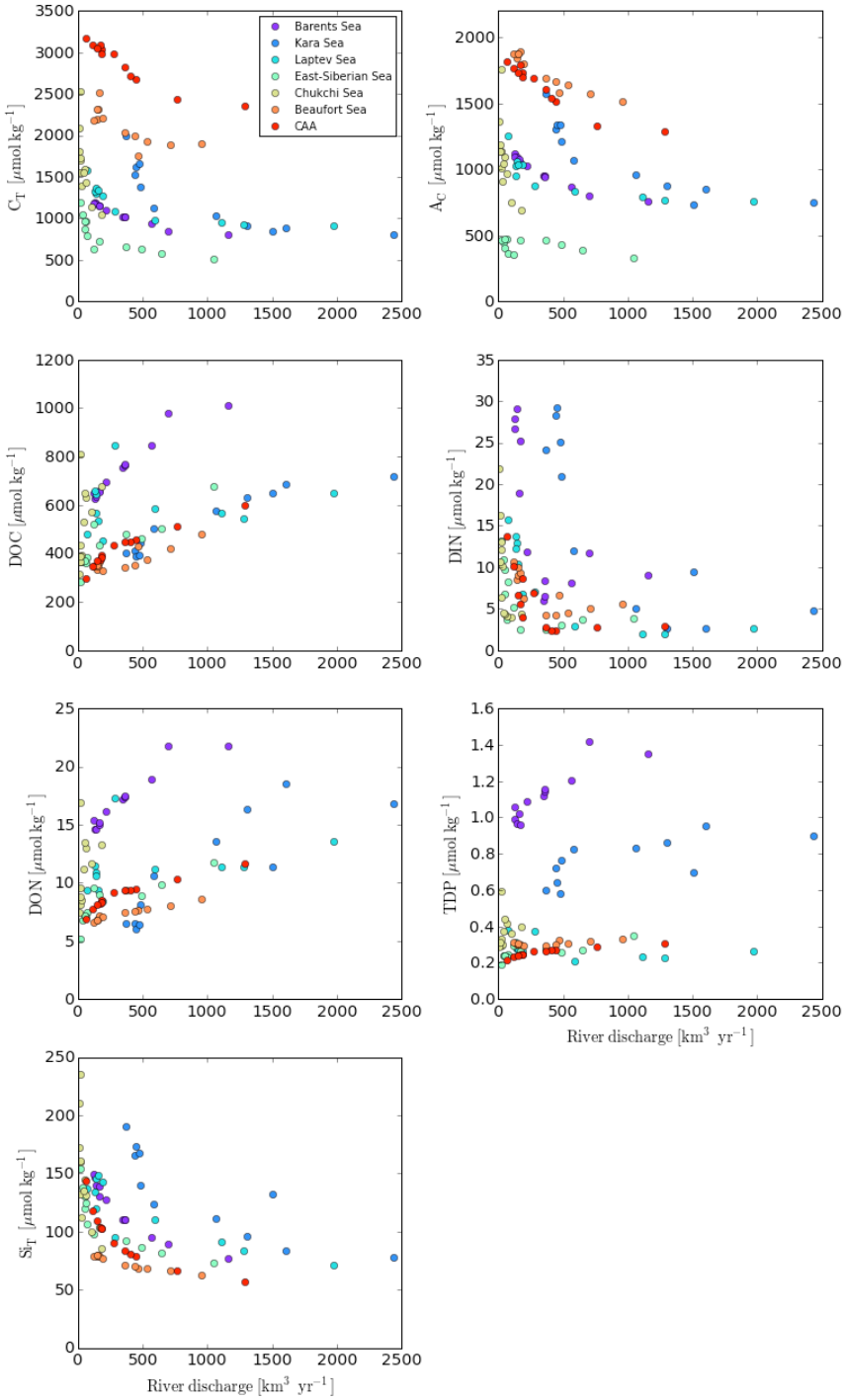

Figure 5.3 – Monthly riverine carbon and nutrient concentrations [µmol kg^{-1}] in dependence of the corresponding monthly river discharge [km^3 yr^{-1}] per regional sea (Figure 6.1).

The model was used with the eddy admitting DRAKKAR configuration ORCA025 [Barnier et al., 2006a]. The configuration has a tripolar, curvilinear horizontal grid with a nominal resolution of 0.25°. While one pole is located on the geographical South Pole over Antarctica, the two remaining poles in the Northern hemisphere are located on land in Northern America and Russia to avoid a computationally expensive singularity at the geographical North pole [Madec et al., 1998]. Consequently the regular Mercator grid is distorted into ellipses north of 20°N. This distortion decreases

the average horizontal gird length to 14 km in the Arctic Ocean. Vertically, the ocean was divided into 46 depth levels with increasing thickness from 6 m at the surface to 500 m at the deepest grid cell. The model bathymetry was calculated from the satellite-data derived ETOPO2 bathymetry [Smith and Sandwell, 1997]. In the Arctic Ocean, the IBACO bathymetry based on measurements from boats and submarines was used [Jakobsson et al., 2000a]. To best match the bathymetry on the model grid, NEMO uses the partial steps approach. In this approach the thickness of the deepest model grid cell is chosen to match the observed bathymetry. The applied lateral isopycnal diffusion coefficient is 300 $m^2\ s^{-1}$ and the viscosity coefficient is $-1.5 \times 10^{11}\ m^2 s^{-1}$.

The biogeochemical model PISCES [Aumont and Bopp, 2006] simulates the cycles of C_T, DOC, A_T, oxygen, nitrate (NO_3), ammonium (NH_4), dissolved inorganic phosphate (P_T), Si_T, and Iron (Fe). At the ocean surface, carbon in the form of CO_2 and oxygen are exchanged with the atmosphere via air-sea gas exchange following Wanninkhof [1992]. In addition to carbon and nutrients, four living pools are simulated: nanophytoplankton and diatoms, and microzooplankton and mesozooplankton. The phytoplankton growth depends on temperature and is limited by light and nutrient availabiliy. Diatoms differ from nanophytoplankton only in their additional need of Si. While the Redfield ratio of C:N:P of 122:16:1 [Takahashi et al., 1985] is prescribed in all living and non-living compartments of PISCES, the Fe:C and Chlorophyll(Chl):C and the Si:C ratio (only for diatoms) are prognostically calculated depending on the light availability and the external concentration of the available nutrients. In addition to the living compartments, PISCES simulates three non-living compartments: semilabile dissolved organic matter (DOM), and small and big sinking organic particles. Similar to the living compartments, the C:N:P ratio is fixed in the non-living compartments (122:16:1), while the iron, silicon and calcite pools are explicitly calculated. The composition of the particles does not affect their sinking velocity.

The nutrients are externally supplied by atmospheric dust deposition, sediment mobilization, and river fluxes. The iron deposition from the atmosphere was calculated from Tegen and Fung [1995] and the iron sediment mobilization was calculated from Moore et al. [2004]. South of 60°N, the riverine fluxes for nutrients and DOC are based on the GN2 model [Mayorga et al., 2010] and the C_T fluxes are calculated by the General Erosion model from Ludwig et al. [1996]. North of 60°N, the riverine fluxes were calculated from the newly generated forcing file based on ArcticGRO observations (Section 5.2.2.2). The fluxes from the regular 1° grid were extrapolated on the curvelinear model grid. To do so, each model grid cell was assigned to its nearest grid cell on the 1° grid. The flux from the 1° grid was then divided between the assigned model grid cells in proportion to the runoff in each cell. This approach ensures the conservation of mass of the calculated fluxes and correlates runoff with carbon and nutrient fluxes. For each horizontal grid cell, the river input was divided on the first two vertical grid levels (0–13 m) to account for a finite depth of rivers.

When using the riverine input for PISCES in the Arctic Ocean, three caveats exist. First, the forcing file contains A_C (based on Tank et al. [2012c]), while PISCES simulates A_T. Tank et al. [2012c] calculated A_C by subtracting organic acids from their A_T measurements. Tank et al.'s def-

inition of A_C thus still includes the contribution of P_T and Si_T and is neither pure A_C nor pure A_T. In PISCES A_T does not include organic acids either. Therefore the definition of A_C by Tank et al. [2012c] corresponds to the definition of A_T in PISCES. Second, the standard version of PISCES does not explicitly simulate DOC, DON, and DOP separately. Instead, DON and DOP are implicitly simulated as part of the explicitly simulated semi-labile DOC pool assuming a stiochiometric C:N:P ratio of 122:16:1. In rivers the stiochiometric C:N ratio is 747:16. Thus, if the riverine DOC flux was added to the marine DOC, the other components of marine DOM would be artificially increased. If on the other hand river DOC flux would be added entirely to marine C_T assuming 100% lability, C_T close to river mouths would be overestimate and induce outgassing artificially. PISCES thus does not allow for an ideal solution. Here, we have chosen to conserve the absolute amount of nutrients, e.g. not to add riverine DOC to the marine DOM tracer. Instead, half of the riverine DOC flux was added to marine C_T, assuming it be very labile [Letscher et al., 2011; Kaiser et al., 2017]. The other half of the riverine DOC flux was discarded, assuming it to be refractory. Discarding half of riverine DOC leads to an underestimation of marine DOC, but allows for a correct representation of marine nutrients and C_T. To conserve the total amount of nutrients,all riverine delivery of organic nutrients was added to PISCES as inorganic nutrients, assuming them to be extremely labile. However, observations suggest that 62–76% of DON is transformed to DIN on the Arctic Ocean shelves within months [Thibodeau et al., 2017; Letscher et al., 2013]. Thus, we overestimated marine inorganic nitrogen, the limiting nutrient, on the Arctic shelves by 24–38%, although it is likely that some of this DON is remineralized while still being inside the Arctic Ocean.

5.2.2.6 Simulation strategy

In this study, we ran two global simulations with the NEMO-PISCES model from 1990 to 2010: (1) one with the newly derived forcing dataset for riverine carbon and nutrient fluxes, (2) and a second one with zero riverine carbon and nutrient fluxes. Apart from the river fluxes, these simulation are identical to the ORCA025 simulations used by Terhaar et al. [2018]. In brief, the simulations were forced with the DRAKKAR forcing sets 4.2 (DFS4.2) from 1990 to 2002 and with DFS4.4 from 2003 to 2010 [Brodeau et al., 2010]. The two datasets provide historical reanalysis data for surface air temperature and humidity at 2 m, wind fields at 10 m, shortwave and longwave radiation, and the net surface freshwater flux (evaporation minus precipitation). The river discharge is taken from Dai and Trenberth [2002]. The historic atmospheric CO_2 levels are taken from [Le Quéré et al., 2015]. The physical and biogeochemical fields were initialized in 1990 with the the simulated fields from Terhaar et al. [2018]. As opposed to the new monthly riverine forcing set used in this study, Terhaar et al. [2018] used yearly riverine carbon fluxes simulated by the GEM model and yearly nutrient fluxes derived from the GEM carbon fluxes assuming stochiometric C:N:P:Si ratios [Aumont and Bopp, 2006]. These yearly fluxes were equally divided between the 12 months of the year and thus do not capture the strong seasonality of Arctic rivers. The change in riverine forcing

from 1989 to 1990 results in a transition period of the state of the Arctic Ocean biogeochemistry over multiple years.

The ORCA025 configuration is capable of reproducing the observed water fluxes through the four passages, which connect the Arctic Ocean to the global ocean [Terhaar et al., 2018]. The good representation of these fluxes is essential for the Arctic Ocean biogeochemistry, as a large part of nutrients [Torres-Valdés et al., 2013] is provided by lateral influx from the Atlantic and Pacific.

5.2.2.7 Ω_A

Ω_A was calculated offline using the 'Routines to model the ocean carbonate system 2.0' (mocsy 2.0) [Orr and Epitalon, 2015] based on simulated temperature, salinity, C_T, A_T, P_T, and Si_T. The dissolution and dissociation constants from Lueker et al. [2000] and Dickson and Riley [1979] were used, respectively.

5.2.2.8 Observational data

The model output was compared to different data sources. For carbon and nutrient concentrations in the ocean, the discrete [Olsen et al., 2016] and gridded [Lauvset et al., 2016] version of the Global Ocean Data Analysis Project version 2 (GLODAPv2) were used. The GLODAPv2 dataset was further used to calculate the data-based Ω_A. NPP was compared to estimates derived from remotely sensed ocean color from SeaWiFS and MODIS [Arrigo and van Dijken, 2011, 2015]. Air-sea CO_2 fluxes were compared to Bates and Mathis [2009] and sources within.

5.2.3 Results

5.2.3.1 Pan-Arctic extrapolation of ArcticGRO river flux measurements

The extrapolated average annual riverine fluxes of C_T, A_C, DOC, DIN, DON, TDP, and Si_T are presented for the total Arctic Ocean and each regional sea separately (Table 5.5). The regional seas, which receive the largest Arctic rivers, are the Kara Sea, the Beaufort Sea, and the Laptev Sea. Together, these coastal seas receive 63–72% of all riverine fluxes in the Arctic Ocean. The regional seas with smaller rivers, the Barents Sea, the East-Siberian Sea, and the Chukchi Sea, receive 14–27% of all Arctic riverine fluxes. The remaining 5–23% drain into the CAA, with nutrient and DOC fluxes at the lower end (5–9%) and C_T and A_C fluxes at the higher end (16–23%).

Riverine fluxes into the Arctic Ocean have a strong seasonal variability driven by low discharge in winter when large parts of the rivers are frozen and high discharge in summer (Table 5.6). For all riverine fluxes, the peak flux is found in June associated to the peak in river discharge. Dependent on the flux component, the amplitude of the seasonality changes. Fluxes of dissolved inorganic species (C_T, A_C, DIN, and Si_T) have has the lowest amplitude with its peak fluxes being 3–7 times larger than the minimum fluxes in winter. Conversely the peak fluxes of dissolved organic matter

Table 5.5 – Regional annual riverine fluxes into the Arctic Ocean in Tg yr^{-1} and the associated river discharge in km^3 yr^{-1}.

	C_T	A_C	DOC	DON	DIN	TDP	Si_T	Discharge
Total	50.6	39.6	27.6	0.67	0.32	0.064	8.8	3519
Barents	4.2	3.9	3.8	0.10	0.06	0.014	1.1	368
Kara	13.9	12.5	10.8	0.27	0.15	0.033	3.7	1296
Laptev	9.4	7.7	7.1	0.17	0.04	0.008	1.8	816
East-Siberian Sea	1.9	1.2	1.7	0.04	0.01	0.002	0.6	260
Chukchi Sea	0.8	0.5	0.3	0.01	0.00	0.001	0.2	47
Beaufort Sea	8.7	7.2	1.8	0.04	0.03	0.004	0.7	366
CAA	11.6	6.5	2.1	0.05	0.02	0.003	0.8	366

(DOC and DON) are 24–26 time larger than the winter minimum fluxes. TDP flux combines inorganic and organic P and is found to have a seasonal amplitude in between the ones of inorganic and organic dissolved species (14 times larger). These strongly diverging ratios of summer and winter fluxes are caused by a different dependence of inorganic and organic species on discharge (Figure 5.3). Inorganic species are diluted when river discharge is highest, e.g. concentrations in rivers are lowest when river discharge is largest, whereas organic dissolved compounds experience a flushing effect, e.g. concentrations in rivers are highest when river discharge is largest.

While the dilution and flushing effects are consistent across all Arctic Ocean regions, concentrations of riverine nutrients and carbon exhibit regional differences (Figure 5.3). Concentrations of C_T and A_C are up to 2 times larger in North American rivers then in Eurasian rivers, while DIN, DON, TDP, and Si_T concentrations are largest in rivers that drain into the Barents and Kara Seas (Figure 5.3). These regional differences in concentrations cause regional differences in the flux ratios between different compartments. For example, the ratio of DOC and C_T fluxes in North American rivers is 0.11–0.24, while it is four to seven times higher in Eurasian rivers (0.80–0.82) (Table 5.5). Similarly, the ratio of A_C and C_T fluxes varies regionally from 0.56 in the CAA, over 0.63–0.67 in the Chukchi and East-Siberian Seas, over 0.82–0.83 in the Beaufort and Laptev Seas, to 0.90–0.93 in the Barents and Kara Seas (Figure 5.4).

5.2.3.2 Dissolved carbon and nutrient concentrations

First, the adjustment period from the old river fluxes (GEM) to the newly derived riverine fluxes is estimated based on the regional surface concentrations of C_T and DIN, the limiting nutrient, in the different regional Arctic seas (Figure 5.5). Based on these time-series, a new equilibrium is identified in all regions after ~15 years. Consequently, the 6-year period from 2005 to 2010 was

Table 5.6 – Extrapolated riverine fluxes into the Arctic Ocean in Tg yr^{-1} and the river discharge in km^3 yr^{-1}.

	C_T	A_C	DOC	DON	DIN	TDP	Si_T	Discharge
Yearly	50.6	39.6	27.6	0.67	0.32	0.064	8.8	3519
January	20.9	16.4	5.5	0.12	0.29	0.018	4.1	1018
February	24.7	18.4	6.0	0.13	0.32	0.018	4.3	1129
March	29.8	21.2	7.0	0.16	0.31	0.019	4.6	1311
April	17.8	13.9	3.9	0.09	0.22	0.013	3.4	769
May	43.6	36.2	26.8	0.61	0.41	0.074	9.9	3252
June	150.9	115.5	132.8	3.12	0.91	0.252	25.4	13216
July	95.9	75.2	54.9	1.39	0.42	0.125	15.2	7192
August	67.0	53.9	32.7	0.89	0.20	0.082	11.2	4764
September	58.9	47.3	27.2	0.72	0.17	0.067	10.4	4034
October	47.8	38.0	19.4	0.50	0.19	0.052	8.5	2944
November	26.3	21.0	8.3	0.21	0.18	0.028	4.8	1442
December	23.2	17.9	6.4	0.15	0.25	0.021	4.2	1160

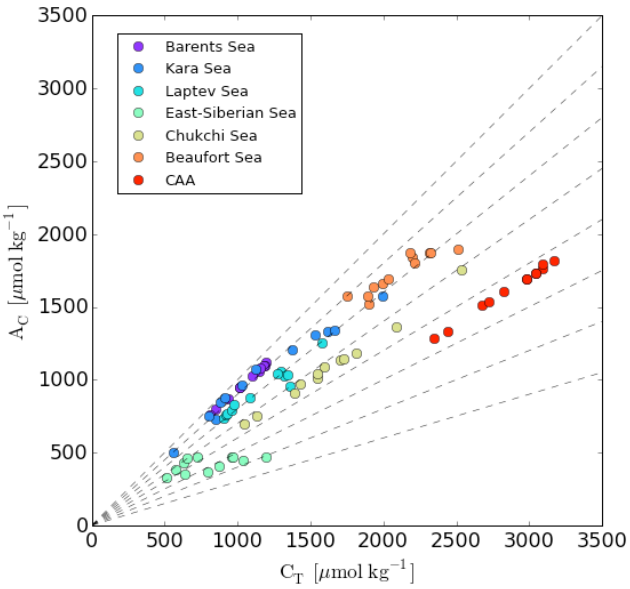

Figure 5.4 – Monthly riverine A_C [µmol kg^{-1}] in dependence of monthly riverine C_T [µmol kg^{-1}] per regional sea (Figure 6.1). The dashed black lines indicate A_C:C_T ratios from 0.3 to 1.0.

used in this work as the period during which the impact of the new riverine forcing file on the Arctic Ocean biogeochemistry was analyzed.

The resulting regional surface concentrations of carbon and nutrients using the ArcticGRO river forcing file are presented in Table 5.7. The average surface C_T concentration in the Arctic Ocean is 2012 µmol kg^{-1}. Regionally, surface ocean C_T is largest in the Barents Sea, Chukchi Sea,

Beaufort Sea, and CAA (2052–2059 µmol kg^{-1}) and smallest in the Kara Sea and Laptev Sea (1887–1904 µmol kg^{-1}). Similar to C_T, A_T is smallest in the Kara and Laptev Seas and larger in the other regions. On average A_T is 113 µmol kg^{-1} smaller than C_T. This difference is largest in the Barents Sea (144 µmol kg^{-1}) and smallest in the Laptev Sea (57 µmol kg^{-1}).

For semi-labile DOC and nutrients, a clear gradient between the coastal zones and the central Arctic Ocean exists (Table 5.7). In all coastal seas, concentrations of semi-labile DOC are 15–54% above the Arctic Ocean semi-labile DOC average concentration of 9.5 µmol C kg^{-1}. Among the coastal regions, highest semi-labile DOC concentrations are found in the Beaufort Sea (14.6 µmol C kg^{-1}) and the Laptev Sea (13.1 µmol C kg^{-1}). In addition to this coastal-open ocean gradient, nutrient concentrations also exhibit a west-east gradient of nutrients across the Arctic Ocean with highest concentrations on the North American side and lowest concentrations on the Eurasian side (Figure 5.6).

Simulated carbon and nutrient surface ocean concentrations are found to have strong sea-

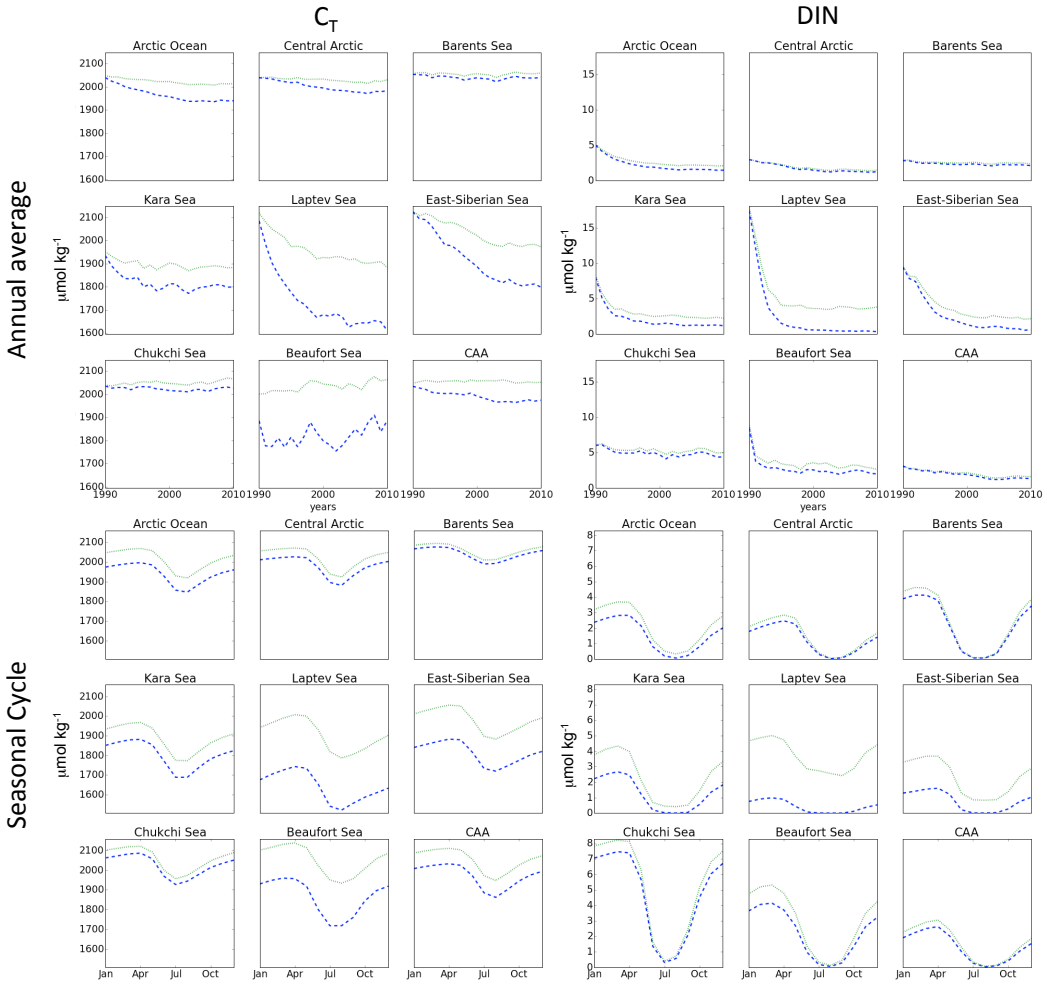

Figure 5.5 – Annual time-series from 1990 to 2010 (top) and the average seasonal cycle from 2005 to 2010 (bottom) of concentrations of C_T (left) and DIN (right) for the surface of the Arctic Ocean and its regional seas. Concentrations for the simulation with the new riverine forcing set (green) and the simulation without riverine input of carbon and nutrients (blue) are shown.

Table 5.7 – Upper part: average surface ocean concentrations of carbon, alkalinity, and nutrients the Arctic Ocean and its regional seas from 2005 to 2010. All values are in µmol kg^{-1}. Simulated values are compared to the gridded GLODAPv2 dataset [Lauvset et al., 2016]. Lower part: Depth-integrated NPP in g C m^{-2} yr^{-1} and Tg C yr^{-1}, air-to-sea CO_2 flux in g C m^{-2} yr^{-1} and Tg C yr^{-1}, and surface ocean Ω_A from 2005 to 2010.

	Arctic Ocean	Central Arctic	Barents Sea	Kara Sea	Laptev Sea	East-Siberian Sea	Chukchi Sea	Beaufort Sea	CAA
C_T									
ArcticGRO	2012	2023	2059	1887	1904	1981	2058	2052	2052
No rivers	1940	1978	2041	1803	1641	1812	2023	1864	1971
GLODAPv2[a]	2009								
A_T									
ArcticGRO	2125	2145	2203	1977	1961	2054	2178	2140	2163
No rivers	2051	2097	2183	1890	1695	1879	2143	1961	2090
GLODAPv2[a]	2089								
DOC (semi-labile)									
ArcticGRO	9.5	7.6	10.9	11.0	13.1	11.0	12.1	14.6	9.2
No rivers	9.3	7.7	10.7	10.1	11.8	10.9	12.3	12.3	8.7
DIN									
ArcticGRO	2.1	1.5	2.5	2.3	3.7	2.3	5.3	3.0	1.6
No rivers	1.5	1.3	2.2	1.3	0.4	0.8	4.7	2.2	1.3
GLODAPv2[a]	1.9								
P_T									
ArcticGRO	0.3	0.3	0.3	0.2	0.1	0.1	0.6	0.4	0.3
No rivers	0.3	0.3	0.2	0.2	0.1	0.2	0.6	0.4	0.3
GLODAPv2[a]	0.5								
Si_T									
ArcticGRO	6.3	3.7	3.2	8.9	20.5	13.0	8.7	9.1	4.6
No rivers	3.0	2.8	2.2	2.3	1.9	3.0	7.1	4.3	3.1
GLODAPv2[a]	6.3								
NPP [g C m^{-2} yr^{-1}]									
ArcticGRO	28.0	12.0	56.6	34.6	21.6	23.5	83.5	56.5	22.2
No rivers	23.0	11.2	48.8	21.2	7.6	13.9	78.3	41.0	19.9
NPP [Tg C yr^{-1}]									
ArcticGRO	296	54	85	31	12	23	52	7	28
No rivers	239	51	73	19	4	13	48	5	25
Arrigo and van Dijken [2015][b]	382	-	127	67	52	39	32	34	31
Air-Sea CO_2 flux [g C m^{-2} yr^{-1}]									
ArcticGRO	7.5	3.5	30.8	6.0	-4.6	1.5	11.7	1.3	2.9
No rivers	9.0	3.6	32.1	9.2	4.8	2.8	13.0	15.4	5.0
Air-Sea CO_2 flux [Tg C yr^{-1}]									
ArcticGRO	77.4	15.8	46.2	5.4	-2.5	1.5	7.2	0.2	3.7
No rivers	93.8	16.0	48.2	8.3	2.6	2.6	8.1	1.8	6.3
Bates and Mathis [2009]	65–199	6–19	44–77	1–6	1–4	-0.3–13	11–53	2–3	16–24
Surface Ω_A									
ArcticGRO	1.3	1.4	1.5	1.1	0.8	1.0	1.4	1.1	1.3
No rivers	1.2	1.3	1.5	1.0	0.7	0.9	1.3	1.1	1.3

[a] The gridded GLODAPv2 product is biased towards summer observations, when C_T and A_T are blow the annual average and nutrients are above their annual average.
[b] Averaged from 1998–2012

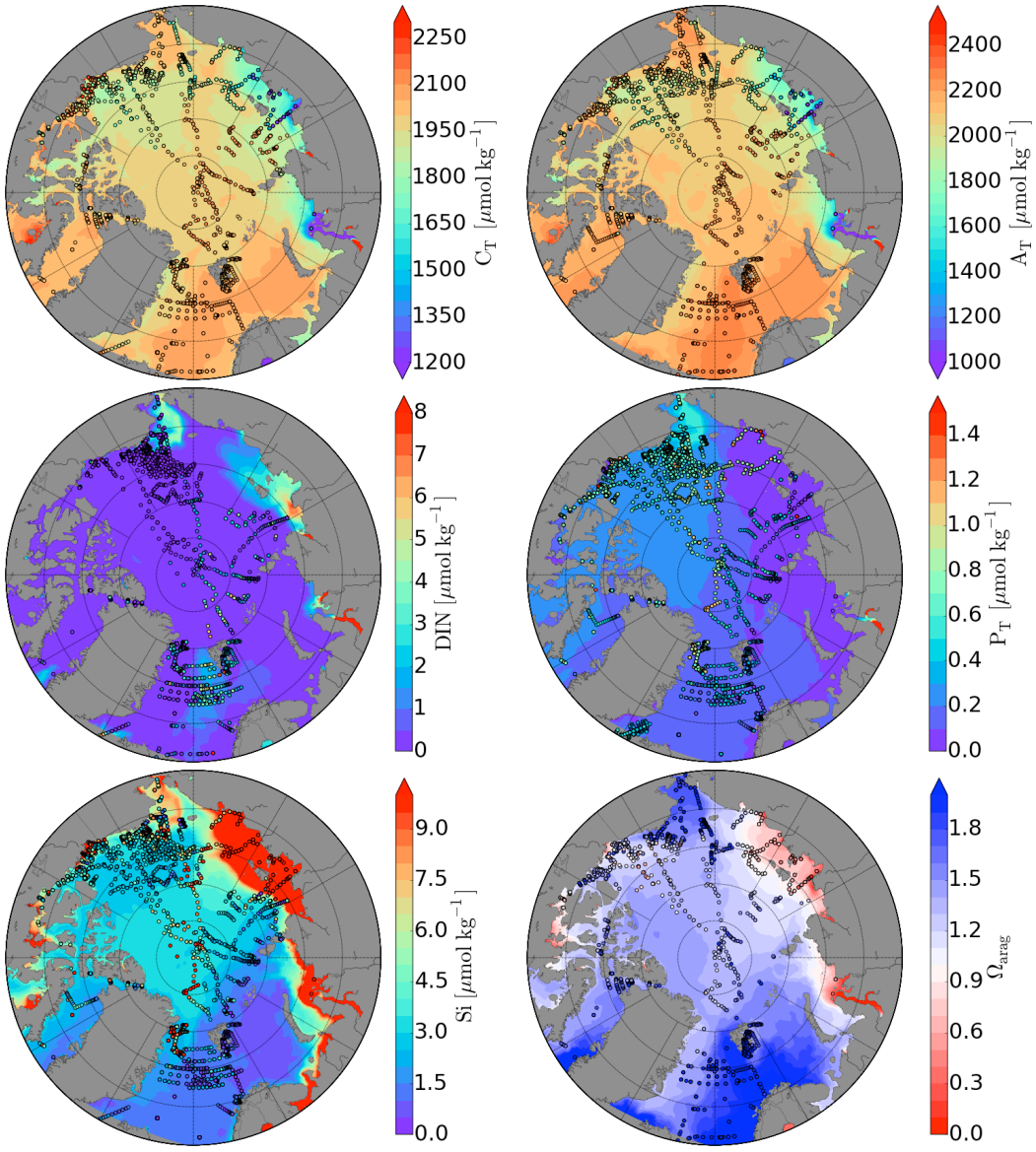

Figure 5.6 – Summer (August-September) averaged C_T, A_T, DIN, P_T, Si_T, and Ω_A (from top left to bottom right) from 2005 to 2010. NEMO-PISCES results are shown as the colored background and discrete surface measurements from GLODAPv2 [Olsen et al., 2016] are shown as points.

sonal cycles in the Arctic Ocean and its shelf seas (Figure 5.5). As N is the limiting nutrient in the Arctic Ocean [Tremblay et al., 2015], we only show the C_T and DIN cycle. Both, C_T and DIN, are reduced during summer and increase in winter. On average, surface Arctic C_T varies seasonally by 150 µmol kg^{-1}, from 1918 µmol kg^{-1} in August to 2068 µmol kg^{-1} in April. Regionally the seasonal amplitude rises to 221 µmol kg^{-1} in the Laptev Sea or decreases to 85 µmol kg^{-1} in the Barents Sea.

As opposed to C_T, the relative strength of the seasonal cycle of surface DIN is larger, with the pan-Arctic average surface concentration in April (3.7 µmol kg^{-1}) being 12 times larger than the summer concentration (0.3 µmol kg^{-1}). Regionally, the largest absolute seasonal amplitude is found in the Barents Sea (0.1–4.6 µmol kg^{-1}), Kara Sea (0.4–4.3 µmol kg^{-1}), the Chukchi Sea (0.7–

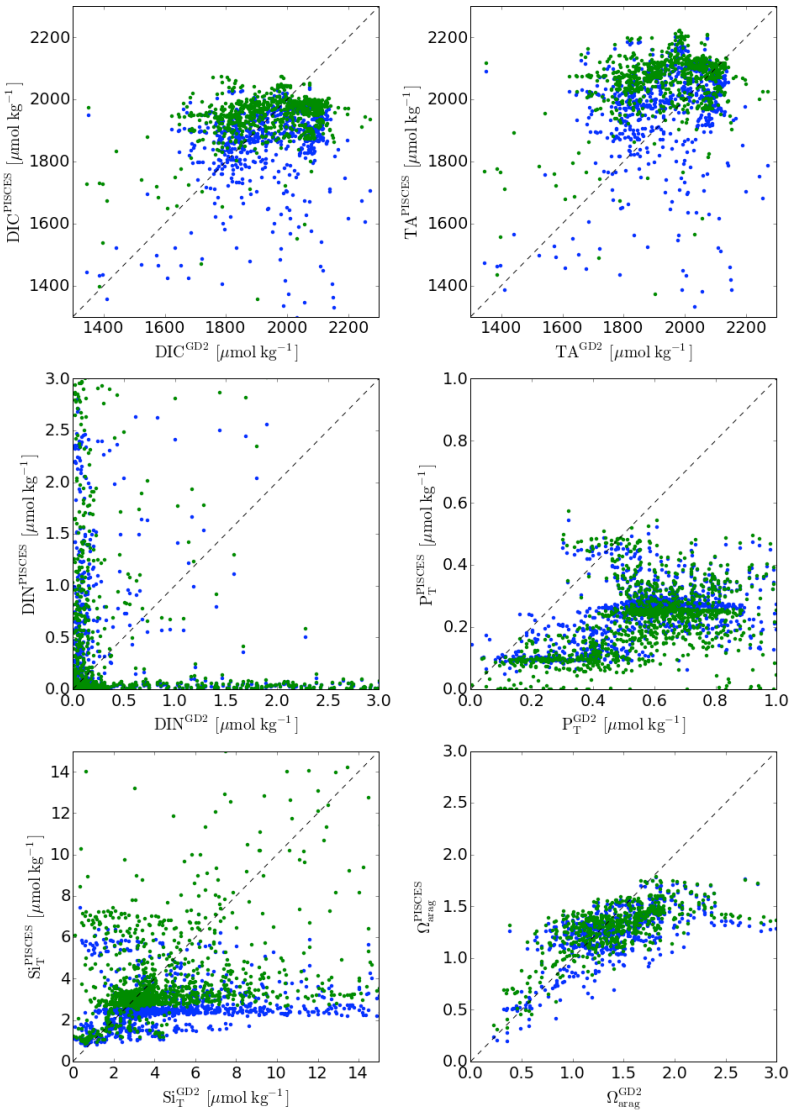

Figure 5.7 – Summer (August-September) averaged surface C_T, A_T, DIN, P_T, Si_T, and Ω_A (from top left to bottom right) from 2005 to 2010. NEMO-PISCES results with ArcticGRO river fluxes (green) and without river fluxes (blue) are plotted against discrete surface measurements from GLODAPv2 [Olsen et al., 2016] at the same location.

8.2 µmol kg^{-1}), and the Beaufort Sea (0.1–5.3 µmol kg^{-1}), whereas the smallest seasonal amplitude is found in the Laptev Sea (2.4–5.0 µmol kg^{-1}), the central Arctic (0.0–2.6 µmol kg^{-1}), and the CAA (0.1–3.1 µmol kg^{-1}).

The simulated surface concentrations were compared to measurements from the GLODAPv2 dataset [Lauvset et al., 2016] (Table 5.7, Figures 5.6 and 5.7). Given the spatially heterogeneous data coverage in the Arctic Ocean (Figure 5.6), the gridded product was used to calculate Arctic Ocean averages. Simulated and data-based average concentrations for C_T and A_T agree within 36 µmol kg^{-1} (2%), while simulated surface basinwide average DIN is 0.2 µmol kg^{-1} (11%) larger than observed DIN, simulated urface basinwide average P_T is 0.2 µmol kg^{-1} (40%) smaller than observed P_T, and simulated urface basinwide average Si_T is equal to observed Si_T.

Table 5.8 – RMSE for simulated surface ocean carbon and nutrient concentrations in comparison to observations from GLODAPv2. All values are in μmol kg^{-1}.

	ArcticGRO	No river fluxes
C_T	142	194
A_C	140	159
DIN	1.7	1.6
P_T	0.4	0.4
Si_T	4.2	6.2
Ω_A	0.4	0.4

Regionally, the model results were compared to the discrete GLODAPv2 data [Olsen et al., 2016] (Figures 5.6 and 5.7). Simulated surface patterns for both, C_T and A_T, are comparable to observations, with largest concentrations in the Northern Seas, smaller concentrations in the Beaufort Gyre, and the lowest concentrations on the Siberian shelf. Despite the large scale agreement, low simulated C_T and A_T in the Laptev Sea don't extend as far off the coast as observed concentrations do.

As opposed to C_T and A_T, regional patterns of simulated and observed surface nutrients show larger differences (Figure 5.6). While both simulated and observed DIN are depleted almost everywhere in the Arctic Ocean, the regions with finite concentrations of DIN are not the same in the model and the observations. For example, simulated surface DIN in the Bering Strait is ~5 μmol kg^{-1}, whereas observations show DIN close to zero. Opposite, simulated DIN in waters in the Fram Strait and the Barents Sea Opening are between 0 and 1.5 μmol kg^{-1}, while observed DIN is found at larger concentrations of 1–7 μmol kg^{-1}. In the central Arctic Ocean, simulated DIN is always depleted, while finite DIN concentrations were observed north of the Laptev and the Barents Sea. In the coastal seas, simulated DIN is largest with concentrations above 8 μmol kg^{-1} at the river mouths of the Lena and the Ob. In these regions, almost no observations of DIN exist. These regional differences lead to a relatively large RMSE for DIN of 1.7 μmol kg^{-1} (~80% of mean concentration) (Table 5.8).

In contrast to simulated DIN, simulated P_T is often close to zero, but almost nowhere completely depleted (Figures 5.6 and 5.7). On average, simulated P_T is found 40% below observed P_T and has a RMSE of 0.4 μmol kg^{-1} (133% of average P_T) (Table 5.8). Higher concentrations of P_T are simulated in the North American side of the Arctic Ocean and lower concentrations on the Eurasian side is reproduced in the simulations. Regionally, largest differences between simulated and observed P_T exist in the East-Siberian Sea, where simulated P_T are well below observed P_T.

Simulated basinwide average Si_T concentrations agree with the observed concentrations (Table 5.7), but a large RMSE of 4.2 μmol kg^{-1} (67%) exists. The large RMSE is mainly caused by strong

underestimation of Si_T in the Central Arctic Ocean (Figure 5.6). Apart from this underestimation, patterns of simulated and observed Si_T generally agree.

Pan-Arctic surface ocean carbon and nutrient concentrations are generally in better agreement with observations when riverine fluxes are included than without river fluxes (Table 5.7 and 5.8). Especially in the coastal areas, surface ocean carbon and nutrient concentrations decrease when the riverine fluxes in PISCES are set to zero (Table 5.7, Figures 5.5 and 5.7). Without river fluxes, the average annual Arctic Ocean C_T concentration drops by 4% from 2012 μmol kg^{-1} to 1940 μmol kg^{-1}. This average Arctic Ocean change is principally driven by C_T decreases in the Laptev Sea by 266 μmol kg^{-1} (14%), in the East-Siberian Sea by 175 μmol kg^{-1} (9%), and in the Beaufort Sea by 179 μmol kg^{-1} (8%).

More than C_T, the average annual Arctic Ocean DIN concentration drops without riverine fluxes by 29% from 2.1 μmol kg^{-1} to 1.5 μmol kg^{-1}. This decrease in average Arctic Ocean DIN is mainly caused by the decrease of DIN in the Siberian shelf seas: 1.0 μmol kg^{-1} (57%) in the Kara Sea, 3.3 μmol kg^{-1} (89%) in the Laptev Sea, and 1.5 μmol kg^{-1} (65%) in the East-Siberian Sea. Reduction of P_T and Si_T concentrations resemble those of DIN (Table 5.7). Only Si_T in the Beaufort Sea stands out, which decreases by 4.8 μmol kg^{-1} (53%), relatively more than the decreases in DIN (27%) and P_T (0%).

Seasonally, reductions in C_T without riverine fluxes are almost constant (Figure 5.5), while reductions of DIN are larger in winter than in summer. Consequently the amplitude of the seasonal DIN cycle decreases by 28% (0.8 μmol kg^{-1}) without riverine fluxes. The attenuation of the seasonal DIN cycle is largest on the Siberian shelf, with 31% (1.2 μmol kg^{-1}) in the Kara Sea, 62% (1.6 μmol kg^{-1}) in the Laptev Sea, and 45% (1.3 μmol kg^{-1}) in the East-Siberian Sea. In these three Siberian shelves, surface DIN is also entirely depleted during summer with zero river fluxes and never depleted when riverine fluxes are included.

5.2.3.3 Net Primary Production

The simulated depth-integrated basinwide annual NPP in the Arctic Ocean averaged over 2005–2010 is 296 Tg C yr^{-1} (Table 5.7). Around 19% of this NPP occurs in the Barents Sea alone. Among the other regions, NPP varies from 23 to 54 Tg C yr^{-1}, with the Beaufort Sea (7 Tg C yr^{-1}) and the Laptev Sea (7 Tg C yr^{-1}) being the exception to this rule. The area-normalized NPP is highest in the Barents Sea (57 g C m^{-2} yr^{-1}), the Chukchi Sea (84 g C m^{-2} yr^{-1}), and the Beaufort Sea (57 g C m^{-2} yr^{-1}) and lowest in the Central Arctic (12.0 g C m^{-2} yr^{-1}).

A strong seasonal cycle of NPP is simulated in the Arctic Ocean (Figure 5.8) with average Arctic NPP being zero in winter and maximal in July with 73 g C m^{-2} yr^{-1}. The highest NPP peak rates are simulated in the Barents Sea (154 g C m^{-2} yr^{-1}), the Chukchi Sea (242 g C m^{-2} yr^{-1}), and the Beaufort Sea (140 g C m^{-2} yr^{-1}). The remaining regional seas have NPP peak rates between 47 and 81 g C m^{-2} yr^{-1}). Depending on the region, the timing of the peak in NPP varies between between

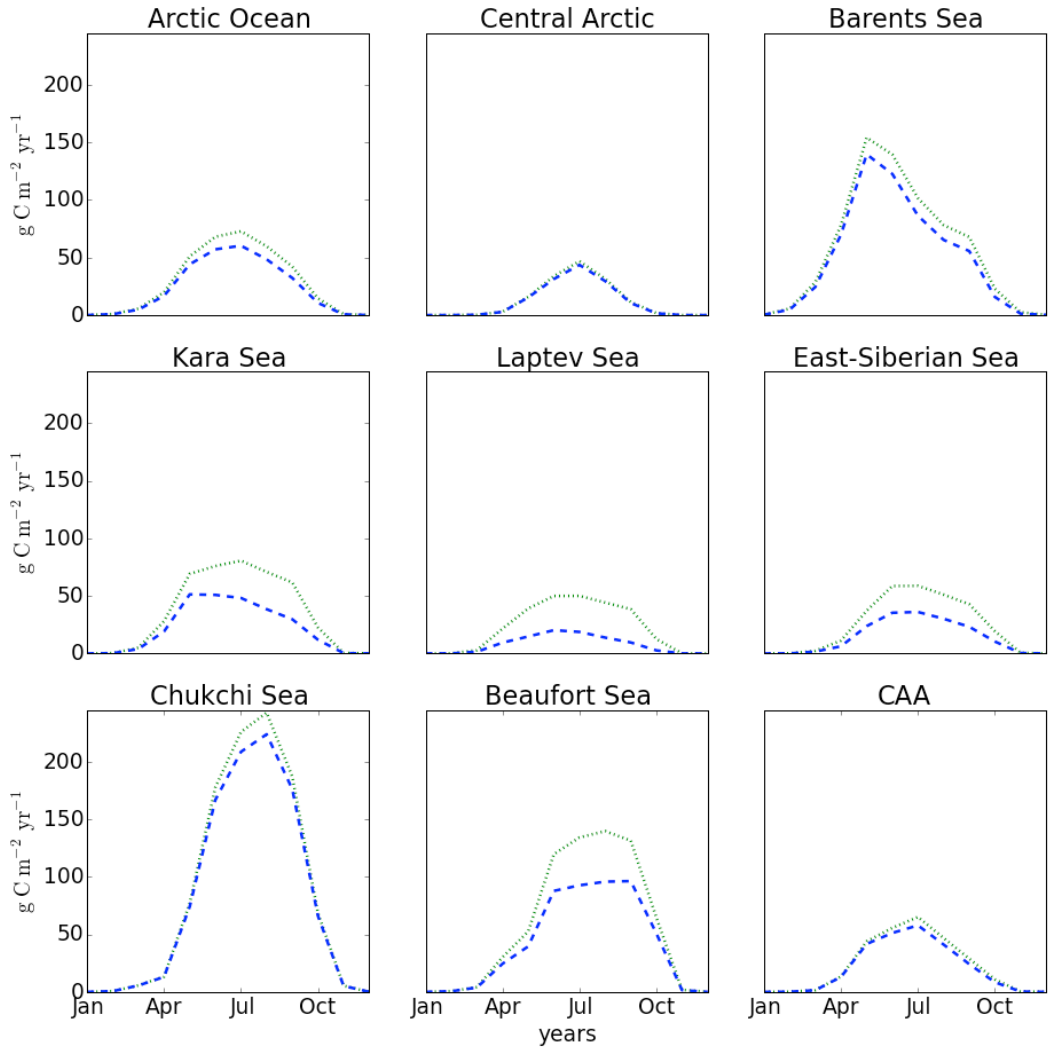

Figure 5.8 – Seasonal cycle of depth integrated NPP averaged over the Arctic Ocean and its regional seas. Results are shown for the simulation with the new riverine forcing set (green) and the simulation without riverine input of carbon and nutrients (blue).

May (Barents Sea) and August (Chukchi Sea and Beaufort Sea). In addition to the timing of the peak, the duration of the NPP bloom also varies regionally. On average, the bloom starts in March and stops in October. The shortest bloom period is observed in the Central Arctic (April–October), and the longest bloom period in the Barents Sea (February–November).

Compared to satellite-derived annual mean NPP averaged over 1998–2012 [Arrigo and van Dijken, 2015], NEMO-PISCES underestimates the Arctic Ocean NPP by 23% (86 Tg C yr^{-1}) (Table 5.7). The horizontal pattern of simulated and satellite-derived NPP agree in most parts, but simulated NPP is smaller than data-based NPP on most parts of the Siberian shelf (Figure 5.9). Simulated NPP was further compared to data-based estimates separately for each regional sea. As opposed to the regional seas defined in this study, Arrigo and van Dijken [2015] did not consider the central Arctic Ocean as a region on its own. Instead they divided the central Arctic Ocean between the different coastal region. Thus, their reported regional estimates should be larger then our simulated regional estimates. Indeed, this is the case for all coastal regions apart from the Chukchi Sea,

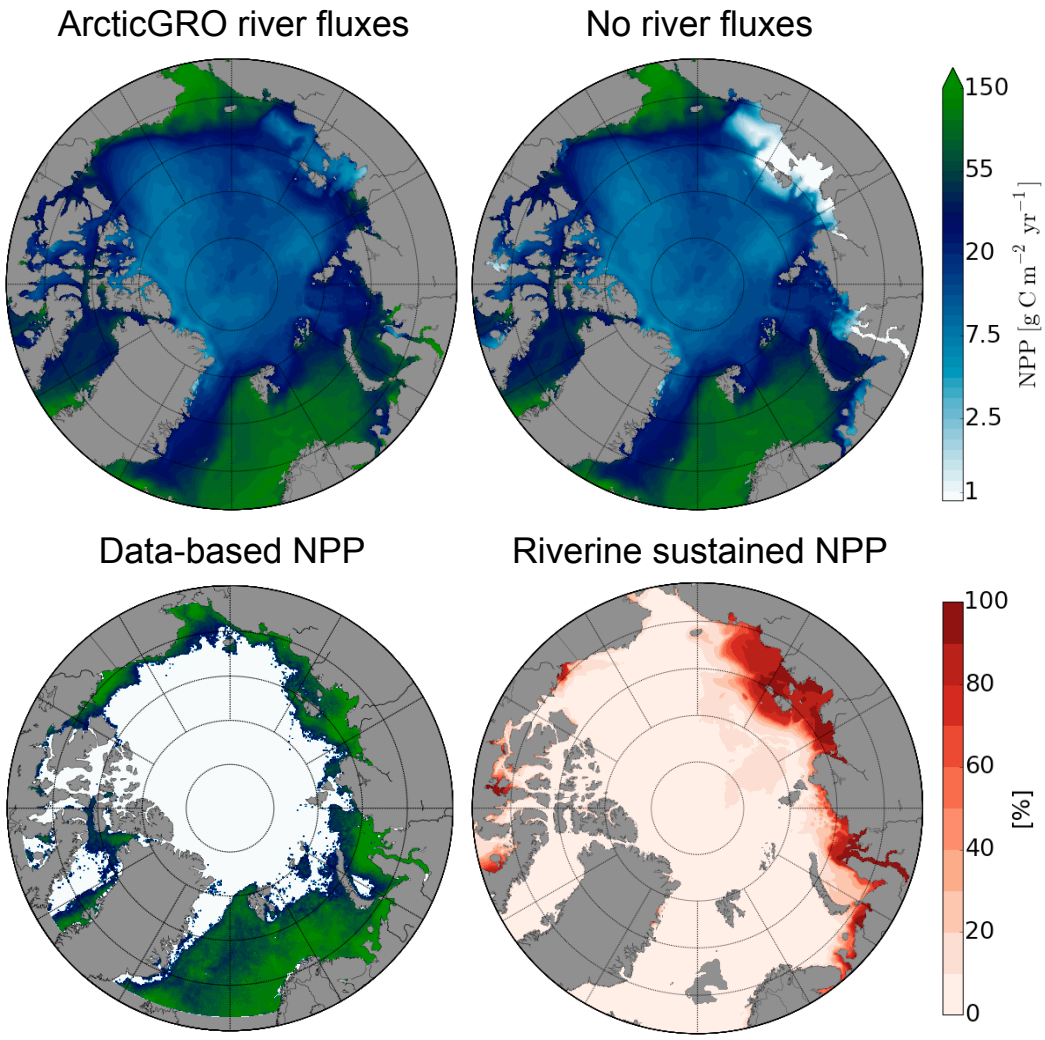

Figure 5.9 – Simulated annual depth integrated NPP from 2005 to 2010 in the Arctic Ocean with ArcticGRO derived riverine fluxes (top left) and with zero riverine fluxes (top right). The data-based NPP is derived from remotely sensed ocean color from SeaWifs over 1998–2005 [Arrigo and van Dijken, 2011] (bottom left). The relative share of riverine driven NPP is shown (bottom right).

where our simulated annual NPP is 63% larger than the observation based NPP.

With riverine fluxes of carbon and nutrients set to zero, the simulated total Arctic Ocean NPP drops by one fifth from 296 Tg C yr^{-1} to 239 Tg C yr^{-1} (Table 5.7 and Figure 5.9). The reduction in NPP without riverine fluxes is largest in the Kara Sea (39%), the Laptev Sea (75%), the East-Siberian Sea (43%), and the Beaufort Sea (29%). The reduction is smaller in the Barents Sea (14%), the Chukchi Sea (8%), the Central Arctic (6%), and the CAA (11%). In addition to the annual NPP, riverine fluxes also influence the seasonal cycle. When riverine fluxes are set to zero, the peak in NPP occurs around 1 month earlier in the Laptev Sea and the Kara Sea (Figure 5.8).

5.2.3.4 Air-to-sea CO_2 flux

The total simulated annual uptake of atmospheric CO_2 via the air-sea interface in the Arctic Ocean is 77.4 Tg C yr^{-1}, corresponding to an average uptake rate of 7.5 g C m^{-2} yr^{-1} (Table 5.7). This total

uptake is within the observation based estimate from Bates and Mathis [2009] (65–199 Tg C yr^{-1}). Out of the simulated uptake, 60% is occurring in the Barents Sea and 20% in the central Arctic Ocean. While almost all regional seas are sinks of atmospheric CO_2, the Laptev Sea is with an air-to-sea CO_2 fluxes of -4.1 Tg C yr^{-1} a source of CO_2 to the atmosphere. Similar to the total uptake of atmospheric CO_2, the regional air-to-sea CO_2 fluxes agree in most regions with the observational estimates (Table 5.7). Exceptions are the Laptev Sea for which observations suggest a net uptake of CO_2 instead of the simulated outgassing, and the Chukchi Sea, the Beaufort Sea, and the CAA, where the simulated air-sea CO_2 uptake is below the lower boundary of the data based estimate. In addition to the absolute annual fluxes, flux rates were computed for each region (Table 5.7).

Seasonally, the air-to-sea CO_2 fluxes are smallest in winter and largest in summer (Figure 5.10). In winter, the average air-to-sea CO_2 flux rate drops to 3.8 g C m^{-2} yr^{-1}. In summer, the peak of the air-to-sea CO_2 flux rate is simulated at 14.8 g C m^{-2} yr^{-1}. The seasonal cycle differs between the regional seas. While most regional air-to-sea CO_2 flux rates continuously increase until September and decrease afterwards, the seasonal cycle is more complicated in the Barents Sea, in the Beaufort Sea, and in the Laptev Sea. In the Barents Sea, the uptake of CO_2 decreases during spring and is smallest in July with 21.3 g C m^{-2} yr^{-1}. Afterwards it increases and reaches its maximum in October with 39.9 g C m^{-2} yr^{-1}. The Beaufort Sea shows an outgassing of CO_2 in July (-7.2 g C m^{-2} yr^{-1}) and an uptake in October (25.7 g C m^{-2} yr^{-1}). In the Laptev Sea, the simulated outgassing of CO_2 peaks in July (19.6 g C m^{-2} yr^{-1}) and only in October a small ingassing is simulated (3.7 g C m^{-2} yr^{-1}).

Riverine fluxes of carbon and nutrients impact the magnitude and the seasonal cycle of the air-to-sea CO_2 flux changes (Figure 5.10). The annual air-sea CO_2 uptake in the Arctic Ocean is reduced by 17% by riverine fluxes of carbon and nutrients (Table 5.7). Regionally the influence of riverine fluxes on air-sea CO_2 fluxes is largest in the Laptev Sea, which turns from a sink of atmospheric CO_2 into a source when riverine fluxes are included, and in the Beaufort Sea, where the uptake of atmospheric CO_2 is divided by 9 with riverine fluxes. Furthermore, the amplitude of most seasonal cycles is reduced by riverine fluxes due to a smaller ingassing of CO_2 in summer. In the Laptev Sea and Beaufort Sea, river fluxes shape the complex seasonal cycles described above. Without riverine fluxes, the seasonal cycles are replaced by a simple monotonous increase of the air-to-sea CO_2 flux until September (Laptev Sea) and October (Beaufort Sea) and a a decrease afterwards.

5.2.3.5 Aragonite saturation state

The simulated annually and spatially averaged surface Arctic Ocean Ω_A is found at 1.3 (Table 5.7). Dependent on the region, annually averaged Ω_A varies from 0.8 in the Laptev Sea to 1.5 in the Barents Sea. The regional Ω_A compares well to observations. On the Siberian shelves, large areas with $\Omega_A < 1$ are found in the model and in the observations (Figure 5.6). Inflowing waters from the Pacific and Atlantic Ocean and outflowing waters in the CAA exhibit Ω_A values above one for both,

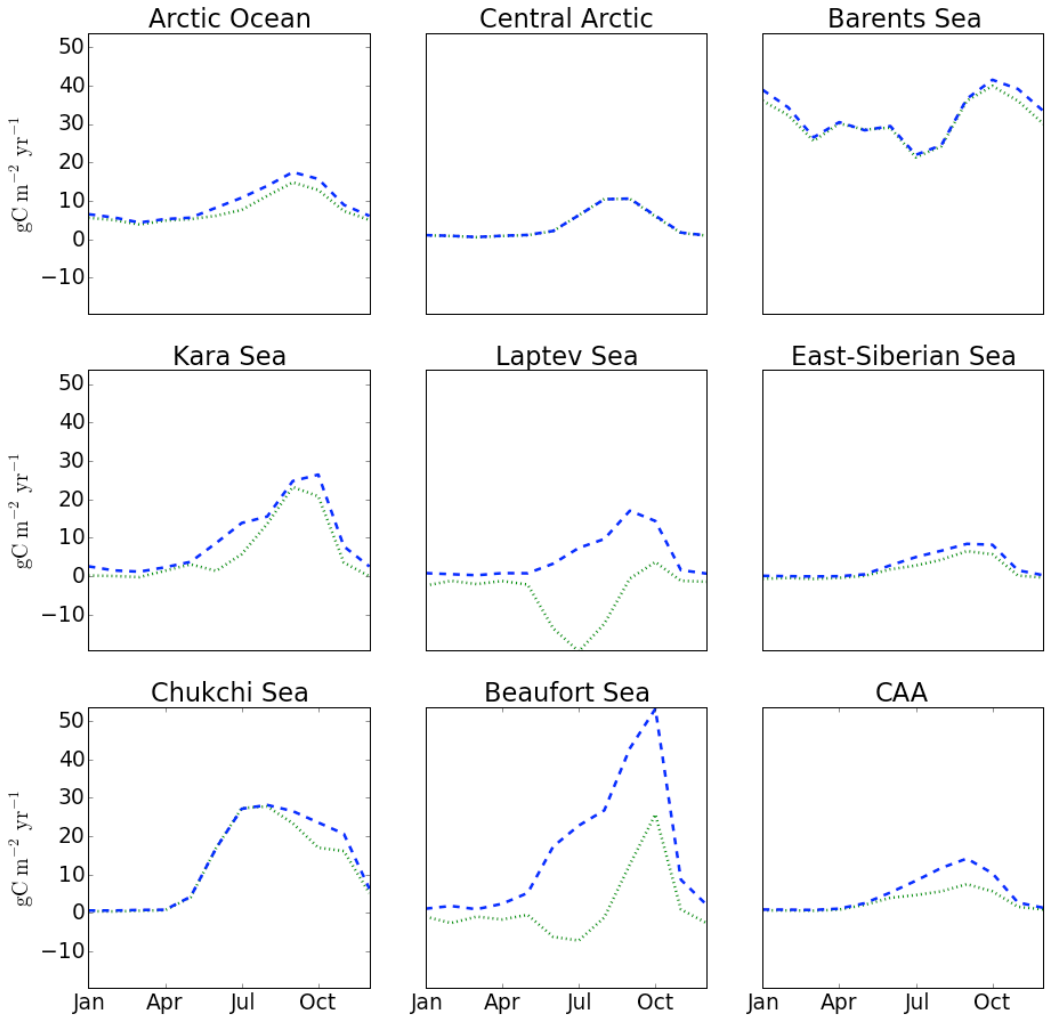

Figure 5.10 – Seasonal cycle of air-to-sea CO_2 flux averaged over the Arctic Ocean and its regional seas. Results are shown for the simulation with the new riverine forcing set (green) and the simulation without riverine input of carbon and nutrients (blue).

model and observations.

Seasonally, average surface Ω_A is largest in June (1.36) and smallest in March (1.25). Regionally, the amplitude of the seasonal cycle varies from 0.05 in the CAA and 0.06 in the Central Arctic over 0.13 in the Laptev Sea and in the East-Siberian Sea to 0.45 in the Chukchi Sea. Ω_A below the threshold of 1.0 is simulated in the Laptev throughout the entire year and in the East-Siberian Sea from October to April.

Without riverine fluxes, average Arctic Ocean surface Ω_A is 0.1 smaller than with riverine fluxes (Table 5.7). The influence of river fluxes on Ω_A is largest in summer, when Ω_A increases by 0.15 in the Laptev and East-Siberian Seas with river fluxes included (Figure 5.11). This river-induced increase in summer Ω_A in the East-Siberian Sea makes this region supersaturated towards aragonite ($\Omega_A > 1$) during the summer months. Without accounting for rivers, both the Laptev and East-Siberian Seas remain undersaturated towards aragonite ($\Omega_A < 1$) throughout the entire year. The increase in Ω_A when river fluxes are included is reduced at the bottom ocean and locally even

changes to a decrease in Ω_A (Figure 5.11).

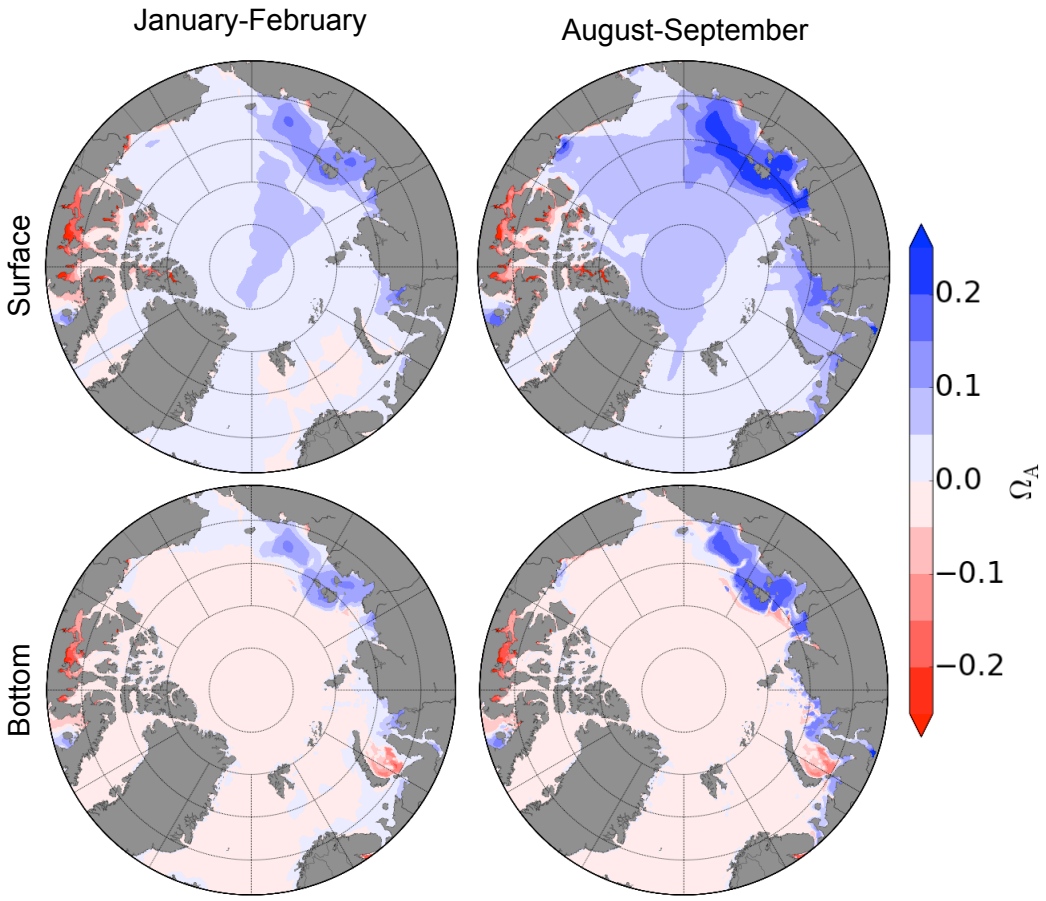

Figure 5.11 – Difference in surface Ω_A in winter (January and February) and summer (August and September) caused by riverine delivery of carbon and nutrients.

5.2.4 Discussion

5.2.4.1 Extrapolated riverine fluxes

5.2.4.1.1 Comparison to previous data-based estimates For the first time, a gridded product of pan-Arctic riverine fluxes of carbon and nutrients was constructed based on a set of coordinated measurements and geo-statistical upscaling techniques accounting for major environmental drivers. Previously, a gridded pan-Arctic flux product only existed for riverine DOC fluxes [Manizza et al., 2009]. For C_T, extrapolated riverine fluxes per region were estimated by Tank et al. [2012c]. For riverine fluxes of A_C, DIN, DON, TDP, and Si_T only discrete measurement existed up to present [Holmes et al., 2012; Le Fouest et al., 2013]. Based on these discrete measurements, Holmes et al. [2012] estimated pan-Arctic fluxes of DOC, DIN, DON, TDP, and Si_T assuming the average yield from the sampled river basins to be representative for the entire Arctic catchment. Additional estimates of pan-Arctic riverine fluxes exist for DOC [Dittmar and Kattner, 2003; Raymond et al., 2007; Manizza et al., 2009] and DIN [Le Fouest et al., 2013]. In this section we compare our gridded product to the estimates mentioned above.

For C_T, we compare our results to Tank et al. [2012c]. Their definition of the regions of the Arctic Ocean agree with ours, apart from the CAA, which is larger in our study as it includes the whole northern Greenland coastline (Figure 6.1). Thus, we compare the summed annual flux only for the consistently defined regions (Barents Sea, Kara Sea, Laptev Sea, East-Siberian Sea, Chukchi Sea, and Beaufort Sea). Tank et al. [2012c] estimated a total C_T flux of 37.9 $\pm$ 6.0 Tg C yr^{-1}, which is in good agreement with our study (39.0 Tg C yr^{-1}). Regionally both estimates agree within the uncertainty range for all regions, but for the Beaufort Sea. There, the estimate from Tank et al. [2012c] (7.6 $\pm$ 0.5 Tg C yr^{-1}) is 13% lower than the estimate presented in this study (8.7 Tg C yr^{-1}).

For riverine DOC fluxes, earlier estimates for the regions defined in this study (excluding the CAA) vary between 18–26 Tg C yr^{-1} [Dittmar and Kattner, 2003], 25 Tg C yr^{-1} [Raymond et al., 2007; Holmes et al., 2012], and 29 Tg C yr^{-1} [Manizza et al., 2009]. These early estimates agrees well with the estimated pan-Arctic DOC flux in this study (25.5 Tg C yr^{-1}) (Table 5.5). However, the estimates from Raymond et al. [2007], Manizza et al. [2009], and Holmes et al. [2012] and the here presented estimate are all based on PARTNERS/ArcticGRO measurements and thus differ only in the way these measurements were extrapolated.

The annual pan-Arctic river flux of DIN (0.32 Tg N yr^{-1}) was compared to estimates by Le Fouest et al. [2013] and Holmes et al. [2012]. Le Fouest et al. [2013] calculated the riverine fluxes from the 9 largest Arctic rivers taking into account observations from Gordeev et al. [1996] and Holmes et al. [2000] and obtained a summed flux of 0.10 (0.05–0.21) Tg N yr^{-1} [Le Fouest et al., 2013]. The difference to the here obtained estimate is partly due to the incomplete coverage of the Arctic rivers and partly due the fact that measurements of riverine DIN concentrations dated from the 20$^{\text{th}}$ century, while an intensification of agricultural land use and the increase of soil organic matter inputs due to permafrost thaw have likely increased the riverine N loads over the last two decades. In addition, inaccuracies in DIN measurements during the 20$^{\text{th}}$ century and the lower number of samples might have led to erroneous flux estimates [Holmes et al., 2000, 2001].

As opposed to Le Fouest et al. [2013], Holmes et al. [2012] extrapolated the observed fluxes from the six largest rivers to all Arctic rivers simply by applying the observed average yield to unmonitored watersheds. Thus, they obtained a pan-Arctic riverine flux of 0.43 Tg N yr^{-1}. However, in contrast to our study, the Hudson Bay and Hudson Strait were included in this estimate. By subtracting the river fluxes from both regions, Holmes et al.'s estimate reduces to 0.35 Tg N yr^{-1}, still 11% larger than our estimate. Having used the same measurements from the six largest rivers for the extrapolations, this difference can only be due to the extrapolation method. As we used a more advanced extrapolation method, we conclude that the difference in total Arctic DIN fluxes of 11% represents the error which is made by not taking into account the spatial distribution of environmental drivers of riverine DIN fluxes.

For DON, TDP, and Si_T, the only existing pan-Arctic estimate is calculated by Holmes et al. [2012] by applying the observed yields to the missing watersheds. When subtracting the fluxes from the Hudson Bay and Hudson Strait (as for DIN fluxes), these estimates are 0.70 Tg N yr^{-1}

(DON), 0.060 Tg P yr^{-1} (TDP), and 9.4 Tg Si yr^{-1} (Si_T). These basinwide fluxes are 4% larger (DON), 6% smaller (TDP), and 7% larger (Si_T) then the calculated fluxes in this study. Similar to DIN, we conclude that this discrepancy is mainly caused by the different method of extrapolation.

5.2.4.1.2 Comparison to land-surface model estimates The here calculated gridded product of pan-Arctic riverine fluxes of carbon and nutrients on the World Ocean Atlas 1° × 1° grid is a valuable new forcing data set for ocean-biogeochemistry models, similar to the NEMO-PISCES model used in this study. Before, river inputs have not been included in climate models [Ilyina et al., 2013; Tjiputra et al., 2013] or estimates of average annual fluxes from empirical models like GN2 or GEM were used [Aumont and Bopp, 2006; Bourgeois et al., 2016; Terhaar et al., 2018]. In the following paragraphs, we compare the estimated C_T and DOC fluxes from GEM and the estimated DOC, DIN, DON, TDP, and Si_T fluxes from GN2 to our observation-based extrapolations.

GEM gives a pan-Arctic C_T flux of 60.6 Tg C yr^{-1} and a DOC flux of 25.5 Tg C yr^{-1}. GN2 yields a DOC flux of 13.7 Tg C yr^{-1}, a DIN flux of 0.54 Tg N yr^{-1}, a DON flux of 0.84 Tg C yr^{-1} , a TDP flux of 0.073 Tg P yr^{-1}, and a Si_T flux of 6.1 Tg Si yr^{-1}. GEM's C_T flux is 20% larger while GEM's and GN2's DOC fluxes are 8% and 50% lower than our results, respectively. Differences between nutrient fluxes from GN2 and the here derived fluxes are of similar magnitude than the differences in carbon fluxes: GN2's DIN flux is 69% larger, its DON flux is 25% larger, its TDP flux is 14% larger, and its Si_T flux is 31% smaller than the here presented estimates. As N is the limiting nutrient in the Arctic Ocean, an overestimation of riverine TDN fluxes by 39% would cause an overestimation of riverine driven NPP by 39% assuming that the additional riverine N would be used for NPP in the same way as the other N. This overestimation of riverine driven NPP by 39% (Table 5.7) corresponds to an overestimation of basinwide simulated Arctic Ocean NPP by 9%.

The difference indicate between the here dervied river fluxes and GEM's and GN2's river fluxes highlight the uncertainty of flux estimates for Arctic rivers by the GN2 and GEM models. The GN2 and GEM models were developed based on global river datasets that did not include the systematic observations from the ArcticGRO data set and thus insufficiently represent the effect of Arctic phenomena, like the large permafrost extend. The identified discrepancies highlight the importance of using a more directly observation-driven forcing file for Arctic river fluxes.

5.2.4.1.3 Carbon and nutrient concentrations The here simulated marine C_T and A_T concentrations have been shown to agree well with the observations. Including riverine fluxes into the model has reduced the RMSE for all variables but DIN (Table 5.8) and has brought the basinwide average surface concentrations closer agreement with observations (Table 5.7). The point-by-point comparison of observed and simulated concentrations (Figure 5.7) shows that simulated surface C_T and A_T exhibit a smaller variability than observed surface C_T and A_T. The smaller variability for simulated concentrations is likely a consequence of averaging the simulated concentrations over 2005-2010, thus smoothing out the inter-annual variability. This elimination of

Table 5.9 – Nutrient flux rates across Arctic Ocean boundaries averaged over the summer (July–September) [kmol s^{-1}] and total annual fluxes Tg yr^{-1}. Summer flux rates are compared to data-based estimates from [Torres-Valdés et al., 2013].

	Summer fluxes						Annual fluxes		
	DIN		P_T		Si_T		DIN	P_T	Si_T
	Model	Data	Model	Data	Model	Data			
Fram Strait	-17.8	-10.3 ± 7.5	-1.3	-0.9 ± 0.8	-12.7	-7.0 ± 5.9	-22.3	-1.6	-18.9
Barents Sea Opening	1.3	33.6 ± 5.1	1.0	2.4 ± 0.4	7.1	13.2 ± 2.1	0.8	1.2	8.3
Bering Strait	8.4	9.0 ± 0.8	1.0	1.3 ± 0.1	16.8	20.9 ± 2.4	10.1	1.0	16.1
CAA	-13.0	-31.3 ± 3.6	-1.3	-3.7 ± 0.4	-16.0	-42.9 ± 5.2	-16.5	-1.5	-19.0
Total	-21.1	1.0 ± 3.2	-0.6	-1.0 ± 0.6	-4.8	-15.7 ± 6.3	-27.9	-0.9	-13.6

the inter-annual variability for the simulated concentrations may well explain the relatively large RMSE for C_T and A_T.

As opposed to C_T and A_T, simulated and observed nutrients show much larger differences. The underestimation of P_T and Si_T is mainly taking place in the Western Arctic Ocean, a part which is largely influenced by waters from the Pacific Ocean. A comparison between simulated river inflow from the Pacific Ocean to data-based estimates shows that the simulated P_T and Si_T fluxes from the Pacific are below the data-based uncertainty range (Table 5.9). This underestimation may well be the main reason for too little P_T and Si_T in the Arctic Ocean. Locally, the highest underestimation of P_T and Si_T by the model is found in the East-Siberian Sea and might be partly caused by the too small nutrient influx from the Pacific Ocean and by higher concentrations of observed nutrients as a consequence of coastal erosion [Fritz et al., 2017], a process which is not included in the model.

In comparison to P_T and Si_T, the comparison of observed and simulated DIN yields larger differences. The point-by-point comparison (Figure 5.7), shows a binary pattern, either DIN is depleted or it is not. The fact that DIN is the only entirely depleted nutrient in the simulations is in agreement with previous studies [Tremblay et al., 2015]. Although simulated and observed DIN is depleted in many parts of the Arctic Ocean, the places where DIN is not depleted differ between observations and the model (Figure 5.6). For example, in the central Arctic Ocean finite DIN is observed, whereas simulated DIN is entirely depleted, indicating that in the model all nutrients are used for NPP in the coastal Ocean. Conversely, simulated surface DIN in the Chukchi Sea and on the Siberian shelf is non-zero, whereas observed DIN is depleted in the Chukchi Sea and close to zero on the Siberian shelf [Anderson et al., 2009; Semiletov et al., 2013]. Both effects, the simulated overestimation of DIN values in the coastal seas and the underestimation of DIN in the central Arctic Ocean can partly be explained by the assumption that riverine DON flux is added to PISCES in the form of DIN. As opposed to this assumption, observations suggest that only 62–76% of riverine

DON is remineralized on the shelf. Consequently the DIN in the coastal regions is overestimated by 24–38%, whereas the offshore transport of riverine DON to the central Arctic is underestimated by 24–38%. Remineralization of this riverine DON may thus cause the observed concentrations of DIN in the central Arctic Ocean. Further the simulated influx of DIN via the Barents Sea Opening is 30 times smaller than the data-based DIN flux estimate. This underestimation of the influx likely contributes to the underestimation of surface DIN by the model.

5.2.4.2 Net Primary production

Simulated basinwide NPP underestimates the data-based NPP by 23%. This can be caused by too strong light or nutrient limitation. The simulated light availability mainly depends on the simulated sea ice extent. As this has been shown to be in good agreement with observed sea ice extent [Terhaar et al., 2018], light limitation is likely not the cause for the underestimation of NPP. Therefore the underestimation of Arctic Ocean NPP must be caused by an underestimation of nutrients close to the ocean surface, more specifically the limiting nutrient N. N is supplied to the Arctic Ocean via atmospheric deposition, riverine fluxes, and lateral influx from the adjacent oceans and leaves the Atlantic via sedimentation and lateral outflux. Atmospheric deposition and riverine fluxes are well constrained by observations, which leaves lateral fluxes and sedimentation. The here used standard version of PISCES has been shown to overestimate sedimentation in shallow areas like the Arctic Ocean [Aumont et al., 2017]. Moreover, the lateral influx of DIN through the Barents Sea Opening represents only 4% of the data-based estimate. Both, a two high sedimentation rate and an underestimated lateral influx of DIN thus lead to the underestimation of the data-based NPP in the simulation.

Riverine delivery of nutrients has been demonstrated to sustain 19% of total simulated Arctic Ocean NPP. This estimate is 19 times higher than the earlier estimate by Le Fouest et al. [2013]. This estimate was based on a comparison of yearly Arctic NPP and riverine DIN fluxes assuming a constant C:N ratio. When taking into account remineralization of riverine DON on the shelf and assuming a recycling rate of 3.2, Tank et al. [2012a] find a riverine N driven Arctic Ocean NPP of 4%, still 5 times smaller than the here presented estimate. Explicitly simulating DON recycling using a coupled ocean-biogeochemistry model has increased the estimate of riverine sustained NPP to 8% [Le Fouest et al., 2015], which is however still only 40% of the here presented estimate.

Among possible reasons for this difference to Le Fouest et al. [2015] are the used river fluxes and the applied lability of riverine DON. As opposed to the here presented model study, Le Fouest et al. [2015] estimated riverine DON fluxes from a gridded flux product for riverine DOC [Manizza et al., 2009] assuming a molar C:N ratio of 40:1. Our flux estimates (Table 5.5) suggest that this ratio of 40:1 is a good first estimate. Seasonally however (Table 5.6), an annual C:N ratio leads to an overestimation of riverine DON fluxes by 6–15% from December to June and to an underestimation of riverine DON fluxes by 1–8% from July to November. A relatively larger discrepancy is

related to the implementation of the riverine DON flux in both models. As opposed to the assumption in this study, where riverine DON fluxes are entirely added as DIN to the ocean, Le Fouest et al. [2015] assume 15% of the riverine DON flux being biodegradable following Wickland et al. [2012]. Recently, a re-assessment of DON removal processes on the Siberian shelf has led to a 4–5 fold increase resulting in a DON removal rate on the shelf seas of 62–77%. Assuming that all additionally available DIN would be consumed by NPP on the shelf seas, would increase Le Fouest et al.'s estimate of riverine driven NPP from 8% to 26–30%, higher than the 19% found in this study.

While the lability of DON seems to be too small in the study byLe Fouest et al. [2015], the lability of 100% used in this study is certainly too high. Assuming that all the DIN from riverine DON fluxes has contributed to coastal NPP and that instead 23–38% should have been transported offshore [Thibodeau et al., 2017; Letscher et al., 2013], would reduce the here presented Arctic Ocean NPP to 274–283 Tg C yr^{-1}. The proportion of riverine driven NPP would consequently be reduced to 13–16%. Nevertheless, the finite DIN concentrations during summer in the Laptev Sea (Figure 5.6) suggest that not all of this available DIN is used by NPP before being transported offshore. Thus, the best estimate for riverine driven NPP is likely to be located between 13 and 19%.

Furthermore, the underestimation of lateral influx of DIN through the Barents Sea Opening (Table 5.9) and the overestimation of sedimentation on the large coastal shelves impact the relative importance of riverine nutrients. While an underestimation of the lateral influx increases the riverine driven NPP, an overestimation of the sedimentation on the shallow shelfs affects relatively more the nutrients from rivers and thus reduces the riverine driven NPP. Due to the complex physical and biogeochemical dynamics, it is not possible to quantify the effect of both on the riverine driven NPP. However, the simulated NPP in previous studies [Le Fouest et al., 2015, Figure 2] for the same region as defined in this study was even lower than the simulated NPP here. Thus, their estimate of riverine driven NPP was even more strongly overestimated than the here presented estimate.

Different to the riverine share of pan-Arctic NPP, the local share of almost 100% close to the river mouths on the Siberian shelf should not be significantly affected by the assumption of adding riverine fluxes of DON as DIN, because the simulations with zero river fluxes exhibit almost zero NPP close to the river mouths of the Yenisey, Ob, and Lena river (Figure 5.9). Thus, even a small absolute riverine driven NPP would lead to a relative riverine driven NPP of almost 100%. For the Mackenzie River, the situation is different. Nutrient-rich waters from the Pacific Ocean follow the coastal current in the Beaufort Sea and sustain between 2 and 7 Tg C yr^{-1} of NPP close to the river mouth (Figure 5.9). Thus, the riverine driven NPP in the Beaufort Sea would experience a larger relative decrease if not all riverine DON would be transformed to DIN.

5.2.4.3 Air-Sea CO_2 fluxes

The simulated integrated annual air-sea CO_2 fluxes in the Arctic Ocean has been shown to generally agree with data-based estimates from Bates and Mathis [2009] and sources within. Regional differences between simulation and data-based estimate were mainly detected in the Laptev and Beaufort Seas, two strongly riverine influenced regions. For the Laptev, the estimate from Bates and Mathis [2009] is based on observational campaigns from 1994. Given the difference between simulated results and observations, we compare our results to more recent observations in the Laptev Sea from 2008 [Anderson et al., 2009]. During summer 2008, observed partial pressure of CO_2 (pCO_2) in the ocean was above atmospheric pCO_2. This oversaturation of CO_2 causes consequent outgassing to the atmosphere. Possible reasons for the increase in surface ocean pCO_2 from 1994 to 2008 are increased river fluxes of DOC [Frey and Smith, 2005] or increased coastal erosion [Vonk and Gustafsson, 2013].

During the same campaign Anderson et al. [2009] find a pCO_2 gradient between the Laptev Sea and the East-Siberian Sea, where pCO_2 is below atmospheric pCO_2, causing an uptake of atmospheric CO_2. The same difference between outgassing in the Laptev Sea and uptake in the East-Siberian Sea is also simulated in this study. When riverine fluxes are not accounted for in the simulations, this simulated difference between the Laptev Sea the East-Siberian Sea disappears and the results do not agree with the observations from Anderson et al. [2009] anymore. The better agreement when using river fluxes suggests indeed that river fluxes, especially DOC fluxes, turn the Laptev Sea into a source of carbon to the atmosphere.

We estimated the riverine fluxes to reduce the air-sea CO_2 uptake in the Arctic Ocean by ~17% (16.4 Tg C yr^{-1}). Previously, Manizza et al. [2009] used an ocean model with an exponential decaying DOC tracer to estimate the impact of riverine DOC on the Arctic Ocean CO_2 flux. They find a reduction of air-sea CO_2 uptake by 10% (6 Tg C yr^{-1}). Both results cannot be compared directly as the here presented simulation includes not only the effect of DOC fluxes, but also the river fluxes of C_T, A_T, and nutrients.

Here, we try to disentangle and quantify the separate impact of riverine DOC, C_T, A_T, and nutrient fluxes in a very simplistic way. First, the impact of nutrient fluxes is estimated. Riverine nutrient fluxes cause an increased NPP, which decreases surface pCO_2, which hence leads to a consequent uptake of atmospheric CO_2. In the global ocean, Orr and Sarmiento [1992] estimated an additional uptake of 0.43 mol C per mol C consumed by NPP. This global estimate would likely represent an overestimation for the Arctic Ocean as observations suggest that export of production in the Arctic Ocean is at least one order of magnitude smaller than NPP due to extensive recycling of nutrients in the upper Arctic Ocean waters [Anderson et al., 2003]. Using a ratio of 0.1 instead of the global ratio of 0.43 would lead to an additional uptake of 5.7 Tg C yr^{-1} due to riverine inputs of nutrients.

The combined effect of riverine fluxes of DOC, C_T, and A_T would thus have to compensate this

additional uptake plus the simulated difference of 18.1 Tg C yr^{-1} (Table 5.7). In total, this would be an air-to-sea CO_2 flux reduction by 23.8 Tg C yr^{-1} due to riverine DOC, C_T, and A_T inputs. In this study, we assumed 50% of riverine DOC to be very labile [Kaiser et al., 2017] and thus added these 50% of riverine DOC to PISCES in the form of C_T. If we now assume this additional C_T to be a simple perturbation to the surface ocean pCO_2 and not being transported to the deep ocean, it would be completely lost to the atmosphere. For simplicity, let us assume that all labile riverine DOC (50% of riverine DOC) would be directly lost to the atmosphere via air-to-sea CO_2 flux. This riverine DOC would hence reduce the air-sea CO_2 uptake by 13.8 Tg C yr^{-1}, which is 18% of the total uptake and almost twice as large as the previous estimate from Manizza et al. [2009].

By closing the budget, the remaining reduction of 10.0 Tg C yr^{-1} can be attributed to the riverine flux of C_T and A_T. The outflux stems from an increase in surface ocean pCO_2 due to the low A_T:C_T ratio of 0.7–0.9 in Arctic rivers (compared to 1.1–1.2 in the ocean).

5.2.4.4 Aragonite saturation state

In high-latitude oceans, surface Ω_A is lower than anywhere else in the ocean [Orr et al., 2005; Steinacher et al., 2009], a consequence of high solubility of CO_2 in cold waters, and thus lower carbonate ion (CO_3) concentrations. Rivers enhance this already strong ocean acidification further by adding water with even lower Ω_A to the coastal ocean [Salisbury et al., 2008; Bates and Mathis, 2009; Bates et al., 2009]. In Arctic rivers, Ω_A varies between 0.15 and 0.65 depending on the river system and the season, with lower Ω_A in spring and higher in summer [Tank et al., 2012c].

Although rivers decrease Ω_A in the coastal ocean, our results show that this decrease is solely driven by the dilution of sea water. Even more, the isolated effect of carbon and nutrient river fluxes in the model increases basinwide average surface Ω_A throughout the whole year. Riverine carbon and nutrient fluxes influence Ω_A in three ways: (1) finite river C_T and A_T concentrations (instead of zero with no river fluxes) reduce the dillution effect of pure freshwater on ocean C_T and A_T and thus increase Ω_A [Yamamoto-Kawai et al., 2009], (2) riverine DOC inputs, which are remineralized in the shelf seas [Kaiser et al., 2017], increase ocean C_T and thus reduce Ω_A [Bates et al., 2009], and (3) riverine nutrient fluxes enhance NPP, hence remove C_T from the surface and increases surface Ω_A, while the exported organic carbon is remineralization at the bottom ocean, where it increases C_T and hence reduces Ω_A [Bates et al., 2009; Anderson et al., 2011b].

In contrast, the simulated combined impact of these three effects on the Siberian shelf is an increase of surface ocean Ω_A by up to 0.3 in summer and 0.2 in winter (Figure 5.11). The increase in Ω_A at the surface aindicates that riverine driven NPP is the decisive factor for changes of Ω_A in the coastal Arctic Ocean. This argument is further supported by the colocation of regions with large riverine driven increases in Ω_A and high riverine driven NPP (Figure 5.9). Waters with increased Ω_A reach the ocean bottom by mixing (Figure 5.11) and thus also increase bottom ocean Ω_A. This increase in Ω_A at the bottom ocean is smaller than at the ocean surface as the remineralization of

organic matter leads to a rise in C_T and a decrease of Ω_A.

5.2.4.5 Past and future changes of river fluxes

Arctic river fluxes have changed during the last centuries and are projected to experience large changes in the coming decades. For example, increased weathering has led to a rise of A_T fluxes in the Ob and Yenisey by 134% and 185% from 1978 to 2015, respectively [Drake et al., 2018]. A_T fluxes in the Mackenzie rivers are projected to increase by 50% until the end of the 21th century [Beaulieu et al., 2012]. Moreover, the increased river discharge during the 2020th century is estimated to have led to a 10% increase in pan-Arctic DOC fluxes [Kicklighter et al., 2013]. A further increase of DOC fluxes with changing climate [Guo et al., 2007] and thawing permafrost [Lawrence and Slater, 2005] is expected for the 21th century. Also expected are increases in concentrations of dissolved organic nitrogen (DON) (32–53%), total dissolved nitrogen (TDN) (30–50%) and total dissolved phosphate (TDP) (29–47%) in the West-Siberian watersheds,[Frey et al., 2007]. Given the importance of river fluxes for the present-day biogeochemistry of the Arctic Ocean, future changes of these fluxes might have a significant influence on projections of NPP, air-to-sea CO_2 fluxes, or ocean acidification. The here presented relative importance of riverine fluxes for the Arctic Ocean biogeochemistry suggest that changes of river fluxes should be accounted for when simulating the future ocean biogeochemistry.

We recommend that these changes should be implemented in Earth-System models. At present, CMIP5 models often implement river fluxes rudimentary or not at all, which might lead to differences in projections for the Arctic Ocean biogoechemistry. For example, a CMIP5 model-intercomparison study has found NPP projections in the Arctic Ocean for 2100 to range from a decline by 110 Tg C yr^{-1} to an increase by 253 Tg C yr^{-1} [Vancoppenolle et al., 2013]. This difference might partly be explained by different or no river fluxes in the models - a hypothesis that was discarded at that time as rivers fluxes were not thought to have a significant influence on Arctic Ocean NPP.

5.2.5 Conclusion

In this study we present the first consistent, data-based, gridded, pan-Arctic dataset for monthly riverine carbon and nutrient fluxes. Compared to earlier gridded model-based data sets, this new dataset has improved nutrient fluxes backed up by the systematic observations from the Arctic-GRO data base. We therefore recommend the use as this dataset for ocean biogeochemoical model studies in the Arctic Ocean.

Further, this dataset was used to force an ocean-biogeochemical model to quantify the impact of riverine fluxes on the Arctic Ocean biogeochemistry. The good agreement of simulated NPP, air-sea CO_2 fluxes, and acidification with observations and data-based estimates highlights the importance of using a well constrained river flux database in the Arctic Ocean. Indeed, our results suggest that river fluxes sustain 13–19% of pan-Arctic Ocean NPP and 75% of the NPP in

the Laptev Sea, reduce the Arctic Ocean air-sea CO_2 uptake by ~17% and make the Laptev Sea to a net sources of CO_2 to the atmosphere, and increase coastal ocean Ω_A regionally by up to 50% during summer. These estimates exceed earlier results and indicate that river fluxes should receive increasing attention when considering the future of the Arctic Ocean biogeochemistry.

Yet, many ocean biogeochemical models do not include riverine fluxes by default [Ilyina et al., 2013; Tjiputra et al., 2013], which might well be the reason for differences of simulated Arctic Ocean NPP between models [Popova et al., 2012; Vancoppenolle et al., 2013], for differences between simulated and observed air-sea CO_2 fluxes [Manizza et al., 2019], and for differences between simulated [Ciais et al., 2013] and observed [Anderson et al., 2017] coastal ocean acidification. We therefore strongly recommend the implementation of river fluxes and their future change in ocean and climate models.

Finally, these results highlight the importance of coordinated measurement efforts of river fluxes, like the Arctic Great River Observatory, for the understanding of the coastal ocean biogeochemistry. Although our extrapolation of river fluxes from the six largest rivers to all Arctic rivers is a first step, an expansion of the observations to more rivers would certainly further increase the capability of coastal ocean biogeochemical modeling.

5.3 Summary

- A first consistent, data-based, gridded, pan-Arctic dataset for monthly carbon and nutrient fluxes was constructed and will be made publicly available for ocean biogeochemoical model studies in the Arctic Ocean
- Simulated net primary production in the Arctic Ocean agrees with data-based NPP when using this river flux dataset
- The amount to which riverine nutrients in the Arctic Ocean sustain primary production was found to be 16–24%, two to three times higher than previous estimates (9%)
- The difference in NPP projections by CMIP5 models might well be caused by different or even non-existing implementations of riverine nutrient fluxes in these models
- Despite the additional uptake of atmospheric carbon from NPP, river fluxes of carbon and alkalinity have been shown to reduce the Arctic Ocean air-sea CO_2 uptake by 20%
- Riverine fluxes have a strong local influence on the seasonal cycle of acidification by reducing surface acidification in summer during the NPP maximum and increasing at the bottom of the shelf seas due to remineralization of organic matter.
- Future changes in river fluxes, driven by permafrost thaw and land-use change might thus have a substantial impact on changes of the Arctic Ocean biogeochemistry, a factor that was not yet included in projections by the CMIP5 models

Chapter 6

Simulated Arctic Ocean response to doubling of riverine carbon and nutrient delivery

“ There is no greatness where there is not simplicity, goodness, and truth ”

Leo Tolstoy

Contents

6.1 Preamble

After having demonstrated and quantified the importance of riverine delivery of carbon and nutrients on the present-state of the Arctic Ocean biogeochemistry, the next chapter is focused on the effect of future changes of riverine fluxes on the Arctic Ocean biogeochemistry.

At present, projections of future riverine delivery of carbon and nutrient in the Arctic are highly uncertain. Although the magnitude of future change is strongly debated, it is almost certain that future riverine fluxes of carbon and nutrients will increase due to advancing tree lines [Harsch et al., 2009], deepening of the active permafrost layer [Oelke et al., 2004], and permafrost degradation during this century. For example, a projected decline of near surface-permafrost from 10.5 million km^2 to 1.0 million km^2 by 2100 under the A2 emission scenario [Lawrence and Slater, 2005] will result in an increase of riverine C_T [Tank et al., 2012a; Walvoord and Striegl, 2007] and alkalinity [Drake et al., 2018] delivery to the Arctic Ocean.

Given the large uncertainties of riverine delivery projections, we decided to calculate sensitivities of the Arctic Ocean biogeochemistry to changing river input, analogous to climate sensitivities. This concept of climate sensitivities was introduced by Friedlingstein et al. [2001], who increased CO_2 in the atmosphere by 1% per year and calculated the amount of carbon taken up by land and ocean separately per ppm of additional atmospheric CO_2.

In this chapter this concept was transferred to river fluxes. An idealized increase of carbon and nutrient fluxes by 1% per year was imposed on the river fluxes in NEMO-PISCES. Over a period of 75 years, the riverine delivery is thus doubled. The influence of river fluxes of C_T, DOC, and nutrients was calculated separately. To put these changes into context, a simulation with increasing atmospheric CO_2 was also made. Following the precedent chapter, the sensitivities of primary production, air-sea CO_2 flux, and acidification are calculated. The total simulation length of 375 years did not allow the use of the high-resolution configuration ORCA025. Instead, ORCA1 was chosen here to calculate the sensitivities.

6.2 Article in preparation for publication in *Global Biogeochemical Cycles*

J. Terhaar[1,2], J. C. Orr[1], C. Ethé[3], P. Regnier[2], and L. Bopp[4]

[1]Laboratoire des Sciences du Climat et de l'Environnement, LSCE/IPSL, CEA-CNRS-UVSQ, Université Paris-Saclay, 91191 Gif-sur-Yvette, France

[2]Biogeochemistry and Earth System Modelling, Department of Geoscience, Environment and Society, Université Libre de Bruxelles, Belgium

[3]Institut Pierre et Simon Laplace, 4 Place Jussieu, 75005 Paris, France

[4]LMD/IPSL, Ecole Normale Supérieure / PSL Research University, CNRS, Ecole Polytechnique, Sorbonne Université, Paris, France

6.2.1 Abstract

The Arctic Ocean, more than any other ocean, is influenced by riverine input of carbon and nutrients. That riverine delivery is likely to change with climate change as runoff increases, permafrost thaws, and tree lines advance. But it is unknown to what extent these changes in riverine delivery will affect Arctic Ocean primary production, air-to-sea CO_2 fluxes, and acidification. To test their sensitivity to changing riverine delivery, we made sensitivity tests using an ocean circulation model coupled to an ocean biogeochemical model. In separate idealized simulations, riverine inputs of dissolved inorganic carbon (C_T), dissolved organic carbon (DOC), and nutrients were increased by 1% per year until doubling. Doubling riverine nutrient delivery increased primary production by 11% on average across the Arctic basin and by up to 34–35% locally. Doubling riverine DOC delivery resulted in 90% of that added carbon being lost from the Arctic Ocean to the atmosphere, partly because it was imposed that once delivered to the ocean, the riverine DOC was instantaneously remineralized to C_T. That additional outgassing, when considered alone, reduced the net ingassing of natural CO_2 into the Arctic Ocean by 25%, while converting the Siberian shelf seas and the Beaufort Sea from net sinks to net sources of carbon to the atmosphere. The remaining 10% of DOC remained in the Arctic Ocean, but having been converted to C_T, it enhanced acidification. Conversely, doubling riverine C_T increased the Arctic Ocean's average surface pH by 0.02 because riverine total alkalinity delivery increased at the same rate as riverine C_T delivery.

6.2.2 Introduction

It is uncertain how river delivery of carbon and nutrients will change and how these changes will affect the coastal and open ocean [Regnier et al., 2013b]. The largest of these changes will occur in the Arctic Ocean, into which 11% of the global river discharge drains [McClelland et al., 2012] even

though it is the world's smallest ocean, representing only 4% of the global ocean area and 1% of its volume [Jakobsson, 2002].

Total Arctic river discharge has continued to increase since the beginning of the last century, e.g., with outflow from the six largest Eurasian rivers draining into the Arctic Ocean growing by 7% from 1939 to 1999 [Peterson et al., 2002; McClelland et al., 2004]. Between 1964 and 2000, river discharge from 16 Eurasian rivers that drain into the Arctic Ocean increased by 11% [McClelland et al., 2006]. Conversely, the Canadian river discharge into the Arctic Ocean declined by 10% from 1964 to 2003 [Déry and Wood, 2005], although that was reversed during 1989 to 2007, a period that showed a 15% increase in river discharge [Déry et al., 2009]. Further increases in Arctic river discharge are expected given projected future increases in precipitation [Peterson et al., 2002]. More precisely, a 16–28% increase of freshwater discharge into the Arctic Ocean during the 21st century is projected by atmosphere-–ocean general circulation models forced under the SRES A1, A2, and B1 scenarios [Lawrence and Slater, 2005; Nohara et al., 2006]. Such increases would in turn affect Arctic Ocean circulation and biogeochemistry, e.g., leading to increased stratification, decreased vertical mixing, decreased nutrient supply from deeper waters, decreased primary production, and enhanced acidification [Carmack et al., 2015].

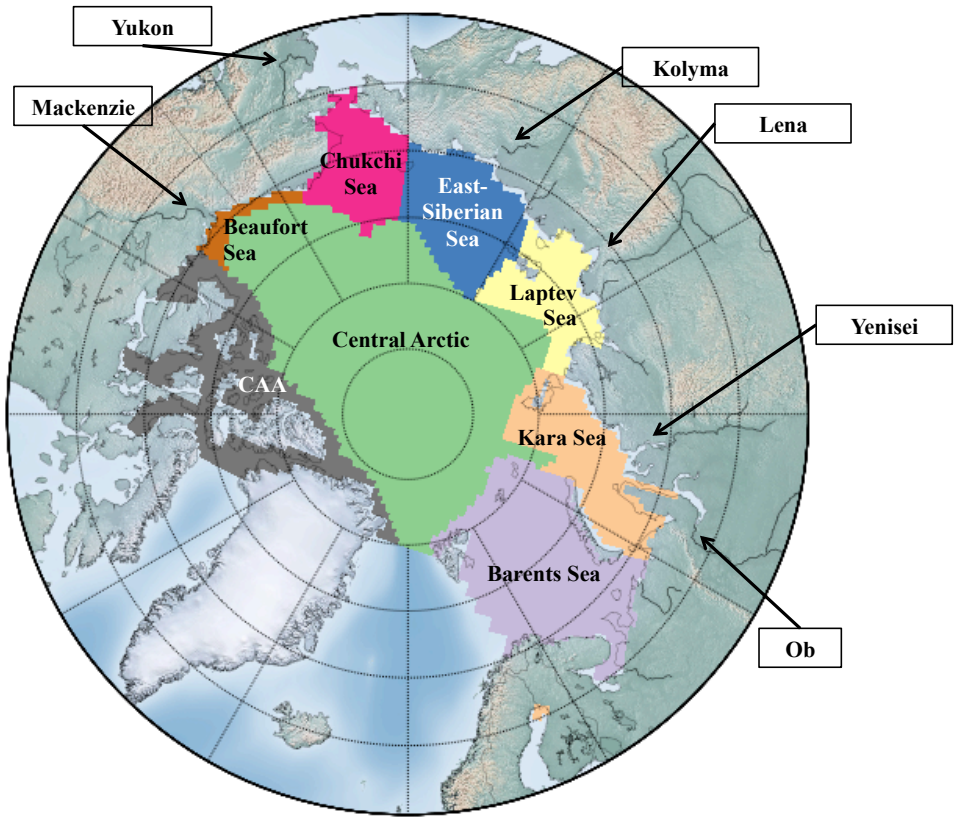

Figure 6.1 – Arctic regional seas and its six major rivers, out of which all but the Yukon drain into the Arctic Ocean.

Primary production and acidification are also affected by riverine delivery of carbon and nutrients [Tremblay et al., 2015; Semiletov et al., 2016]. Out of all the dissolved inorganic carbon (C_T)

that is delivered to the global ocean by rivers, 13 to 15% is delivered into the Arctic Ocean [Tank et al., 2012c]. In addition, the ocean delivery of DOC from the six largest Arctic rivers is 2.5 times larger than that from temperate rivers having similar watershed size and water discharge [Raymond et al., 2007]. Riverine carbon and nutrient delivery influences Arctic Ocean biogeochemistry in multiple ways, e.g. by increasing primary production due to riverine nutrient delivery [Letscher et al., 2013; Le Fouest et al., 2013, 2015, 2018], reducing CO_2 uptake over the Siberian shelf seas due to their large riverine DOC delivery [Anderson et al., 2009; Manizza et al., 2011], and enhancing coastal ocean acidification also due to DOC delivery [Semiletov et al., 2016].

Despite the substantial riverine delivery of carbon and nutrients to the Arctic Ocean and the associated potentially large impacts on its biogeochemistry, long-term measurements of ammonium and dissolved organic nitrogen (DON) fluxes in Russian rivers were found to be unreliable [Holmes et al., 2000, 2001]. To establish a better database for riverine fluxes to the Arctic Ocean, the Pan-Arctic River Transport of Nutrients, Organic Matter, and Suspended Sediments project (PARTNERS) was launched in 2003 [McClelland et al., 2008]. PARTNERS made time–coordinated measurements of nutrients and carbon throughout the year in the six largest Arctic rivers (Ob, Yenisei, Lena, Kolyma, Yukon, Mackenzie), which cover a combined watershed area of 11.3×10^6 km^2 (55% of Arctic watersheds). In 2008, the the measurements of the PARTNERS project continue within the Arctic Great Rivers Observatory (ArcticGRO).

These observational programs have advanced the ability to assess present-day Arctic riverine fluxes, but of course they do not tell us how those fluxes could change in the future nor the corresponding effects on the biogeochemistry of the Arctic Ocean. Future riverine fluxes of carbon and nutrients are likely to increase due to advancing tree lines [Harsch et al., 2009], deepening of the active permafrost layer [Oelke et al., 2004], and degrading permafrost. Near-surface permafrost is projected to decline from 10.5 to 1.0 million km^2 by 2100 in a fully coupled global climate model (CCSM3) forced under the SRES A2 emission scenario [Lawrence and Slater, 2005], a trend that is expected to enhance riverine delivery of C_T [Tank et al., 2012a; Walvoord and Striegl, 2007] and total alkalinity (A_T) [Drake et al., 2018] to the Arctic Ocean. Simultaneously, there may be an associated 29–46% increase in DOC flux from peatlands, namely from the West Siberian watersheds, based on the observed relationship between atmospheric temperature and riverine DOC concentrations and projected temperature increases under both the SRES A2 and B2 scenarios [Frey and Smith, 2005]. Also projected for the same watersheds are simultaneous increases in concentrations of DON (32–53%), total dissolved nitrogen (TDN) (30–50%), and total dissolved phosphorus (TDP) (29–47%) [Frey et al., 2007]. Nevertheless, Frey and McClelland [2008] question these projected increases in inorganic nitrogen and organic matter delivery, because of the large uncertainties associated with river discharge projections.

Faced with uncertainties, scientists have used idealized forcing scenarios to characterize the response of complex systems. For example, Friedlingstein et al. [2001] used idealized simulations to characterize the response of the land and ocean sinks to increasing atmospheric CO_2 and

changing climate. That is, with a system that combines a coupled ocean-atmosphere general circulation model and models of the carbon cycle on land and in the ocean, they increased atmospheric CO_2 by 1% yr^{-1} and assessed the amount of atmospheric CO_2 that was taken up by land and by ocean. The responses of these land and ocean sinks was then divided into those from increasing atmospheric CO_2 and from changing climate by making two different simulations. Likewise, Boer and Arora [2010] and Roy et al. [2011] calculated the same responses, but with more plausible socioeconomic scenarios. Yet calculated climate sensitivities depend on the scenario, so there has been a return to using the classical 1% yr^{-1} idealized increase scenario [Arora et al., 2013].

This same idealized approach could be transposed to assess sensitivities of how changes in atmospheric CO_2 and riverine input of carbon and nutrients, driven in part by climate change, will alter projected changes of ocean acidification [Steinacher et al., 2009; Steiner et al., 2013], air-to-sea CO_2 fluxes [Bates et al., 2006], ocean C_T [Anderson and Kaltin, 2001], and primary production [Vancoppenolle et al., 2013], all of which may directly or indirectly affect the marine ecosystem [Darnis et al., 2012; Riebesell et al., 2013]. Quantifying such sensitivities would offer common ground from which to compare models and gauge their developments regarding how river fluxes affect Arctic Ocean biogeochemistry. For example, models disagree on the sign of change for primary production during the 21st century [Vancoppenolle et al., 2013]. They also disagree among themselves concerning the extent of future shoaling of the deep aragonite saturation horizon [Steiner et al., 2013]. Likewise, the sign of the future change in the air-to-sea CO_2 flux in the Arctic Ocean projected by models [Roy et al., 2011] is opposite that estimated by an observational study [Cai et al., 2010] but it agrees with another [Bates et al., 2006]. Yet none of these model studies consider increases in the partial pressure of CO_2 (pCO_2) from changes in riverine DOC. Few earth system models account for riverine input of carbon and nutrients. Those that do only do so in a rudimentary way even though observations indicate that such riverine input affects Arctic Ocean acidification [Chierici and Fransson, 2009; Semiletov et al., 2016], air-to-sea CO_2 fluxes [Cai et al., 2010; Manizza et al., 2011], and primary production [Tank et al., 2012b; Le Fouest et al., 2015].

Our aim here is to assess how changes in riverine fluxes affect simulated biogeochemistry, in part by providing sensitivities that quantify the effects from changes in riverine delivery of carbon and nutrients and those from increasing atmospheric CO_2. For simplicity, this study neglects effects of climate change on Arctic Ocean biogeochemistry, such as warming, stratification, and sea-ice melt.

6.2.3 Methods

6.2.3.1 Arctic regions

To assess spatial patterns in the extent of how changes in riverine carbon and nutrient delivery affect its biogeochemistry, the Arctic Ocean is divided into eight regions (Figure 6.1). The Central Arctic includes all waters where the seafloor is deeper than 500 m. The remaining area is then divided into 7 coastal seas, classed as "exterior" (Barents Sea, Chukchi Sea and Canadian Arctic Archipelago (CAA)) because of their direct exchange with the Atlantic or Pacific Ocean and "interior" (Kara Sea, Laptev Sea, East-Siberian Sea, and Beaufort Sea) because they have no such exchange.

6.2.3.2 Coupled Ocean-biogeochemical model

This study relies on the ocean general circulation modeling platform Nucleus for European Modelling of the Ocean (NEMO) more specifically its version "v3.6 stable". The here applied version of NEMO consists of the ocean general circulation model OPA from Madec [2008], the Louvain-la-Neuve Sea Ice Model (LIM3.6) [Rousset et al., 2015] and the "Tracers in the Ocean Paradigm" (TOP) model. In our case, TOP couples NEMO-LIM to the biogeochemical model "Pelagic Interactions Scheme for Carbon and Ecosystem Studies" (PISCES-v2) [Aumont et al., 2015].

Our simulations were made with the same global configuration of NEMO known as ORCA1 (1° nominal horizontal resolution), having a normal Mercator grid south of 20°N but a distorted grid north of that boundary to avoid the standard grid singularity at the North Pole (over ocean). Instead, that North-Pole singularity is replaced for numerical efficiency by two grid singularities over land (over North America and over Eurasia) [Madec and Imbard, 1996]. That distortion also causes the model's horizontal resolution to be higher in the Arctic Ocean, where the horizontal grid length varies from 25 to 63 km. Vertically, the model is split into 75 depth levels whose thicknesses increase with depth from 1 m (level 1) to 204 m (level 74). The depth of the deepest cell (level 74) can reach up to 408 m, being extended into level 75 as a function of the bathymetry (partial steps) [Barnier et al., 2006b]. Also at other vertical levels, the partial steps approach allows the depth of the deepest grid cell to be variable and thus permits a better representation of the ocean bathymetry. The ORCA1 global bathymetry map is derived from three different sources: (1) the 2-minute ETOPO2 bathymetry map from the National Geophysical Data Center, applied over most of the ocean [Smith and Sandwell, 1997]; (2) the IBCAO bathymetric data, applied in the Arctic [Jakobsson et al., 2000a]; and (3) the BEDMAP bathymetric data, applied south of 72°S [Lythe and Vaughan, 2001]. Because ORCA1 does not explicitly resolve ocean eddies, subgrid-scale eddy effects are parameterized by implementing the Gent and McWilliams [1990] scheme with an eddy diffusion coefficient of 1000 $m^2\ s^{-1}$. The corresponding lateral diffusivity coefficient is 1000 $m^2\ s^{-1}$ while its lateral viscosity coefficient is $2 \times 10^4\ m^2\ s^{-1}$.

A detailed description of the biogeochemical model PISCES is provided by Aumont et al. [2015].

Briefly, it simulates four plankton types (nanophytoplankton, diatoms, micro-, and meso-zooplankton) as well as the biogeochemical cycles of the main nutrients (N, P, Fe, and Si), C_T, A_T, and dissolved O_2. Its total net primary production (NPP) depends on temperature and is limited by light and nutrients. In PISCES, N, P, and Fe limit growth of all phytoplankton, while Si also limits growth of diatoms. For all plankton, the C:N:P molar ratio of organic matter is held constant at 122:16:1 [Takahashi et al., 1985], while the O_2:C molar ratio is fixed at 1.34 [Körtzinger et al., 2001]. The same C:N:P ratio is also fixed for the PISCES non-living compartments of marine semi-labile dissolved organic matter as well as small and large sinking particles. The PISCES model explicitly simulates, as separate tracers, phytoplankton chlorophyll, Fe, and Si (for diatoms only) concentrations. The air-to-sea CO_2 flux in PISCES is calculated from the air-sea difference in the partial pressure of CO_2, wind speed, sea-ice fraction, and CO_2 solubility and Schmidt number as summarized by Bourgeois et al. [2016]. In PISCES, calcite is the only form of $CaCO_3$ that is explicitly simulated. It is transported as a passive tracer in the model and its internal sources and sinks are dissolution and precipitation. That "$CaCO_3$ concentration" is not used to compute the aragonite saturation state (Ω_{arag}) which would be erroneous. Rather Ω_{arag} is calculated offline from $[Ca^{2+}]$ and $[CO_3^{2-}]$ concentrations using the routines from Orr and Epitalon [2015] with equilibrium constants recommended for best practices and simulated temperature, salinity, C_T, A_T, total dissolved silicon (Si_T), and total dissolved inorganic phosphorus (P_T).

6.2.3.3 River input

At the beginning of all simulations, the river inputs into the Arctic Ocean are based on annual fluxes of terrigenous DOC, dissolved inorganic nitrogen (DIN), DON, P_T, dissolved organic phosphate (DOP), and Si_T from the Global NEWS 2 model (GN2) [Mayorga et al., 2010] and C_T from the Global Erosion Model (GEM) [Ludwig et al., 1998]. The GN2 model is a composite of independent submodels for dissolved inorganic, dissolved organic, and particulate C, N, and P, as well as dissolved Si. The GN2 submodels for dissolved elements use a unified formulation. All GN2 submodels use hydrological and physical factors, hydrography, and basin characteristics to estimate annual riverine exports of DOC and nutrients. The GN2 submodels consider both, natural processes and anthropogenic activities. GEM establishes a relationship between C_T yield and hydroclimatic and geomorphological factors for four different climatic zones in 60 different river basins. These relationships depend on the climatic zone and are then applied to all rivers around the world. In our simulations, lateral boundary conditions at river mouths are applied based on contemporary annual river fluxes from GEM's C_T (R_{C_T}) and GN2's DOC (R_{DOC}), DIN and DON (R_N), P_T and DOP (R_P), and Si (R_{Si}). Along with the corresponding freshwater discharge rates given with GEM and GN2, riverine concentrations of carbon and nutrients are calculated. These concentrations are then multiplied with the monthly river discharge from Dai and Trenberth [2002] used in NEMO. The resulting river fluxes are presented in Table 6.1.

Table 6.1 – River-to-ocean fluxes[a] of C_T derived from GEM and of DOC and nutrients derived from GN2 compared to data-based estimates of R_{C_T}, R_{DOC}, R_N, R_P, and R_{Si} [Holmes et al., 2012; Tank et al., 2012c] (Section 6.2.4.1).

	R_{DOC} [Tg C yr^{-1}]		R_{C_T} [Tg C yr^{-1}]		R_N [Tg N yr^{-1}]		R_P [Tg P yr^{-1}]		R_{Si} [Tg Si yr^{-1}]	
	Model	Data	Model	Data	Model	Data	Model	Data	Model	Data
Arctic Ocean	20.3		49.8	40.8	2.30		0.090		13.4	
Barents Sea	1.9		7.1	4.7	0.22		0.010		1.4	
Kara Sea	7.8		10.0	14.7	1.09		0.037		6.6	
Ob river	3.3	4.1	1.5	5.9	0.45	0.19	0.015	0.017	3.1	1.5
Yenisei river	2.9	4.6	5.0	7.0	0.43	0.16	0.015	0.010	2.0	1.7
Laptev Sea	4.0		18.5	8.2	0.42		0.020		1.8	
Lena river	2.6	5.7	4.7	5.8	0.24	0.17	0.013	0.006	1.1	1.3
East Siberian Sea	1.5		1.9	1.7	0.12		0.005		0.7	
Kolyma river	0.8	0.8	0.9	0.8	0.06	0.03	0.003	0.001	0.2	0.3
Chukchi Sea	0.6		1.1	1.0	0.05		0.002		0.5	
Beaufort Sea	2.4		7.9	7.6	0.16		0.007		1.4	
Mackenzie river	1.9	1.4	6.3	6.3	0.12	0.06	0.006	0.003	0.8	0.6
CAA	2.0		3.3	3.0	0.24		0.008		0.9	

[a]Fluxes into the Arctic Ocean and its regional seas are given as cumulative amount draining into each region from all Arctic rivers.

For simplicity, in the ORCA1-PISCES model it is assumed that the riverine A_T:C_T ratio is 1.0. Conversely, the observed A_T:C_T ratio in rivers ranges from 0.6 in the Congo river [Wang et al., 2013] to 1.1 in the Delaware Estuary [Joesoef et al., 2017]. That ratio in the Mississippi river is 1.0 [Cai, 2003]. For the six largest Arctic rivers, Tank et al. [2012c] observed an average carbonate alkalinity(A_C):C_T ratio of 0.91 (0.72–0.94). Although they measured A_T, they report A_C, after subtracting the measured contribution from organic acids, assuming that alkalinity contributions from P_T and Si_T are negligible. Thus, their A_C is directly comparable to the simulated A_T in PISCES, which neglects organic acids. By using a globally constant A_T:C_T ratio of 1.0, we overestimate the riverine A_T flux (R_{A_T}) by 6–28% depending on the river.

Simplifications were also made to model R_{DOC}. In the standard version of PISCES the imposed river flux of terrigenous DOC (R_{DOC}) is assumed to be 100% labile, and is immediately converted to C_T as it is added to the ocean [Aumont et al., 2015]. That simplicity is maintained here, considering that as a first sensitivity assessment, our preference is to provide a limit rather than a best estimate for ocean behavior. Indeed, there are large uncertainties concerning the lability of terrigenous DOC. In North American rivers, Holmes et al. [2008] estimate that 20–40% of terrigenous DOC remineralizes within three months, whereas in Eurasian rivers Kaiser et al. [2017] estimate that close to 50% of terrigenous DOC remineralizes within a year. That partitioning may also change in the near future, as more old, labile terrestrial carbon becomes available due to thawing of permafrost [Vonk and Gustafsson, 2013].

Given our two simplifications, i.e., that the riverine flux of A_T (R_{A_T}) equals R_{C_T} and that R_{DOC}

is immediately converted to C_T as it is added to the ocean, the effective $R^{\star}_{A_T}$:$R^{\star}_{C_T}$ ratio, imposed as the river flux boundary condition for PISCES is

$$\frac{R^{\star}_{A_T}}{R^{\star}_{C_T}} = \frac{R_{C_T}}{R_{C_T} + R_{DOC}}, \tag{6.1}$$

where $R^{\star}_{C_T}$ and $R^{\star}_{A_T}$ are the river flux boundary conditions for PISCES calculated from the river fluxes derived from GEM (R_{C_T}) and Global NEWS 2 (R_{DOC}). Thus, an increase in R_{C_T} would increase the $R^{\star}_{A_T}$:$R^{\star}_{C_T}$ ratio, while an increase in R_{DOC} would reduce it. To illustrate the uncertainties associated with the two simplifications, we compared our calculated $R^{\star}_{A_T}$:$R^{\star}_{C_T}$ boundary condition for the five major rivers that drain directly into the Arctic Ocean to what it would have been had we used a more realistic R_{DOC} lability of 50% [Kaiser et al., 2017] and the R_{A_T}:R_{C_T} from Tank et al. [2012c], which varies among those rivers (Figure S1). Relative to our simplified case, an R_{DOC} lability of 50% would increase the $R^{\star}_{A_T}$:$R^{\star}_{C_T}$ ratio, while imposing a R_{A_T}:R_{C_T} below one, as observed, would reduce it. Combined, the two simplifications cause the $R^{\star}_{A_T}$:$R^{\star}_{C_T}$ ratio to be overestimated in the CTL simulation by 6% in the Kolyma river and to be underestimated by 5-22% in the remaining four rivers. Due to our two simplifications, the change of the $R^{\star}_{A_T}$:$R^{\star}_{C_T}$ ratio when riverine DOC is doubled is underestimated by 7% for the Ob and overestimated by 26–55% in the remaining four rivers. However, our two simplifications do not alter the direction of the change in the $R^{\star}_{A_T}$:$R^{\star}_{C_T}$ ratio, as discussed in section 4.2. Invariably, that ratio declines when the riverine DOC flux is doubled, and it increases when the riverine C_T flux is doubled.

6.2.3.4 Transient simulations

We made five 75-year simulations, each with the same physical forcing, the daily climatological DRAKKAR Forcing Set 4.4 (DFS4.4) [Brodeau et al., 2010]. The DFS4.4 forcing files include historical reanalyses of atmospheric air temperature and humidity at 2 m, zonal and meridional wind fields at 10 m, downward shortwave and longwave radiation at 2 m, and the net surface freshwater flux (precipitation minus evaporation). The first version of DFS4.4 is based on the ERA40 reanalysis [Uppala et al., 2005] and covers 45 years (1958-2002). DFS4.4 was extended until 2012 using ERA-interim reanalysis [Dee et al., 2011] thus covering 55 years in total. For our 75-year simulations, after the first 55 years we reused the initial 20 years of DFS4.4. This relooping of DFS4.4 is facilitated by efforts made during its construction to make adjustments for global and regional biases and to reduce time discontinuities in data from different sources, which would otherwise result in spurious trends [Brodeau et al., 2010].

To quantify the effect of changes in riverine delivery on Arctic biogeochemistry, we separately altered one aspect of each of the simulations: (1) a preindustrial control simulation (CTL) with a constant atmospheric CO_2 fixed at 284.7 ppm (1850) having constant riverine input as prescribed in section 6.2.4.1; (2) a simulation just like CTL except that atmospheric CO_2 is increased by 1% per year (CO2); (3) a simulation just like CO2 except that R_{DOC} is also increased by 1% per year (ROC),

Table 6.2 – Scheme of the five simulations for the sequential 1% yr^{-1} increases in atmospheric CO_2 and riverine C_T, DOC, and nutrient fluxes.

Simulation	CO_2^{atm}	R_{DOC}	R_{C_T}	R_{NUT}(N, P, Si)
CTL	-	-	-	-
CO2	•	-	-	-
ROC	•	•	-	-
RIC	•	•	•	-
RUT	•	•	•	•

which is instantaneously and completely remineralized thus increasing $R^{\star}_{C_T}$; (4) a simulation just like ROC except that R_{C_T} is also increased by 1% per year (RIC), which increases $R^{\star}_{A_T}$ as well as $R^{\star}_{C_T}$; and (5) a simulation just like RIC except that the nutrient river flux (R_{NUT}) is also increased by 1% per year (RUT) (Table 6.2). The 1% per year increase in riverine inputs concerns all rivers, not just those in the Arctic. That rate of increase leads to a doubling after 70 years. The differences between the simulations, allows us to distinguish the effects of increases in atmospheric CO_2, R_{DOC}, R_{C_T}, and R_{NUT} on Arctic Ocean biogeochemistry. The differences between these simulations are referred to as ΔCO_2 (CO2-CTL), ΔROC (ROC-CO2), ΔRIC (RIC-ROC), and ΔRUT (RUT-RIC).

To smooth out interannual variations, all model results were compared in terms of their averages over simulated years 66–75, i.e., centered around the time when the simulated atmospheric CO_2 doubled from the imposed 1% yr^{-1} increase. To assess air-to-sea CO_2 fluxes, NPP, pH, and Ω_{arag}, we also calculated 10-year averages for years 26 to 35 when atmospheric CO_2 varies between 369 and 399 ppm, similar to values observed at the beginning of this century. Initial conditions for atmospheric CO_2 represent the preindustrial level, while those for river input and climate are based on modern data.

6.2.3.5 Sensitivity factors

Sensitivities of Arctic Ocean primary production, C_T storage, air-to-sea CO_2 flux, and pH to increases in atmospheric CO_2, R_{DOC}, R_{C_T}, and R_{NUT} were calculated following the approach first proposed by Friedlingstein et al. [2003] to assess the sensitivities of land and ocean carbon sinks to increasing atmospheric CO_2 and to anthropogenic climate change. That approach was extended here to calculate sensitivities not only for the air-to-sea CO_2 flux (β) but also for ocean carbon storage (ζ), primary production (η), and pH (ξ), all with respect to increasing atmospheric CO_2. Corresponding sensitivities were also calculated with respect to the three other drivers (R_{DOC}, R_{C_T}, and R_{NUT}). For these sensitivity factors only riverine delivery from rivers draining directly into the Arctic Ocean were taken account.

To quantify the sensitivity of global ocean carbon storage to the atmospheric CO_2 increase ($\beta^{global}_{\Delta CO_2}$), our approach exactly follows that of Friedlingstein et al. [2006],

$$\beta^{global}_{\Delta CO_2} = \frac{\Delta C_O^{global}}{\Delta C_A} = \frac{\int F^{global} dt}{\Delta C_A}, \tag{6.2}$$

where ΔC_A is the change in the atmospheric CO_2 mixing ratio (in ppm) between the beginning and end of the simulation, ΔC_O^{global} is the change of C_T in the global ocean during the same period, and F^{global} is the difference in global air-to-sea CO_2 flux in response to increasing atmospheric CO_2. At the global scale, the time-integrated air-to-sea CO_2 flux and the change in carbon storage are identical. Regionally though, they are unlikely to be the same. In the Arctic Ocean, much of the anthropogenic carbon enters laterally [Terhaar et al., 2018], causing these two diagnostics to differ. To distinguish the two diagnostics in the Arctic Ocean, β is used to indicate the sensitivity of the air-to-sea CO_2 flux (Equation 6.3), while ζ is used for the sensitivity of ocean carbon storage,

$$\beta_{\Delta CO_2} = \frac{\int F^{\Delta CO_2} dt}{\Delta C_A}, \text{ and} \tag{6.3}$$

$$\zeta_{\Delta CO_2} = \frac{\Delta C_O^{\Delta CO_2}}{\Delta C_A}, \tag{6.4}$$

where $F^{\Delta CO_2}$ is the difference in air-to-sea CO_2 flux in response to increasing atmospheric CO_2 areally integrated over the Arctic Ocean, and $\Delta C_O^{\Delta CO_2}$ is the change in C_T storage within the Arctic Ocean in response to an increase in atmospheric CO_2.

Likewise, the sensitivities of the air-to-sea CO_2 flux to changes in R_{DOC}, R_{C_T}, and R_{NUT} are as follows:

$$\beta_{\Delta ROC} = \frac{\int F^{\Delta ROC} dt}{\int \Delta R_{DOC} dt}, \tag{6.5}$$

$$\beta_{\Delta RIC} = \frac{\int F^{\Delta RIC} dt}{\int \Delta R_{C_T} dt}, \text{ and} \tag{6.6}$$

$$\beta_{\Delta RUT} = \frac{\int F^{\Delta RUT} dt}{\int \Delta R_{NUT} dt}, \tag{6.7}$$

where ΔR_{DOC}, ΔR_{C_T}, and ΔR_{NUT} are differences of riverine input of each of those species into the Arctic Ocean between a given year and that at the beginning of each simulation, while $F^{\Delta ROC}$, $F^{\Delta RIC}$, and $F^{\Delta RUT}$ are the differences in air-to-sea CO_2 fluxes in response to increases in R_{DOC}, R_{C_T}, and R_{NUT} between the same two times after integrating areally over the Arctic Ocean. Similarly, the sensitivities of Arctic Ocean carbon storage to increasing riverine inputs of DOC, C_T, and nutrients are defined as

$$\zeta_{\Delta ROC} = \frac{C_O^{\Delta ROC}}{\int \Delta R_{DOC} dt}, \tag{6.8}$$

$$\zeta_{\Delta RIC} = \frac{C_O^{\Delta RIC}}{\int \Delta R_{C_T} dt}, \text{ and} \tag{6.9}$$

$$\zeta_{\Delta RUT} = \frac{C_O^{\Delta RUT}}{\int \Delta R_{NUT} dt}, \tag{6.10}$$

where $C_O^{\Delta ROC}$, $C_O^{\Delta RIC}$, and $C_O^{\Delta RUT}$ are the time differences in Arctic Ocean C_T, integrated vertically and areally over the Arctic, induced by the corresponding increases in riverine input. The $\zeta_{\Delta RUT}$ does not account for ocean POC and organic carbon burial.

It follows that the sensitivity of NPP (η) to changes in riverine nutrients is

$$\eta_{\Delta RUT} = \frac{\int NPP^{\Delta RUT} dt}{\int \Delta R_{NUT}(t) dt}, \tag{6.11}$$

where $NPP^{\Delta RUT}$ is the change in the vertically and horizontally integrated primary production from increased riverine nutrients. In the same way, sensitivities of pH (ξ) to changes in atmospheric CO_2 and inputs of riverine DOC and C_T are

$$\xi_{\Delta CO_2} = \frac{pH^{\Delta CO_2}}{\Delta C_A}, \tag{6.12}$$

$$\xi_{\Delta ROC} = \frac{pH^{\Delta ROC}}{\int \Delta R_{DOC} dt}, \text{ and} \tag{6.13}$$

$$\xi_{\Delta_{RIC}} = \frac{pH^{\Delta RIC}}{\int \Delta R_{C_T} dt}, \tag{6.14}$$

where $pH^{\Delta CO2}$, $pH^{\Delta ROC}$, and $pH^{\Delta RIC}$ are the areally averaged changes in surface pH in response to increases in atmospheric CO_2, river input of DOC, and river input of C_T, respectively. To calculate these basinwide differences, the pH values at every grid cell in the Arctic Ocean were first converted to hydrogen ion concentrations $[H^+]$ on the total scale. The $[H^+]$ was then areally averaged at each time, the results were converted back to pH units, and the difference between the two simulations was taken.

6.2.4 Evaluation

6.2.4.1 Riverine forcing

To evaluate the Arctic river flux estimates derived from GN2 and GEM, they were compared to data-based fluxes from the five largest Arctic rivers that drain directly into the Arctic Ocean (Table 6.1), i.e. R_{C_T} is from Tank et al. [2012c], and R_{DOC} and R_{NUT} from Holmes et al. [2012]. The model's GEM derived total R_{C_T} flux to our Arctic Ocean domain (50 Tg C yr^{-1}) falls within the uncertainty range of Tank et al.'s data-based estimate (41 ± 10 Tg C yr^{-1}) from their extrapolation of the fluxes from the six major Arctic rivers to all rivers that discharge into the Arctic Ocean. The GEM derived R_{C_T} fluxes typically overestimate the extrapolated fluxes but by no more than 12% in the East Siberian Sea, East-Siberian Sea, the Chukchi Sea, the Beaufort Sea, and the CAA. Larger overestimates are found for the Barents Sea (+51%) and the Laptev Sea (+126%), while the general tendency is reversed in the Kara Sea (-32%).

For R_{DOC} and R_{NUT}, data-based fluxes have not been extrapolated to all Arctic rivers. They are available only for the five largest rivers draining directly into the Arctic Ocean [Holmes et al., 2012]. The GN2-based R_{DOC} fluxes for the Lena river are 55% smaller than data-based estimates, while those for the Ob and Yenisei are 20–37% smaller. Those fluxes for the Kolyma agree with the data-based estimates. Unlike for those Siberian rivers, the GN2-based R_{DOC} flux for Canada's Mackenzie river is 36% larger than the data-based estimate. For R_N, the GN2-based flux for the five observed rivers is 41–169% larger than data-based estimates. For R_P, the GN2-based flux estimates for the Yenisei, Lena, Kolyma, and Mackenzie are 50–200% larger then data-based estimates while that for the Ob is 12% smaller. For R_{Si}, the GN2-based estimates for the Lena and Kolyma rivers are 15–33% smaller than data-based estimates, while those for the Ob, Yenisei, and Mackenzie rivers are 18–107% larger.

6.2.4.2 Net Primary Production

Simulated NPP from the CTL simulation was compared to the data product from Hill et al. [2013] derived from remotely sensed ocean color and observed vertical profiles of *in situ* chlorophyll *a*. From this data product, the estimated annual-mean NPP, integrated vertically and areally over the Arctic Ocean, is 433 Tg C yr^{-1}. The simulated NPP is much less (165 Tg C yr^{-1}), but captures similar regional patterns (Figure 6.2 and Table 6.3).

Regionally, the largest model-data differences are found in the three exterior shelf seas: out of the basinwide integrated bias, 49% (132 Tg C yr^{-1}) is located in the Barents Sea, 31% (84 Tg C yr^{-1}) in the CAA, and 24% (63 Tg C yr^{-1}) in the Chukchi Sea (Table 6.3). The Barents Sea is strongly influenced by inflow from the adjacent Atlantic Ocean while the Chukchi Sea is influenced by inflow from the adjacent Pacific Ocean. Inflow of nutrients from those neighboring oceans fuel at least 20% of the Arctic Ocean NPP [Popova et al., 2013]. That nutrient inflow may well be underestimated in the coarse resolution model used here (ORCA1). Lateral water fluxes into the Arctic Ocean are underestimated using a coarser resolution version (ORCA2) of the same NEMO-PISCES model, and they are improved when using higher-resolution eddying versions ORCA05 and ORCA025 [Terhaar et al., 2018]. Thus our weak modeled lateral nutrient inflow may result in the low simulated NPP in the Barents Sea and Chukchi Sea. In the CAA, the discrepancy appears to be mainly caused by differences in the definition of the regional borders of the CAA, which is defined here to be bounded on the south by the Baffin Bay, but for Hill et al. [2013] it extends further south to the Davis Strait. The latter domain includes additional ice-free areas with strong primary production. Unlike for these "exterior" seas, the integrated simulated NPP in the "interior" seas is 4% (2 Tg C yr^{-1}) smaller than the data-based estimates. The total underestimation in these "exterior" and "interior" seas adds up to more than 100% of the total bias, because the latter is reduced by an overestimation of simulated NPP in the Central Arctic by 540% (12 Tg C yr^{-1}).

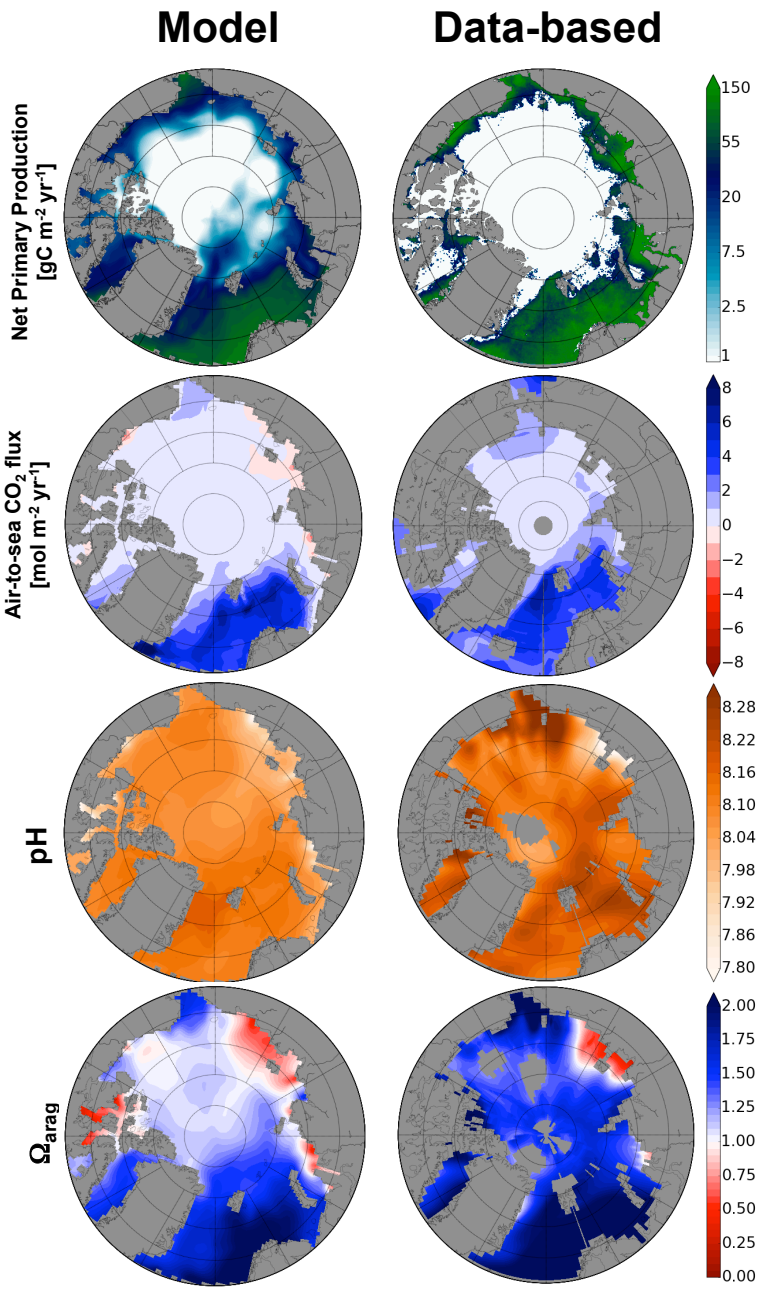

Figure 6.2 – Simulated (left) and data-based (right) NPP (integrated vertically), air-to-sea CO_2 flux, and surface pH and Ω_{arag} (top to bottom). Data-based depth-integrated NPP is derived from remotely sensed ocean color from SeaWiFS over 1998–2005 [Arrigo and van Dijken, 2011]. The data-based, annual-mean air-to-sea fluxes of total CO_2 from 1997 to 2013 are estimates derived with self-organizing pCO_2 maps [Yasunaka et al., 2016]. Data-based surface pH and Ω_{arag} are from the GLODAPv2 gridded data product that normalizes observations to 2002 [Lauvset et al., 2016]. The modeled air-to-sea CO_2 flux is the decadal average over years 26–35, over which the average atmospheric CO_2 was similar to that during the time span of the data-based estimates. The modeled pH and Ω_{arag} are averaged over July, August, and September to compare with the summer-biased GLODAPv2 data in the Arctic; conversely, the simulated air-to-sea CO_2 fluxes and NPP are annual average conditions as are the data-based estimates.

Table 6.3 – Simulated NPP (CTL), data-based NPP, and changes in NPP from ΔRUT at doubling, all in Tg C yr^{-1}.

	CTL	Data-based[a]	ΔRUT
Arctic Ocean	164.7	432.9	18.0
Barents Sea	80.0	212.0	4.8
Kara Sea	21.8	16.0	4.4
Laptev Sea	7.3	21.9[b]	2.5
East-Siberian Sea	6.2		1.6
Chukchi Sea	22.6	85.5	0.4
Beaufort Sea	3.4	2.3	1.2
CAA	9.3	93.0[c]	2.1
Central Arctic	14.1	2.2	1.0

[a] Hill et al. [2013]

[b] In the data-based estimates, the Laptev and East-Siberian Seas are only reported as a combined estimate.

[c] In the data-based estimate, the CAA extends further south (to the Davis Strait) than in our study.

6.2.4.3 Total air-to-sea CO_2 flux

At present, all subregions of the Arctic Ocean take up both natural and anthropogenic carbon from the atmosphere. Eventually most of that absorbed carbon is transported out of Arctic Ocean laterally [Bates and Mathis, 2009; Yasunaka et al., 2016], although some local outgassing is observed in the Pacific dominated sectors immediately after sea-ice retreat in spring [Arrigo et al., 2010] and on the Siberian shelf in summer after high river discharge of terrigenous DOC [Anderson et al., 2009]. The annually average total air-to-sea CO_2 flux in the Arctic Ocean is estimated to be 66–199 Tg C yr^{-1} over 2000–2009 [Bates and Mathis, 2009]. The simulated Arctic Ocean air-to-sea CO_2 flux at the same level of atmospheric CO_2 is 92 Tg C yr^{-1} falling within the data-based range (Table 6.4). Three-fourths of that air-to-sea CO_2 flux occurs in the Barents Sea. The next largest simulated air-to-sea CO_2 flux occurs in the Chukchi Sea, but is ten times smaller. The same regional pattern is displayed by data-based estimates with the Barents Sea absorbing 44–77 Tg C yr^{-1} and the Chukchi Sea taking up 11–53 Tg C yr^{-1}. This underestimation of total air-to-sea CO_2 flux in the Chukchi Sea is consistent with the same region's underestimated NPP (Table 6.3).

6.2.4.4 Carbonate chemistry

We evaluate the simulated surface ocean pH by comparing preindustrial, present-day, and future pH estimates to the simulated pH at the corresponding atmospheric CO_2 levels in the CO2 sim-

Table 6.4 – Simulated total air-to-sea CO_2 fluxes [Tg C yr^{-1}] for the CTL simulation, the CO2 simulation at 379 ppm, and the data-based estimates, as well as the differences between simulations

	CTL	ΔCO2	ΔROC	ΔRIC	ΔRUT	CO2	Data-based[a]
Arctic Ocean	69.1	19.3	-18.2	-2.1	5.4	91.6	65–199
Barents Sea	51.8	14.0	-2.1	-0.3	1.9	68.1	44–77
Kara Sea	4.9	-0.8	-6.1	-0.2	1.2	5.5	1–6
Laptev Sea	-1.0	-0.1	-3.6	-0.6	0.7	-1.0	1–4
East-Siberian Sea	1.0	-0.1	-1.5	-0.1	0.4	1.2	0–13
Chukchi Sea	5.4	1.8	-0.5	-0.1	0.1	6.8	11–53
Beaufort Sea	-0.3	0.0	-1.6	-0.2	0.4	-0.2	2–3
CAA	1.3	1.5	-1.6	-0.2	0.6	2.5	16–24[b]
Central Arctic	6.0	3.0	-1.3	-0.4	0.3	8.9	6–19

[a] Bates and Mathis [2009]

[b] Scaled to the area of the CAA assuming the same flux rate as in the Beaufort Sea

ulation. Our simulated preindustrial surface pH averaged over the Arctic Ocean is 8.17, which is 0.06 less than that from a previous study with a coupled carbon-climate model [Steinacher et al., 2009].

When doubling atmospheric CO_2 in our model (569 ppm), average surface-ocean pH decreases by 0.3. One third of this decrease occurs by the time that the model's atmospheric CO_2 reaches 347–379 ppm (equivalent to observed values over 1986–2005). The 0.1 decrease in pH when atmospheric CO_2 reaches 347–379 ppm agrees with the data-based estimate for that historical surface pH change for the Arctic Ocean [Anderson et al., 2010]. The further 0.2 pH reduction by the time of atmospheric CO_2 doubling agrees with the projected decrease for Arctic Ocean surface pH calculated by an ensemble of CMIP5 models forced under the RCP4.5 scenario [Steiner et al., 2013], where atmospheric CO_2 reached 583 ppm 2100.

The simulated mean Arctic surface pH averaged over years 26–35, when the atmospheric CO_2 forcing averages 374 ppm, was further compared to the gridded GLODAPv2 climatology [Lauvset et al., 2016]. Although the simulated surface pH is on average 0.01 too high, the model and data product both indicate notably lower pH in regions with high freshwater input (on the East Siberian shelf, along the transpolar drift, and near the mouths of the Ob and Yenisei rivers) and higher pH along the east coast of Greenland, in the Kara Sea, and near the St. Anna trough (Figure 6.2). Besides model deficiencies, differences between the model and the data-based product might be caused by the relatively sparse observations in space and time.

Regional averages of simulated preindustrial Ω_{arag} are all supersaturated (Table 6.5), consistent with other studies [Steinacher et al., 2009; Anderson et al., 2010], but are spatially heteroge-

neous, varying from 1.17 to 2.01. The highest Ω_{arag} regions are those that are strongly influenced by outside inflow, i.e., the Barents Sea (Ω_{arag} = 2.01) adjacent to the Atlantic, and the Chukchi Sea (Ω_{arag} = 1.66) adjacent to the Pacific. The low Ω_{arag} regions are more influenced by riverine input, e.g., the Laptev Sea (Ω_{arag} = 1.17) and the East-Siberian Sea (Ω_{arag} = 1.17) (Table 6.5). The simulated spatial patterns in Ω_{arag} are similar to those found in the GLODAPv2 gridded data product [Lauvset et al., 2016] (Figure 6.2) as well as in several other observational studies, all of which which indicate near-zero Ω_{arag} values near the mouths of the Mackenzie [Chierici and Fransson, 2009], Yukon [Mathis et al., 2011], and Lena rivers [Semiletov et al., 2016].

The low Ω_{arag} in the coastal Arctic Ocean is driven by the dilution from Arctic river waters, with not only relatively low A_T:C_T ratios (0.7–0.9) but also low A_T (500–1600 µmol kg^{-1}) and C_T (650–1700 µmol kg^{-1}) [Tank et al., 2012c]. Typical open ocean values are higher for the A_T:C_T ratio (1.1–1.2) and for both A_T (2300 µmol kg^{-1}) and C_T (2150 µmol kg^{-1}). Out of the five major rivers that drain into the Arctic Ocean, the lowest A_T and C_T (500–1000 µmol kg^{-1}) concentrations and the lowest A_T:C_T ratio (0.73) are found in the Kolyma river, perhaps because of rapid degradation of large amounts of labile terrigenous DOC originating from the Arctic's largest watershed that is entirely covered by permafrost [Mann et al., 2015].

6.2.5 Changes due to increasing riverine input

6.2.5.1 Effect of riverine nutrient increase

Doubling R_{NUT} increases the simulated NPP in the Arctic Ocean by 11% (18 Tg C yr^{-1}) (Table 6.3). That increase in NPP is driven by an additional fixation of 2.36 Tg N yr^{-1}, about the same as the additional supply of riverine nitrogen to the Arctic Ocean (2.30 Tg N yr^{-1}), suggesting that this input may be completely consumed by primary production. Regionally, the largest absolute increases in NPP are simulated in the Barents Sea (+4.8 Tg C yr^{-1}, i.e., +6%)) and the Kara Sea (+4.4 Tg C yr^{-1}, i.e., +20%)) (Table 6.3). The large increase in the Barents Sea represents 27% of total Arctic NPP increase, although the increase in the R_{NUT} boundary condition represents only 10% of the total Arctic R_{NUT} increase (Table 6.1). This discrepancy suggests that that region's increase in NPP is mainly driven by the additional influx of nutrients from outside the Arctic, given that the imposed R_{NUT} boundary condition increases in all rivers across the globe. The large increase in the Kara Sea represents 24% of total Arctic NPP increase. As opposed to the Barents Sea, the increase of R_{NUT} into the Kara Sea is 47% of total Arctic R_{NUT} increase. This large amount of extra nutrients thus solely explains Kara Sea's strong increase in NPP. Although the largest absolute changes in NPP occur in the Barents and Kara Seas, the largest relative changes occur in the Laptev and Beaufort Seas (+34% and +35%, respectively) (Table 6.3).

Basinwide, the largest absolute changes in NPP are typically found within 100–200 km of the coastline, where they are often twice as large as average changes in adjacent waters further offshore (Figure 6.3). Yet the coastal-to-open ocean gradients in NPP may well be overestimated be-

Table 6.5 – Modeled average surface pH and Ω_{arag} for CTL and the differences between simulations.

	CTL	ΔCO2	ΔROC	ΔRIC	ΔRUT
pH					
Arctic Ocean	8.17	-0.30	-0.02	0.02	0.00
Barents Sea	8.22	-0.30	0.00	0.01	0.00
Kara Sea	8.15	-0.32	-0.04	0.02	0.00
Laptev Sea	8.10	-0.29	-0.05	0.06	0.00
East-Siberian Sea	8.13	-0.30	-0.02	0.02	0.00
Chukchi Sea	8.20	-0.30	0.00	0.01	0.00
Beaufort Sea	8.10	-0.27	-0.08	0.04	0.00
CAA	8.16	-0.28	-0.03	0.02	0.00
Central Arctic	8.18	-0.29	-0.01	0.01	0.00
Ω_{arag}					
Arctic Ocean	1.53	-0.71	-0.02	0.06	0.00
Barents Sea	2.01	-0.93	0.00	0.02	0.00
Kara Sea	1.44	-0.70	-0.03	0.06	0.00
Laptev Sea	1.17	-0.55	-0.06	0.19	0.00
East-Siberian Sea	1.17	-0.57	-0.02	0.06	0.00
Chukchi Sea	1.66	-0.78	-0.01	0.02	0.00
Beaufort Sea	1.29	-0.58	-0.09	0.11	0.01
CAA	1.38	-0.63	-0.04	0.05	0.00
Central Arctic	1.50	-0.69	-0.02	0.05	0.00

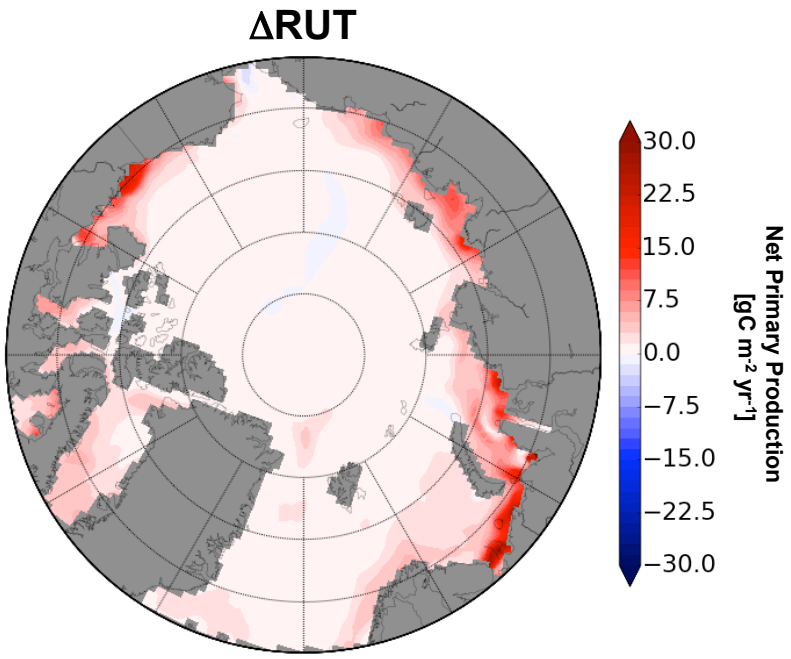

Figure 6.3 – Simulated changes in depth-integrated NPP (gC m^{-2} yr^{-1}) from the doubling of riverine nutrients (ΔRUT)

cause in our simulations it is imposed that DON and DOP river fluxes (R_N and R_P) are immediately transformed to inorganic N and P as they enter the Arctic Ocean (section 6.2.4.1). In the real ocean, portions of the DON and DOP are transported offshore before being transferred to inorganic N and P, thus reducing the coastal-to-open ocean gradients in inorganic nutrients and NPP.

Changes in NPP from the doubling of R_{C_T} and R_{DOC} are generally more than a hundred times smaller than changes induced by doubling nutrients. Yet the version of PISCES used here does not account for any direct effect of increasing CO_2 on phytoplankton productivity. Indirectly, it only accounts for effects of the CO_2-driven changes in carbonate chemistry on calcite dissolution, which affects sinking of inorganic particles and the scavenging of iron.

The simulated increase in NPP from the increase in R_{NUT} may be put into context by comparing it to NPP changes from climate-related reductions in sea-ice projected by an ensemble of 11 CMIP5 models [Vancoppenolle et al., 2013]. When these models were forced under the RCP8.5 scenario, the projected changes in Arctic Ocean NPP ranged from -110 Tg C yr^{-1} to 253 Tg N yr^{-1} for the average over 2080–2099 minus that over 1980–1999. Over that period, their average increase (58 Tg C yr^{-1}) from climate change is around 3 times larger than the Arctic's basinwide increase due to the doubling of nutrient delivery in our RUT simulation.

The NPP increase from increased river nutrient fluxes also reduces surface C_T and thus surface-ocean pCO_2, consequently enhancing the Arctic Ocean's air-to-sea CO_2 flux. The regions with the largest simulated increase in NPP (Barents Sea, Kara Sea, Laptev Sea, and the CAA) (Table 6.3) also have the largest increase in the air-to-sea CO_2 flux (> 0.6 Tg C yr^{-1} for each sea) at year 70 (Table 6.4). These ties between NPP and air-to-sea CO_2 flux are similar to those seen in the other

regional seas (Figures 6.3 and 6.4). At the time of R_{NUT} doubling, the change in NPP (18 Tg C yr^{-1}) enhances the air-to-sea CO_2 flux and hence the Arctic Ocean's carbon storage by 1.83 Tg C yr^{-1}, of which 74% is stored in the Central Arctic Ocean, 11% in the CAA, and 6% in the Barents Sea. The remaining 7% is spread over the other Arctic shelf seas.

6.2.5.2 Effect of riverine carbon increase

The simulated doubling of R_{DOC} reduces the net Arctic Ocean air-to-sea CO_2 flux by 18.2 Tg C yr^{-1}, compensating 94% of the increase in the Arctic Ocean's air-to-sea CO_2 flux from the doubling of atmospheric CO_2 (Table 6.4). However, even if the air-to-sea CO_2 flux from the doubling of atmospheric CO_2 was completely compensated by R_{DOC}, the Arctic Ocean would still remain a sink of anthropogenic carbon, which mainly enters the Arctic Ocean laterally from the adjacent ocean basins [Olsen et al., 2015; Terhaar et al., 2018].

Out of the added R_{DOC}, which is instantaneously converted to C_T, 90% is lost from the Arctic Ocean via outgassing of CO_2, 7% is transported out of the Arctic Ocean laterally, and 3% remains there. That outgassing is strongest in the Kara Sea (6.1 Tg C yr^{-1}), which changes from a net sink to a net source of CO_2 (Table 6.4). The same change from CO_2 sink to source occurs in the East-Siberian Sea. Although the Laptev and Beaufort Seas already exhibit outgassing at the end of the CO2 simulation, the doubling of R_{DOC} increases that outgassing by up to several times. Thus, when R_{DOC}, is doubled, all interior Arctic shelf seas become sources of carbon to the atmosphere even when atmospheric CO_2 levels have also doubled. Nevertheless, the Barents Sea, the Chukchi Sea, and the Arctic Ocean as a whole remain as sinks of atmospheric CO_2.

When R_{DOC} is doubled, the shelf waters immediately adjacent to large river mouths become small hotspots of CO_2 outgassing with intensities that are roughly two to four times as strong as associated outgassing from each surrounding regional sea (Figure 6.4). Away from river mouths, the associated outgassing declines rapidly as river waters are diluted in the sea and surface ocean pCO_2 plummets.

The assumption that the R_{DOC} boundary flux for PISCES is immediately converted to a flux of C_T is merely a first limiting case for an idealized case study and is much simpler than what occurs in the real world. From observed concentration gradients of terrigenous DOC in the Beaufort Gyre, Hansell et al. [2004] estimate that the half-life of terrigenous DOC in the Arctic Ocean is 7.1 ± 3.0 yr, assuming exponential degradation and average residence time of river waters in the Arctic Ocean of 11 to 15 years based on isotopic water mass tracers. Hansell et al. [2004] further estimate that 21–32% of R_{DOC} is exported laterally to the North Atlantic before being remineralized to C_T in the Arctic. More recent studies suggest larger uncertainties, i.e. that 20–50% of terrigenous DOC is remineralized in estuaries or the shelf seas [Letscher et al., 2011; Kaiser et al., 2017; Holmes et al., 2008; Spencer et al., 2009]. Besides those large uncertainties, the future rate of degradation of terrestrial carbon may increase in the future as old, terrestrial DOC, which is more labile, is

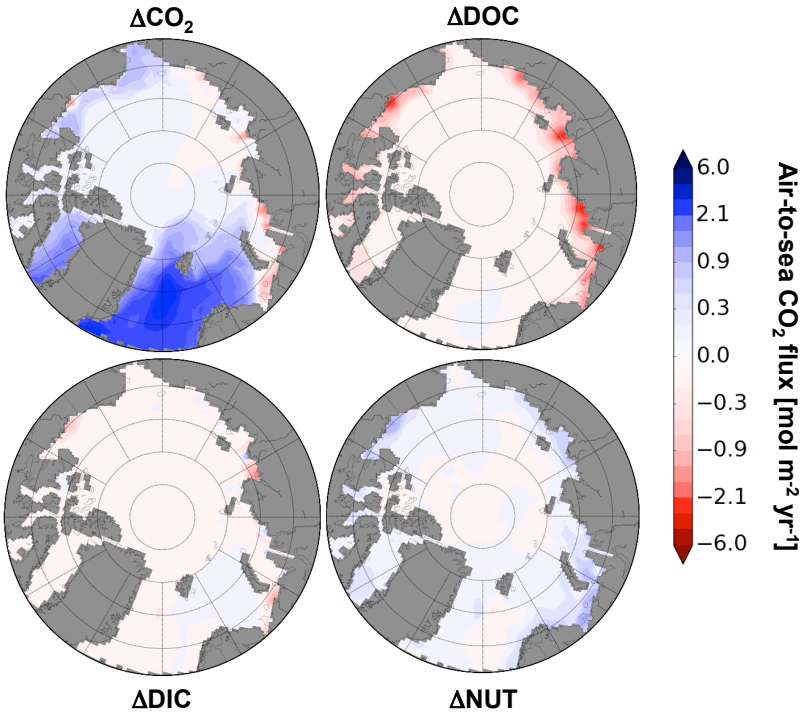

Figure 6.4 – Modeled changes in air-to-sea CO_2 flux (mol m^{-2} yr^{-1}) for ΔCO2, ΔROC, ΔRIC, and ΔRUT. The colorbar axis is not regular.

mobilized during continuous thawing of permafrost [Holmes et al., 2008; Vonk and Gustafsson, 2013; Letscher et al., 2011].

The model assumption that R_{DOC} is added to PISCES as C_T, equivalent to a immediate remineralization of terrigenous DOC, allows only 7% of that carbon to leave the Arctic (in the form of C_T), a smaller amount than estimated by Hansell et al. [2004], especially because their estimate does not consider the outflow of C_T from remineralized terrigenous DOC. That comparison emphasizes further that our model overestimates the loss of terrigenous DOC to the atmosphere and underestimates the export of that dissolved carbon out of the Arctic. Specifying a semi-labile pool of terrigenous DOC in the model would lead to greater offshore transport of DOC before it could be remineralized to C_T. Consequently surface ocean pCO_2 and hence CO_2 outgassing would decrease near the river mouths and increase of pCO_2 elsewhere in the Arctic Ocean as this semi-labile terrigenous DOC were remineralized later.

Unlike the effect from a doubling of R_{DOC}, the doubling of R_{C_T} allows 96% of the added C_T to remain in the ocean (~3/4 in the Arctic and ~1/4 in the Atlantic after 70 years of simulation). Out of the C_T that remains in the Arctic Ocean, 71% ends up in the central Arctic Ocean, while the remainder is distributed between the CAA (10%), the Barents Sea (6%), the Laptev Sea (5%), the Kara Sea (4%), the East-Siberian Sea (3%), and the Chukchi and Beaufort Seas (1% each). Only 4% of that additional C_T is emitted to the atmosphere (Table 6.4) because R_{A_T} is assumed to increase exactly in step with R_{C_T}. Therefore the $R^{\star}_{A_T}$:$R^{\star}_{C_T}$ (Equation 6.1) ratio increases in RIC compared to its decrease in ROC.

For simplicity, the PISCES model assumes that R_{A_T} equals R_{C_T}. In contrast, in three out of the five major Arctic rivers that drain directly into the Arctic Ocean, the A_T:C_T ratio varies from 0.91 to 0.94 [Tank et al., 2012c]. In the remaining two major Arctic rivers, the Kolyma and Ob, that ratio is 0.7 and 0.84, respectively. Thus, in the RIC simulation, the amount of added C_T that is not buffered by an equivalent increase in A_T, is up to 30%, a fraction that behaves as does the pure C_T added in the ROC simulation where terrigenous DOC is assumed to be instantaneously remineralized to C_T at the river mouth. Thus, by assuming R_{A_T} to be equal to R_{C_T}, we underestimate the outgassing of CO_2 in RIC and overestimate the corresponding increase in pH and Ω_{arag} as detailed in the following section.

6.2.5.3 $R^{\star}_{A_T}$:$R^{\star}_{C_T}$ ratio and coastal ocean acidification

Doubling R_{DOC} decreases the $R^{\star}_{A_T} : R^{\star}_{C_T}$ flux ratio (equation 6.1) from 0.71 to 0.55, i.e. for ΔROC, which in turn lowers the Arctic coastal ocean A_T:C_T ratio along with pH and Ω_{arag}. Basinwide average changes of pH and Ω_{arag} both reach -0.02, at most 7% of the respective changes due to the atmospheric CO_2 increase (Table 6.5). Larger changes occur in the regional seas, e.g. reaching up to -0.08 for pH and -0.09 for Ω_{arag}, at most 30% of the respective changes due to the atmospheric CO_2 increase. The largest simulated changes occur very near to river mouths and are up to 3–37 times larger than surrounding regional averages (Figure 6.5), as they decline sharply with distance away from each river mouth while the added C_T (from R_{DOC}) is mostly lost via CO_2 outgassing (Section 6.2.5.2). Thus doubling R_{DOC} mainly affects the waters very close to river mouths, where local CO_2 outgassing nearly reach levels seen for basinwide average ingassing from the doubling of atmospheric CO_2 (Figure 6.5). In the model, there is also some signature of low pH and low Ω_{arag} along the transpolar drift (Figures 6.5 and 6.6) from offshore transport of coastal waters into the central Arctic Ocean.

Contrary to case for R_{DOC}, doubling the model's R_{C_T} comes along with an equal, simultaneous increase in $R^{\star}_{A_T}$ by definition. Thus, doubling R_{C_T} increases the $R^{\star}_{A_T} : R^{\star}_{C_T}$ ratio (equation 6.1) from 0.55 to 0.71 because R_{DOC} is nonzero (equation 6.1) and in the model that is instantly converted to a flux of C_T only. Furthermore, this increase in the $R^{\star}_{A_T} : R^{\star}_{C_T}$ ratio leads to an increase in the ocean A_T:C_T ratio. Hence there are increases in the Arctic Ocean's surface average pH (0.02) and Ω_{arag} (0.06) (Table 6.5). The largest simulated regional average pH increases from doubling of R_{C_T} occur in the Laptev Sea (0.06) and Beaufort Sea (0.04). There that doubling cancels 21% and 15% of the corresponding pH declines from the atmospheric CO_2 doubling, based on our idealized assumption that atmospheric CO_2, R_{C_T}, and R_{DOC} all increase at the same rate. The largest changes in surface pH occur near river mouths and are two to three times larger than surrounding regional changes, a smaller factor than for the case of R_{DOC} doubling where river-mouth maxima were 3–37 times larger than corresponding regional changes. These lower river mouth-coastal sea gradients from the doubling of R_{C_T} are attributed to the lack of CO_2 outgassing from increasing R_{C_T} and the

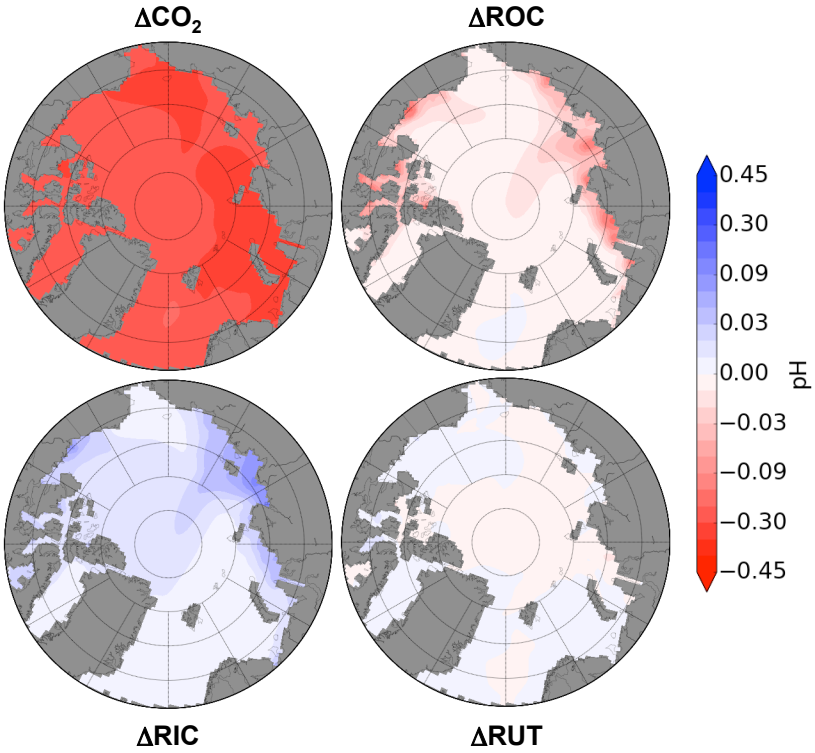

Figure 6.5 – Modeled changes in pH for ΔCO2, ΔROC, ΔRIC, and ΔRUT.

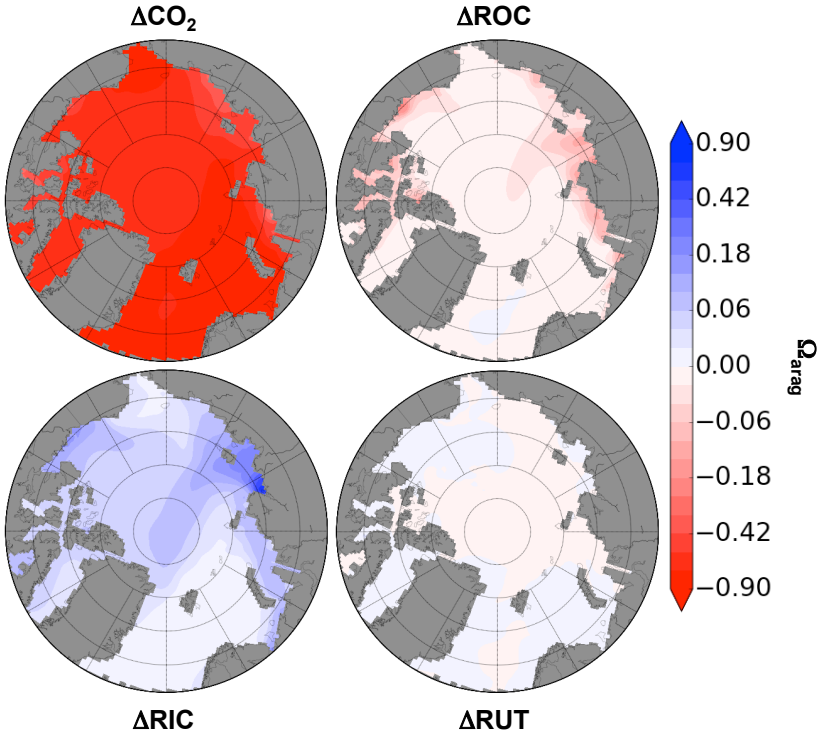

Figure 6.6 – Modeled changes in Ω_{arag} for ΔCO2, ΔROC, ΔRIC, and ΔRUT

transport of the additional C_T and A_T from rivers away from river mouths.

Regarding simulated Ω_{arag}, its largest regional changes from the doubling of R_{C_T} occur in the Laptev Sea (0.19) and Beaufort Sea (0.11) (Table 6.5), both regions with relatively higher R_{C_T} to R_{DOC} ratios (Table 6.1). Those increases in those two seas offset 35% and 19% of the declines from doubling of atmospheric CO_2. As seen for pH, the maximal changes of Ω_{arag} occur very near river mouths and are two to three times larger than surrounding regional changes.

However, our results are subject to two simplifications concerning riverine fluxes: the instantaneous conversion of terrigenous DOC to C_T and R_{A_T}:R_{C_T}=1. These two simplifications partly compensate one another, as the comparison between our $R^{\star}_{A_T}$:$R^{\star}_{C_T}$ ratio and a reconstructed $R^{\star}_{A_T}$:$R^{\star}_{C_T}$ ratio based on more realistic cases (R_{DOC} lability of 50%, and R_{A_T}:R_{C_T} as in Tank et al. [2012c]) suggest (Figure S1). The two simplifications also cause the temporal change of the $R^{\star}_{A_T}$:$R^{\star}_{C_T}$ ratio in the ROC and RIC simulations to be 26–55% larger than the more realistic cases in four out of five major Arctic rivers. Only for the Ob river, do the two simplifications lead to a reduction (by 7%) of the change in $R^{\star}_{A_T}$:$R^{\star}_{C_T}$ from the doubling of R_{DOC} and R_{C_T}. Basinwide then, our estimates of the effects of doubling R_{DOC} and R_{C_T} on pH and Ω_{arag} are likely overestimated.

6.2.6 Sensitivity factors

The sensitivity factors evolve over time but tend to stabilize by year 70 (Figures S2-S5). Sensitivity factors for carbon storage (ζ) take longer to stabilize because the timescale for penetration of anthropogenic carbon into the deep ocean is much longer than our 70-year simulation, unlike for the shorter timescales of the other sensitivity factors, which are tied to the surface.

These sensitivity factors for air-to-sea CO_2 flux (β), ocean carbon storage (ζ), NPP (η), and surface pH (ξ) are summarized as time-integrated values at year 70 when forcing variables are doubled. Our simulated sensitivity of global ocean anthropogenic carbon uptake to increasing atmospheric CO_2 ($\beta^{\text{global}}_{\Delta CO_2}$) may be compared to estimates from an ensemble of CMIP5 models forced under a 1% yr^{-1} atmospheric CO_2 increase scenario [Arora et al., 2013]. Our $\beta^{global}_{\Delta CO_2}$ of 0.9 Pg C ppm^{-1} lies at the upper limit of the CMIP5 model range (0.7-0.9 Pg C ppm^{-1}). The model sensitivity for the Arctic Ocean alone ($\beta_{\Delta CO_2}$) is 4.8 Tg C ppm^{-1}, only 0.5% of the analogous global sensitivity $\beta^{global}_{\Delta CO_2}$ even though the Arctic Ocean surface comprises 4% of the global ocean surface area. The relatively low $\beta_{\Delta CO_2}$ for the Arctic Ocean is consistent with the regional distribution of the CMIP5 results [Ciais et al., 2013, Figure 6.22], which show a lower air-to-sea flux sensitivity to increasing atmospheric CO_2 for the Arctic Ocean compared to global values. In contrast, the sensitivity for Arctic Ocean carbon storage $\zeta_{\Delta CO_2}$ (22.3 Tg C ppm^{-1}) is 2% of the corresponding global sensitivity, although the Arctic Ocean contains only 1% of the global ocean's water volume. That 2:1 ratio is consistent with that seen for the data-based estimates of anthropogenic carbon storage in the Arctic Ocean [Tanhua et al., 2009]. The difference between the Arctic $\beta_{\Delta CO_2}$ and $\zeta_{\Delta CO_2}$ confirms that most of today's anthropogenic carbon stored in the Arctic Ocean is imported from the

Atlantic and Pacific [Terhaar et al., 2018].

In a consistent fashion, we calculated the sensitivity of the air-to-sea CO_2 flux and carbon storage to changes in riverine carbon input. The sensitivity of the air-to-sea CO_2 flux to changes in R_{DOC} ($\beta_{\Delta ROC}$) is -0.86 Tg C (Tg C)$^{-1}$, indicating that 86% of additional C_T from R_{DOC} has been lost by CO_2 outgassing (Table 6.6). Conversely with the increase in R_{C_T}, only 5% of the additional C_T is lost to the atmosphere ($\beta_{\Delta RIC}$ = -0.05 Tg C (Tg C)$^{-1}$). In terms of Arctic Ocean carbon storage, increasing R_{DOC} enhances that by 0.05 Tg C for every Tg C of R_{DOC} that is added to the ocean as C_T. This low regional $\zeta_{\Delta ROC}$ is in line with the corresponding largely negative $\beta_{\Delta ROC}$, which is consistent with most of the added C_T from the increase in R_{DOC} being lost to the atmosphere. Conversely, the Arctic's $\zeta_{\Delta RIC}$ of 0.71 Tg C (Tg C)$^{-1}$ is 14 times larger than its $\zeta_{\Delta ROC}$ (Table 6.6), highlighting that most of the additional C_T from R_{C_T} remains in the ocean since there is an equal increase in $R^{\star}_{A_T}$ and hence surface ocean pCO_2 is hardly affected (Section 6.2.5.2). For both ΔROC and ΔRIC, the sum of the absolute numbers of β and ζ are below one, indicating that after 70 years, the remainder (difference relative to 1.0) has left the Arctic Ocean laterally to the North Atlantic, i.e. 0.09 Tg C (Tg C)$^{-1}$ for ΔROC and 0.24 Tg C (Tg C)$^{-1}$ for ΔRIC.

Likewise we are interested in the sensitivities of NPP, the air-to-sea CO_2 flux, and ocean carbon storage to riverine nutrient input. The increase in Arctic Ocean NPP from the increase in the riverine nitrogen flux is $\eta_{\Delta RUT}$ = 1.07 Tg N (Tg N)$^{-1}$ (Table 6.6), i.e., more than is fueled from Arctic rivers alone. That extra Arctic NPP may be fueled in part by additional river nutrients added from outside the Arctic, given that R_{NUT} is increased in all rivers globally and assuming there is sufficient transport from adjacent regions. It could also come in part from the remineralization of the additional organic matter produced by the increases in R_{NUT}, e.g., on the Arctic shelf. The increase in NPP also drives increases in the Arctic Ocean air-to-sea CO_2 flux ($\beta_{\Delta RUT}$ = 2.29 Tg C (Tg N)$^{-1}$) and carbon storage ($\zeta_{\Delta RUT}$ = 0.58 Tg C (Tg N)$^{-1}$). The difference between $\beta_{\Delta RUT}$ and $\zeta_{\Delta RUT}$ can be explained by lateral export to the Atlantic Ocean and the enhanced storage of carbon in organic matter and POC by enhanced NPP. Based on the model's C:N molar ratio of 122:16, an additional carbon uptake of 6.99 Tg C (Tg N)$^{-1}$ would have been expected if every mole of C consumed by NPP would have been replaced via the air-to-sea CO_2 flux. Yet, the simulated $\beta_{\Delta RUT}$ reveals that only 33% of the C_T removed by NPP is replaced via invasion of atmospheric CO_2. This result is consistent with an earlier estimate of air-to-sea CO_2 flux enhancement from NPP by Orr and Sarmiento [1992] for the global ocean (43%), although here the focus is on the Arctic Ocean with its large shelf seas and high riverine inputs.

Lastly, sensitivities of surface ocean pH were assessed with respect to increases in atmospheric CO_2, R_{DOC}, and R_{C_T}. The sensitivity of Arctic surface pH to the increase in R_{DOC} ($\xi_{\Delta ROC}$) is -0.029 (Pg C)$^{-1}$. Increasing R_{C_T} along with $R^{\star}_{A_T}$ leads to an increase in pH by 0.011 (Pg C)$^{-1}$ ($\xi_{\Delta RIC}$) because the simultaneous and equal increases in R_{C_T} and $R^{\star}_{A_T}$ increase the $R^{\star}_{A_T} : R^{\star}_{C_T}$ ratio (equation 6.1). Relative to these basinwide average sensitivities, locally sensitivities can be several times larger, e.g., near river mouths (Sections 6.2.5.1, 6.2.5.2, and 6.2.5.3).

Table 6.6 – Mean Arctic Ocean sensitivities of carbon storage (ζ), air-to-sea CO_2 flux (β), NPP (η), and pH (ξ) to changes in atmospheric CO_2, R_{DOC}, R_{C_T}, and R_{NUT} as defined in section 6.2.3.5 and integrated changes over years 0–70.

	Sensitivity		Integrated change	
Carbon storage				
$\zeta_{\Delta CO_2}$	22.27	Tg C ppm^{-1}	6.38	Pg C
$\zeta_{\Delta ROC}$	0.05	Tg C (Tg C)$^{-1}$	0.03	Pg C
$\zeta_{\Delta RIC}$	0.71	Tg C (Tg C)$^{-1}$	1.12	Pg C
$\zeta_{\Delta RUT}$	0.58	Tg C (Tg N)$^{-1}$	0.04	Pg C
Air-to-sea CO_2 flux				
$\beta_{\Delta CO_2}$	4.82	Tg C ppm^{-1}	1.38	Pg C
$\beta_{\Delta ROC}$	-0.86	Tg C (Tg C)$^{-1}$	-0.55	Pg C
$\beta_{\Delta RIC}$	-0.05	Tg C (Tg C)$^{-1}$	-0.07	Pg C
$\beta_{\Delta RUT}$	2.29	Tg C (Tg N)$^{-1}$	0.17	Pg C
Net primary production				
$\eta_{\Delta RUT}$	1.07	Tg N (Tg N)$^{-1}$	0.08	Pg N
pH				
$\xi_{\Delta CO_2}$	-0.001	ppm^{-1}	-0.30	
$\xi_{\Delta ROC}$	-0.029	(Pg C)$^{-1}$	-0.02	
$\xi_{\Delta RIC}$	0.011	(Pg C)$^{-1}$	0.02	

When integrated over the 70-year simulation, carbon storage from the doubling of riverine R_{DIC} fluxes amounts to 18% of carbon storage from the doubling of atmospheric CO_2 (Table 6.6). In comparison, carbon storage from the doubling of riverine R_{DOC} and R_{NUT} fluxes each amount to 0.5% of carbon storage from the doubling of atmospheric CO_2. In terms of the air-to-sea CO_2 flux, the doubling of R_{DOC} causes an outgassing that amounts to 40% of the magnitude of the ingassing from the doubling of atmospheric CO_2, while the doubling of R_{DIC} has the same opposing effect but amounts to only 5%. Conversely, the doubling of R_{NUT} increased the simulated air-to-sea CO_2 flux by an amount that is equivalent to 12% of that from the doubling of atmospheric CO_2. Changes in mean surface pH from the doubling of riverine R_{DOC} and R_{DIC} fluxes each amount to 7% of the change from the doubling of atmospheric CO_2.

6.2.7 Conclusions

This study offers a preliminary assessment of the extent to which certain key biogeochemical characteristics of the Arctic Ocean are sensitive to changes in river fluxes of carbon and nutrients. It provides a quantitative view that helps to disentangle how these characteristics are affected across the Arctic Ocean by riverine inputs of terrigenous organic carbon, inorganic carbon, and nutrients. Doubling the riverine nutrient flux increases Arctic NPP by 11% on average, by more than 30% in the Laptev and Beaufort Seas, and by up to 100% near river mouths. Doubling riverine DOC fluxes enhances ocean CO_2 outgassing, nearly offsetting the influx of anthropogenic CO_2 through the Arctic Ocean's air-sea interface from an imposed simultaneous doubling of atmospheric CO_2. However, much more anthropogenic carbon enters the Arctic Ocean laterally. Doubling riverine DOC fluxes also reduces the $R^{\star}_{A_T}$:$R^{\star}_{C_T}$ ratio, thus enhancing ocean acidification. Average changes in surface pH and Ω_{arag} due to the doubling riverine DOC fluxes amount to at most 7% of the changes due to the doubling of atmospheric CO_2, while that proportion reaches up to 30% in regional seas and up to 100% close to river mouths. Conversely, doubling river C_T fluxes increases the $R^{\star}_{A_T}$:$R^{\star}_{C_T}$ ratio and thus reduces ocean acidification. That reduction is at most 8% of the opposite effect from the doubling of atmospheric CO_2 in terms of the basinwide average, but it amounts to up to 21% the regional sea averages and up to 50% near river mouths.

These results suggest that the effects of riverine DOC fluxes should also be considered in the debate about whether the Arctic Ocean will become a source or a sink of CO_2 [Bates and Mathis, 2009; Cai et al., 2010; Roy et al., 2011; Manizza et al., 2019]. Likewise, riverine nutrient fluxes should be accounted for in another debate, the one about how nutrient supply to the surface Arctic Ocean will change and whether those changes will enhance or reduce NPP in the future [Cai et al., 2010; Arrigo and van Dijken, 2015; Vancoppenolle et al., 2013]. Indeed, the wide divergence between NPP projections among the CMIP5 models [Vancoppenolle et al., 2013] may be partly due to the lack of accounting of riverine nutrient fluxes in some models. Not accounting for the effects of riverine carbon fluxes may also lead to biased projections of pH and Ω_{arag} in Arctic shelf seas. Our

finding that doubling riverine C_T fluxes reduces coastal ocean acidification is counterintuitive if one does not consider the implicit simultaneous increase in A_T. Although this finding is based on two simplifications, more realistic assumptions still lead to a future increase in $R^{\star}_{A_T}$:$R^{\star}_{C_T}$ and hence reduced acidification from an increase in riverine inorganic carbon delivery.

Overall, our results suggest that even in the Arctic Ocean, where riverine inputs are proportionally the largest, the effects of decadal-to-centennial changes in river fluxes of carbon and nutrients on open-ocean biogeochemistry is relatively small. Yet they also suggest that for coastal seas, the influence of riverine input of carbon and nutrients should not be neglected, as often is the case in ocean models.

6.2.8 Supplementary material

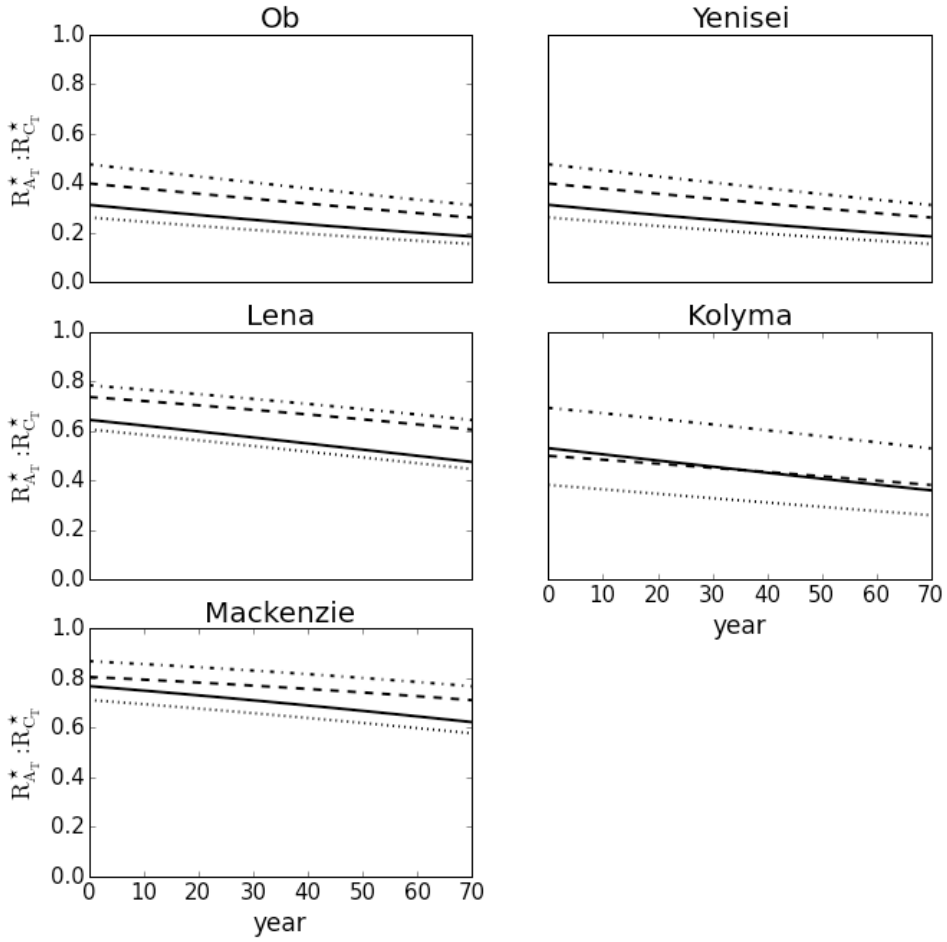

Figure 6.7 – Time evolution of $R^{\star}_{A_T}$:$R^{\star}_{C_T}$ ratio during ROC simulation from the imposed riverine fluxes (equation 1): (1) as used in the model with the two simplifications, where R_{A_T}:R_{C_T}=1 and terrigenous DOC is 100% labile (solid), (2) the same as (1), but assuming a R_{A_T}:R_{C_T} ratio as in Tank et al. [2012c] (dotted), (3) the same as (1), but assuming the R_{DOC} lability to be 50% (dash-dotted), and (4) assuming a R_{A_T}:R_{C_T} ratio as in Tank et al. [2012c] and the R_{DOC} lability to be 50% (dashed). During the RIC simulation the $R^{\star}_{A_T}$:$R^{\star}_{C_T}$ follows the same lines, but in the other direction (from year 70 to year 0).

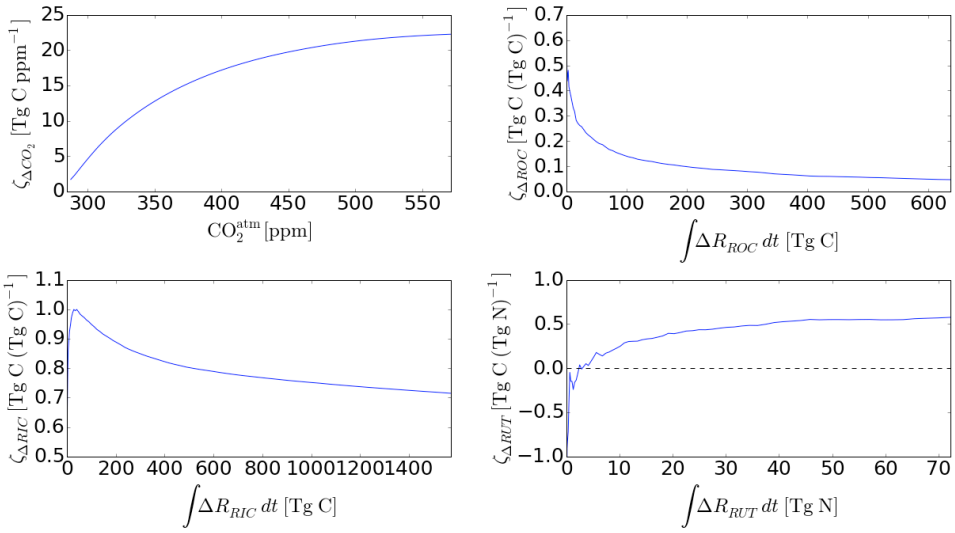

Figure 6.8 – $\zeta_{\Delta CO_2}$, $\zeta_{\Delta ROC}$, $\zeta_{\Delta RIC}$, and $\zeta_{\Delta RUT}$ over years 0–70.

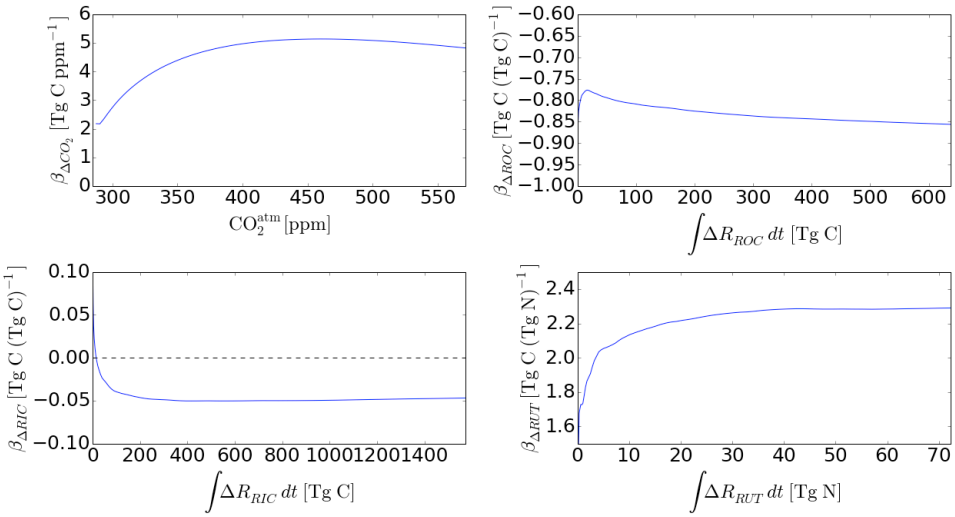

Figure 6.9 – $\beta_{\Delta CO_2}$, $\beta_{\Delta ROC}$, $\beta_{\Delta RIC}$, and $\beta_{\Delta RUT}$ over years 0–70.

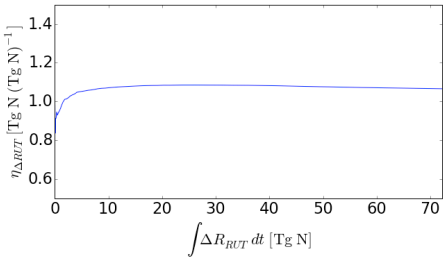

Figure 6.10 – $\eta_{\Delta RUT}$ over years 0–70.

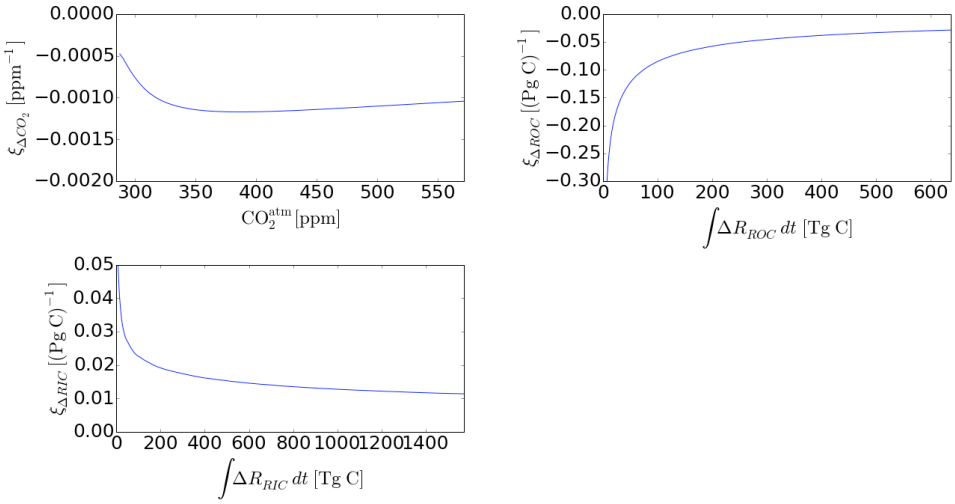

Figure 6.11 – $\xi_{\Delta CO_2}$, $\xi_{\Delta ROC}$, and $\xi_{\Delta RIC}$ over years 0–70.

6.3 Summary

- Doubling the nutrient flux of Arctic rivers increases Arctic NPP on average by 11%, by more than 30% in the Laptev and Beaufort Seas and by up to 100% near river mouths.
- Doubling river DOC fluxes enhances ocean CO_2 outgassing, nearly offsetting the influence of anthropogenic CO_2 through the Arctic Ocean's air-sea interface from an imposed simultaneous doubling of atmospheric CO_2.
- When riverine DOC fluxes are doubled, all Arctic interior seas become sources of carbon to the atmosphere
- The decline of pH and Ω_{arag} due to doubling river DOC fluxes is at most 7% of the decline due to the atmospheric CO_2 on a basinwide scale, up to 30% in regional seas, and up to 100% close to river mouth.
- Doubling riverine C_T fluxes revealed the counter-intuitive result coastal ocean acidification is reduced due to the implicit increase also the A_T.
- The importance of riverine delivery on the future state of the Arctic Ocean biogeochemistry calls for an implementation of changes in riverine delivery in Earth-System Models

Chapter 7

Conclusion and Outlook

" We don't read and write poetry because it's cute. We read and write poetry because we are members of the human race. And the human race is filled with passion. And medicine, law, business, engineering, these are noble pursuits and necessary to sustain life. But poetry, beauty, romance, love, these are what we stay alive for. "

John Keating, Dead Poets Society

Contents

7.1 Conclusion

The aim of this thesis as expressed in the title “River delivery of nutrients and carbon on the biogeochemistry of the Arctic Ocean"" was to better understand the impact of carbon and nutrient river fluxes on the biogeochemistry of the Arctic Ocean and to estimate how future changes of these riverine inputs may impact the future Arctic Ocean (Figure 7.1). To do so, we have first assessed the capacity of an ocean biogeochemical model at different horizontal resolutions to simulate the complex Arctic Ocean circulation and have improved our understanding of C_{ant} uptake in the Arctic Ocean (Chapter 3). In in a second step, we have used the highest resolution version of the model to improve a previously published method to estimate C_{ant} based on transient tracers, which enabled us to update the earlier C_{ant} estimate, and to estimate future uptake of C_{ant} and the associated future Arctic Ocean acidification (Chapter 4). Third, data-based riverine carbon and nutrient fluxes from the six largest Arctic rivers have been used to produce a river-flux estimate for all Arctic rivers based on watershed characteristics. This first consistent observation-based dataset of riverine fluxes has then been used to force the highest resolution of the same model to quantify the impact of riverine fluxes on the Arctic Ocean biogeochemistry (Chapter 5). Finally, we have used idealized simulations to estimate the sensitivity of the Arctic Ocean biogeochemistry to increasing river fluxes in the future (Chapter 6). In the following sections, we present and summarize the main conclusions for each part of the work and illustrate the findings using Figure 7.1.

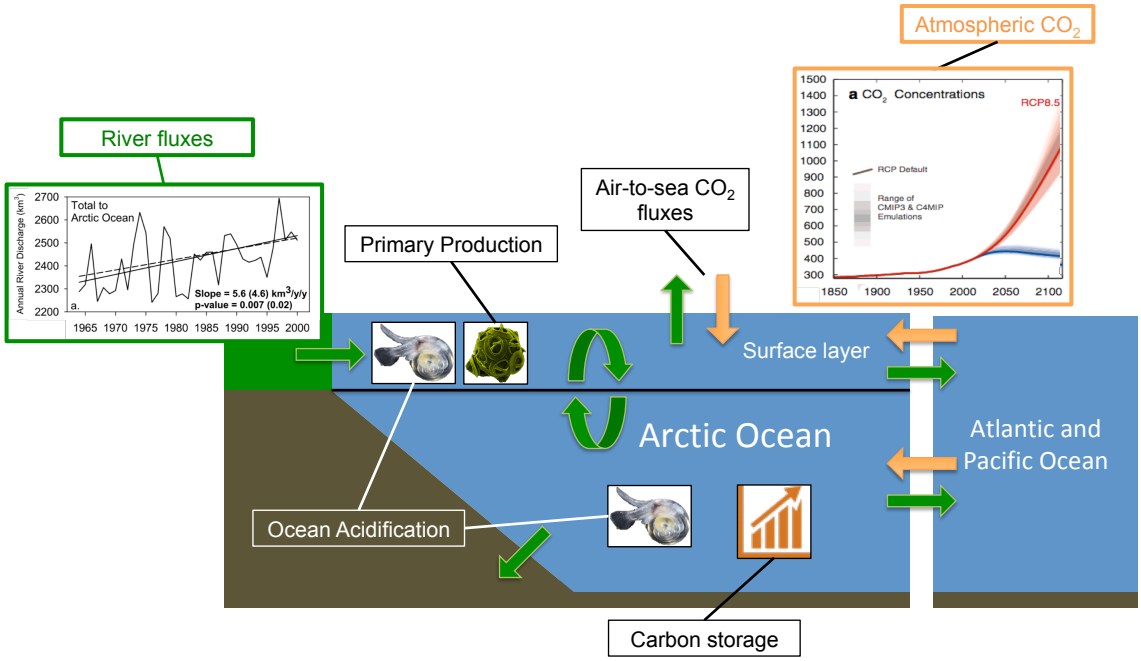

Figure 7.1 – Scheme of the Arctic Ocean, the fluxes of anthropogenic carbon (orange) and the carbon and nutrient fluxes from rivers (green).

7.1.1 Model resolution and C_{ant} uptake

We have calculated the uptake of C_{ant} in the Arctic Ocean with three different horizontal model resolutions. Our sensitivity tests suggest that more realistic results of the Arctic Ocean circulation and C_{ant} budget are obtained with higher-resolution model configurations that begin to explicitly resolve ocean eddies. Further, the estimate of the C_{ant} inventory from our highest resolution model falls within the uncertainty range of Tanhua et al. [2009]'s data-based estimate for C_{ant} storage in the Arctic Ocean (2.5–3.3 Pg C in 2005).

Our forced ocean simulations suggest that Arctic Ocean storage of C_{ant} is driven mostly by net lateral inflow, the total input of which is about three times that from the air-sea flux. That 3:1 ratio varies little with resolution because the lateral flux and the air-sea flux both increase as resolution is refined. Lateral fluxes in the CMIP5 models are generally less dominant but are also highly inconsistent both in magnitude and in the lateral:air-sea flux ratio. Some CMIP5 models even simulate net lateral outflow of C_{ant} and unrealistically low C_{ant} inventories. The only CMIP5 models that succeed in reaching the lower limit of the data-based C_{ant} inventory range are those that have a large net lateral input.

As the mass of simulated anthropogenic carbon in the Arctic Ocean increases with resolution, so does the simulated acidification. For instance, during 1960–2012, the average ASH in the Arctic shoals four times faster in ORCA025 than in ORCA2. Higher resolution is also needed to capture local extremes.

7.1.2 Constrained estimates of C_{ant} and future ocean acidification

C_{ant} in the ocean is estimated by the TTD method based on observations of transient tracers, such as CFC's. Here, We evaluated the TTD method with the high-resolution model configuration, which was shown to represent the Arctic Ocean circulation features relatively well. This evaluation demonstrated the method's good performance in the Arctic Ocean and validates its application in this region of the ocean.

Moreover, the model evaluation of the TTD method allowed us to identify a bias towards too low C_{ant} values in water masses that are formed at the Arctic Ocean surface. These too low C_{ant} values are a consequence of the surface disequilibrium for C_{ant} and CFC-12 during deep water formation. By correcting the C_{ant} inventory for this bias, this inventory increases by 7.5% to 3.3 Pg C in 2005. This refined estimate of past accumulation, albeit its relatively small magnitude, will help to further restrain the future accumulation of C_{ant} in the Arctic Ocean, which is necessary for better constraining projections of ocean acidification in the Arctic Ocean.

Based on this revision, an entirely undersaturated Arctic Ocean towards aragonite could occur at lower atmospheric CO_2 levels (450–540 ppm) than previously assumed. This threshold will be reached in 2051 if we follow the RCP8.5 trajectory, and not as previously thought at the end of the 21st century. A completely undersaturated Arctic can only be avoided by following the RCP2.6

trajectory.

7.1.3 Impact of riverine fluxes of carbon and nutrients

Having assessed the model performance in the Arctic Ocean, we used the highest resolution version of the model to quantify the impact of riverine fluxes of carbon and nutrients. To simulate the impact of river fluxes on the Arctic Ocean biogeochemistry in the most realistic way possible, we have created the first consistent, data-based, gridded, pan-Arctic dataset for monthly riverine carbon and nutrient fluxes. Compared to earlier gridded model-based data sets, this new dataset improves nutrient fluxes and is backed up by the systematic observations from the ArcticGRO data base. We therefore recommend the use as this dataset for ocean biogeochemical model studies in the Arctic Ocean.

Further, this dataset was used to force an ocean-biogeochemical model to quantify the impact of riverine fluxes on the Arctic Ocean biogeochemistry. The good agreement of simulated NPP, air-sea CO_2 fluxes, and acidification with observations and data-based estimates highlights the importance of using a well constrained river flux database in the Arctic Ocean. Indeed, our results suggest that river fluxes sustain 16–25% of pan-Arctic Ocean NPP and 79% of the NPP in the Laptev Sea, reduce the Arctic Ocean air-sea CO_2 uptake by ~20% and make the Laptev and Beaufort Seas net sources of CO_2 to the atmosphere, and increase coastal ocean Ω_{arag} regionally by up to 50% during summer. These estimates exceed earlier results and indicate that river fluxes should receive increasing attention when considering the future of the Arctic Ocean biogeochemistry.

Yet, many ocean biogeochemical models do not include riverine fluxes by default [Ilyina et al., 2013; Tjiputra et al., 2013], which might well be the reason for differences of simulated Arctic Ocean NPP between models [Popova et al., 2012; Vancoppenolle et al., 2013], for differences between simulated and observed air-sea CO_2 fluxes [Manizza et al., 2019], and for differences between simulated [Ciais et al., 2013] and observed [Anderson et al., 2017] coastal ocean acidification. We therefore strongly recommend the implementation of river fluxes and their future change in ocean and climate models.

7.1.4 Response to doubling of riverine carbon and nutrient delivery

The sensitivity tests offered a preliminary assessment of the extent to which certain key biogeochemical characteristics of the Arctic Ocean are sensitive to changes in river fluxes of carbon and nutrients. The calculated sensitivities provide a quantitative view that helps disentangle how these characteristics are affected on a pan-Arctic scale by terrigenous organic carbon, inorganic carbon and nutrient inputs. Doubling the nutrient flux of Arctic rivers increases Arctic NPP on average by 11%, by more than 30% in the Laptev and Beaufort Seas and by up to 100% near river mouths. Doubling river DOC fluxes enhances ocean CO_2 outgassing, nearly offsetting the influence of anthropogenic CO_2 through the Arctic Ocean's air-sea interface from an imposed simultaneous dou-

bling of atmospheric CO_2. Doubling river DOC enhances ocean acidification, while doubling river C_T fluxes together with C_T fluxes reduce ocean acidification.

These results provide some first insight into how future changes in river fluxes may affect the Arctic Ocean biogeochemistry. They suggest that the effects of riverine DOC fluxes should also be included in the debate over whether or not the Arctic Ocean will become a source or a sink of CO_2 [Cai et al., 2010; Roy et al., 2011; Manizza et al., 2019]. Likewise, riverine nutrient fluxes should be considered in the debate about how nutrient supply to the surface Arctic Ocean will change and if NPP will increase or decrease in the future [Cai et al., 2010; Arrigo and van Dijken, 2015; Vancoppenolle et al., 2013]. Along the same lines, not accounting for the effect of river carbon fluxes changes on Arctic Ocean pH and Ω_{arag} [Steinacher et al., 2009] may lead to erroneous results in the shelf seas, which are locally strongly influenced by river inputs [Semiletov et al., 2016; Chierici and Fransson, 2009]. Moreover, doubling riverine C_T fluxes revealed the counter-intuitive result that coastal ocean acidification is reduced due to the implicit increase of A_T. Taking into account observed changes of A_T fluxes of 134–185% over the past three and half decades in the Yenisei and Ob [Drake et al., 2018], river fluxes may even increase the buffer capacity of coastal regions to ocean acidification.

7.2 Outlook

While this thesis has led to advances in the understanding of the biogeochemistry of the Arctic Ocean and the influence of rivers, it opened up new questions and demonstrated areas where improvement is needed.

7.2.1 Towards more complex processes in ocean biogeochemical models

7.2.1.1 Variable carbon-nitrogen stoichiometry in the organic matter

One of the most far-reaching caveats is that the model NEMO-PISCES assumes a fixed stoichiometric C:N ratio of 122:16 in organic matter. This fixed ratio does not allow to add external fluxes of organic matter separately. Therefore, when riverine DOC is externally added to PISCES, the DON and DOP concentrations are increased according to the fixed stoichiometric ratios. Unfortunately, the average C:N ratio of organic matter in the six largest Arctic rivers is 747:16 [Holmes et al., 2012] instead of 122:16.

In this work, we have confronted this problem in two different ways. In the first approach, all riverine organic matter fluxes (DOC, DON, and DOP) were added to their respective inorganic pool (C_T, NO_3, PO_4) in PISCES assuming all riverine organic matter to be very labile and thus being remineralized instantaneously at the river mouth (Chapter 3, 4, and 6). The second approach differs from the first one in the way riverine DOC fluxes are treated. Instead of assuming 100% of this riverine DOC flux to be labile, we only assumed 50% to be very labile and thus being remineralized directly at the river mouth [Kaiser et al., 2017] and added the other half to the marine DOM pool (Chapter 5). Thus, we artificially increased the DON and DOP fluxes from Arctic rivers. As the Arctic Ocean organic matter is already abundant, especially in the productive coastal regions, the river flux of DOC had little effect on the availability of nutrients.

Although the effects of both approaches could be estimated in this work, it would be preferable to use a model, which does not rely on a fixed stoichiometric ratio in organic matter. For PISCES, such a version (PISCES-QUOTA) was developed in the last years and was already exploited to assess the impact of a variable C:N:P stoichiometric ratio on global estimates of NPP, "food quality" (relative amount of nutrients in organic matter compared to carbon), and ocean carbon uptake [Kwiatkowski et al., 2018] or on the trophic amplification of marine biomass decline [Kwiatkowski et al., 2019]. Unfortunately, the explicit simulation of N and P in DOM, phytoplankton, zooplankton, and sinking particles increases the number of simulated tracers by PISCES from 24 to 42. This leads to a significant rise in computational costs and make simulations with PISCES-QUOTA using high resolution configurations like ORCA025 impossible.

With present-day computational capacities, a choice has to be made between using PISCES-QUOTA with a coarse resolution or using PISCES with a fixed stoichiometric C:N:P at a high-resolution. In this work we opted for the second choice. As a next step, it would be valuable

information to evaluate the effect of the stoichiometric ratio on the Arctic Ocean biogeochemistry. This information would help to make decisions for future studies that are confronted with the same question: Using PISCES-QUOTA with a coarse resolution or using PISCES with a fixed stoichiometric C:N:P but a high-resolution?

On the long run, increased computational capacities may permit simulations with PISCES-QUOTA at higher resolutions, which would allow to quantify the effect of river fluxes on the Arctic and global ocean more accurately.

7.2.1.2 Variable lability of riverine organic matter

The lability of riverine organic matter from Arctic rivers is still highly uncertain [Wickland et al., 2012; Letscher et al., 2013; Le Fouest et al., 2015; Kaiser et al., 2017; Thibodeau et al., 2017; Spencer et al., 2009]. Riverine DOM tends to be more refractory when river discharge is low and more labile when river discharge is high [Holmes et al., 2008]. Further, the lability of old DOC, which is expected to be released with the thawing of permafrost, has been observed to be far more labile than relatively young riverine DOC [Vonk and Gustafsson, 2013; Spencer et al., 2015].

These differences in the lability of organic matter lead to very different rates of remineralization in the coastal ocean, which can not be simulated by PISCES yet. The simplest possibility to overcome this would be to introduce three new tracers of terrigenous DOC, DON, and DOP with an exponential decay following Manizza et al. [2009]; Tank et al. [2012a]. By adding these three new tracers, the computational costs would only be slightly increased (compared to PISCES-QUOTA) and riverine organic matter could have a different lability than marine organic matter.

A more complex solution, would be the implementation of a variable lability of DOC in PISCES. Such a variable lability has already been used for POC and has led to better agreement between simulated and observed POC concentrations in the ocean's interior [Aumont et al., 2017]. To account for different labilities, they divided the total POC into 30 different pools with changing lability. As this representation would more than double the computational costs, they assumed POC to be independent of the ocean circulation. POC thus only sinks vertically, is consumed and produced by biology, and is affected by vertical mixing. Thus, this approach used by Aumont et al. [2017] increased the computational time by around 20% despite using 30 POC pools. However, the assumption of no horizontal movement will likely not work for DOC because offshore transport is not accounted for. For a computationally feasible solution and for DOC classes moving with the circulation, the number of DOC classes would need to be reduced drastically. To limit the increase in computer time to 20%, 5 (20% of 24 tracers) classes of DOC would be possible.

Furthermore, a combination of both approaches, tracers of terrigenous DOC, DON, and DOP with variable lability would likely provide the best solution. Thus, stiochiometric ratio of terrigenious organic matter would be respected and the different labilities could be applied. To keep this approach computational feasible, it should be limited to 3 or 4 classes per tracer. Even using only

3 classes per tracer, would add 9 additional tracers to PISCES and increase the computational time by ~38%.

7.2.1.3 Deltas and estuaries

In the simulations in this work, river fluxes of carbon and nutrients were directly added to the ocean biogeochemical model. In reality, this approach that riverine carbon and nutrient fluxes transit through estuaries before entering the coastal ocean. These estuaries are often significant filters that modify fluxes by biogeochemical processes, such as burial, air-sea CO_2 exchange, remineralization, and production of organic matter [Regnier et al., 2013a]. Despite their potential importance, processes in estuaries are not well constrained, especially for the Arctic, due to large scale temporal and spatial variability at relatively small scales, which make the observation of these effects a difficult task [Borges et al., 2005; Regnier et al., 2013b].

To improve the understanding of processes and to complete observational studies, reactive transport models are helpful tools [Arndt and Regnier, 2007; Volta et al., 2014]. These tools consider hydrodynamics, biogeochemistry, transport, and tides in the estuary and might be notably useful in the Arctic Ocean, where estuarine science is still at its very beginning compared to estuaries in lower latitudes [McClelland et al., 2012] and measurements of riverine fluxes are often placed many kilometers upstream [McClelland et al., 2008].

The coupling of such reactive transport models to an ocean biogeochemical model would certainly improve our understanding of the impact of riverine fluxes on the Arctic Ocean biogeochemistry. For example, it could shed light on the question of lability of organic matter, as potentially produced young organic matter would have much lower labilities. Moreover, the use of such a model in itself would be of high interest in the Arctic estuaries to understand the relative importance of these important systems of the land-ocean aquatic continuum.

7.2.2 Refining the physical settings of the modeling approach

7.2.2.1 Nested models

In chapter 3, we could demonstrate that higher resolution leads to a better representation of the Arctic Ocean circulation. Unfortunately, higher resolution requires higher computational costs. An option to reduce computational costs and to use high model resolution in the Arctic Ocean is the use of a nested model. For the NEMO platform, a nested version called AGRIF exists [Debreu et al., 2008] and was already successfully used, e.g. to resolve the small scale dynamics of the Agulhas current [Biastoch et al., 2009] or the equatorial undercurrents in the Atlantic Ocean [Duteil et al., 2014].

Unfortunately AGRIF is not yet operational in combination with the sea ice component of NEMO (LIM) and thus cannot be used in the Arctic Ocean yet. Nonetheless, the here presented improvements of Arctic Ocean circulation with increasing resolution highlight the large potential

of AGRIF for Arctic Ocean modeling. It would allow to substantially increase the model resolution, while still keeping computation costs relatively low. Even more, AGRIF would eventually allow the use of the costly expensive PISCES-QUOTA model in combination with a high model resolution in the Arctic Ocean.

7.2.2.2 Sea-ice coupling – brine rejection

The storage of C_{ant} in the Arctic Ocean was shown to depend largely on model resolution (Chapter 3). Even more, the vertical profiles of C_{ant} and CFC-12 (Figure 3.5 and 3.7) led to the assumption that the vertical mixing and the deep water formation is underestimated when using coarse resolution.

Large parts of the deep water formation within the Arctic Ocean occur in the Barents Sea and in the Chukchi Sea [Aagaard et al., 1981; Jones et al., 1995; Swift et al., 1997; Smedsrud et al., 2013]. To reach the deep Arctic Ocean, surface waters must match the density of the deepest waters, which is just above 1028.0 kgm^{-3}. At the surface ocean these densities are reached by cooling and brine rejection. This process is happening on very small scales (0.1–1.0 km) and during short time periods [Rudels, 1995]. These small scale phenomena will likely not be resolved by the used configurations of NEMO with their average grid length in the Arctic Ocean of 121 km (ORCA2), 29 km (ORCA05), and 14 km (ORCA025). Indeed, monthly averaged surface ocean density in ORCA05 and ORCA025 during the period of deep water formation indicates large differences in maximum density with increasing resolution, although both simulations have been shown to simulate a very similar sea ice extent (Chapter 3). Even ORCA025 surface water do not reach 1028.0 kg m^{-3}, the density of the deep Arctic Ocean (Figure 7.2). Without reaching higher densities locally, the waters in the deep Arctic Ocean can not be renewed, and C_{ant} cannot be transported deeper than 2000 m.

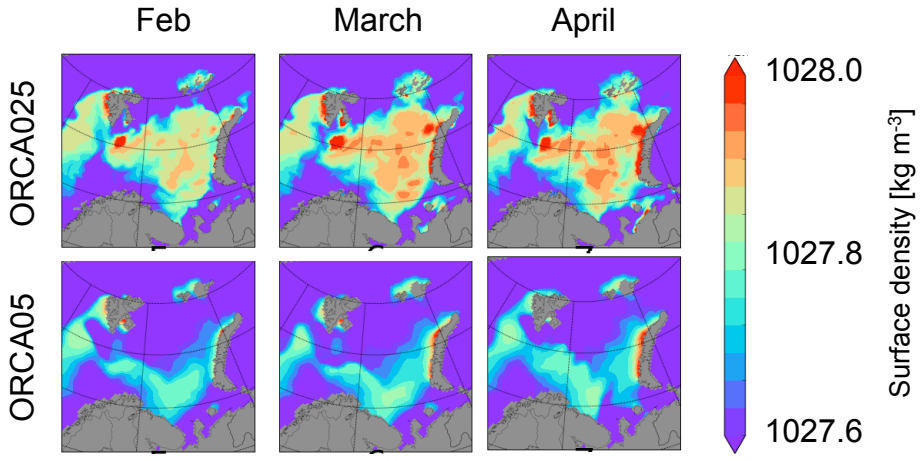

Figure 7.2 – Monthly averaged surface ocean density in February, March, and April in 2010 simulated with ORCA05 and ORCA025.

To resolve phenomena on the scale of 1 km, a model resolution of 1/56° would be needed.

This is for a long time no feasible solution when using global ocean models. Instead, I think that an additional module in NEMO could be used to artificially increase density in regions of deep-water formation. This module should conserve the total salinity and temperature on a regional scale and should only automatically detect regions of likely deep-water formation so that it could still be used in a changing climate.

More specifically, the module would detect fast reductions in sea ice extent in grid cells of the model. The simulation of sea ice is robust across model resolution. Once a strong reduction of sea ice extent is detected in a cell, the module would subtract a very small amount of salinity from the eight surrounding cells and add it to the cell with the detected reduction of sea ice extent. Thus, the salinity in this cell would be increased artificially and a hot spot of dense water would have been created.

At this stage, this is just an idea of how to parameterize small scale deep water formation in a coarse resolution model. This module, once it is build, would need to be tuned, e.g. the detection threshold for changing sea ice extent must be estimated as well as the amount of salinity that is transferred from one cell to another. Many more possible problems will likely arose, but the result, a coarse resolution configuration of NEMO that is capable of simulating deep water formation in the Arctic Ocean, would make the work worthwhile.

7.2.3 Moving to the future – climate change

7.2.3.1 Winter heat wave simulations

With climate change, marine heat waves are projected to become more frequent. Between 1982 and 2016, marine heatwaves have doubled and are projected to increase by a factor of 16 under a warming of 1.5° [Frölicher et al., 2018]. Just last year, the Arctic Ocean has experienced a very warm winter, with sea surface temperature anomalies of up to 20°C, and a warm autumn (Figure 7.3). Due to these high temperatures, the Arctic Ocean winter sea ice extent was exceptionally low (Figure 1.5).

Marine heatwaves have shown that the global ocean ecosystem is especially vulnerable to these extreme events. For a region, which is already extremely vulnerable to ocean acidification [Steinacher et al., 2009], the effect of heat waves might be especially important. Given the good agreement between model results and data-based products of NPP and Ω_{arag} using the simulations from Chapter 5 with the ORCA025 configuration and the ArcticGRO river input, these simulations could be prolonged with more recent historic reanalysis data to simulate the impact of the 2018 heat wave on the Arctic Ocean biogeochemistry.

7.2.3.2 Climate change simulations

The simulations used in this thesis are all forced with climate conditions from 1958 to 2012. When projections about the future are made (Chapter 4 and 6), only impacts from changing atmospheric

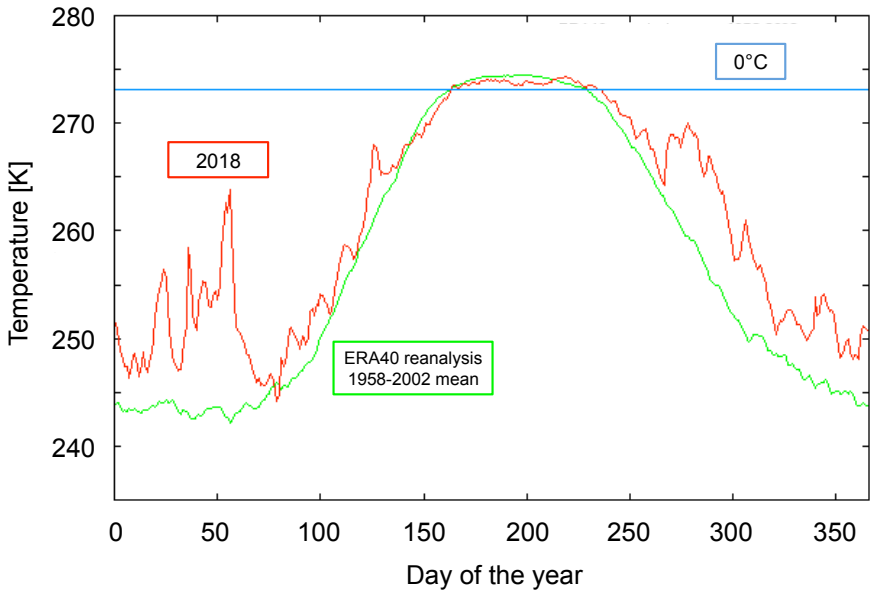

Figure 7.3 – Daily mean temperatures for the Arctic area north of the 80th northern parallel, plotted with daily climate values calculated from the period 1958–2002. (adapted from the Danish Meteorological Institute, http://ocean.dmi.dk/arctic/index.php)

CO_2 are considered.

However, the Arctic Ocean is undergoing profound changes, such as declining sea-ice cover. This declining sea ice cover increases the potential for air-sea exchanges of heat and CO_2. At the same time, declining sea ice will change the circulation, e.g. increased deep water formation [Lique et al., 2018]increased influence of wind on the Arctic Ocean that will increase mixing, reduced damping of waves below the sea ice. These changes in the circulation make the prediction of changes of the air-sea CO_2 and NPP a very difficult task [Cai, 2011; Bates et al., 2006; Vancoppenolle et al., 2013].

These changes might also change the importance of river fluxes and changes of river fluxes. The ongoing debate for air-sea CO_2 flux shows that the different effects are very difficult to predict: Will more wind lead to a stronger mixing of Arctic waters and enhanced nutrient supply from the deeper layers or will the sea ice melting and more river discharge increase stratification enough that less nutrients will be supplied? Dependent on these questions, the influence of river fluxes will change. If less nutrients are supplied from deeper layers, riverine fluxes will gain importance, while they will loose importance if more nutrients will be supplied to the surface.

It would therefore be of great interest if river fluxes of carbon and nutrients could be included in the next generation of CMIP simulations. This would allow to assess the impact of rivers in a changing climate across a wide range of climate models.

7.2.3.3 Emergent constraints

Another possibility would be to exploit the concept of emergent constraints for the Arctic Ocean. An emergent constraint is a relationship, across an ensemble of climate models, between an observable variable in the climate system (e.g. present-day lateral influx of C_{ant}) and a projected future change (e.g. future storage of C_{ant}). By combining the model derived emergent relationship with observations, an emergent constraint on the projected future change can be derived. This concept does not only accept the imperfections of Earth system models, but exploits them by assuming that a deficit in simulating a measurable present-day process translates to a similar deficit in the future. If the link between a present-day process and a projection for the future can be established, observations of the present-day process allow consequently an improvement of the projections.

This concept has already led to major scientific advances, such as better constrained projections of projected land photosynthesis [Wenzel et al., 2016] and tropical ocean primary production [Kwiatkowski et al., 2017]. For the Arctic Ocean, novel emergent constraints on NPP or carbon uptake could be developed, which will also allow to improve and better constrain projections of ocean acidification extreme events in the high-latitude ocean.

These improved projections have a high potential in the Arctic Ocean as models disagree strongly in this region. For example, climate model projections of Arctic Ocean net primary productivity do not even agree on sign of changes [Vancoppenolle et al., 2013]. Potentially, an emergent constraint could be established between the amount of nutrients available in the Arctic Ocean at present-day and the projection of Arctic Ocean primary production.

Another example is the anthropogenic carbon storage in the Arctic Ocean. Under the RCP8.5 scenario, 11 CMIP5 models estimate the C_{ant} inventory in 2100 to be 7.2 ($\pm$3.3) Pg C. When using an emergent constraint between the anthropogenic carbon stored below 800 m in the Arctic Ocean and the future storage of anthropogenic carbon in the Arctic Ocean, this value would increase to 9.7 (6.8 – –12.7) Pg C. Here, the anthropogenic carbon below 800 m represents the model capacity to form deep waters and thus to transport anthropogenic carbon to the deep ocean. By exploiting this linear relationship, I assume that models, which do not store enough anthropogenic carbon in the ocean by today, will also not store enough in the future.

7.2.4 Data availability

7.2.4.1 Rivers

The coordinated measurements of river fluxes in the six largest Arctic rivers by PARTERNS/ArcticGRO has led to significant advances in the quantification of river fluxes in the Arctic Ocean [Tank et al., 2012c; Holmes et al., 2012] and their ongoing changes [Drake et al., 2018]. These data-based fluxes have also been used to force model studies [Manizza et al., 2009; Tank et al., 2012a; Le Fouest et al., 2015] and have been a central part of this thesis (Chapter 5).

Despite the great advances thanks to these observations, the observed watersheds cover only about half of the watersheds and the extrapolation of these fluxes on a pan-Arctic scale remains necessary. Although the here presented extrapolation of river fluxes is an important step forward, it would always be preferential to have direct observations of smaller rivers. The watersheds of these smaller rivers don't extend as far south as the watersheds of the large rivers. Given the strong changes in ecosystem along this north-south gradient, carbon and nutrient fluxes in the small rivers may be considerably different. More observations from small rivers would be necessary to capture this difference and would in turn allow for a more accurate statistical extrapolation of Arctic Ocean river fluxes.

Moreover, observations of carbon and nutrient concentrations in Arctic rivers are often not taken directly at the river mouth, but further upstream. Especially for the Lena river, the distance between the delta and the measurement station (Zhigansk) is several hundred kilometers. Until the water finally reaches the Arctic Ocean river fluxes might be significantly altered [Regnier et al., 2013b]. Observations close to the delta would help to quantify this effect and to improve the data-based estimates of river fluxes that flow into the Arctic Ocean.

7.2.4.2 Ocean

During the work in this thesis, data availability in the Arctic Ocean was often an obstacle. For example, during winter no measurements exist as sea ice cover makes it impossible to pass the Arctic Ocean with a research vessel. Even in summer, observations are only punctually and not continuous. The missing data makes it difficult to evaluate the model performance and to identify the most important caveats.

Fortunately, three major projects will help to improve the situation in the future: The international year-around MOSAiC expedition (https://www.mosaic-expedition.org/), the "Nansen legacy" project (https://arvenetternansen.com/), and the "Synoptic Arctic Survey" (http://www.synopticarcticsurv
During the international MOSAiC expedition (2019-2020), the German icebreaker "Polarstern" will be drifting for one year in the Arctic Ocean, trapped by sea ice. During this time, researchers from institutions of 17 different countries will constantly take physical and biogeochemical measurements. Being the first year-around expedition in the Arctic Ocean, the obtained data has the potential to bring environmental research to a completely new level. At the same time the 'Nansen legacy' project, organized by 10 Norwegian research institutes, will improve data sampling in the Barents Sea and the adjacent Arctic Ocean basin, the Nansen basin. During 2018 to 2020 data will be sampled at 235 days. This data from the Barents Sea provides an especially valuable source of information, as it is a hot spot of primary production and the most important region for deep-water formation in the Arctic Ocean. While MOSAiC is aiming at covering the seasonal cycle and the "Nansen legacy" is concentrating on an important regional sea, the 'Synoptic Arctic Survey" will provide unprecedented spatial coverage of the Arctic Ocean's circulation and biogeochem-

istry (Figure 7.4). This bottom-up initiative from researchers from 9 different countries will create a first unique baseline for the Arctic Ocean against which future changes can be quantified.

Figure 7.4 – Map with tentative cruise sections for a Synoptic Arctic Survey. (taken from http://www.synopticarcticsurvey.info/splan.html)

These three projects will significantly advance the understanding of the Arctic directly by observations, but also indirectly by providing data against which ocean biogeochemichal models can be evaluated. This evaluation will eventually lead to a significant improvement of the models, which in turn allows a better understanding of the Arctic Ocean.

Bibliography

Aagaard, K., Coachman, L., and Carmack, E. (1981). On the halocline of the Arctic Ocean. *Deep-Sea Res. Pt. I*, 28(6):529–545. 90, 185

Aksenov, Y., Karcher, M., Proshutinsky, A., Gerdes, R., De Cuevas, B., Golubeva, E., Kauker, F., Nguyen, A. T., Platov, G. A., Wadley, M., et al. (2016). Arctic pathways of Pacific Water: Arctic Ocean model intercomparison experiments. *J. Geophys. Res. - Oceans*, 121(1):27–59. 49

Anderson, L., Tanhua, T., Jones, E., and Karlqvist, A. (2011a). Hydrographic, chemical and carbon dioxide data from R/V Oden cruise 77DN20050819, August 19 - September 25, 2005. 59, 63

Anderson, L. G., Björk, G., Jutterström, S., Pipko, I., Shakhova, N., Semiletov, I., and Wåhlström, I. (2011b). East Siberian Sea, an Arctic region of very high biogeochemical activity. *Biogeosciences*, 8(6):1745–1754. 17, 23, 138

Anderson, L. G., Ek, J., Ericson, Y., Humborg, C., Semiletov, I., Sundbom, M., and Ulfsbo, A. (2017). Export of calcium carbonate corrosive waters from the East Siberian Sea. *Biogeosciences*, 14(7):1811–1823. 140, 180

Anderson, L. G., Jones, E. P., and Swift, J. H. (2003). Export production in the central Arctic Ocean evaluated from phosphate deficits. *J. Geophys. Res. - Oceans*, 108(C6). 11, 137

Anderson, L. G., Jutterström, S., Hjalmarsson, S., Wåhlström, I., and Semiletov, I. P. (2009). Outgassing of CO_2 from Siberian Shelf seas by terrestrial organic matter decomposition. *Geophys. Res. Lett.*, 36(20). 17, 108, 134, 137, 147, 158

Anderson, L. G. and Kaltin, S. (2001). Carbon fluxes in the Arctic Ocean-potential impact by climate change. *Polar Res.*, 20(2):225–232. 148

Anderson, L. G. and Macdonald, R. W. (2015). Observing the Arctic Ocean carbon cycle in a changing environment. *Polar Res.*, 34(1):26891. xiii, 8

Anderson, L. G., Olsson, K., Jones, E. P., Chierici, M., and Fransson, A. (1998). Anthropogenic carbon dioxide in the Arctic Ocean: Inventory and sinks. *J. Geophys. Res. - Oceans*, 103(C12):27707–27716. 19

Anderson, L. G., Tanhua, T., Björk, G., Hjalmarsson, S., Jones, E., Jutterström, S., Rudels, B., Swift, J., and Wåhlström, I. (2010). Arctic ocean shelf-basin interaction: An active continental shelf CO_2 pump and its impact on the degree of calcium carbonate solubility. *Deep-Sea Res. Pt. 1*, 57(7):869 – 879. 3, 14, 20, 21, 46, 84, 86, 87, 90, 93, 94, 159

Anderson, L. G., Tanhua, T., Jones, E., and Karlqvist, A. (2011c). Hydrographic, chemical and carbon dioxide data from R/V Oden cruise 77DN20050819, August 19 – September 25, 2005. 41, 90

Arndt, S. and Regnier, P. (2007). A model for the benthic-pelagic coupling of silica in estuarine ecosystems: Sensitivity analysis and system scale simulation. *Biogeosciences*, 4(3):331–352. 184

Arora, V. K., Boer, G. J., Friedlingstein, P., Eby, M., Jones, C. D., Christian, J. R., Bonan, G., Bopp, L., Brovkin, V., Cadule, P., Hajima, T., Ilyina, T., Lindsay, K., Tjiputra, J. F., and Wu, T. (2013). Carbon-concentration and carbon-climate feedbacks in CMIP5 Earth system models. *J. Clim.*, 26(15):5289–5314. 148, 167

Arrhenius, P. S. (1896). XXXI. On the influence of carbonic acid in the air upon the temperature of the ground. *Lond. Edinb. Dubl. Phil. Mag.*, 41(251):237–276. 2

Arrigo, K. R., Pabi, S., van Dijken, G. L., and Maslowski, W. (2010). Air-sea flux of CO_2 in the Arctic Ocean, 1998–2003. *J. Geophys. Res.*, 115(G4). 158

Arrigo, K. R. and van Dijken, G. L. (2011). Secular trends in Arctic Ocean net primary production. *J. Geophys. Res. - Oceans*, 116(C9). xviii, xix, 118, 128, 157

Arrigo, K. R. and van Dijken, G. L. (2015). Continued increases in Arctic Ocean primary production. *Prog. Oceanogr.*, 136:60–70. 3, 15, 16, 41, 42, 96, 118, 122, 127, 170, 181

Asselin, R. (1972). Frequency filter for time integrations. *Mon. Weather Rev.*, 100(6):487–490. 31

Aumont, O. (2012). *PISCES - An ocean biogeochemical model for carbon and ecosystem studies*. xiv, 33

Aumont, O. and Bopp, L. (2006). Globalizing results from ocean in situ iron fertilization studies. *Global Biogeochem. Cy.*, 20(2). 33, 34, 35, 36, 50, 52, 114, 116, 117, 133

Aumont, O., Ethé, C., Tagliabue, A., Bopp, L., and Gehlen, M. (2015). PISCES-v2: an ocean biogeochemical model for carbon and ecosystem studies. *Geosci. Model Dev.*, 8(8):2465–2513. 25, 28, 32, 34, 37, 106, 149, 151

Aumont, O., van Hulten, M., Roy-Barman, M., Dutay, J.-C., Éthé, C., and Gehlen, M. (2017). Variable reactivity of particulate organic matter in a global ocean biogeochemical model. *Biogeosciences*, 14(9):2321–2341. 135, 183

Backman, J., Jakobsson, M., Løvlie, R., Polyak, L., and Febo, L. A. (2004). Is the central Arctic Ocean a sediment starved basin? *Quaternary Sci. Rev.*, 23(11):1435–1454. 11

Barnier, B., Madec, G., Penduff, T., Molines, J.-M., Treguier, A.-M., Le Sommer, J., Beckmann, A., Biastoch, A., Böning, C., Dengg, J., et al. (2006a). Impact of partial steps and momentum advection schemes in a global ocean circulation model at eddy-permitting resolution. *Ocean Dyn.*, 56(5-6):543–567. 30, 115

Barnier, B., Madec, G., Penduff, T., Molines, J.-M., Treguier, A.-M., Le Sommer, J., Beckmann, A., Biastoch, A., Böning, C., Dengg, J., et al. (2006b). Impact of partial steps and momentum advection schemes in a global ocean circulation model at eddy-permitting resolution. *Ocean Dyn.*, 56(5-6):543–567. 51, 53, 149

Bates, N. and Mathis, J. (2009). The Arctic Ocean marine carbon cycle: evaluation of air-sea CO_2 exchanges, ocean acidification impacts and potential feedbacks. *Biogeosciences*, 6(11):2433–2459. 11, 12, 42, 57, 118, 122, 129, 137, 138, 158, 159, 170

Bates, N. R., Best, M. H., and Hansell, D. A. (2005). Spatio-temporal distribution of dissolved inorganic carbon and net community production in the Chukchi and Beaufort Seas. *Deep-Sea Res. Pt. II*, 52(24):3303–3323. 17

Bates, N. R., Mathis, J. T., and Cooper, L. W. (2009). Ocean acidification and biologically induced seasonality of carbonate mineral saturation states in the western Arctic Ocean. *J. Geophys. Res. Oceans*, 114(C11). 16, 17, 87, 138

Bates, N. R., Moran, S. B., Hansell, D. A., and Mathis, J. T. (2006). An increasing CO_2 sink in the Arctic Ocean due to sea-ice loss. *Geophys. Res. Lett.*, 33(23). 3, 148, 187

Bauer, J. E., Cai, W.-J., Raymond, P. A., Bianchi, T. S., Hopkinson, C. S., and Regnier, P. A. (2013). The changing carbon cycle of the coastal ocean. *Nature*, 504(7478):61. 107

Beaulieu, E., Goddéris, Y., Donnadieu, Y., Labat, D., and Roelandt, C. (2012). High sensitivity of the continental-weathering carbon dioxide sink to future climate change. *Nat. Clim. Change*, 2(5):346. 18, 139

Behrendt, H. and Opitz, D. (1999). Retention of nutrients in river systems: dependence on specific runoff and hydraulic load. In Garnier, J. and Mouchel, J.-M., editors, *Man and River Systems: The Functioning of River Systems at the Basin Scale*, pages 111–122, Dordrecht. Springer Netherlands. 110

Bekryaev, R. V., Polyakov, I. V., and Alexeev, V. A. (2010). Role of polar amplification in long-term surface air temperature variations and modern Arctic warming. *J. Clim.*, 23(14):3888–3906. 48

Beszczynska-Möller, A., Woodgate, R. A., Lee, C., Melling, H., and Karcher, M. (2011). A synthesis of exchanges through the main oceanic gateways to the Arctic Ocean. *Oceanography*, 24(3):82–99. 9

Biastoch, A., Böning, C. W., Schwarzkopf, F. U., and Lutjeharms, J. (2009). Increase in Agulhas leakage due to poleward shift of Southern Hemisphere westerlies. *Nature*, 462(7272):495. 184

Boé, J., Hall, A., and Qu, X. (2009). September sea-ice cover in the Arctic Ocean projected to vanish by 2100. *Nat. Geosci.*, 2(5):341. 10

Boer, G. J. and Arora, V. (2010). Geographic aspects of temperature and concentration feedbacks in the carbon budget. *J. Clim.*, 23(3):775–784. 148

Bopp, L., Resplandy, L., Orr, J. C., Doney, S. C., Dunne, J. P., Gehlen, M., Halloran, P., Heinze, C., Ilyina, T., Séférian, R., Tjiputra, J., and Vichi, M. (2013). Multiple stressors of ocean ecosystems in the 21st century: projections with CMIP5 models. *Biogeosciences*, 10(10):6225–6245. 3, 16

Borges, A. V., Delille, B., and Frankignoulle, M. (2005). Budgeting sinks and sources of CO_2 in the coastal ocean: Diversity of ecosystems counts. *Geophys. Res. Lett.*, 32(14). 184

Bourgain, P., Gascard, J. C., Shi, J., and Zhao, J. (2013). Large-scale temperature and salinity changes in the upper Canadian Basin of the Arctic Ocean at a time of a drastic Arctic Oscillation inversion. *Ocean Sci.*, 9(2):447–460. 87

Bourgeois, T., Orr, J. C., Resplandy, L., Terhaar, J., Ethé, C., Gehlen, M., and Bopp, L. (2016). Coastal-ocean uptake of anthropogenic carbon. *Biogeosciences*, 13(14):4167–4185. 50, 107, 109, 133, 150

Breitburg, D., Levin, L. A., Oschlies, A., Grégoire, M., Chavez, F. P., Conley, D. J., Garçon, V., Gilbert, D., Gutiérrez, D., Isensee, K., Jacinto, G. S., Limburg, K. E., Montes, I., Naqvi, S. W. A., Pitcher, G. C., Rabalais, N. N., Roman, M. R., Rose, K. A., Seibel, B. A., Telszewski, M., Yasuhara, M., and Zhang, J. (2018). Declining oxygen in the global ocean and coastal waters. *Science*, 359(6371). 107

Brewer, P. G. (1978). Direct observation of the oceanic CO_2 increase. *Geophys. Res. Lett.*, 5(12):997–1000. 48

Bring, A. and Destouni, G. (2009). Hydrological and hydrochemical observation status in the pan-Arctic drainage basin. *Polar Res.*, 28(3):327–338. 18

Brodeau, L., Barnier, B., Treguier, A.-M., Penduff, T., and Gulev, S. (2010). An ERA40-based atmospheric forcing for global ocean circulation models. *Ocean Model.*, 31(3):88–104. 35, 36, 53, 117, 152

Broecker, W., Takahashi, T., and Peng, T. (1985). Reconstruction of past atmospheric CO_2 contents from the chemistry of the contemporary ocean: an evaluation. Technical Report DOE/OR-857, US Department of Energy, Washington DC. 48

Broecker, W. S. and Peng, T.-H. (1974). Gas exchange rates between air and sea. *Tellus*, 26:21–35. 86

Bronselaer, B., Winton, M., Russell, J., Sabine, C. L., and Khatiwala, S. (2017). Agreement of CMIP5 Simulated and Observed Ocean Anthropogenic CO_2 Uptake. *Geophys. Res. Lett.*, 44(24):12298–12305. 38, 54, 55, 65

Brown, J., Ferrians Jr, O., Heginbottom, J., and Melnikov, E. (1997). *Circum-Arctic map of permafrost and ground-ice conditions*. US Geological Survey Reston. 111

Buitenhuis, E. T., Hashioka, T., and Quéré, C. L. (2013). Combined constraints on global ocean primary production using observations and models. *Global Biogeochem. Cy.*, 27(3):847–858. 15

Bullister, J. L. (2015). Atmospheric histories (1765-2015) for CFC-11, CFC-12, CFC-113, CCl_4, SF_6 and N_2O. *Carbon Dioxide Information Analysis Center, Oak Ridge National Laboratory, US Department of Energy, Oak Ridge, Tennessee*. 39, 56, 88

Cai, W.-J. (2003). Riverine inorganic carbon flux and rate of biological uptake in the Mississippi River plume. *Geophys. Res. Lett.*, 30(2). 151

Cai, W.-J. (2011). Estuarine and Coastal Ocean Carbon Paradox: CO_2 Sinks or Sites of Terrestrial Carbon Incineration? *Annu. Rev. Mar. Sci.*, 3(1):123–145. 107, 187

Cai, W.-J., Chen, L., Chen, B., Gao, Z., Lee, S. H., Chen, J., Pierrot, D., Sullivan, K., Wang, Y., Hu, X., et al. (2010). Decrease in the CO_2 uptake capacity in an ice-free Arctic Ocean basin. *Science*, 329(5991):556–559. 3, 17, 148, 170, 181

Carmack, E. and Chapman, D. C. (2003). Wind-driven shelf/basin exchange on an Arctic shelf: The joint roles of ice cover extent and shelf-break bathymetry. *Geophys. Res. Lett.*, 30(14). 15

Carmack, E. and Wassmann, P. (2006). Food webs and physical-biological coupling on pan-Arctic shelves: Unifying concepts and comprehensive perspectives. *Prog. Oceanog.*, 71(2):446–477. 11

Carmack, E. C., Yamamoto-Kawai, M., Haine, T. W. N., Bacon, S., Bluhm, B. A., Lique, C., Melling, H., Polyakov, I. V., Straneo, F., Timmermans, M., and Williams, W. J. (2015). Freshwater and its role in the Arctic Marine System: Sources, disposition, storage, export, and physical and biogeochemical consequences in the Arctic and global oceans. *J. Geophys. Res.*, 121(3):675–717. 146

Chen, G.-T. and Millero, F. J. (1979). Gradual increase of oceanic CO_2. *Nature*, 277(5693):205–206. 48

Chierici, M. and Fransson, A. (2009). Calcium carbonate saturation in the surface water of the Arctic Ocean: undersaturation in freshwater influenced shelves. *Biogeosciences*, 6(11):2421–2431. 4, 14, 17, 21, 23, 85, 107, 108, 148, 160, 181

Ciais, P., Sabine, C., Bala, G., Bopp, L., Brovkin, V., Canadell, J., Chhabra, A., DeFries, R., Galloway, J., Heimann, M., Jones, C., Le Quéré, C., Myneni, R., Piao, S., and Thornton, P. (2013). Carbon and other biogeochemical cycles. In Stocker, T., Qin, D., Plattner, G.-K., Tignor, M., Allen, S., Boschung, J., Nauels, A., Xia, Y., Bex, V., and Midgley, P., editors, *Climate Change 2013: The Physical Science Basis. Contribution of Working Group I to the Fifth Assessment Report of the Intergovernmental Panel on Climate Change*, book section 6, pages 465–570. Cambridge University Press, Cambridge, United Kingdom and New York, NY, USA. xiv, 20, 21, 22, 140, 167, 180

Cloern, J. E., Foster, S. Q., and Kleckner, A. E. (2014). Phytoplankton primary production in the world's estuarine-coastal ecosystems. *Biogeosciences*, 11(9):2477–2501. 107

Coachman, L. and Barnes, C. (1962). Surface water in the Eurasian Basin of the Arctic Ocean. *Arctic*, 15(4). 7

Codispoti, L., Kelly, V., Thessen, A., Matrai, P., Suttles, S., Hill, V., Steele, M., and Light, B. (2013). Synthesis of primary production in the Arctic Ocean: III. Nitrate and phosphate based estimates of net community production. *Prog. Oceanog.*, 110:126–150. 15

Cohen, J., Screen, J. A., Furtado, J. C., Barlow, M., Whittleston, D., Coumou, D., Francis, J., Dethloff, K., Entekhabi, D., Overland, J., et al. (2014). Recent Arctic amplification and extreme mid-latitude weather. *Nat Geosci.*, 7(9):627. 2

Conkright, M. E., Locarnini, R. A., Garcia, H. E., O'Brien, T. D., Boyer, T. P., Stephens, C., and Antonov, J. I. (2002). World Ocean Atlas 2001: Objective analyses, data statistics, and figures: CD-ROM documentation. 36, 53

Curry, B., Lee, C., Petrie, B., Moritz, R., and Kwok, R. (2014). Multiyear volume, liquid freshwater, and sea ice transports through Davis Strait, 2004–10. *J. Phys. Oceanogr.*, 44(4):1244–1266. 8, 9, 59, 60

Dai, A. and Trenberth, K. E. (2002). Estimates of freshwater discharge from continents: Latitudinal and seasonal variations. *J. Hydrometeorol.*, 3(6):660–687. 36, 38, 110, 112, 117, 150

Darnis, G., Robert, D., Pomerleau, C., Link, H., Archambault, P., Nelson, R. J., Geoffroy, M., Tremblay, J.-É., Lovejoy, C., Ferguson, S. H., Hunt, B. P. V., and Fortier, L. (2012). Current state and trends in Canadian Arctic marine ecosystems: II. Heterotrophic food web, pelagic-benthic coupling, and biodiversity. *Climatic Change*, 115(1):179–205. 148

de Baar, H. and de Jong, J. (2001). Distributions, sources and sinks of iron in seawater. In Turner, D. and Hunter, K., editors, *Biogeochemistry of Iron in Seawater*, pages 123–253. Wiley. 37

Debreu, L., Vouland, C., and Blayo, E. (2008). AGRIF: Adaptive grid refinement in Fortran. *Comput. Geosci.*, 34(1):8–13. 184

Dee, D. P., Uppala, S. M., Simmons, A. J., Berrisford, P., Poli, P., Kobayashi, S., Andrae, U., Balmaseda, M. A., Balsamo, G., Bauer, P., Bechtold, P., Beljaars, A. C. M., van de Berg, L., Bidlot, J., Bormann, N., Delsol, C., Dragani, R., Fuentes, M., Geer, A. J., Haimberger, L., Healy, S. B., Hersbach, H., Hólm, E. V., Isaksen, L., Kållberg, P., Köhler, M., Matricardi, M., McNally, A. P., Monge-Sanz, B. M., Morcrette, J.-J., Park, B.-K., Peubey, C., de Rosnay, P., Tavolato, C., Thépaut, J.-N., and Vitart, F. (2011). The ERA-Interim reanalysis: configuration and performance of the data assimilation system. *Q. J. Roy. Meteor. Soc.*, 137(656):553–597. 35, 152

Déry, S. J., Hernández-Henríquez, M. A., Burford, J. E., and Wood, E. F. (2009). Observational evidence of an intensifying hydrological cycle in northern Canada. *Geophys. Res. Lett.*, 36(13). 16, 146

Déry, S. J. and Wood, E. F. (2005). Decreasing river discharge in northern Canada. *Geophys. Res. Lett.*, 32(10). 16, 146

Dickson, A. and Riley, J. (1979). The estimation of acid dissociation constants in sea-water media from potentiometric titrations with strong base. II. The dissociation of phosphoric acid. *Mar. Chem.*, 7(2):101 – 109. 118

Dickson, A. G. (1990). Standard potential of the reaction: AgCl(s) + $12H_2$(g) = Ag(s) + HCl(aq), and and the standard acidity constant of the ion HSO_4^- in synthetic sea water from 273.15 to 318.15 K. *J. Chem. Thermodyn.*, 22(2):113–127. 40, 88

Dickson, A. G., Sabine, C. L., and Christian, J. R. (2007). Guide to best practices for ocean CO_2 measurements. Technical report, PICES Special Publication 3, 191 pp. 39, 55, 90

Dittmar, T. and Kattner, G. (2003). The biogeochemistry of the river and shelf ecosystem of the Arctic Ocean: a review. *Mar. Chem.*, 83(3):103–120. 131, 132

Doney, S. C., Bopp, L., and Matthew (2014). Historical and future trends in ocean climate and biogeochemistry . *Oceanography*, 27. 13

Drake, T. W., Tank, S. E., Zhulidov, A. V., Holmes, R. M., Gurtovaya, T., and Spencer, R. G. M. (2018). Increasing alkalinity export from large russian Arctic rivers. *Environ. Sci. Technol.*, 52(15):8302–8308. 18, 139, 144, 147, 181, 188

Dunne, J. P., Sarmiento, J. L., and Gnanadesikan, A. (2007). A synthesis of global particle export from the surface ocean and cycling through the ocean interior and on the seafloor. *Global Biogeochem. Cy.*, 21(4). 34

Dürr, H. H., Meybeck, M., and Dürr, S. H. (2005). Lithologic composition of the Earth's continental surfaces derived from a new digital map emphasizing riverine material transfer. *Global Biogeochem. Cy.*, 19(4). 110, 111

Dutay, J.-C., Bullister, J., Doney, S., Orr, J., Najjar, R., Caldeira, K., Campin, J.-M., Drange, H., Follows, M., Gao, Y., Gruber, N., Hecht, M., Ishida, A., Joos, F., Lindsay, K., Madec, G., Maier-Reimer, E., Marshall, J., Matear, R., Monfray, P., Mouchet, A., Plattner, G.-K., Sarmiento, J., Schlitzer, R., Slater, R., Totterdell, I., Weirig, M.-F., Yamanaka, Y., and Yool, A. (2002). Evaluation of ocean model ventilation with CFC-11: comparison of 13 global ocean models. *Ocean Model.*, 4(2):89–120. 39, 56, 58, 88

Duteil, O., Schwarzkopf, F. U., Böning, C. W., and Oschlies, A. (2014). Major role of the equatorial current system in setting oxygen levels in the eastern tropical Atlantic Ocean: A high-resolution model study. *Geophys. Res. Lett.*, 41(6):2033–2040. 73, 184

Falkowski, P. G., Barber, R. T., and Smetacek, V. (1998). Biogeochemical controls and feedbacks on ocean primary production. *Science*, 281(5374):200–206. 15

Fekete, B. M., Vörösmarty, C. J., and Grabs, W. (2002). High-resolution fields of global runoff combining observed river discharge and simulated water balances. *Global Biogeochem. Cy.*, 16(3):15–1–15–10. 108, 111, 112

Fichefet, T. and Maqueda, M. A. M. (1997). Sensitivity of a global sea ice model to the treatment of ice thermodynamics and dynamics. *J. Geophys. Res. - Oceans*, 102(C6):12609–12646. 28, 32, 114

Frey, K. E. and McClelland, J. W. (2008). Impacts of permafrost degradation on arctic river biogeochemistry. *Hydrol. Process.*, 23(1):169–182. 147

Frey, K. E. and McClelland, J. W. (2009). Impacts of permafrost degradation on arctic river biogeochemistry. *Hydrol. Process.*, 23(1):169–182. 15

Frey, K. E., McClelland, J. W., Holmes, R. M., and Smith, L. C. (2007). Impacts of climate warming and permafrost thaw on the riverine transport of nitrogen and phosphorus to the Kara Sea. *J. Geophys. Res. - Biogeosci.*, 112(G4). 18, 139, 147

Frey, K. E. and Smith, L. C. (2005). Amplified carbon release from vast West Siberian peatlands by 2100. *Geophys. Res. Lett.*, 32(9). 137, 147

Friedlingstein, P., Bopp, L., Ciais, P., Dufresne, J.-L., Fairhead, L., LeTreut, H., Monfray, P., and Orr, J. (2001). Positive feedback between future climate change and the carbon cycle. *Geophys. Res. Lett.*, 28(8):1543–1546. 144, 147

Friedlingstein, P., Cox, P., Betts, R., Bopp, L., von Bloh, W., Brovkin, V., Cadule, P., Doney, S., Eby, M., Fung, I., Bala, G., John, J., Jones, C., Joos, F., Kato, T., Kawamiya, M., Knorr, W., Lindsay, K.,

Matthews, H. D., Raddatz, T., Rayner, P., Reick, C., Roeckner, E., Schnitzler, K.-G., Schnur, R., Strassmann, K., Weaver, A. J., Yoshikawa, C., and Zeng, N. (2006). Climate-carbon cycle geedback analysis: Results from the C4MIP model intercomparison. *J. Clim.*, 19(14):3337–3353. 154

Friedlingstein, P., Dufresne, J. L., Cox, P. M., and Rayner, P. (2003). How positive is the feedback between climate change and the carbon cycle? *Tellus B*, 55(2):692–700. 35, 153

Fritz, M., Vonk, J. E., and Lantuit, H. (2017). Collapsing arctic coastlines. *Nat. Clim. Chang.*, 7(1):6. 134

Frölicher, T. L., Fischer, E. M., and Gruber, N. (2018). Marine heatwaves under global warming. *Nature*, 560(7718):360. 186

Frölicher, T. L. and Joos, F. (2010). Reversible and irreversible impacts of greenhouse gas emissions in multi-century projections with the NCAR global coupled carbon cycle-climate model. *Clim. Dyn.*, 35(7):1439–1459. 20

Gammelsrød, T., Leikvin, Ø., Lien, V., Budgell, W. P., Loeng, H., and Maslowski, W. (2009). Mass and heat transports in the NE Barents Sea: Observations and models. *Journal of Marine Systems*, 75(1):56–69. 9, 87, 92

Garneau, M.-È., Gosselin, M., Klein, B., Tremblay, J.-É., and Fouilland, E. (2007). New and regenerated production during a late summer bloom in an Arctic polynya. *Mar. Ecol. Prog. Ser.*, 345:13–26. 109

Gattuso, J.-P., Frankignoulle, M., Bourge, I., Romaine, S., and Buddemeier, R. (1998). Effect of calcium carbonate saturation of seawater on coral calcification. *Global Planet. Change*, 18(1):37–46. 13

Gattuso, J.-P. and Hansson, L. (2011). *Ocean acidification*. Oxford University Press, Oxford. 3, 13, 48

Gent, P. R. and McWilliams, J. C. (1990). Isopycnal mixing in ocean circulation models. *J. Phys. Oceanogr.*, 20(1):150–155. 31, 52, 149

Gloersen, P., Campbell, W. J., Cavalieri, D. J., Comiso, J. C., Parkinson, C. L., and Jay Zwally, H. (1993). Satellite passive microwave observations and analysis of Arctic and Antarctic sea ice, 1978–1987. *Annals of Glaciology*, 17:149–154. 9

Gordeev, V., Martin, J., Sidorov, I., and Sidorova, M. (1996). A reassessment of the Eurasian river input of water, sediment, major elements, and nutrients to the Arctic Ocean. *Am. J. Sci.*, 296(6):664–691. 132

Gruber, N., Gloor, M., Mikaloff Fletcher, S. E., Doney, S. C., Dutkiewicz, S., Follows, M. J., Gerber, M., Jacobson, A. R., Joos, F., Lindsay, K., Menemenlis, D., Mouchet, A., Müller, S. A., Sarmiento, J. L., and Takahashi, T. (2009). Oceanic sources, sinks, and transport of atmospheric CO_2. *Global Biogeochem. Cy.*, 23(1). 78, 79

Gruber, N., Sarmiento, J. L., and Stocker, T. F. (1996). An improved method for detecting anthropogenic CO_2 in the oceans. *Global Biogeochem. Cy.*, 10(4):809–837. 12, 48

Guo, L., Ping, C.-L., and Macdonald, R. W. (2007). Mobilization pathways of organic carbon from permafrost to Arctic rivers in a changing climate. *Geophys. Res. Lett.*, 34(13). 139

Hall, T. M., Haine, T. W., and Waugh, D. W. (2002). Inferring the concentration of anthropogenic carbon in the ocean from tracers. *Global Biogeochem. Cy.*, 16(4). 12, 40, 48, 86, 88

Hall-Spencer, J. M., Rodolfo-Metalpa, R., Martin, S., Ransome, E., Fine, M., Turner, S. M., Rowley, S. J., Tedesco, D., and Buia, M.-C. (2008). Volcanic carbon dioxide vents show ecosystem effects of ocean acidification. *Nature*, 454(7200):96. xiv, 13, 14

Hansell, D. A., Kadko, D., and Bates, N. R. (2004). Degradation of terrigenous dissolved organic carbon in the western Arctic Ocean. *Science*, 304(5672):858–861. 163, 164

Harsch, M. A., Hulme, P. E., McGlone, M. S., and Duncan, R. P. (2009). Are treelines advancing? A global meta-analysis of treeline response to climate warming. *Ecol. Lett.*, 12(10):1040–1049. 18, 144, 147

Hill, V. J., Matrai, P. A., Olson, E., Suttles, S., Steele, M., Codispoti, L., and Zimmerman, R. C. (2013). Synthesis of integrated primary production in the Arctic Ocean: II. In situ and remotely sensed estimates. *Prog. Oceanog.*, 110:107–125. 15, 41, 42, 156, 158

Hoegh-Guldberg, O., Mumby, P. J., Hooten, A. J., Steneck, R. S., Greenfield, P., Gomez, E., Harvell, C. D., Sale, P. F., Edwards, A. J., Caldeira, K., Knowlton, N., Eakin, C. M., Iglesias-Prieto, R., Muthiga, N., Bradbury, R. H., Dubi, A., and Hatziolos, M. E. (2007). Coral reefs under rapid climate change and ocean acidification. *Science*, 318(5857):1737–1742. 13

Holmes, R., Peterson, B., Zhulidov, A., Gordeev, V., Makkaveev, P., Stunzhas, P., Kosmenko, L., Köhler, G., and Shiklomanov, A. (2001). Nutrient chemistry of the Ob' and Yenisey Rivers, Siberia: results from June 2000 expedition and evaluation of long-term data sets. *Mar. Chem.*, 75(3):219–227. 18, 109, 132, 147

Holmes, R. M., McClelland, J. W., Peterson, B. J., Tank, S. E., Bulygina, E., Eglinton, T. I., Gordeev, V. V., Gurtovaya, T. Y., Raymond, P. A., Repeta, D. J., Staples, R., Striegl, R. G., Zhulidov, A. V., and Zimov, S. A. (2012). Seasonal and Annual Fluxes of Nutrients and Organic Matter from Large Rivers to the Arctic Ocean and Surrounding Seas. *Estuaries Coast*, 35(2):369–382. xxii, 11, 12, 18, 36, 37, 42, 106, 109, 110, 131, 132, 151, 155, 156, 182, 188

Holmes, R. M., McClelland, J. W., Raymond, P. A., Frazer, B. B., Peterson, B. J., and Stieglitz, M. (2008). Lability of DOC transported by Alaskan rivers to the Arctic Ocean. *Geophys. Res. Lett.*, 35(3). 151, 163, 164, 183

Holmes, R. M., Peterson, B. J., Gordeev, V. V., Zhulidov, A. V., Meybeck, M., Lammers, R. B., and Vörösmarty, C. J. (2000). Flux of nutrients from Russian rivers to the Arctic Ocean: Can we establish a baseline against which to judge future changes? *Water Resour. Res.*, 36(8):2309–2320. 18, 109, 132, 147

Honjo, S., Krishfield, R. A., Eglinton, T. I., Manganini, S. J., Kemp, J. N., Doherty, K., Hwang, J., McKee, T. K., and Takizawa, T. (2010). Biological pump processes in the cryopelagic and hemipelagic Arctic Ocean: Canada Basin and Chukchi Rise. *Prog. Oceanog.*, 85(3):137–170. 11

Humborg, C., Geibel, M. C., Anderson, L. G., Björk, G., Mörth, C.-M., Sundbom, M., Thornton, B. F., Deutsch, B., Gustafsson, E., Gustafsson, B., Ek, J., and Semiletov, I. (2017). Sea-air exchange patterns along the central and outer East Siberian Arctic Shelf as inferred from continuous CO_2, stable isotope, and bulk chemistry measurements. *Global Biogeochem. Cy.*, 31(7):1173–1191. 108

Humborg, C., Smedberg, E., Medina, M. R., and Mörth, C.-M. (2008). Changes in dissolved silicate loads to the Baltic Sea - The effects of lakes and reservoirs. *J. of Marine Syst.*, 73(3):223–235. 110

Ilyina, T., Six, K. D., Segschneider, J., Maier-Reimer, E., Li, H., and Núñez-Riboni, I. (2013). Global ocean biogeochemistry model HAMOCC: Model architecture and performance as component of the MPI-Earth system model in different CMIP5 experimental realizations. *J. Adv. Model. Earth Sy.*, 5(2):287–315. 20, 106, 133, 140, 180

Jähne, B. and Haußecker, H. (1998). Air-water gas exchange. *Annu. Rev. Fluid Mech.*, 30(1):443–468. 11

Jakobsson, M. (2002). Hypsometry and volume of the Arctic Ocean and its constituent seas. *Geochem. Geophys.*, 3(5):1–18. 6, 49, 146

Jakobsson, M., Cherkis, N., Woodward, J., Macnab, R., and Coakley, B. (2000a). New grid of Arctic bathymetry aids scientists and mapmakers. *Eos Trans. AGU*, 81(9):89–96. 30, 116, 149

Jakobsson, M., Cherkis, N., Woodward, J., Macnab, R., and Coakley, B. (2000b). New grid of Arctic bathymetry aids scientists and mapmakers. *Eos Trans. AGU*, 81(9):89–96. 51

Jakobsson, M., Macnab, R., Mayer, L., Anderson, R., Edwards, M., Hatzky, J., Schenke, H. W., and Johnson, P. (2008). An improved bathymetric portrayal of the Arctic Ocean: Implications for ocean modeling and geological, geophysical and oceanographic analyses. *Geophys. Res. Lett.*, 35(7). xiii, 6

Jeansson, E., Olsen, A., Eldevik, T., Skjelvan, I., Omar, A. M., Lauvset, S. K., Nilsen, J. E. O., Bellerby, R. G. J., Johannessen, T., and Falck, E. (2011). The Nordic Seas carbon budget: Sources, sinks, and uncertainties. *Global Biogeochem. Cy.*, 25(4). 12, 60, 71, 84

Joesoef, A., Kirchman, D. L., Sommerfield, C. K., and Cai, W.-J. (2017). Seasonal variability of the inorganic carbon system in a large coastal plain estuary. *Biogeosciences*, 14(21):4949–4963. 151

Jones, E., Rudels, B., and Anderson, L. (1995). Deep waters of the Arctic Ocean: origins and circulation. *Deep-Sea Res. Pt. I*, 42(5):737–760. 49, 72, 73, 90, 185

Jones, E. P. (2001). Circulation in the Arctic Ocean. *Pol. Res.*, 20(2):139–146. 90

Jones, P., Azetsu-Scott, K., Aagaard, K., Carmack, E., and Swift, J. (2007). L.S. St. Laurent 18SN19940724, AOS94 cruise data from the 1994 cruises, CARINA Data Set. 41, 59

Kaiser, K., Benner, R., and Amon, R. M. W. (2017). The fate of terrigenous dissolved organic carbon on the Eurasian shelves and export to the North Atlantic. *J. Geophys. Res. - Oceans*, 122(1):4–22. 117, 138, 151, 152, 163, 182, 183

Kaltin, S. and Anderson, L. G. (2005). Uptake of atmospheric carbon dioxide in Arctic shelf seas: evaluation of the relative importance of processes that influence pCO2 in water transported over the Bering-Chukchi Sea shelf. *Mar. Chem.*, 94(1):67–79. 91

Kawaguchi, S., Ishida, A., King, R., Raymond, B., Waller, N., Constable, A., Nicol, S., Wakita, M., and Ishimatsu, A. (2013). Risk maps for Antarctic krill under projected Southern Ocean acidification. *Nat. Clim. Change*, 3(9):843. 13

Key, R. M., Kozyr, A., Sabine, C. L., Lee, K., Wanninkhof, R., Bullister, J. L., Feely, R. A., Millero, F. J., Mordy, C., and Peng, T.-H. (2004). A global ocean carbon climatology: Results from Global Data Analysis Project (GLODAP). *Global Biogeochem. Cy.*, 18(4). 36, 53

Khatiwala, S., Primeau, F., and Hall, T. (2009). Reconstruction of the history of anthropogenic CO_2 concentrations in the ocean. *Nature*, 462(7271):346. 48, 65

Khatiwala, S., Tanhua, T., Fletcher, S. M., Gerber, M., Doney, S., Graven, H., Gruber, N., McKinley, G., Murata, A., Ríos, A., et al. (2013). Global ocean storage of anthropogenic carbon. *Biogeosciences*, 10(4):2169–2191. 12, 40, 48, 71, 86

Kicklighter, D. W., Hayes, D. J., McClelland, J. W., Peterson, B. J., McGuire, A. D., and Melillo, J. M. (2013). Insights and issues with simulating terrestrial DOC loading of Arctic river networks. *Ecol. Appl.*, 23(8):1817–1836. 18, 139

Körtzinger, A., Hedges, J. I., and Quay, P. D. (2001). Redfield ratios revisited: Removing the biasing effect of anthropogenic CO_2. *Limnol. Oceanog.*, 46(4):964–970. 32, 150

Kwiatkowski, L., Aumont, O., and Bopp, L. (2019). Consistent trophic amplification of marine biomass declines under climate change. *Global Change Biol.*, 25(1):218–229. 182

Kwiatkowski, L., Aumont, O., Bopp, L., and Ciais, P. (2018). The impact of variable phytoplankton stoichiometry on projections of primary production, food quality, and carbon uptake in the global ocean. *Global Biogeochem. Cy.*, 32(4):516–528. 182

Kwiatkowski, L., Bopp, L., Aumont, O., Ciais, P., Cox, P. M., Laufkötter, C., Li, Y., and Séférian, R. (2017). Emergent constraints on projections of declining primary production in the tropical oceans. *Nat. Clim. Change*, 7(5):355. 188

Lachkar, Z., Orr, J. C., Dutay, J.-C., and Delecluse, P. (2007). Effects of mesoscale eddies on global ocean distributions of CFC-11, CO_2, and ^{14}C. *Ocean Sci.*, 3(4):461–482. 73, 87

Langdon, C., Takahashi, T., Sweeney, C., Chipman, D., Goddard, J., Marubini, F., Aceves, H., Barnett, H., and Atkinson, M. J. (2000). Effect of calcium carbonate saturation state on the calcification rate of an experimental coral reef. *Global Biogeochem. Cy.*, 14(2):639–654. 13

Langehaug, H. R. and Falck, E. (2012). Changes in the properties and distribution of the intermediate and deep waters in the Fram Strait. *Prog. Oceanog.*, 96(1):57–76. 96

Lauerwald, R., Hartmann, J., Ludwig, W., and Moosdorf, N. (2012). Assessing the nonconservative fluvial fluxes of dissolved organic carbon in North America. *J. Geophys. Res. - Biogeo.*, 117(G1). 112

Lauvset, S. K., Gruber, N., Landschützer, P., Olsen, A., and Tjiputra, J. (2015). Trends and drivers in global surface ocean pH over the past 3 decades. *Biogeosciences*, 12(5):1285–1298. 13

Lauvset, S. K., Key, R. M., and Perez, F. F. (2016). A new global interior ocean mapped climatology: the 1° × 1° GLODAP version 2. *Earth Syst. Sci. Data*, 8(2):325. xix, xxii, 41, 59, 66, 118, 122, 124, 157, 159, 160

Lawrence, D. M. and Slater, A. G. (2005). A projection of severe near-surface permafrost degradation during the 21st century. *Geophys. Res. Lett.*, 32(24). 4, 16, 18, 139, 144, 146, 147

Le Fouest, V., Babin, M., and Tremblay, J.-E. (2013). The fate of riverine nutrients on Arctic shelves. *Biogeosciences*, 10(6):3661–3677. 4, 17, 20, 109, 131, 132, 135, 147

Le Fouest, V., Manizza, M., Tremblay, B., and Babin, M. (2015). Modelling the impact of riverine DON removal by marine bacterioplankton on primary production in the Arctic Ocean. *Biogeosciences*, 12(11):3385–3402. 17, 19, 20, 23, 109, 135, 136, 147, 148, 183, 188

Le Fouest, V., Matsuoka, A., Manizza, M., Shernetsky, M., Tremblay, B., and Babin, M. (2018). Towards an assessment of riverine dissolved organic carbon in surface waters of the western Arc-

tic Ocean based on remote sensing and biogeochemical modeling. *Biogeosciences*, 15(5):1335–1346. 17, 147

Le Quéré, C., Andrew, R. M., Friedlingstein, P., Sitch, S., Pongratz, J., Manning, A. C., Korsbakken, J. I., Peters, G. P., Canadell, J. G., Jackson, R. B., Boden, T. A., Tans, P. P., Andrews, O. D., Arora, V. K., Bakker, D. C. E., Barbero, L., Becker, M., Betts, R. A., Bopp, L., Chevallier, F., Chini, L. P., Ciais, P., Cosca, C. E., Cross, J., Currie, K., Gasser, T., Harris, I., Hauck, J., Haverd, V., Houghton, R. A., Hunt, C. W., Hurtt, G., Ilyina, T., Jain, A. K., Kato, E., Kautz, M., Keeling, R. F., Klein Goldewijk, K., Körtzinger, A., Landschützer, P., Lefèvre, N., Lenton, A., Lienert, S., Lima, I., Lombardozzi, D., Metzl, N., Millero, F., Monteiro, P. M. S., Munro, D. R., Nabel, J. E. M. S., Nakaoka, S.-I., Nojiri, Y., Padin, X. A., Peregon, A., Pfeil, B., Pierrot, D., Poulter, B., Rehder, G., Reimer, J., Rödenbeck, C., Schwinger, J., Séférian, R., Skjelvan, I., Stocker, B. D., Tian, H., Tilbrook, B., Tubiello, F. N., van der Laan-Luijkx, I. T., van der Werf, G. R., van Heuven, S., Viovy, N., Vuichard, N., Walker, A. P., Watson, A. J., Wiltshire, A. J., Zaehle, S., and Zhu, D. (2018). Global Carbon Budget 2017. *Earth Syst. Sci. Data*, 10(1):405–448. 11, 35, 39

Le Quéré, C., Moriarty, R., Andrew, R. M., Peters, G. P., Ciais, P., Friedlingstein, P., Jones, S. D., Sitch, S., Tans, P., Arneth, A., Boden, T. A., Bopp, L., Bozec, Y., Canadell, J. G., Chini, L. P., Chevallier, F., Cosca, C. E., Harris, I., Hoppema, M., Houghton, R. A., House, J. I., Jain, A. K., Johannessen, T., Kato, E., Keeling, R. F., Kitidis, V., Klein Goldewijk, K., Koven, C., Landa, C. S., Landschützer, P., Lenton, A., Lima, I. D., Marland, G., Mathis, J. T., Metzl, N., Nojiri, Y., Olsen, A., Ono, T., Peng, S., Peters, W., Pfeil, B., Poulter, B., Raupach, M. R., Regnier, P., Rödenbeck, C., Saito, S., Salisbury, J. E., Schuster, U., Schwinger, J., Séférian, R., Segschneider, J., Steinhoff, T., Stocker, B. D., Sutton, A. J., Takahashi, T., Tilbrook, B., van der Werf, G. R., Viovy, N., Wang, Y.-P., Wanninkhof, R., Wiltshire, A., and Zeng, N. (2015). Global carbon budget 2014. *Earth Syst. Sci. Data*, 7(1):47–85. 12, 54, 88, 117

Lehner, B. and Döll, P. (2004). Development and validation of a global database of lakes, reservoirs and wetlands. *J. Hydrol.*, 296(1):1–22. 111

Letscher, R. T., Hansell, D. A., and Kadko, D. (2011). Rapid removal of terrigenous dissolved organic carbon over the Eurasian shelves of the Arctic Ocean. *Mar. Chem.*, 123(1):78–87. 117, 163, 164

Letscher, R. T., Hansell, D. A., Kadko, D., and Bates, N. R. (2013). Dissolved organic nitrogen dynamics in the Arctic Ocean. *Mar. Chem.*, 148:1–9. 17, 117, 136, 147, 183

Levitus, S., Boyer, T., Conkright, M., O'brien, T., Antonov, J., Stephens, C., Stathoplos, L., Johnson, D., and Gelfeld, R. (1998). NOAA Atlas NESDIS 18, World Ocean Database 1998: vol. 1: Introduction. *US Government Printing Office, Washington DC*, 346. 36

Lique, C., Johnson, H. L., and Plancherel, Y. (2018). Emergence of deep convection in the Arctic Ocean under a warming climate. *Clim. Dyn.*, 50(9):3833–3847. 96, 187

Loeng, H. (1991). Features of the physical oceanographic conditions of the Barents Sea. *Polar Res.*, 10(1):5–18. 92

Ludwig, W., Amiotte-Suchet, P., Munhoven, G., and Probst, J.-L. (1998). Atmospheric CO_2 consumption by continental erosion: present-day controls and implications for the last glacial maximum. *Glob. Planet. Change*, 16:107–120. 52, 150

Ludwig, W., Probst, J.-L., and Kempe, S. (1996). Predicting the oceanic input of organic carbon by continental erosion. *Global Biogeochem. Cy.*, 10(1):23–41. 36, 37, 109, 110, 116

Lueker, T. J., Dickson, A. G., and Keeling, C. D. (2000). Ocean pCO_2 calculated from dissolved inorganic carbon, alkalinity, and equations for K1 and K2: validation based on laboratory measurements of CO_2 in gas and seawater at equilibrium. *Mar. Chem.*, 70(1):105–119. 118

Luo, Y., Boudreau, B. P., and Mucci, A. (2016). Disparate acidification and calcium carbonate desaturation of deep and shallow waters of the Arctic Ocean. *Nat. Commun.*, 7:12821. 19, 49

Lythe, M. B. and Vaughan, D. G. (2001). BEDMAP: A new ice thickness and subglacial topographic model of Antarctica. *J. Geophys. Res.*, 106(B6):11335–11351. 30, 51, 149

MacGilchrist, G., Garabato, A. N., Tsubouchi, T., Bacon, S., Torres-Valdes, S., and Azetsu-Scott, K. (2014). The Arctic Ocean carbon sink. *Deep-Sea Res. Pt. I*, 86:39–55. 11, 12, 90

Madec, G. (2008). *NEMO ocean engine*. Note du Pôle de modélisation, Institut Pierre-Simon Laplace (IPSL), France, No 27, ISSN No 1288-1619. 28, 50, 51, 87, 114, 149

Madec, G., Delecluse, P., Imbard, M., and Levy, C. (1998). *Ocean general circulation model reference manual*. Note du Pôle de modélisation, Institut Pierre-Simon Laplace (IPSL), France. 50, 115

Madec, G. et al. (2015). *NEMO ocean engine*. Institut Pierre-Simon Laplace. xiv, 25, 28, 30

Madec, G. and Imbard, M. (1996). A global ocean mesh to overcome the North Pole singularity. *Climate Dynamics*, 12(6):381–388. 30, 51, 149

Manizza, M., Follows, M. J., Dutkiewicz, S., McClelland, J. W., Menemenlis, D., Hill, C. N., Townsend-Small, A., and Peterson, B. J. (2009). Modeling transport and fate of riverine dissolved organic carbon in the Arctic Ocean. *Global Biogeochem. Cy.*, 23(4). 18, 19, 106, 109, 131, 132, 135, 137, 138, 183, 188

Manizza, M., Follows, M. J., Dutkiewicz, S., Menemenlis, D., Hill, C. N., and Key, R. M. (2013). Changes in the Arctic Ocean CO_2 sink (1996–2007): A regional model analysis. *Global Biogeochem. Cy.*, 27(4):1108–1118. 19, 20

Manizza, M., Follows, M. J., Dutkiewicz, S., Menemenlis, D., McClelland, J. W., Hill, C. N., Peterson, B. J., and Key, R. M. (2011). A model of the Arctic Ocean carbon cycle. *J. Geophys. Res. - Oceans*, 116(C12). 4, 17, 19, 20, 23, 108, 147, 148

Manizza, M., Menemenlis, D., Miller, Charles, E., and Zhang, H. (2019). Modeling the recent changes in the Arctic Ocean CO_2 sink (2006–2013). *Global Biogeochem. Cy.*, 0(ja). 3, 19, 20, 140, 170, 180, 181

Mann, P. J., Eglinton, T. I., McIntyre, C. P., Zimov, N., Davydova, A., Vonk, J. E., Holmes, R. M., and Spencer, R. G. (2015). Utilization of ancient permafrost carbon in headwaters of Arctic fluvial networks. *Nat. Commun.*, 6:7856. 160

Matear, R. J., Wong, C. S., and Xie, L. (2003). Can CFCs be used to determine anthropogenic CO_2? *Global Biogeochem. Cy.*, 17(1). 87

Mathis, J. T., Cross, J. N., and Bates, N. R. (2011). Coupling primary production and terrestrial runoff to ocean acidification and carbonate mineral suppression in the eastern Bering Sea. *J. Geophys. Res. - Oceans*, 116(C2). 160

Mathis, J. T., Pickart, R. S., Byrne, R. H., McNeil, C. L., Moore, G. W. K., Juranek, L. W., Liu, X., Ma, J., Easley, R. A., Elliot, M. M., Cross, J. N., Reisdorph, S. C., Bahr, F., Morison, J., Lichendorf, T., and Feely, R. A. (2012). Storm-induced upwelling of high pCO_2 waters onto the continental shelf of the western Arctic Ocean and implications for carbonate mineral saturation states. *Geophys. Res. Lett.*, 39(7). 10

Mayorga, E., Seitzinger, S. P., Harrison, J. A., Dumont, E., Beusen, A. H., Bouwman, A., Fekete, B. M., Kroeze, C., and Drecht, G. V. (2010). Global Nutrient Export from WaterSheds 2 (NEWS 2): Model development and implementation. *Environ. Model. Softw.*, 25(7):837–853. 36, 37, 109, 116, 150

McClelland, J. W., Déry, S. J., Peterson, B. J., Holmes, R. M., and Wood, E. F. (2006). A pan-arctic evaluation of changes in river discharge during the latter half of the 20th century. *Geophys. Res. Lett.*, 33(6). 16, 60, 146

McClelland, J. W., Holmes, R. M., Dunton, K. H., and Macdonald, R. W. (2012). The Arctic Ocean estuary. *Estuaries Coast*, 35(2):353–368. 7, 16, 108, 145, 184

McClelland, J. W., Holmes, R. M., Peterson, B. J., Amon, R., Brabets, T., Cooper, L., Gibson, J., Gordeev, V. V., Guay, C., Milburn, D., Staples, R., Raymond, P. A., Shiklomanov, I., Striegl, R., Zhulidov, A., Gurtovaya, T., and Zimov, S. (2008). Development of a pan-Arctic database for river chemistry. *Eos Trans. AGU*, 89(24):217–218. 18, 42, 109, 147, 184

McClelland, J. W., Holmes, R. M., Peterson, B. J., and Stieglitz, M. (2004). Increasing river discharge in the Eurasian Arctic: Consideration of dams, permafrost thaw, and fires as potential agents of change. *J. Geophys. Res. - Atmos.*, 109(D18). 16, 146

Meinshausen, M., Smith, S. J., Calvin, K., Daniel, J. S., Kainuma, M. L. T., Lamarque, J.-F., Matsumoto, K., Montzka, S. A., Raper, S. C. B., Riahi, K., Thomson, A., Velders, G. J. M., and van

Vuuren, D. P. (2011). The RCP greenhouse gas concentrations and their extensions from 1765 to 2300. *Clim. Change*, 109(1):213. 90

Meinshausen, M., Vogel, E., Nauels, A., Lorbacher, K., Meinshausen, N., Etheridge, D. M., Fraser, P. J., Montzka, S. A., Rayner, P. J., Trudinger, C. M., Krummel, P. B., Beyerle, U., Canadell, J. G., Daniel, J. S., Enting, I. G., Law, R. M., Lunder, C. R., O'Doherty, S., Prinn, R. G., Reimann, S., Rubino, M., Velders, G. J. M., Vollmer, M. K., Wang, R. H. J., and Weiss, R. (2017). Historical greenhouse gas concentrations for climate modelling (CMIP6). *Geosci. Model Dev.*, 10(5):2057–2116. 39, 55, 87

Mesinger, F. and Arakawa, A. (1976). Numerical methods used in atmospheric models. 29, 30

Meybeck, M. (1982). Carbon, nitrogen, and phosphorus transport by world rivers. *Am. J. Sci*, 282(4):401–450. 36, 52

Michaelis, L. and Menten, M. (1913). Die Kinetik der Invertinwirkung. *Biochem Z*, 49:333–369. 33

Midttun, L. (1985). Formation of dense bottom water in the Barents Sea. *Dee-Sea Res. Pt. I*, 32(10):1233–1241. 9, 91

Millero, F. J., Pierrot, D., Lee, K., Wanninkhof, R., Feely, R., Sabine, C. L., Key, R. M., and Takahashi, T. (2002). Dissociation constants for carbonic acid determined from field measurements. *Deep-Sea Res. Pt. I*, 49(10):1705 – 1723. 40, 88

Moore, J. K., Doney, S. C., and Lindsay, K. (2004). Upper ocean ecosystem dynamics and iron cycling in a global three-dimensional model. *Global Biogeochem. Cy.*, 18(4). 52, 116

Nachtergaele, F., van Velthuizen, H., Verelst, L., Batjes, N., Dijkshoorn, K., van Engelen, V., Fischer, G., Jones, A., and Montanarela, L. (2010). The harmonized world soil database. In *Proceedings of the 19th World Congress of Soil Science, Soil Solutions for a Changing World, Brisbane, Australia, 1-6 August 2010*, pages 34–37. 111

Nohara, D., Kitoh, A., Hosaka, M., and Oki, T. (2006). Impact of climate change on river discharge projected by multimodel ensemble. *J. Hydrometeorol.*, 7(5):1076–1089. 4, 16, 146

Notz, D. and Stroeve, J. (2016). Observed Arctic sea-ice loss directly follows anthropogenic CO_2 emission. *Science*, 354(6313):747–750. 9

Oelke, C., Zhang, T., and Serreze, M. C. (2004). Modeling evidence for recent warming of the Arctic soil thermal regime. *Geophy. Res. Lett.*, 31(7). 144, 147

Olsen, A., Anderson, L. G., and Heinze, C. (2015). Arctic Carbon Cycle: Patterns, Impacts and Possible Changes. In Evengård, B., Nymand Larsen, J., and Paasche, Ø., editors, *The New Arctic*, pages 95–115. Springer International Publishing, Cham. 12, 46, 60, 71, 72, 163

Olsen, A., Key, R. M., van Heuven, S., Lauvset, S. K., Velo, A., Lin, X., Schirnick, C., Kozyr, A., Tanhua, T., Hoppema, M., Jutterström, S., Steinfeldt, R., Jeansson, E., Ishii, M., Pérez, F. F., and Suzuki, T. (2016). The Global Ocean Data Analysis Project version 2 (GLODAPv2) - an internally consistent data product for the world ocean. *Earth Syst. Sci. Data*, 8(2):297–323. xviii, 41, 118, 123, 124, 125

Olsen, A., Omar, A. M., Jeansson, E., Anderson, L. G., and Bellerby, R. G. J. (2010). Nordic seas transit time distributions and anthropogenic CO_2. *J. Geophys. Res. - Oceans*, 115(C5):n/a–n/a. 40, 88

Orr, J. C. and Epitalon, J.-M. (2015). Improved routines to model the ocean carbonate system: mocsy 2.0. *Geosci. Model Dev.*, 8(3):485–499. 90, 118, 150

Orr, J. C., Epitalon, J.-M., Dickson, A. G., and Gattuso, J.-P. (2018). Routine uncertainty propagation for the marine carbon dioxide system. *Mar. Chem.*, 207:84–107. 90

Orr, J. C., Fabry, V. J., Aumont, O., Bopp, L., Doney, S. C., Feely, R. A., Gnanadesikan, A., Gruber, N., Ishida, A., Joos, F., et al. (2005). Anthropogenic ocean acidification over the twenty-first century and its impact on calcifying organisms. *Nature*, 437(7059):681–686. 3, 13, 85, 138

Orr, J. C., Monfray, P., Maier-Reimer, E., Mikolajewicz, U., Palmer, J., Taylor, N. K., Toggweiler, J. R., Sarmiento, J. L., Quéré, C. L., Gruber, N., Sabine, C. L., Key, R. M., and Boutin, J. (2001). Estimates of anthropogenic carbon uptake from four three-dimensionsal global ocean models. *Global Biogeochem. Cy.*, 15(1):43–60. 48

Orr, J. C., Najjar, R. G., Aumont, O., Bopp, L., Bullister, J. L., Danabasoglu, G., Doney, S. C., Dunne, J. P., Dutay, J.-C., Graven, H., et al. (2017). Biogeochemical protocols and diagnostics for the CMIP6 Ocean Model Intercomparison Project (OMIP). *Geosci. Model Dev.*, 10(6):2169. 59

Orr, J. C. and Sarmiento, J. L. (1992). Potential of marine macroalgae as a sink for CO_2: Constraints from a 3-D general circulation model of the global ocean. *Water Air Soil Pollut.*, 64(1):405–421. 3, 137, 168

Overland, J. E. and Wang, M. (2013). When will the summer Arctic be nearly sea ice free? *Geophys. Res. Lett.*, 40(10):2097–2101. 2, 10

Pabi, S., van Dijken, G. L., and Arrigo, K. R. (2008). Primary production in the Arctic Ocean, 1998–2006. *J. Geophys. Res. - Oceans*, 113(C8). xiv, 15

Palmiéri, J., Orr, J., Dutay, J.-C., Béranger, K., Schneider, A., Beuvier, J., and Somot, S. (2015). Simulated anthropogenic CO_2 storage and acidification of the Mediterranean Sea. *Biogeosciences*, 12(3):781–802. 87

Peterson, B. J., Holmes, R. M., McClelland, J. W., Vörösmarty, C. J., Lammers, R. B., Shiklomanov, A. I., Shiklomanov, I. A., and Rahmstorf, S. (2002). Increasing river discharge to the Arctic Ocean. *Science*, 298(5601):2171–2173. 4, 16, 146

Pickart, R. S., Weingartner, T. J., Pratt, L. J., Zimmermann, S., and Torres, D. J. (2005). Flow of winter-transformed Pacific water into the Western Arctic. *Deep-Sea Res. Pt II*, 52(24):3175–3198. 87

Popova, E. E., Yool, A., Aksenov, Y., and Coward, A. C. (2013). Role of advection in Arctic Ocean lower trophic dynamics: A modeling perspective. *J. Geophys. Res. - Oceans*, 118(3):1571–1586. 15, 19, 20, 49, 156

Popova, E. E., Yool, A., Coward, A. C., Dupont, F., Deal, C., Elliott, S., Hunke, E., Jin, M., Steele, M., and Zhang, J. (2012). What controls primary production in the Arctic Ocean? Results from an intercomparison of five general circulation models with biogeochemistry. *J. Geophys. Res. - Oceans*, 117(C8). 20, 140, 180

Proshutinsky, A., Steele, M., and Timmermans, M.-L. (2016). Forum for Arctic Modeling and Observational Synthesis (FAMOS): Past, current, and future activities. *J. Geophys. Res. - Oceans*, 121(6):3803–3819. 49

Raymond, P. A., McClelland, J. W., Holmes, R. M., Zhulidov, A. V., Mull, K., Peterson, B. J., Striegl, R. G., Aiken, G. R., and Gurtovaya, T. Y. (2007). Flux and age of dissolved organic carbon exported to the Arctic Ocean: A carbon isotopic study of the five largest Arctic rivers. *Global Biogeochem. Cy.*, 21(4). 4, 17, 108, 131, 132, 147

Regnier, P., Arndt, S., Goossens, N., Volta, C., Laruelle, G. G., Lauerwald, R., and Hartmann, J. (2013a). Modelling estuarine biogeochemical dynamics: From the local to the global scale. *Aquat. Geochem.*, 19(5):591–626. 184

Regnier, P., Friedlingstein, P., Ciais, P., Mackenzie, F. T., Gruber, N., Janssens, I. A., Laruelle, G. G., Lauerwald, R., Luyssaert, S., Andersson, A. J., et al. (2013b). Anthropogenic perturbation of the carbon fluxes from land to ocean. *Nat. Geosci.*, 6(8):597. 107, 145, 184, 189

Resplandy, L., Keeling, R., Rödenbeck, C., Stephens, B., Khatiwala, S., Rodgers, K., Long, M., Bopp, L., and Tans, P. (2018). Revision of global carbon fluxes based on a reassessment of oceanic and riverine carbon transport. *Nat Geosci.*, 11(7):504. 10

Revelle, R. and Suess, H. E. (1957). Carbon dioxide exchange between atmosphere and ocean and the question of an increase of atmospheric CO_2 during the past decades. *Tellus*, 9(1):18–27. 12

Riebesell, U., Gattuso, J.-P., Thingstad, T. F., and Middelburg, J. J. (2013). Preface "Arctic ocean acidification: pelagic ecosystem and biogeochemical responses during a mesocosm study". *Biogeosciences*, 10(8):5619–5626. 3, 13, 148

Robert, A. J. (1966). The integration of a low order spectral form of the primitive meteorological equations. *J. Meteorol. Soc. Jpn.*, 44(5):237–245. 31

Rousset, C., Vancoppenolle, M., Madec, G., Fichefet, T., Flavoni, S., Barthélemy, A., Benshila, R., Chanut, J., Levy, C., Masson, S., and Vivier, F. (2015). The Louvain-La-Neuve sea ice model LIM3.6: global and regional capabilities. *Geosci. Model Dev.*, 8(10):2991–3005. 149

Roy, T., Bopp, L., Gehlen, M., Schneider, B., Cadule, P., Frölicher, T. L., Segschneider, J., Tjiputra, J., Heinze, C., and Joos, F. (2011). Regional impacts of climate change and atmospheric CO_2 on future ocean carbon uptake: A multimodel linear feedback analysis. *J. Clim.*, 24(9):2300–2318. 148, 170, 181

Rudels, B. (1995). The thermohaline circulation of the Arctic Ocean and the Greenland Sea. *Philos. T. Roy. Soc. A*, 352(1699):287–299. 185

Rudels, B. (2015). Arctic Ocean circulation, processes and water masses: A description of observations and ideas with focus on the period prior to the International Polar Year 2007–2009. *Prog. Oceanog.*, 132:22–67. xiii, 6

Rudels, B., Friedrich, H. J., and Quadfasel, D. (1999). The Arctic circumpolar boundary current. *Deep-Sea Res. Pt. II*, 46(6):1023–1062. 9

Rudels, B., Jones, E. P., Erson, L. G., and Kattner, G. (1994). On the intermediate depth waters of the Arctic ocean. *AGU Geophysical Monograph*, 85:33–46. 9, 49

Rudels, B., Marnela, M., and Eriksson, P. (2008). Constraints on estimating mass, heat and freshwater transports in the Arctic Ocean: An exercise. In *Arctic-Subarctic Ocean Fluxes*, pages 315–341. Springer, Dordrecht, Netherlands. 7, 8, 9, 60

Sabine, C. L., Feely, R. A., Gruber, N., Key, R. M., Lee, K., Bullister, J. L., Wanninkhof, R., Wong, C., Wallace, D. W., Tilbrook, B., et al. (2004). The oceanic sink for anthropogenic CO_2. *Science*, 305(5682):367–371. 48

Sakshaug, E. (2004). Primary and secondary production in the Arctic seas. In Stein, R. and MacDonald, R. W., editors, *The Organic Carbon Cycle in the Arctic Ocean*, pages 57–81. Springer Berlin Heidelberg, Berlin, Heidelberg. 11

Salisbury, J., Green, M., Hunt, C., and Campbell, J. (2008). Coastal acidification by rivers: A threat to shellfish? *Eos, Trans. AGU*, 89(50):513–513. 138

Sarmiento, J. L., Orr, J. C., and Siegenthaler, U. (1992). A perturbation simulation of CO_2 uptake in an ocean general circulation model. *J. Geophys. Res. - Oceans*, 97(C3):3621–3645. 38, 39, 54, 55, 87, 88

Schauer, U., Beszczynska-Möller, A., Walczowski, W., Fahrbach, E., Piechura, J., and Hansen, E. (2008). Variation of measured heat flow through the Fram Strait between 1997 and 2006. In *Arctic-Subarctic Ocean Fluxes*, pages 65–85. Springer, Dordrecht, Netherlands. 7, 8, 9, 60

Schauer, U., Loeng, H., Rudels, B., Ozhigin, V. K., and Dieck, W. (2002). Atlantic Water flow through the Barents and Kara Seas. *Deep-Sea Res. Pt. I*, 49(12):2281–2298. 9, 87, 92

Schuur, E. A., Bockheim, J., Canadell, J. G., Euskirchen, E., Field, C. B., Goryachkin, S. V., Hagemann, S., Kuhry, P., Lafleur, P. M., Lee, H., et al. (2008). Vulnerability of permafrost carbon to climate change: Implications for the global carbon cycle. *AIBS Bulletin*, 58(8):701–714. 4

Screen, J. A. and Simmonds, I. (2010). The central role of diminishing sea ice in recent Arctic temperature amplification. *Nature*, 464(7293):1334. 2

Semiletov, I., Pipko, I., Gustafsson, Ö., Anderson, L. G., Sergienko, V., Pugach, S., Dudarev, O., Charkin, A., Gukov, A., Bröder, L., et al. (2016). Acidification of east siberian arctic shelf waters through addition of freshwater and terrestrial carbon. *Nat. Geosci.*, 9(5):361–365. 4, 14, 16, 17, 21, 23, 75, 85, 107, 108, 146, 147, 148, 160, 181

Semiletov, I. P., Shakhova, N. E., Pipko, I. I., Pugach, S. P., Charkin, A. N., Dudarev, O. V., Kosmach, D. A., and Nishino, S. (2013). Space-time dynamics of carbon and environmental parameters related to carbon dioxide emissions in the Buor-Khaya Bay and adjacent part of the Laptev Sea. *Biogeosciences*, 10(9):5977–5996. 134

Serreze, M. C., Barrett, A. P., Slater, A. G., Woodgate, R. A., Aagaard, K., Lammers, R. B., Steele, M., Moritz, R., Meredith, M., and Lee, C. M. (2006). The large-scale freshwater cycle of the Arctic. *J. Geophys. Res. - Oceans*, 111(C11). 7

Serreze, M. C. and Barry, R. G. (2011). Processes and impacts of Arctic amplification: A research synthesis. *Global Planet. Change*, 77(1):85–96. 96

Serreze, M. C., Holland, M. M., and Stroeve, J. (2007). Perspectives on the Arctic's shrinking sea-ice cover. *Science*, 315(5818):1533–1536. 9

Serreze, M. C. and Stroeve, J. (2015a). Arctic sea ice trends, variability and implications for seasonal ice forecasting. *Phil. Trans. R. Soc. A*, 373(2045):20140159. 2, 9

Serreze, M. C. and Stroeve, J. (2015b). Arctic sea ice trends, variability and implications for seasonal ice forecasting. *Phil. Trans. R. Soc. A*, 373(2045). 96

Shimada, K., McLaughlin, F., Carmack, E., Proshutinsky, A., Nishino, S., and Itoh, M. (2004). Penetration of the 1990s warm temperature anomaly of Atlantic Water in the Canada Basin. *Geophys. Res. Lett.*, 31(20). 9

Skagseth, Ø., Furevik, T., Ingvaldsen, R., Loeng, H., Mork, K. A., Orvik, K. A., and Ozhigin, V. (2008). Volume and heat transports to the Arctic Ocean via the Norwegian and Barents Seas. In *Arctic-Subarctic Ocean Fluxes*, pages 45–64. Springer, Dordrecht, Netherlands. 8, 9, 60

Smedsrud, L. H., Esau, I., Ingvaldsen, R. B., Eldevik, T., Haugan, P. M., Li, C., Lien, V. S., Olsen, A., Omar, A. M., Otterå, O. H., Risebrobakken, B., Sandø, A. B., Semenov, V. A., and Sorokina, S. A. (2013). The role of the Barents Sea in the Arctic climate system. *Rev. Geophys.*, 51(3):415–449. 87, 90, 185

Smedsrud, L. H., Ingvaldsen, R., Nilsen, J. E. Ø., and Skagseth, Ø. (2010). Heat in the Barents Sea: transport, storage, and surface fluxes. *Ocean Sci.*, 6(1):219–234. 8, 9, 60

Smethie, W. M., Schlosser, P., Bönisch, G., and Hopkins, T. S. (2000). Renewal and circulation of intermediate waters in the Canadian Basin observed on the SCICEX 96 cruise. *J. Geophys. Res. - Oceans*, 105(C1):1105–1121. 90

Smith, J. N., McLaughlin, F. A., Smethie Jr., W. M., Moran, S. B., and Lepore, K. (2011). Iodine-129, ^{137}Cs, and CFC-11 tracer transit time distributions in the Arctic Ocean. *J. Geophys. Res. - Oceans*, 116(C4). 92, 98

Smith, W., Gosselin, M., Legendre, L., Wallace, D., Daly, K., and Kattner, G. (1997). New production in the Northeast Water Polynya: 1993. *J. Mar. Sys.*, 10(1):199–209. 109

Smith, W. H. F. and Sandwell, D. T. (1997). Global Sea Floor Topography from Satellite Altimetry and Ship Depth Soundings. *Science*, 277(5334):1956–1962. 30, 51, 116, 149

Somavilla, R., Schauer, U., and Budéus, G. (2013). Increasing amount of Arctic Ocean deep waters in the Greenland Sea. *Geophys. Res. Lett.*, 40(16):4361–4366. 96

Spall, M. A. (2007). Circulation and water mass transformation in a model of the Chukchi Sea. *J. Geophys. Res. - Oceans*, 112(C5). 92

Spencer, R. G. M., Aiken, G. R., Butler, K. D., Dornblaser, M. M., Striegl, R. G., and Hernes, P. J. (2009). Utilizing chromophoric dissolved organic matter measurements to derive export and reactivity of dissolved organic carbon exported to the Arctic Ocean: A case study of the Yukon River, Alaska. *Geophys. Res. Lett.*, 36(6). 163, 183

Spencer, R. G. M., Mann, P. J., Dittmar, T., Eglinton, T. I., McIntyre, C., Holmes, R. M., Zimov, N., and Stubbins, A. (2015). Detecting the signature of permafrost thaw in Arctic rivers. *Geophys. Res. Lett.*, 42(8):2830–2835. 183

Stammerjohn, S., Massom, R., Rind, D., and Martinson, D. (2012). Regions of rapid sea ice change: An inter-hemispheric seasonal comparison. *Geophys. Res. Lett.*, 39(6). 16

Steele, M., Morison, J., Ermold, W., Rigor, I., Ortmeyer, M., and Shimada, K. (2004). Circulation of summer Pacific halocline water in the Arctic Ocean. *J. Geophys. Res. - Oceans*, 109(C2). 7, 87

Steinacher, M., Joos, F., Frolicher, T. L., Plattner, G.-K., and Doney, S. C. (2009). Imminent ocean acidification in the Arctic projected with the NCAR global coupled carbon cycle-climate model. *Biogeosciences*, 6(4):515–533. 3, 14, 19, 20, 46, 48, 85, 86, 94, 96, 138, 148, 159, 181, 186

Steiner, N. S., Christian, J. R., Six, K. D., Yamamoto, A., and Yamamoto-Kawai, M. (2013). Future ocean acidification in the Canada Basin and surrounding Arctic Ocean from CMIP5 earth system models. *J. Geophys. Res.*, 119(C1):332–347. 94, 148, 159

Stendel, M. and Christensen, J. H. (2002). Impact of global warming on permafrost conditions in a coupled GCM. *Geophys. Res. Lett.*, 29(13):10–1–10–4. 18

Stöven, T., Tanhua, T., Hoppema, M., and Wilken-Jon, v. A. (2016). Transient tracer distributions in the Fram Strait in 2012 and inferred anthropogenic carbon content and transport. *Ocean Sci.*, 12(1):319–333. 12, 60, 71, 84, 98

Straneo, F. and Saucier, F. (2008). The outflow from Hudson Strait and its contribution to the Labrador Current. *Deep-Sea Res. Pt. I*, 55(8):926–946. 59

Swift, J., Jones, E., Aagaard, K., Carmack, E., Hingston, M., MacDonald, R., McLaughlin, F., and Perkin, R. (1997). Waters of the Makarov and Canada basins. *Deep-Sea Res. Pt II*, 44(8):1503–1529. 90, 185

Swiney, K. M., Foy, R. J., and Long, W. C. (2015). Effects of high pCO_2 on Tanner crab reproduction and early life history-Part I: long-term exposure reduces hatching success and female calcification, and alters embryonic development. *ICES J. Mar. Sci.*, 73(3):825–835. 13

Takahashi, T., Broecker, W. S., and Langer, S. (1985). Redfield ratio based on chemical data from isopycnal surfaces. *J. Geophys. Res.: Oceans*, 90(C4):6907–6924. 32, 36, 52, 116, 150

Tanhua, T., Jones, E. P., Jeansson, E., Jutterström, S., Smethie, W. M., Wallace, D. W., and Anderson, L. G. (2009). Ventilation of the Arctic Ocean: Mean ages and inventories of anthropogenic CO_2 and CFC-11. *J. Geophys. Res. - Oceans*, 114(C1). xvi, 3, 12, 40, 41, 46, 48, 59, 66, 67, 72, 74, 84, 86, 87, 88, 89, 91, 93, 96, 98, 167, 179

Tank, S. E., Frey, K. E., Striegl, R. G., Raymond, P. A., Holmes, R. M., McClelland, J. W., and Peterson, B. J. (2012a). Landscape–level controls on dissolved carbon flux from diverse catchments of the circumboreal. *Global Biogeochem. Cy.*, 26(4). 4, 23, 109, 135, 144, 147, 183, 188

Tank, S. E., Manizza, M., Holmes, R. M., and Peterson, J. W. M. B. J. (2012b). The processing and impact of dissolved riverine nitrogen in the Arctic Ocean. *Estuaries and Coasts*, 35(2):401–415. 148

Tank, S. E., Raymond, P. A., Striegl, R. G., McClelland, J. W., Holmes, R. M., Fiske, G. J., and Peterson, B. J. (2012c). A land-to-ocean perspective on the magnitude, source and implication of DIC flux

from major Arctic rivers to the Arctic Ocean. *Global Biogeochem. Cy.*, 26(4). xiv, xix, xxii, 11, 12, 17, 18, 36, 37, 42, 106, 108, 109, 110, 111, 116, 117, 131, 132, 138, 147, 151, 152, 155, 160, 165, 167, 172, 188

Taylor, K. E., Stouffer, R. J., and Meehl, G. A. (2012). An overview of CMIP5 and the experiment design. *Bull. Am. Meteorol. Soc.*, 93(4):485–498. 54

Tegen, I. and Fung, I. (1995). Contribution to the atmospheric mineral aerosol load from land surface modification. *J. Geophys. Res.*, 100:18707–18726. 36, 52, 116

Terhaar, J., Orr, J., Gehlen, M., Ethe, C., and Bopp (2018). Model constraints on the anthropogenic carbon budget of the arctic ocean. *Biogeosciences*. 88, 89, 90, 91, 92, 96, 102, 109, 117, 118, 133, 135, 154, 156, 163, 168

Thibodeau, B., Bauch, D., and Voss, M. (2017). Nitrogen dynamic in Eurasian coastal Arctic ecosystem: Insight from nitrogen isotope. *Global Biogeochem. Cy.*, 31(5):836–849. 109, 117, 136, 183

Timmermann, R., Goosse, H., Madec, G., Fichefet, T., Ethe, C., and Dulière, V. (2005). On the representation of high latitude processes in the ORCA-LIM global coupled sea ice-ocean model. *Ocean Model.*, 8(1):175–201. 32

Tjiputra, J. F., Roelandt, C., Bentsen, M., Lawrence, D. M., Lorentzen, T., Schwinger, J., Seland, Ø., and Heinze, C. (2013). Evaluation of the carbon cycle components in the Norwegian Earth System Model (NorESM). *Geosci. Model Dev.*, 6(2):301–325. 20, 106, 133, 140, 180

Torres-Valdés, S., Tsubouchi, T., Bacon, S., Naveira-Garabato, A. C., Sanders, R., McLaughlin, F. A., Petrie, B., Kattner, G., Azetsu-Scott, K., and Whitledge, T. E. (2013). Export of nutrients from the arctic ocean. *J. Geophys. Res. - Oceans*, 118(4):1625–1644. xxii, 7, 118, 134

Tréguer, P., Nelson, D. M., Van Bennekom, A. J., DeMaster, D. J., Leynaert, A., and Quéguiner, B. (1995). The silica balance in the World Ocean: A reestimate. *Science*, 268(5209):375–379. 37

Tremblay, J.-E., Anderson, L. G., Matrai, P., Coupel, P., Bélanger, S., Michel, C., and Reigstad, M. (2015). Global and regional drivers of nutrient supply, primary production and CO_2 drawdown in the changing Arctic Ocean. *Prog. Oceanogr.*, 139:171–196. 4, 14, 23, 123, 134, 146

Tremblay, J.-E., Bélanger, S., Barber, D. G., Asplin, M., Martin, J., Darnis, G., Fortier, L., Gratton, Y., Link, H., Archambault, P., Sallon, A., Michel, C., Williams, W. J., Philippe, B., and Gosselin, M. (2011). Climate forcing multiplies biological productivity in the coastal Arctic Ocean. *Geophys. Res. Lett.*, 38(18). 16

Tremblay, J.-E., Michel, C., Hobson, K. A., Gosselin, M., and Price, N. M. (2006). Bloom dynamics in early opening waters of the Arctic Ocean. *Limnol. Oceanog.*, 51(2):900–912. 109

Tremblay, J.-E., Simpson, K., Martin, J., Miller, L., Gratton, Y., Barber, D., and Price, N. M. (2008). Vertical stability and the annual dynamics of nutrients and chlorophyll fluorescence in the coastal, southeast Beaufort Sea. *J. Geophys. Res. - Oceans*, 113(C7). 16

Uppala, S. M., K˚ allberg, P. W., Simmons, A. J., Andrae, U., Bechtold, V. D. C., Fiorino, M., Gibson, J. K., Haseler, J., Hernandez, A., Kelly, G. A., Li, X., Onogi, K., Saarinen, S., Sokka, N., Allan, R. P., Andersson, E., Arpe, K., Balmaseda, M. A., Beljaars, A. C. M., Berg, L. V. D., Bidlot, J., Bormann, N., Caires, S., Chevallier, F., Dethof, A., Dragosavac, M., Fisher, M., Fuentes, M., Hagemann, S., Hólm, E., Hoskins, B. J., Isaksen, L., Janssen, P. A. E. M., Jenne, R., Mcnally, A. P., Mahfouf, J.-F., Morcrette, J.-J., Rayner, N. A., Saunders, R. W., Simon, P., Sterl, A., Trenberth, K. E., Untch, A., Vasiljevic, D., Viterbo, P., and Woollen, J. (2005). The ERA-40 re-analysis. *Q. J. Roy. Meteor. Soc.*, 131(612):2961–3012. 35, 152

van Heuven, S., Pierrot, D., Rae, J., Lewis, E., and Wallace, D. (2011). CO2SYS, MATLAB program developed for CO_2 system calculations. *Carbon Dioxide Information Analysis Center, Oak Ridge National Laboratory, US*. 40, 88

Vancoppenolle, M., Bopp, L., Madec, G., Dunne, J., Ilyina, T., Halloran, P. R., and Steiner, N. (2013). Future Arctic Ocean primary productivity from CMIP5 simulations: Uncertain outcome, but consistent mechanisms. *Global Biogeochem. Cy.*, 27(3):605–619. xiv, 3, 16, 19, 20, 21, 22, 139, 140, 148, 162, 170, 180, 181, 187, 188

Vancoppenolle, M., Fichefet, T., Goosse, H., Bouillon, S., Madec, G., and Maqueda, M. A. M. (2009). Simulating the mass balance and salinity of Arctic and Antarctic sea ice. 1. Model description and validation. *Ocean Model.*, 27(1):33–53. 32, 50

Vázquez-Rodríguez, M., Touratier, F., Lo Monaco, C., Waugh, D. W., Padin, X. A., Bellerby, R. G. J., Goyet, C., Metzl, N., Ríos, A. F., and Pérez, F. F. (2009). Anthropogenic carbon distributions in the Atlantic Ocean: data-based estimates from the Arctic to the Antarctic. *Biogeosciences*, 6(3):439–451. 71

Volta, C., Arndt, S., Savenije, H. H. G., Laruelle, G. G., and Regnier, P. (2014). C-GEM (v 1.0): a new, cost-efficient biogeochemical model for estuaries and its application to a funnel-shaped system. *Geosci. Model Dev.*, 7(4):1271–1295. 184

Vonk, J. E. and Gustafsson, Ö. (2013). Permafrost-carbon complexities. *Nat. Geosci.*, 6(9):675. 137, 151, 164, 183

Vörösmarty, C., Fekete, B., Meybeck, M., and Lammers, R. (2000). Geomorphometric attributes of the global system of rivers at 30-minute spatial resolution. *J. Hydrol.*, 237(1):17–39. 110

Walsh, J., McRoy, C., Coachman, L., Goering, J., Nihoul, J., Whitledge, T., Blackburn, T., Parker, P., Wirick, C., Shuert, P., Grebmeier, J., Springer, A., Tripp, R., Hansell, D., Djenidi, S., Deleersnijder,

E., Henriksen, K., Lund, B., Andersen, P., Müller-Karger, F., and Dean, K. (1989). Carbon and nitrogen cycling within the Bering/Chukchi Seas: Source regions for organic matter effecting AOU demands of the Arctic Ocean. *Prog. Oceanog.*, 22(4):277–359. 15

Walsh, J. E., Chapman, W. L., and Fetterer, F. (2015). Gridded Monthly Sea Ice Extent and Concentration, 1850 Onward, Version 1. [1979 to 2010]. Boulder, Colorado USA. NSIDC: National Snow and Ice Data Center. 42, 61

Walvoord, M. A. and Striegl, R. G. (2007). Increased groundwater to stream discharge from permafrost thawing in the Yukon River basin: Potential impacts on lateral export of carbon and nitrogen. *Geophys. Res. Lett.*, 34(12). 144, 147

Wang, Z. A., Bienvenu, D. J., Mann, P. J., Hoering, K. A., Poulsen, J. R., Spencer, R. G. M., and Holmes, R. M. (2013). Inorganic carbon speciation and fluxes in the Congo River. *Geophys. Res. Lett.*, 40(3):511–516. 151

Wanninkhof, R. (1992). Relationship between wind speed and gas exchange over the ocean. *J. Geophys. Res. - Oceans*, 97(C5):7373–7382. 34, 39, 56, 116

Warner, M. and Weiss, R. (1985). Solubilities of chlorofluorocarbons 11 and 12 in water and seawater. *Deep-Sea Res. Pt. I*, 32(12):1485–1497. 39, 40, 56, 88

Waugh, D. W., Haine, T. W., and Hall, T. M. (2004). Transport times and anthropogenic carbon in the subpolar North Atlantic Ocean. *Deep-Sea Res. Pt. I*, 51(11):1475–1491. 12, 40, 48, 86, 88

Waugh, D. W., Hall, T. M., McNeil, B. I., Key, R., and Matear, R. J. (2006). Anthropogenic CO_2 in the oceans estimated using transit time distributions. *Tellus B*, 58(5):376–389. 40, 84, 86, 87, 88, 93

Weiss, R. (1974). Carbon dioxide in water and seawater: the solubility of a non-ideal gas. *Mar. Chem.*, 2(3):203–215. 11, 34

Weiss, R., Östlund, H., and Craig, H. (1979). Geochemical studies of the Weddell sea. *Deep-Sea Res. Pt. I*, 26(10):1093–1120. 86

Wenzel, S., Cox, P. M., Eyring, V., and Friedlingstein, P. (2016). Projected land photosynthesis constrained by changes in the seasonal cycle of atmospheric CO_2. *Nature*, 538(7626):499. 188

Wickland, K. P., Aiken, G. R., Butler, K., Dornblaser, M. M., Spencer, R. G. M., and Striegl, R. G. (2012). Biodegradability of dissolved organic carbon in the Yukon River and its tributaries: Seasonality and importance of inorganic nitrogen. *Global Biogeochem. Cy.*, 26(4). 136, 183

Willey, D. A., Fine, R. A., Sonnerup, R. E., Bullister, J. L., Smethie Jr., W. M., and Warner, M. J. (2004). Global oceanic chlorofluorocarbon inventory. *Geophys. Res. Lett.*, 31:L01303, doi:10.1029/2003GL018816. 48

Winton, M. (2006). Amplified arctic climate change: What does surface albedo feedback have to do with it? *Geophys. Res. Lett.*, 33(3). 2

Woodgate, R. (2013). Arctic Ocean circulation: Going around at the top of the world. *Nat. Edu. Knowl.*, 4(8):8. 61, 87

Woodgate, R. A., Aagaard, K., Muench, R. D., Gunn, J., Björk, G., Rudels, B., Roach, A., and Schauer, U. (2001). The Arctic Ocean Boundary Current along the Eurasian slope and the adjacent Lomonosov Ridge: Water mass properties, transports and transformations from moored instruments. *Deep-Sea Res. Pt. I*, 48(8):1757–1792. 9

Woodgate, R. A., Aagaard, K., and Weingartner, T. J. (2005). Monthly temperature, salinity, and transport variability of the Bering Strait through flow. *Geophys. Res. Lett.*, 32(4). 7

Woodgate, R. A., Weingartner, T., and Lindsay, R. (2010). The 2007 Bering Strait oceanic heat flux and anomalous Arctic sea-ice retreat. *Geophys. Res. Lett.*, 37(1). 7, 8, 9, 60, 87

Yamamoto-Kawai, M., McLaughlin, F. A., Carmack, E. C., Nishino, S., and Shimada, K. (2009). Aragonite undersaturation in the Arctic Ocean: effects of ocean acidification and sea ice melt. *Science*, 326(5956):1098–1100. 14, 16, 138

Yang, D. (1999). An improved precipitation climatology for the Arctic Ocean. *Geophys. Res. Lett.*, 26(11):1625–1628. 60

Yasunaka, S., Murata, A., Watanabe, E., Chierici, M., Fransson, A., van Heuven, S., Hoppema, M., Ishii, M., Johannessen, T., Kosugi, N., Lauvset, S. K., Mathis, J. T., Nishino, S., Omar, A. M., Olsen, A., Sasano, D., Takahashi, T., and Wanninkhof, R. (2016). Mapping of the air-sea CO_2 flux in the Arctic Ocean and its adjacent seas: Basin-wide distribution and seasonal to interannual variability. *Polar Sci.*, 10(3):323–334. xix, 42, 157, 158

Zalesak, S. T. (1979). Fully multidimensional flux-corrected transport algorithms for fluids. *J. Comput. Phys.*, 31(3):335–362. 31

Appendix A

Annexes

A.1 Résumé en français

Les océans côtiers jouent un rôle important dans le cycle du carbone et représentent des zones clefs pour la production primaire des océans et leurs acidifications. Ces régions côtières sont fortement influencées par les fleuves. Bien qu'un fort impact des fleuves soit attendu dans l'océan Arctique, c'est un phénomène encore très peu étudié en raison du faible nombre d'observations disponible due aux conditions hostiles qui règnent dans cette zone. Ce travail de thèse avait donc pour objectifs d'améliorer la compréhension de l'influence de l'apport de carbone et de nutriments par les rivières Arctique en utilisant le modèle biogéochimique océanique NEMO-PISCES.

La première partie de ce travail de thèse se concentre sur l'évaluation du fonctionnement du modèle dans l'océan Arctique. Nous avons calculés l'absorption de carbone anthropique dans l'océan Arctique avec un modèle en utilisant des résolutions horizontales différentes. Trois résolutions ont été testées. Nos tests de sensibilité suggèrent que des résultats plus réalistes de la circulation océanique dans l'océan Arctique et du bilan de carbone anthropique sont obtenus avec des configurations de modèle à haute résolutionCette amelioration est principalement associé à une meilleure représentation de la circulation dans l'océan arctique et des échanges avec les océans adjacents. On a montré que Les flux latéraux de carbone anthropique représentent trois quart du carbone anthropique stocké dans l'ocean arctique. Comme la masse de carbone anthropique simulée dans l'océan Arctique augmente avec la résolution, l'acidification augmente aussi. Concernant la profondeur moyenne en dessous de laquelle l'eau est sous-saturé par rapport a l'aragonite dans l'océan Arctique, elle augmente quatre fois plus rapidement avec les simulations a haute résolution qui resolvent explicitement les tourbillons océaniques comparés aux simulations avec une résolution grossière. Le carbone anthropique dans l'océan peut aussi être estimé basée sur des observations de traceurs transitoires, tels que les CFC, par la méthode TTD (transient time distribution). Nous avons évalué la méthode TTD avec notre modèle. Cette évaluation a permis de démontrer les bonnes performances de cette méthode dans l'océan Arctique et de valider son application dans cette région de l'océan. De plus, l'évaluation de la méthode TTD

à partir du modèle nous a permis d'identifier un biais négatif de carbone anthropique dans les masses d'eau formées à la surface de l'océan Arctique. Ces valeurs de carbone anthropiques trop faibles sont dues à un déséquilibre en surface entre le carbone anthropique et le CFC-12 lors de la formation des masses d'eau profondes. En corrigeant l'inventaire de carbone anthropique pour tenir compte de ce biais, l'inventaire augmente de 7,5% pour atteindre 3.3 Pg C (normalisé pour 2005).

Dans la deuxième partie de cette thèse, l'impact des flux provenant des rivières sur la biogéochimie de l'océan Arctique a été estimé à l'aide du modèle NEMO-PISCES évalué précédemment. Pour cela, une estimation des flux de carbone et de nutriments provenant de l'ensemble des fleuves arctiques a été construite à partir d'une série d'observations. Cet estimation des flux a ensuite été utilisé pour forcer le modèle NEMO-PISCES et l'impact des flux provenant des rivières a été quantifiés. Le bon accord entre la production primaire net, les flux de CO_2 air-mer et l'acidification simulés avec le modèle et les observations et des estimations basées sur des données met en évidence l'importance d'utiliser une base de données de flux provenant des rivières bien contrainte dans l'océan Arctique. En effet, nos résultats suggèrent que les flux des rivières soutiennent 16 à 25% de la production primaire net de l'océan Arctique global et 79% de la production primaire net dans la mer de Laptev. Ils suggèrent aussi une réduction de 20% de l'absorption de CO_2 par l'océan Arctique. De plus, les mers de Laptev et de Beaufort deviennent des sources nettes de CO_2 pour l'atmosphère et régionalement une réduction de plus de 50% de l'acidification des océans côtiers durant l'été est simulée. Ces estimations dépassent les résultats antérieurs et indiquent que les flux provenant des rivières devraient faire l'objet d'une attention croissante lors de l'étude du devenir de la biogéochimie dans l'océan Arctique.

Pour estimer l'impact des changements futurs des flux de carbone et de nutriments provenant des rivières, des simulations idéalisées ont été réalisées afin de quantifier la sensibilité de la biogéochimie de l'océan Arctique à ces changements. Les sensibilités calculées fournissent une vue quantitative qui permet de mieux comprendre comment ces caractéristiques sont affectées à l'échelle globale de l'océan Arctique par les apports terrigènes de carbone organique, de carbone inorganique et de nutriments. Doubler le flux de nutriment provenant des rivières Arctiques augmente la production primaire net de 11% en moyenne globales sur tout le bassin Arctique , de plus de 30% dans les mers de Laptev et de Beaufort et jusqu'à 100% près de l'embouchure des rivières. Le doublement des flux de carbone organique dissous provenant des rivières renforce les émissions de CO_2 des océans. Cela compense presque l'influence du CO_2 anthropique à travers l'interface air-mer de l'océan Arctique qui provient d'un doublement simultané imposé du CO_2 atmosphérique. Doubler le carbone organique dissous d'une rivière renforce l'acidification des océans, tandis que doubler les flux de carbone inorganique dissous provenant des rivières et réduit l'acidification des océans.

Ces résultats fournissent un premier aperçu de la manière dont les flux provenant des rivières affectent la biogéochimie de l'océan Arctique. Ils suggèrent que les effets des flux de carbone or-

ganique dissous provenant des rivières devraient également être inclus dans le débat sur la question du devenir de l'océan Arctique, qui deviendra une source ou un puits de CO_2. De même, les flux de nutriments provenant des rivières devraient être pris en compte dans le débat sur la manière dont l'approvisionnement en éléments nutritifs de la surface de l'océan Arctique changera et si la production primaire net augmentera ou diminuera à l'avenir. Dans le même ordre d'idées, ne pas tenir compte de l'effet des changements des flux de carbone provenant des rivières sur le pH et l'état de saturation en aragonite de l'océan Arctique peut conduire à des résultats erronés dans les mers du plateau continental, qui sont fortement influencées localement par les apports des rivières.

A.2 Paper as co-author

Biogeosciences, 13, 4167–4185, 2016
www.biogeosciences.net/13/4167/2016/
doi:10.5194/bg-13-4167-2016

Biogeosciences Open Access EGU

Coastal-ocean uptake of anthropogenic carbon

Timothée Bourgeois[1], **James C. Orr**[1], **Laure Resplandy**[2], **Jens Terhaar**[1], **Christian Ethé**[3], **Marion Gehlen**[1], **and Laurent Bopp**[1]

[1]Laboratoire des Sciences du Climat et de l'Environnement, LSCE/IPSL, CEA-CNRS-UVSQ, Université Paris-Saclay, 91191 Gif-sur-Yvette, France
[2]Scripps Institution of Oceanography, University of California San Diego, La Jolla, CA, USA
[3]Institut Pierre Simon Laplace, 4 Place Jussieu, 75005 Paris, France

Correspondence to: Timothée Bourgeois (timothee.bourgeois@lsce.ipsl.fr)

Received: 18 February 2016 – Published in Biogeosciences Discuss.: 22 February 2016
Revised: 15 June 2016 – Accepted: 17 June 2016 – Published: 22 July 2016

Abstract. Anthropogenic changes in atmosphere–ocean and atmosphere–land CO_2 fluxes have been quantified extensively, but few studies have addressed the connection between land and ocean. In this transition zone, the coastal ocean, spatial and temporal data coverage is inadequate to assess its global budget. Thus we use a global ocean biogeochemical model to assess the coastal ocean's global inventory of anthropogenic CO_2 and its spatial variability. We used an intermediate resolution, eddying version of the NEMO-PISCES model (ORCA05), varying from 20 to 50 km horizontally, i.e. coarse enough to allow multiple century-scale simulations but finer than coarse-resolution models ($\sim$ 200 km) to better resolve coastal bathymetry and complex coastal currents. Here we define the coastal zone as the continental shelf area, excluding the proximal zone. Evaluation of the simulated air–sea fluxes of total CO_2 for 45 coastal regions gave a correlation coefficient R of 0.8 when compared to observation-based estimates. Simulated global uptake of anthropogenic carbon results averaged 2.3 $\mathrm{Pg\,C\,yr^{-1}}$ during the years 1993–2012, consistent with previous estimates. Yet only 0.1 $\mathrm{Pg\,C\,yr^{-1}}$ of that is absorbed by the global coastal ocean. That represents 4.5 % of the anthropogenic carbon uptake of the global ocean, less than the 7.5 % proportion of coastal-to-global-ocean surface areas. Coastal uptake is weakened due to a bottleneck in offshore transport, which is inadequate to reduce the mean anthropogenic carbon concentration of coastal waters to the mean level found in the open-ocean mixed layer.

1 Introduction

The ocean mitigates climate change by absorbing atmospheric CO_2 produced by combustion of fossil fuels, land-use change, and cement production. During the 2005–2014 period, the global ocean absorbed 2.6 ± 0.5 $\mathrm{Pg\,C\,yr^{-1}}$ of anthropogenic carbon, an estimated 26 % of the total anthropogenic CO_2 emissions (Le Quéré et al., 2015). The global anthropogenic carbon budget relies on separate estimates for atmosphere, land, and ocean reservoirs. Yet it neglects what happens in the aquatic continuum between land and ocean (Cai, 2011; Regnier et al., 2013), for which there is no consensus on anthropogenic carbon uptake (Wanninkhof et al., 2013; Mackenzie et al., 2004; Bauer et al., 2013; Regnier et al., 2013; Le Quéré et al., 2015; Ciais et al., 2013).

The land–ocean aquatic continuum includes inland waters, estuaries, and the coastal ocean, i.e. the succession of active physical–biogeochemical systems that connect upland terrestrial soils to the open ocean (Regnier et al., 2013). Our focus here is on the coastal ocean, which plays an inordinately large role relative to the open ocean in terms of primary productivity, export production, and carbon burial. Although the coastal ocean covers only 7–10 % of the global ocean surface area, it accounts for up to 30 % of oceanic primary production, 30–50 % of oceanic inorganic carbon burial, and 80 % of oceanic organic carbon burial (Gattuso et al., 1998; Longhurst et al., 1995; Walsh, 1991); moreover, the coastal-ocean supplies about half of the organic carbon that is delivered to the deep open ocean (Liu et al., 2010). All these estimates suffer from high uncertainties as do those for coastal-ocean air–sea CO_2 exchange (Laruelle et al., 2014), particu-

larly its anthropogenic component. Indeed, in addition to the effect of increasing atmospheric CO_2, potential changes in coastal-ocean physics (e.g. temperature) and biology (e.g. net ecosystem production) as well as changes in riverine input, and interactions with the sediment may be of primary importance (Mackenzie et al., 2004; Hu and Cai, 2011). These changes would modify the distribution of carbon and alkalinity, hence change the potential of the coastal ocean to absorb anthropogenic carbon.

To date, few studies have distinguished anthropogenic carbon uptake by the global coastal ocean. Estimating air–sea fluxes of anthropogenic CO_2 in the coastal ocean would require multi-decadal time series of coastal CO_2 observations in order to extract an anthropogenic signal from the strong coastal natural variability. Such time series are still rare and probably not long enough. To our knowledge, the only available equivalent time series are the Ishii et al. (2011) 1994–2008 time series along 137° E on Japanese coasts and the Astor et al. (2013) 1996–2008 time series at the CARIACO station on Venezuelan coasts. Therefore, estimates of anthropogenic carbon uptake by the global coastal ocean have been based on modelling studies, extrapolating data and model output from the open-ocean, and estimating residuals with budget calculations. An early modelling approach was proposed by Andersson and Mackenzie (2004) and Mackenzie et al. (2004). They used a 2-box model (Shallow-water Ocean Carbonate Model, SOCM) that separated the coastal ocean into surface waters and sediment pore waters. They estimated that the preindustrial coastal ocean was a source of CO_2 to the atmosphere and had recently switched to a CO_2 sink. This source-to-sink switch is mainly caused by a shift in net ecosystem production (NEP) due to increased anthropogenic nutrient inputs (Andersson and Mackenzie, 2004; Mackenzie et al., 2004). Another proposed mechanism is simply linked to the anthropogenic increase in atmospheric CO_2, considering constant NEP (Bauer et al., 2013). The difference between the simulated air–sea CO_2 fluxes from the SOCM model for the years 1700 and 2000 suggests that in 2000 the coastal ocean absorbed $0.17\,\mathrm{Pg\,C\,yr^{-1}}$ of anthropogenic carbon from the atmosphere (Borges, 2005). As for extrapolation, Wanninkhof et al. (2013) used coarse-resolution global-ocean models and observations and estimated a similar uptake of $0.18\,\mathrm{Pg\,C\,yr^{-1}}$ by extrapolating open-ocean air–sea fluxes of anthropogenic CO_2 into the coastal zone. Finally, Liu et al. (2010) combined estimates from the same SOCM model for the preindustrial coastal zone with observational estimates of the contemporary flux to deduce a corresponding anthropogenic carbon uptake of $0.5\,\mathrm{Pg\,C\,yr^{-1}}$ for the 1990s.

In addition, there exist 3-D regional-circulation–biogeochemistry–ecosystem models that have been used to study other aspects of coastal-ocean carbon cycling as summarized by Hofmann et al. (2011). Typically, such models have been implemented in regions where sufficient measurements are available for model validation, e.g. the Middle Atlantic Bight (eastern US coast) (Fennel et al., 2008; Fennel, 2010), the California current system (Fiechter et al., 2014; Turi et al., 2014; Lachkar and Gruber, 2013), and the European shelf seas (Artioli et al., 2014; Phelps et al., 2014; Wakelin et al., 2012; Allen et al., 2001; Cossarini et al., 2015; Prowe et al., 2009). Because of their limited regional domains, such models are typically able to make simulations with horizontal resolutions of 10 km or less, which remains a challenge for global-circulation–biogeochemical models. The reduced computational requirements of regional models also allow biogeochemistry and ecosystem components to be more complex. Unfortunately, joining together a network of regional models to allow efficient simulations that cover all parts of the global coastal ocean remains a technical challenge (Holt et al., 2009).

The alternative to using a global model is computationally more challenging because few of them have adequate resolution to properly simulate many critical coastal-ocean processes (Griffies et al., 2010; Holt et al., 2009). Coarse-resolution global models fail to adequately resolve the coastal bathymetry, which substantially alters coastal-ocean circulation (Fiechter et al., 2014) as well as mesoscale dynamics, upwelling, and coastal currents, all of which are thought to strongly affect the variability of air–sea CO_2 fluxes along ocean margins (Borges, 2005; Lachkar et al., 2007; Kelley et al., 1971). Global models also typically lack a benthic component, i.e. early diagenesis in sediments, which in some regions is likely to affect simulated coastal-ocean biogeochemistry of overlying waters. Moreover, input of carbon and nutrients from rivers and groundwater is usually lacking. Even in models such as ours, where that input is imposed as boundary conditions (Aumont et al., 2015), temporal variability and trends are neglected (Bauer et al., 2013; Cotrim da Cunha et al., 2007).

Nonetheless, coarse-resolution models are no longer state of the art. Recently, there have been improvements in spatial resolution of global ocean models and the spatio-temporal resolution of surface forcing fields (Brodeau et al., 2010), thereby improving the representation of bathymetry and ocean processes in the highly variable coastal zone (Capet, 2004; Hofmann et al., 2011; McKiver et al., 2014). In any case, models currently provide the only means to estimate coastal uptake of anthropogenic carbon due to the lack of data-based estimates.

Here our aim is to estimate the air-to-sea flux of anthropogenic CO_2 into the coastal ocean and how it varies from region to region across the globe. We focus solely on the geochemical effect of anthropogenic CO_2 addition from the atmosphere to the ocean and neglect the role of varying river input and interactions with the sediment, as well as feedback from a changing climate. To do so, we rely on an eddying version of the global NEMO circulation model (Madec, 2008), which also includes the LIM2 sea ice model and is coupled to the PISCES biogeochemical model (Aumont and Bopp, 2006). More precisely, we use the ORCA05 eddy-admitting resolution, which ranges from 0.2 to 0.5° (i.e. 20 to 50 km).

Although this resolution does not fully resolve coastal-ocean bathymetry and dynamics, it does provide a first step into the eddying regime and a starting point upon which to compare future studies that will model the coastal ocean, globally, at higher resolution.

2 Methods

2.1 Coupled physical–biogeochemical model

For this study, we use version 3.2 of the ocean model known as NEMO (Nucleus for European Modelling of the Ocean), which includes (1) the primitive equation model Océan Parallélisé (OPA, Madec, 2008), (2) the dynamic-thermodynamic Louvain-La-Neuve sea ice model (LIM, Fichefet and Morales Maqueda, 1997), and (3) the Tracer in the Ocean Paradigm (TOP), a passive tracer module. Here the latter is connected to version 1 of the ocean biogeochemical model PISCES (Pelagic Interaction Scheme for Carbon and Ecosystem Studies) (Aumont and Bopp, 2006). For the NEMO model, we use a global-scale configuration from the DRAKKAR community (see Barnier et al., 2006; Timmermann et al., 2005). Namely, we use the ORCA05 global configuration, which possesses a curvilinear, tripolar grid with a horizontal resolution that ranges between 0.2° near the North Pole to 0.5° at the Equator (Fig. 1). Vertically, ORCA05 is discretized into 46 levels with thicknesses that range from 6 m at the surface to 250 m for the deepest ocean level (centred at 5625 m). Model bathymetry is computed from the 2 min bathymetry file ETOPO2 from the National Geophysical Data Center. The numerical characteristics of our ORCA05 configuration follow the lead of Barnier et al. (2006) for the ORCA025 configuration with resolution-dependent modifications for the horizontal eddy diffusivity for tracers modified to $600\,m^2\,s^{-1}$ and horizontal eddy viscosity fixed to $-4 \times 10^{11}\,m^2\,s^{-1}$. To simulate the advective transport driven by geostrophic eddies, our ORCA05 simulation uses the eddy parameterization scheme of Gent and McWilliams (1990) applied with an eddy diffusion coefficient of $1000\,m^2 s^{-1}$.

The biogeochemical model PISCES includes four plankton functional types: two phytoplankton (nanophytoplankton and diatoms) and two zooplankton (micro- and mesozooplankton). PISCES also uses a mixed-quota Monod approach where (1) phytoplankton growth is limited by five nutrients (nitrate, ammonium, phosphate iron, and silicate), following Monod (1949) and (2) elemental ratios of Fe, Si, and Chl to C are prognostic variables based on the external concentrations of the limiting nutrients. In addition PISCES assumes a fixed C : N : P Redfield ratio set to 122 : 16 : 1 from Takahashi et al. (1985) for both living and non-living pools. Similar to Geider et al. (1998), the phytoplankton Chl:C ratio in PISCES varies with photoadaptation. Furthermore, PISCES includes non-living pools, namely a pool of semilabile dissolved organic matter and two size classes of particulate organic matter. PISCES also explicitly accounts for biogenic silica and calcite particles. In PISCES, the sediment–water interface is treated as a reflective boundary condition where mass fluxes from particles are remineralized instantaneously, except that small proportions of particle fluxes of organic matter, calcite, and biogenic silica escape the system through burial. Those burial rates are hence dependent on the local sinking fluxes, but are set to balance inputs from rivers and atmospheric deposition at the global scale. Thus global budgets of alkalinity and nutrients are balanced. For further details, we refer readers to Aumont and Bopp (2006).

To simulate carbon chemistry and air–sea CO_2 fluxes, the model follows the protocol from phase 2 of the Ocean Carbon-Cycle Model Intercomparison Project (OCMIP, Najjar and Orr, 1999) protocol. The sea-to-air CO_2 flux F_{CO_2} is computed using the following equation:

$$F\mathrm{CO}_2 = \alpha\, k\, \Delta p\mathrm{CO}_2, \tag{1}$$

where α is the solubility of CO_2 computed from Weiss (1974) and ΔpCO_2 is the difference between the partial pressures of sea surface and atmospheric CO_2. Thus F_{CO_2} is positive when CO_2 is transferred from the ocean to the atmosphere. The piston velocity k is based on Eq. (3) of Wanninkhof (1992):

$$k = 0.30\, u_{\mathrm{w}}^2 \sqrt{\frac{660}{Sc}}(1 - f_{\mathrm{ice}}), \tag{2}$$

where u_{w} is the wind speed at 10 m, Sc is the CO_2 Schmidt number, and f_{ice} is the ice fraction.

2.2 Simulations

The dynamic model was started from rest and spun up for 50 years. Initial conditions for temperature and salinity are as described by Barnier et al. (2006). Initial biogeochemical fields of nitrate, phosphate, oxygen, and silicate are from the 2001 World Ocean Atlas (Conkright et al., 2002), whereas preindustrial dissolved inorganic carbon (DIC) and total alkalinity (Alk) come from the GLODAP gridded product (Key et al., 2004). Conversely, because data for iron and dissolved organic carbon (DOC) are more limited, both those fields were initialized with model output from a 3000-year spin up simulation of a global 2° configuration of the same NEMO-PISCES model (Aumont and Bopp, 2006). All other biogeochemical tracers have much shorter timescales; hence, they were initialized to globally uniform constants.

After the 50-year spin-up, we launched two parallel simulations: the first was a historical simulation run from 1870 to 2012 (143 years), and forced with a spatially uniform and temporally increasing atmospheric mole fraction of CO_2 (from which PISCES computes atmospheric pCO_2^{atm} following OCMIP2) reconstructed from ice core and atmospheric records (Le Quéré et al., 2014); the second simulation is a

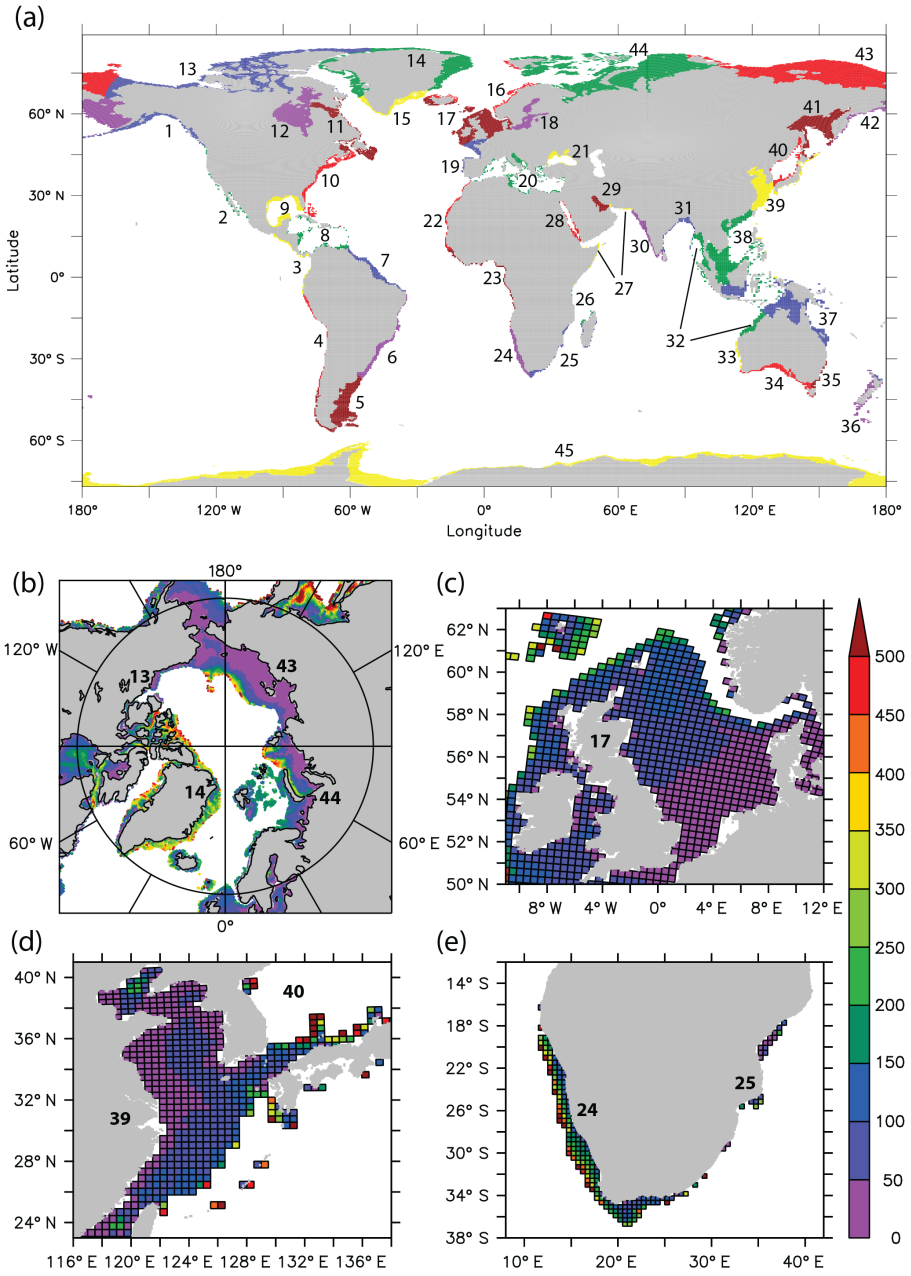

Figure 1. (a) Global segmentation of the coastal ocean following Laruelle et al. (2013) as regridded on the ORCA05 model grid. Colours distinguish limits between the MARCATS regions, numbers indicate regions defined in LA13. To perceive the spatial resolution of the ORCA05 configuration in the MARCATS context, we show zoomed-in images of bathymetry in four regions: **(b)** the Arctic polar margins, **(c)** the North Sea, **(d)** the Sea of Japan, the China Sea, and Kuroshio, and **(e)** south-western Africa and the Agulhas current. In the latter three panels, grid resolution is indicated by thin black lines.

parallel control run, where the 143-year simulation is identical except that it is forced with the preindustrial level of atmospheric mole fraction of CO_2 (287 ppm, constant in time). The preindustrial reference year is defined as 1870, thus neglecting changes in anthropogenic carbon storage in the ocean from 1750 to 1870. The F_{CO_2} computed with the historical simulation is for total carbon (total F_{CO_2}), whereas the F_{CO_2} from the control simulation is for natural carbon (natural F_{CO_2}). The corresponding anthropogenic F_{CO_2} is computed as the total minus natural F_{CO_2}.

All simulations were forced identically with atmospheric fields from the DRAKKAR Forcing Set (DFS, Brodeau et al., 2010). These fields include zonal and meridional components of 10 m winds, 2 m air humidity, 2 m air tempera-

ture, downward shortwave and longwave radiation at the sea surface, and precipitation. More specifically the NEMO-PISCES model is forced with version 4.2 of this forcing (DFS4.2, based on the ERA40 reanalysis) over 1958–2001, and that is followed by forcing from version 4.4 (DFS4.4) over 2002–2012. For the 1870–1957 period, where atmospheric reanalyses are unavailable, we repeatedly cycled the 1958–2007 DFS4.2 forcing.

Boundary conditions are also needed for biogeochemical tracers, i.e. besides the atmospheric CO_2 connection mentioned already. The model's lateral input from river discharge of DIC and DOC are taken from the annual estimates of the Global Erosion Model (Ludwig et al., 1996), constant in time. The DOC from river discharge is assumed to be labile and is directly converted to DIC upon its delivery to the ocean. Inputs of dissolved iron (Fe), nitrate (NO_3^{2-}), phosphate (PO_4^{3-}), and silicate (SiO_2) are computed from the sum of DIC and DOC river input using a constant set of ratios for $C:N:P:Si:Fe$, namely $320:16:1:53.3:3.64\times10^{-3}$, as computed from Meybeck (1982) for C : N, from Takahashi et al. (1985) for N : P, from de Baar and de Jong (2001) for Fe : C, and from Treguer et al. (1995) for Si : C. River discharge assumes no seasonal variation. Atmospheric deposition of iron comes from Tegen and Fung (1995).

Here, we use the conventional definition of anthropogenic carbon in the ocean used by previous global-ocean model studies (OCMIP, http://ocmip5.ipsl.jussieu.fr/OCMIP/ and e.g. Bopp et al., 2015), namely that anthropogenic carbon comes only from the direct geochemical effect of increasing atmospheric CO_2 and its subsequent invasion into the ocean. By definition, this anthropogenic F_{CO_2} does not include any effect from potential changes in ocean physics or biology. In the model, there are no changes nor variability in riverine delivery of carbon and nutrients, and anthropogenic carbon is not buried in sediments.

Following the 50-year spin-up and 143-year control simulation, the simulation remains far from equilibrium. Its global natural carbon flux is $-0.33\pm0.3\,\mathrm{Pg\,C\,yr^{-1}}$ (corresponding to CO_2 uptake by the ocean) during the last 10 years of the control simulation (2003–2012), compared to the estimate of natural carbon outgassing of $0.45\,\mathrm{Pg\,C\,yr^{-1}}$ by Jacobson et al. (2007). That difference is partly due to the strategy for our simulations, which were initialized with data and spun up for only 50 years because of the computational constraints to make higher-resolution simulations (ORCA05). At lower resolution (ORCA2), after a spin-up of 3000 years, there is $0.26\,\mathrm{Pg\,C\,yr^{-1}}$ greater globally integrated sea-to-air flux, relative to results after only a 50-year spin-up. Nearly all of that enhanced sea-to-air CO_2 flux due to the longer spin-up comes from the Southern Ocean. Anthropogenic F_{CO_2} estimates are expected to be influenced very little by model drift because of the way anthropogenic carbon is defined (i.e. drift affects both natural carbon and total carbon in the same way).

2.3 Defining the global coastal ocean

To sample the global coastal-ocean area, the model grid cells were selected following the MARgins and CATchments Segmentation (MARCATS) of Laruelle et al. (2013), hereafter LA13. The outer limit of the coastal ocean is defined as the maximum slope at the shelf break, while the inner limit is taken as the coastline, thus excluding the proximal zone of the coastal ocean (Fig. 1). Hence, only the continental shelf area is taken into account. The MARCATS segmentation divides the global coastal ocean into 45 regional units (Table 2). The limits of each of these units delineate areas that present roughly homogenous oceanic features such as coastal currents or the boundaries of marginal seas. Following the Liu et al. (2010) classification of the continental shelf seas, LA13 aggregated the 45 units into seven classes with similar physical and oceanographic large-scale characteristics such as the eastern boundary currents and the polar margins. The high-resolution geographical information system (GIS) file describing the MARCATS segmentation from LA13 was regridded using the QGIS software (QGIS Development Team, 2015) on the ORCA05 model grid in order to sample the model results on its own grid. This regridding technique implies some modifications to the regions initially described in LA13. In the model, the global coastal ocean has a total surface area of $27.0\times10^6\,\mathrm{km^2}$, which is 8 % less than the original value from Laruelle et al. (2014). Here, the model's total coastal-ocean surface area represents 7.5 % of the total area of the global ocean. Subsequently we refer to the individual MARCATS regions using the terminology of LA13.

2.4 Evaluation dataset

To evaluate the total F_{CO_2} simulated by the model (historical simulation), we compare it to the database from Laruelle et al. (2014), hereafter LA14, which provides observation-based estimates for the flux over the MARCATS regions. This database was constructed by aggregating 3×10^6 coastal-sea surface pCO_2 measurements collected over 1990 to 2011 and included in the Surface Ocean CO_2 Atlas version 2.0 (SOCAT v2.0, Pfeil et al., 2013; Bakker et al., 2014). These measurements represent about 30 % of the SOCAT v2.0 dataset. To compute the flux, LA14 also relied on wind speeds from the multiplatform CCMP wind speed database (Atlas et al., 2011), atmospheric CO_2 from GLOBALVIEW-CO2 (2012), and the flux parameterization from Wanninkhof (1992) as modified by Takahashi et al. (2009). As sensitivity tests, LA14 also used the flux parameterizations from Ho et al. (2006) as well as the original formulation from Wanninkhof (1992).

Thus LA14 computed mean annual F_{CO_2} estimates for 42 of the 45 MARCATS regions defined in LA13. The remaining MARCATS areas (12: Hudson Bay, 21: Black Sea and 29: Persian Gulf) are devoid of observations in the SOCAT database and were neglected. For the remaining regions, be-

cause of the large heterogeneity in both the spatial and temporal coverage of ocean pCO_2 observations, the uncertainties for each of the MARCATS F_{CO_2} estimates from LA14 vary greatly. For example, only 28 % of the sub-units of MARCATS regions used in LA14 have an estimate for F_{CO_2} uncertainty of less than 0.25 mol C m^{-2} yr^{-1}. The data-based F_{CO_2} estimate for the Sea of Okhotsk is not taken into account due to the extremely poor data coverage of this region and its strong divergence with the local literature (LA14). Here, we do not evaluate the simulated annual cycle of flux of total carbon because few MARCATS regions provide adequate temporal coverage. Finally, LA14 is the first and only study to provide coastal-ocean observation-based F_{CO_2} estimates at global scale taking into account the reduction in F_{CO_2} due to sea ice cover along coasts; hence it is directly comparable to our model results.

Besides the coastal data-based estimates of F_{CO_2} from LA14, we also compare our model results to those for the open ocean from Takahashi et al. (2009) and Landschützer et al. (2014). Both the global and coastal observational estimates are compared to the average modelled F_{CO_2} over the last 20 years (1993–2012) of the historical simulation. For the coastal comparison, simulated total F_{CO_2} are spatially averaged over each MARCATS regions. In addition, the model's uncertainty, computed as the interannual variability over 1993–2012, is compared to uncertainties in the observational estimates, computed as the standard deviation between flux parameterizations from Wanninkhof (1992) as modified by Takahashi et al. (2009), Ho et al. (2006) and Wanninkhof (1992).

2.5 Revelle factor calculation

To assess how the capacity of the coastal ocean to absorb anthropogenic carbon differs from open-ocean surface waters, we computed the Revelle factor (R_f, Sundquist et al., 1979) using the CO2SYS MATLAB software (Van Heuven et al., 2011(@). CO2SYS was used with the simulated sea surface temperature, salinity, alkalinity, and DIC for model years 1993–2012 while choosing the total pH scale, the K_1 and K_2 constants from Lueker et al. (2000), the K_{SO_4} constant from Dickson (1990), and the formulation of the borate-to-salinity ratio from Uppström (1974).

2.6 Residence time

To compute water residence time in each MARCATS region, we divided the volume of each region by the integrated outflow of water from 5-day mean current velocities at coastal boundaries from 2011.

3 Results

3.1 Global ocean fluxes

The simulated global-ocean uptake of anthropogenic carbon increases roughly linearly from 1950 to 2012, reaching an average of 2.3 Pg C yr^{-1} during the period 1993–2012. That is comparable to the estimate from the fifth assessment report of the Intergovernmental Panel on Climate Change (IPCC) (Ciais et al., 2013) of 2.3 ± 0.7 Pg C yr^{-1} for 2000–2009 (Fig. 2).

Regionally, overall patterns in the total F_{CO_2} are similar between the model and data-based estimates from Landschützer et al. (2014) and Takahashi et al. (2009) (Fig. 3). Carbon is lost from the ocean in the equatorial band and in coastal upwelling regions, while it is gained by the ocean in the northern high latitudes. Quantitative comparison of the annual-mean map from the model with that from the Takahashi et al. (2009) observation-based database gives a root mean square error (RMSE) of 0.73 mol C m^{-2} yr^{-1} and a correlation coefficient R of 0.80; likewise, comparison with the Landschützer et al. (2014) observational-based database gives a similar RMSE (0.70 mol C m^{-2} yr^{-1}) and R (0.81). Integrating over latitudinal bands, (Table 1), the model overestimates carbon uptake for the 90–30° S region, where it absorbs 1.50 Pg C yr^{-1} of total carbon vs. 0.73–0.77 Pg C yr^{-1} from Takahashi et al. (2009) and Landschützer et al. (2014) observational databases. This overestimate may result from the model simulation still being far from equilibrium (see Sect. 2.2 paragraph 5 for details). The model also underestimates outgassing in the tropical band, where it releases 0.13 Pg C yr^{-1} vs. 0.13–0.20 Pg C yr^{-1} for the two data-based estimates. Further north in the 30–90° N band, the model takes up 0.93 Pg C yr^{-1} vs. 1.53–1.59 Pg C yr^{-1} for Takahashi et al. (2009) and Landschützer et al. (2014).

3.2 Coastal-ocean fluxes

3.2.1 Total CO_2

The simulated uptake of total carbon by the coastal-ocean averages 267 Tg C yr^{-1} during the 1993–2012 period. Most of the 45 MARCATS regions act as carbon sinks; together, they absorb 283 Tg C yr^{-1}. The largest uptake is 3.4 mol C m^{-2} yr^{-1} in the South Greenland region. Few MARCATS regions act as carbon sources to the atmosphere (Table 2 and Fig. 4.a), i.e. only 14 % of the global coastal-ocean surface area, together losing 16 Tg C of carbon to the atmosphere every year. The mean annual carbon loss per square metre in these MARCATS regions is usually relatively weak, less than 1.5 mol C m^{-2} yr^{-1}). When grouped into MARCATS classes (see Table 3), all classes are carbon sinks, absorbing from 0.06 to 1.65 mol C m^{-2} yr^{-1}. By class, the largest specific fluxes occur in the western boundary current regions and the subpolar margins, which absorb 1.65

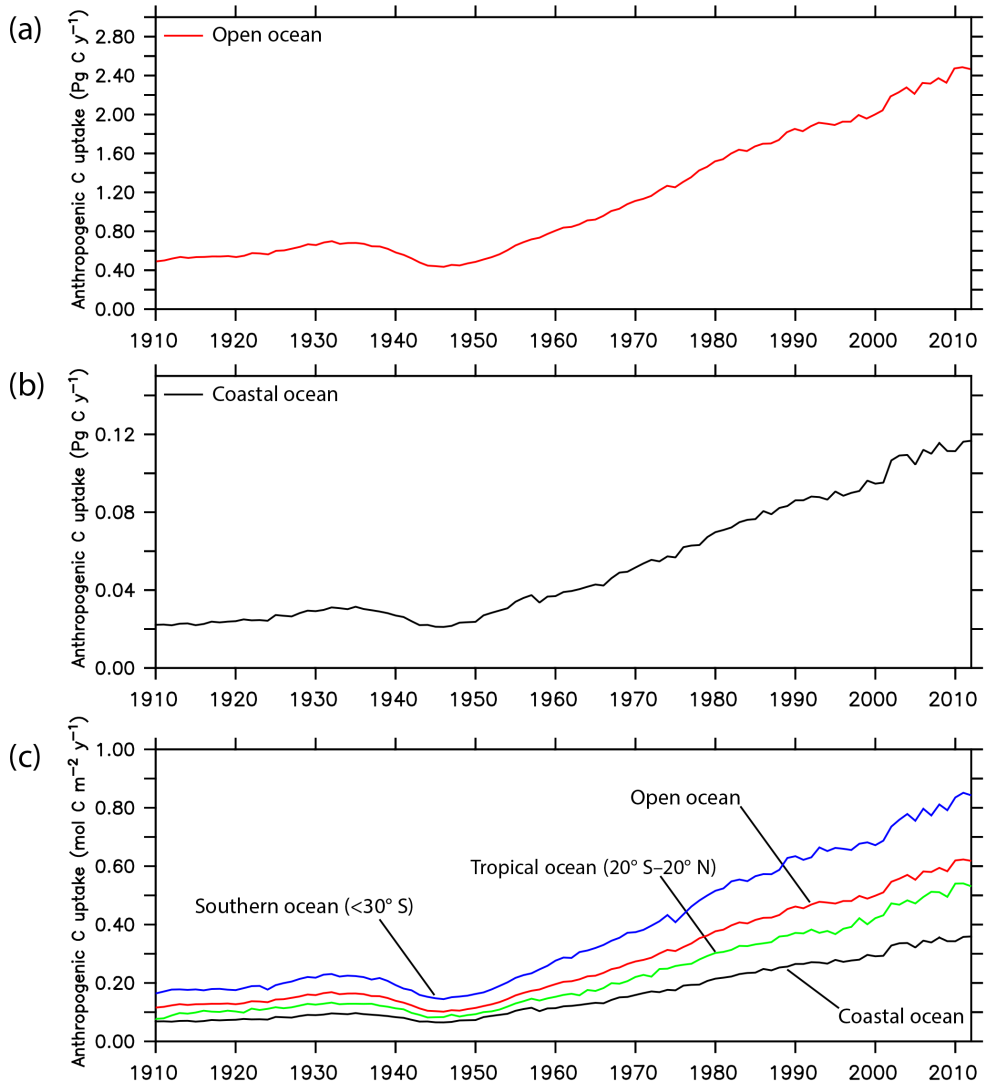

Figure 2. Simulated temporal evolution of area-integrated anthropogenic carbon uptake for **(a)** the open ocean and **(b)** the coastal ocean. **(c)** Analogous evolution of anthropogenic carbon uptake for the open ocean, the coastal ocean, the Southern Ocean, and the tropical oceans, but given as the average flux per unit area.

Table 1. Sea-to-air total CO_2 fluxes ($Pg\,C\,yr^{-1}$) given as zonal means from Takahashi et al. (2009) for the reference year 2000, from Landschützer et al. (2014) for 1998–2011 and the ORCA05 model for 1993–2012.

Latitudinal bands	Observation-based climatologies		This study
	Takahashi et al. (2009)	Landschützer et al. (2014)	ORCA05
90–30° S	−0.77	−0.73	−1.50
30° S–30° N	0.20	0.13	0.13
30–90° N	−1.59	−1.53	−0.93

and $1.61\,mol\,C\,m^{-2}\,yr^{-1}$ respectively. More generally, the tropical MARCATS regions act as weak carbon sources and the mid-to-high-latitude regions act as strong carbon sinks (Fig. 4a). The same trend is also apparent in the zonal-mean distribution (Fig. 5).

A comparison of the simulated vs. observed F_{CO_2} estimates for each MARCATS region is reported in Table 2 and Fig. 6. The Pearson correlation coefficient R is 0.8 for specific fluxes. In the model, 79 % of the MARCATS regions act as carbon sinks, whereas that proportion is 64 % for LA14.

Table 2. MARCATS regions as described by Laruelle et al. (2013, 2014), along with means for data-based fluxes of total CO_2 from LA14 during the period 1990–2011 as well as simulated anthropogenic and total CO_2 fluxes, and residence time during the period 1993–2012. Uncertainties are the interannual variability over the averaged period. Abbreviations are included for north (N), south (S), east (E), west (W), eastern boundary current (EBC), western boundary current (WBC), sea-to-air flux of total carbon (FCO_2^{tot}), anthropogenic carbon (FCO_2^{ant}). Surface areas indicated as "from LA14" actually differ slightly from those published in LA13 as they have been modified for subsequent computations (Goulven G. Laruelle, personal communication, January 2015).

N°	System Name	Class	Surface (10^3 km^2)		FCO_2^{tot} (mol C m^{-2} yr^{-1})		FCO_2^{tot} (Tg C yr^{-1})		FCO_2^{ant}		Residence
			Model	LA14	Simulated	LA14	Simulated	LA14	mol C m^{-2} yr^{-1}	Tg C yr^{-1}	time (month)
1	N-E Pacific	Subpolar	397	350	−2.29 ± 0.17	−1.61	−10.935 ± 0.823	−6.775	−0.45 ± 0.05	−2.16 ± 0.23	0.83 ± 0.23
2	Californian current	EBC	118	208	−0.34 ± 0.10	−0.05	−0.477 ± 0.148	−0.135	−0.35 ± 0.09	−0.50 ± 0.13	1.00 ± 0.23
3	Tropical E Pacific	Tropical	152	183	−0.12 ± 0.05	0.09	−0.222 ± 0.095	0.192	−0.36 ± 0.05	−0.65 ± 0.10	0.51 ± 0.09
4	Peruvian upwelling current	EBC	138	143	1.44 ± 0.80	0.65	2.386 ± 1.325	1.073	−0.39 ± 0.09	−0.64 ± 0.15	0.72 ± 0.15
5	Southern America	Subpolar	1126	1190	−1.51 ± 0.13	−1.31	−20.460 ± 1.705	−18.715	−0.46 ± 0.05	−6.28 ± 0.74	0.65 ± 0.05
6	Brazilian current	WBC	475	484	−0.33 ± 0.08	0.10	−1.872 ± 0.479	0.567	−0.34 ± 0.05	−1.95 ± 0.29	0.26 ± 0.06
7	Tropical W Atlantic	Tropical	479	488	0.86 ± 0.10	0.07	4.934 ± 0.551	0.394	−0.26 ± 0.05	−1.50 ± 0.31	0.20 ± 0.02
8	Caribbean Sea	Tropical	303	358	0.10 ± 0.10	0.81	0.366 ± 0.348	3.460	−0.31 ± 0.04	−1.12 ± 0.14	0.32 ± 0.03
9	Gulf of Mexico	Marginal sea	469	532	−0.79 ± 0.11	−0.33	−4.478 ± 0.633	−2.100	−0.32 ± 0.03	−1.81 ± 0.16	1.01 ± 0.15
10	Florida upwelling	WBC	545	591	−2.25 ± 0.21	−0.38	−14.692 ± 1.351	−2.723	−0.66 ± 0.05	−4.29 ± 0.36	0.39 ± 0.02
11	Sea of Labrador	Subpolar	576	638	−1.27 ± 0.18	−1.72	−8.808 ± 1.244	−13.172	−0.32 ± 0.03	−2.19 ± 0.21	1.20 ± 0.35
12	Hudson Bay	Marginal sea	998	1064	0.31 ± 0.29	n.d	3.757 ± 3.423	n.d.	−0.08 ± 0.04	−0.99 ± 0.46	51.22 ± 22.75
13	Canadian Archipelago	Polar	1001	1145	−0.52 ± 0.06	−1.02	−6.234 ± 0.748	−13.986	−0.09 ± 0.02	−1.03 ± 0.21	2.82 ± 0.46
14	N Greenland	Polar	544	602	−0.97 ± 0.15	−0.61	−6.333 ± 1.000	−4.400	−0.26 ± 0.05	−1.67 ± 0.33	2.38 ± 0.44
15	S Greenland	Polar	238	262	−3.35 ± 0.44	−3.81	−9.564 ± 1.259	−11.972	−0.86 ± 0.19	−2.45 ± 0.53	0.48 ± 0.09
16	Norwegian Basin	Polar	141	162	−2.87 ± 0.23	−1.72	−4.855 ± 0.396	−3.342	−0.60 ± 0.09	−1.02 ± 0.15	0.31 ± 0.10
17	NE Atlantic	Subpolar	1020	1073	−2.16 ± 0.12	−1.33	−26.501 ± 1.419	−17.165	−0.53 ± 0.05	−6.52 ± 0.59	0.93 ± 0.11
18	Baltic Sea	Marginal sea	324	364	0.30 ± 0.07	0.51	1.184 ± 0.288	2.245	−0.01 ± 0.01	−0.05 ± 0.03	17.37 ± 9.52
19	Iberian upwelling	EBC	251	267	−1.13 ± 0.12	0.04	−3.393 ± 0.352	0.122	−0.27 ± 0.03	−0.82 ± 0.10	2.31 ± 0.54
20	Mediterranean Sea	Marginal sea	423	529	−0.24 ± 0.06	0.62	−1.196 ± 0.327	3.925	−0.30 ± 0.02	−1.52 ± 0.12	0.72 ± 0.09
21	Black Sea	Marginal sea	131	172	−0.24 ± 0.11	n.d.	−0.375 ± 0.174	n.d.	−0.18 ± 0.02	−0.28 ± 0.03	1.60 ± 0.48
22	Moroccan upwelling	EBC	177	206	0.18 ± 0.12	2.92	0.385 ± 0.263	7.220	−0.33 ± 0.03	−0.71 ± 0.07	0.67 ± 0.14
23	Tropical E Atlantic	Tropical	225	259	0.09 ± 0.08	−0.06	0.239 ± 0.208	−0.174	−0.19 ± 0.02	−0.52 ± 0.05	0.59 ± 0.09
24	SW Africa	EBC	300	298	0.43 ± 0.40	−1.43	1.544 ± 1.448	−5.103	−0.59 ± 0.08	−2.14 ± 0.28	2.17 ± 0.55
25	Agulhas current	WBC	189	239	−1.20 ± 0.09	−0.58	−2.730 ± 0.206	−1.664	−0.53 ± 0.05	−1.21 ± 0.12	0.13 ± 0.01
26	Tropical W Indian	Tropical	46	68	−0.06 ± 0.08	1.00	−0.031 ± 0.044	0.815	−0.16 ± 0.04	−0.09 ± 0.03	0.20 ± 0.04
27	W Arabian Sea	Indian margins	82	92	0.35 ± 0.04	1.14	0.342 ± 0.043	1.257	−0.31 ± 0.04	−0.31 ± 0.04	0.12 ± 0.04
28	Red Sea	Marginal sea	158	174	0.24 ± 0.03	0.16	0.460 ± 0.065	0.330	−0.15 ± 0.01	−0.28 ± 0.02	0.57 ± 0.15
29	Persian Gulf	Marginal sea	208	233	0.04 ± 0.08	n.d.	0.092 ± 0.203	n.d.	−0.12 ± 0.02	−0.31 ± 0.04	24.67 ± 12.09
30	E Arabian Sea	Indian margins	298	317	0.21 ± 0.12	0.67	0.749 ± 0.427	2.555	−0.30 ± 0.04	−1.07 ± 0.15	0.67 ± 0.15
31	Bay of Bengal	Indian margins	197	203	−0.69 ± 0.12	−0.22	−1.641 ± 0.276	−0.530	−0.31 ± 0.04	−0.74 ± 0.09	0.43 ± 0.11
32	Tropical E Indian	Indian margins	727	763	−0.06 ± 0.07	−0.02	−0.482 ± 0.569	−0.170	−0.20 ± 0.02	−1.78 ± 0.17	0.50 ± 0.04
33	Leeuwin current	EBC	81	117	−2.05 ± 0.15	−0.98	−2.010 ± 0.148	−1.379	−0.60 ± 0.07	−0.58 ± 0.07	0.56 ± 0.16
34	S Australia	Subpolar	392	436	−1.37 ± 0.18	−1.14	−6.438 ± 0.859	−5.983	−0.27 ± 0.03	−1.29 ± 0.14	0.74 ± 0.25
35	E Australian current	WBC	98	130	−1.74 ± 0.18	−1.09	−2.036 ± 0.205	−1.695	−0.50 ± 0.07	−0.58 ± 0.08	0.37 ± 0.04
36	New Zealand	Subpolar	263	286	−1.23 ± 0.16	−1.25	−3.882 ± 0.498	−4.274	−0.52 ± 0.07	−1.64 ± 0.23	0.49 ± 0.04
37	N Australia	Tropical	2278	2292	−0.29 ± 0.11	0.44	−7.872 ± 3.114	12.120	−0.23 ± 0.04	−6.19 ± 1.00	0.38 ± 0.03
38	SE Asia	Tropical	2130	2160	−0.29 ± 0.07	−0.91	−7.344 ± 1.908	−23.609	−0.20 ± 0.03	−5.01 ± 0.72	0.49 ± 0.05
39	China Sea and Kuroshio	WBC	1132	1129	−1.99 ± 0.15	−1.41	−27.046 ± 1.991	−19.100	−0.45 ± 0.05	−6.13 ± 0.72	0.32 ± 0.01
40	Sea of Japan	Marginal sea	233	147	−3.07 ± 0.17	−3.47	−8.613 ± 0.475	−6.113	−0.51 ± 0.06	−1.44 ± 0.18	1.64 ± 0.24
41	Sea of Okhotsk	Marginal sea	933	952	−1.66 ± 0.07	1.31	−18.623 ± 0.761	14.955	−0.36 ± 0.03	−4.00 ± 0.34	3.52 ± 1.38
42	NW Pacific	Subpolar	1025	1000	−1.85 ± 0.14	−0.70	−22.760 ± 1.726	−8.419	−0.24 ± 0.04	−2.99 ± 0.52	1.48 ± 0.59
43	Siberian Shelves	Polar	1848	1889	−0.47 ± 0.10	−0.90	−10.499 ± 2.117	−20.322	−0.05 ± 0.01	−1.09 ± 0.28	4.10 ± 0.64
44	Barents and Kara seas	Polar	1559	1680	−0.75 ± 0.14	−1.60	−14.176 ± 2.585	−32.225	−0.11 ± 0.02	−2.05 ± 0.43	1.58 ± 0.46
45	Antarctic Shelves	Polar	2452	2936	−0.90 ± 0.14	−0.15	−26.630 ± 3.989	−5.381	−0.69 ± 0.07	−20.30 ± 2.18	2.08 ± 0.29

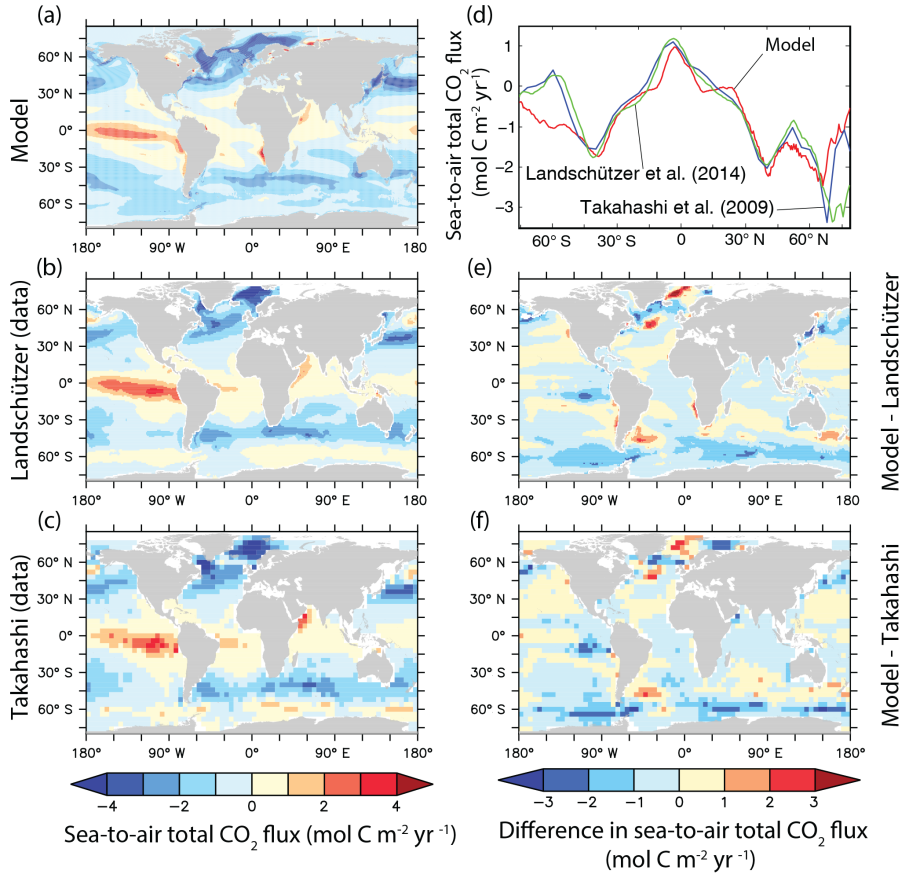

Figure 3. Climatological mean of sea-to-air flux of total carbon fluxes in mol C m^{-2} y^{-1} for **(a)** the model average during the 1993–2012 period, **(b)** the data-based estimate from Landschützer et al. (2014) for 1998–2011, and **(c)** the data-based estimate from Takahashi et al. (2009) for 2000–2009. Panels **(d)** and **(f)** present differences between simulated and observed sea-to-air total carbon fluxes (mol C m^{-2} yr^{-1}) relative to **(b)** and **(c)** respectively. Panel **(d)** presents the latitudinal distribution of the simulated and the observed mean sea-to-air total carbon fluxes.

Table 3. Weighted mean of simulated and data-based sea-to-air CO_2 fluxes and simulated residence time for each MARCATS class, excluding the Sea of Okhotsk (see text). Abbreviations are included for eastern boundary current (EBC) and western boundary current (WBC).

Class	Sea-to-air CO_2 flux (mol C m^{-2} yr^{-1})			Residence
	Total (LA14)	Total (model)	Anthropogenic (model)	time (month)
EBC	0.12	-0.12 ± 0.16	-0.42 ± 0.03	1.52 ± 0.22
Indian margins	0.19	-0.06 ± 0.05	-0.24 ± 0.02	0.49 ± 0.04
Marginal Seas	−0.56	-0.92 ± 0.07	-0.29 ± 0.01	10.34 ± 3.50
Polar margins	−0.88	-0.83 ± 0.06	-0.32 ± 0.03	2.18 ± 0.20
Subpolar margins	−1.23	-1.61 ± 0.07	-0.36 ± 0.02	0.92 ± 0.16
Tropical margins	−0.10	-0.15 ± 0.06	-0.22 ± 0.02	0.42 ± 0.03
WBC	−0.80	-1.65 ± 0.08	-0.48 ± 0.03	0.31 ± 0.01

After aggregating the specific flux estimates into the different MARCATS classes (Table 3 and Fig. 7), the correlation coefficient R increases to 0.9. Generally, our model results tend to simulate larger sinks and weaker sources than observed (i.e. 76 % of the specific simulated fluxes of total carbon have lower relative values than the data-based estimates). For some MARCATS classes, even the sign of the simulated flux differs from the data-based estimates, e.g. for the Indian margins and the eastern boundary currents. The latter class contains two regions (Moroccan and SW Africa upwelling) having the worst overall agreement. Otherwise, in

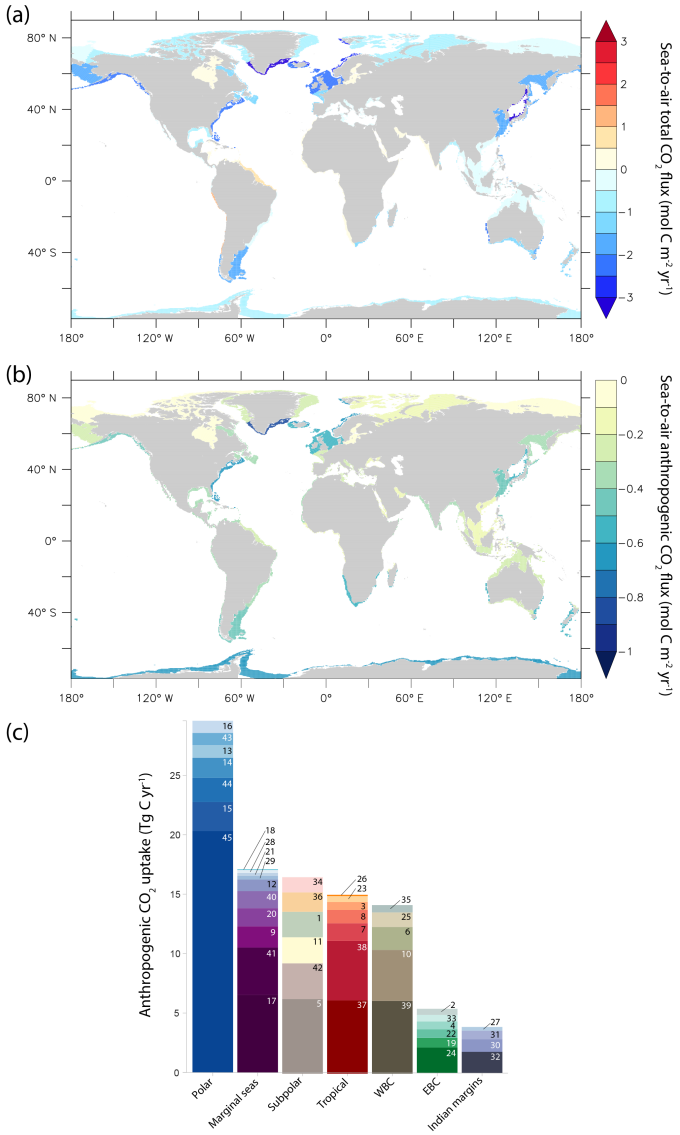

Figure 4. Global mean distribution of the simulated sea-to-air flux of **(a)** total carbon and **(b)** anthropogenic carbon over 1993–2012 as $\mathrm{mol\,C\,m^{-2}\,yr^{-1}}$ in the global coastal ocean segmented following MARCATS from LA13. **(c)** Bar chart of the anthropogenic carbon uptake in $\mathrm{Tg\,C\,yr^{-1}}$ according to the MARCATS classification. Abbreviations are included for eastern boundary current (EBC) and western boundary current (WBC). Links between numbers and regions are reported in Table 2. Interactive illustrations can be found at http://lsce-datavisgroup.github.io/CoastalCO2Flux/.

the Arctic polar regions, the simulated uptake is too low, with $52\,\mathrm{Tg\,C\,yr^{-1}}$ from the model vs. $86\,\mathrm{Tg\,C\,yr^{-1}}$ from LA14.

3.2.2 Anthropogenic CO_2

The anthropogenic F_{CO_2} is computed as the difference between the total flux (historical simulation) and natural flux (control simulation). When integrated over the global coastal ocean, the mean anthropogenic flux from 1993 to 2012 is $0.10 \pm 0.01\,\mathrm{Pg\,C\,yr^{-1}}$. That amounts to 4.5 % of the simulated global anthropogenic carbon uptake, substantially less than the 7.5 % proportion of the coastal-to-global ocean surface areas. During the period 1950–2000, the uptake of anthropogenic carbon by the coastal ocean essentially grows linearly as it does for the global ocean. That is, it grows at a nearly constant rate of $0.0015\,\mathrm{Pg\,C\,yr^{-2}}$, which is 4.4 % of the rate for the global ocean increase in anthropogenic carbon uptake over the same period (Fig. 2).

All MARCATS regions absorb anthropogenic carbon at rates ranging from $0.01\,\mathrm{mol\,C\,m^{-2}\,yr^{-1}}$ for the Baltic Sea to $0.86\,\mathrm{mol\,C\,m^{-2}\,yr^{-1}}$ for the South Greenland region (Table 2 and Fig. 4.b). By class, the strongest specific fluxes of anthropogenic carbon into the ocean occur in the boundary

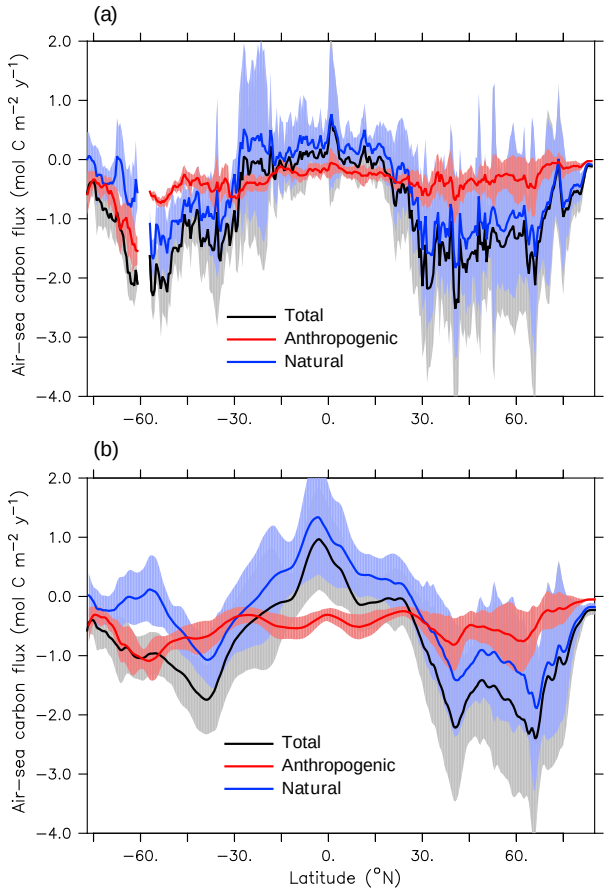

Figure 5. Zonal-mean, sea-to-air fluxes of total, anthropogenic, and natural CO_2 (mol C m^{-2} yr^{-1}) given as the average over 1993–2012 for **(a)** the coastal ocean and **(b)** the global ocean. Shaded areas indicate the standard deviation of environmental variability of all ocean grid cells within each latitudinal band. Interannual variations are not shown.

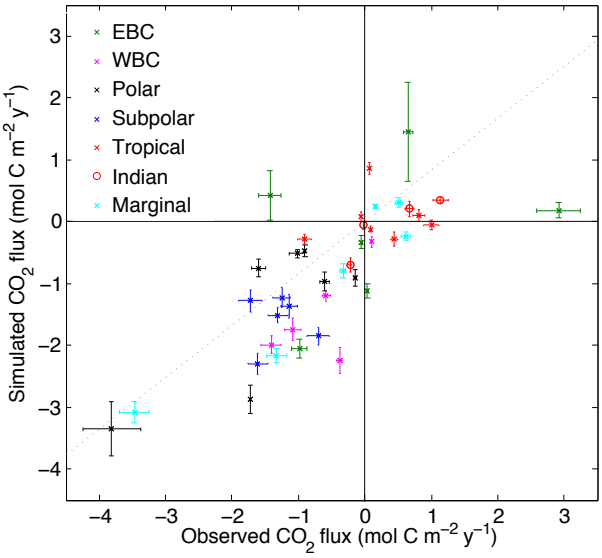

Figure 6. Simulated vs. observed MARCATS sea-to-air flux of total carbon in **(a)** mol C m^{-2} yr^{-1} and **(b)** Tg C yr^{-1}. Vertical error bars show the standard deviation from the 1993–2012 interannual variability for model results and the horizontal bars correspond to the 1990–2011 variability from computational methods used in LA14 for observation-based estimates. Here, regression line (grey dotted) have y intercepts forced to 0. All MARCATS regions have been used except the Black Sea, the Persian Gulf (no data estimate), and the Sea of Okhotsk (see text).

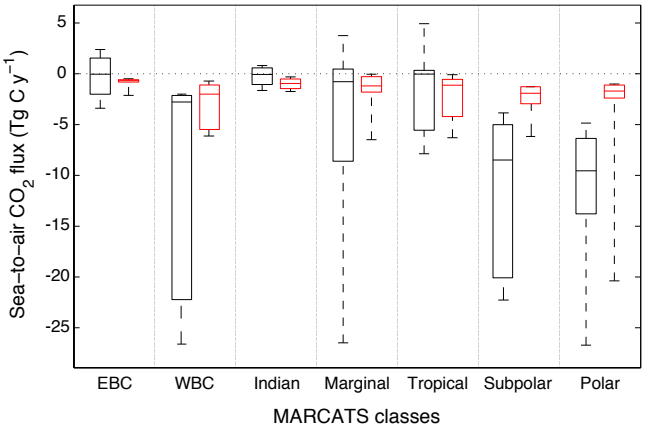

Figure 7. Box plots of the simulated sea-to-air CO_2 fluxes (Tg C yr^{-1}) grouped into the MARCATS classes of the coastal ocean. Black boxes indicate total fluxes, and red boxes indicate anthropogenic fluxes. Shown are the lowest estimate, the first quartile, the median, the third quartile, and the highest estimate for each class.

current regions, namely the EBC and WBC, with 0.42 and 0.48 mol C m^{-2} yr^{-1} respectively. Conversely, the weakest anthropogenic carbon uptake occurs in the tropical margins and the Indian margins with 0.22 and 0.24 mol C m^{-2} yr^{-1} respectively. But specific fluxes can be misleading. Although the polar and subpolar margins do not have the highest specific fluxes, their integrated uptake of anthropogenic carbon is large because of their large surface areas (Fig. 4b and c). Together they absorb 46 Tg C yr^{-1}, which is 45 % of total uptake of anthropogenic carbon by the global coastal ocean.

These results emphasize that there is no link between anthropogenic and total carbon fluxes when comparing patterns between regions. For example, even though the EBC and WBC regions are the most efficient regions in anthropogenic carbon uptake (both above 0.4 mol C m^{-2} yr^{-1}), their behaviour differs greatly in terms of the flux of total carbon, i.e. −1.65 vs. −0.12 mol C m^{-2} yr^{-1} respectively (Fig. 7). The same lack of correlation between anthropogenic and total flux patterns is even clearer in the zonal mean distributions (Fig. 5). For instance, the specific fluxes of anthropogenic carbon into the coastal ocean between 55° S and 90° N are nearly uniform, remaining near −0.5 mol C m^{-2} yr^{-1}; conversely, the total carbon fluxes vary greatly between −2

and $+0.5\,\mathrm{mol\,C\,m^{-2}\,yr^{-1}}$. These variations in the total carbon flux are dictated by variations in the natural carbon flux (Fig. 5).

4 Discussion

4.1 Comparison with previous coastal estimates

4.1.1 Total flux

Our mean simulated uptake of total carbon by the global coastal ocean over 1993 to 2012 is $0.27 \pm 0.07\,\mathrm{Pg\,C\,yr^{-1}}$, which falls within the range of previous data-based estimates of 0.2–0.4 $\mathrm{Pg\,C\,yr^{-1}}$ (Borges et al., 2005; Cai et al., 2006; Chen and Borges, 2009; Laruelle et al., 2010; Cai, 2011; Chen et al., 2013; Laruelle et al., 2014). Out of those, estimates provided since 2011 gather closer to the lower limit, e.g. the estimate of $0.2\,\mathrm{Pg\,C\,yr^{-1}}$ from LA14, as is also the case for our model-based estimate. Some aspects of the LA14 data-based approach are shared by our model-based approach, i.e. the same reference period, essentially the same definition of the coastal ocean, and the same correction for the effect of sea ice cover on F_{CO_2}. LA14 is the first observation-based study to take into account this sea ice effect for coastal-ocean F_{CO_2} estimates at the global scale.

Using a box model, Andersson and Mackenzie (2004) and Mackenzie et al. (2004) estimated that the global coastal ocean acted as a carbon source to the atmosphere prior to industrialization; however, they also estimate that industrialization has recently led to a reversal in the sign of this flux (the global coastal ocean became a carbon sink) mainly due to the enhancement of NEP from increased riverine inputs. In contrast, our model simulations indicate that the preindustrial coastal ocean was already a carbon sink, and that this sink has strengthened over the industrial period. This discrepancy appears to be explained by different definitions of the coastal ocean. Both the box model and our 3-D model include the distal coastal zone, but only the box model includes the proximal coastal zone (bays, estuaries, deltas, lagoons, salt marshes, mangroves, and banks). That proximal zone is known generally as a strong source of carbon to the atmosphere (Rabouille et al., 2001).

The model representation of riverine DOC input and its instantaneous remineralization has potential implications for our estimates of total F_{CO_2}. In the Amazon plume for instance, we underestimate CO_2 absorption because of this instantaneous addition of DIC without input of alkalinity. However this assumption has no direct implication on our anthropogenic F_{CO_2} estimates.

Furthermore, our simplified representation of sedimentary processes affects simulated total CO_2 fluxes (Krumins et al., 2013; Soetaert et al., 2000). First, the model lacks an explicit representation of sedimentary processes. Thus it cannot reproduce the temporal dynamics of interactions between sediments and the overlying water column, e.g. resulting in potential delays between sediment burial and remineralization. Second, our model neglects any alkalinity source from sediment anaerobic degradation, such as denitrification and sulfate reduction of deposited organic matter. Even if not well constrained (Chen, 2002; Thomas et al., 2009; Hu and Cai, 2011; Krumins et al., 2013), this source of alkalinity could partially balance the total CO_2 uptake of the coastal ocean. However, the simplified representation of these sediment processes has no direct effect on our anthropogenic F_{CO_2} estimates.

4.1.2 Anthropogenic flux

The strongest specific fluxes of anthropogenic carbon into the ocean occur in the boundary current regions, namely the EBC and WBC. Indeed, these regions show significant vertical and lateral mixing features such as filaments and eddies from the strong adjacent western boundary currents and upwelling from Eastern boundary upwelling systems (EBUS). Those physical processes lead to the deepening of the mixed layer depth, export of the absorbed anthropogenic carbon from shallow water to deeper water layers, and its transfer to the adjacent open ocean.

Our estimate of the simulated anthropogenic carbon uptake of $0.10\,\mathrm{Pg\,C\,yr^{-1}}$ for the global coastal ocean (Fig. 9) is about half that found by Wanninkhof et al. (2013) for a similar period. The latter study estimates coastal anthropogenic CO_2 uptake by extrapolating specific F_{CO_2} from the adjacent open ocean into coastal areas, exploiting coarse-resolution models and data. To compare approaches, we applied the Wanninkhof et al. (2013) extrapolation method to our model output; we found the same result as theirs for global coastal-ocean uptake of anthropogenic CO_2 ($0.18\,\mathrm{Pg\,C\,yr^{-1}}$). Thus the extrapolation technique leads to an overestimate of anthropogenic CO_2 uptake in the model's global coastal ocean.

Nonetheless, the Wanninkhof et al. (2013) estimate for the anthropogenic carbon uptake by the coastal ocean was used by Regnier et al. (2013) for their coastal carbon budget. That budget also accounts for the increase in river discharge of carbon ($0.1\,\mathrm{Pg\,C\,yr^{-1}}$) and nutrients during the industrial era, which promotes organic carbon production, some of which is buried in the coastal zone (up to $0.15\,\mathrm{Pg\,C\,yr^{-1}}$). Unfortunately, these numbers remain particularly uncertain. Hence we have chosen to ignore them, adopting the conventional definition of anthropogenic carbon in the ocean used by previous global-ocean model studies, namely that anthropogenic carbon comes only from the direct geochemical effect of the anthropogenic increase in atmospheric CO_2 and its subsequent invasion into the ocean. The future challenge of improving estimates of changes and variability in riverine delivery of carbon and nutrient and sediment burial is critical to refine land contributions to the coastal-ocean carbon budget.

Our estimate of $0.10\,\mathrm{Pg\,C\,yr^{-1}}$ for the anthropogenic F_{CO_2} into the coastal ocean is 40 % less than the $0.17\,\mathrm{Pg\,C\,yr^{-1}}$ estimated by Borges (2005) from Andersson and Mackenzie (2004) and Mackenzie et al. (2004). Causes for this difference may stem from (1) the different definitions of the coastal ocean (proximal coastal zone included in the box model but not the 3-D model), (2) the different approaches (uniform coastal ocean in the box model but not in the 3-D model), and (3) the role of sediments (pore waters included in the box model but neglected in the 3-D model).

4.2 Coastal vs. open ocean

Patterns in our simulated total F_{CO_2} in the coastal ocean generally follow those for the open ocean, with net carbon sources in the low latitudes and carbon sinks in the middle to high latitudes (Fig. 5). The same tendency was pointed out by Gruber (2014) when discussing the LA14 data-based fluxes. The patterns in our simulated total CO_2 flux are mainly driven by patterns in the natural CO_2 flux both in the coastal and open oceans (Fig. 5). Yet the pattern for anthropogenic CO_2 flux differs greatly from that of natural CO_2, having its strongest uptake in the Southern Ocean in both the open and coastal oceans, i.e. where zonally averaged specific uptake reaches up to $1.5\,\mathrm{mol\,C\,m^{-2}\,yr^{-1}}$. The bathymetry of MARCATS regions around the Antarctic continent is much deeper than in the other coastal regions (500 m vs. 160 m for the global coastal ocean); this probably reduces the contrast between the coastal and open ocean in the Southern Ocean and explains the similarities of anthropogenic carbon uptake rates there.

Despite large-scale similarities between coastal- and open-ocean fluxes of total carbon, some coastal regions differ substantially from those in the adjacent open-ocean waters (Fig. 3a). These local differences are particularly apparent around coastal upwelling systems, i.e. in the western Arabian Sea and in eastern boundary upwelling systems (EBUS), such as the Peruvian upwelling current, the Moroccan upwelling, and the south-western Africa upwelling. Some of these coastal regions act as strong total carbon sources, with mean carbon fluxes of up to $1.44\,\mathrm{mol\,C\,m^{-2}\,yr^{-1}}$, whereas surrounding open-ocean waters exhibit little F_{CO_2} (fluxes close to $0\,\mathrm{mol\,C\,m^{-2}\,yr^{-1}}$). Other regions also exhibit large contrast between their coastal waters and the adjacent open ocean, including the tropical western Atlantic where there is a massive loss of carbon at the location of the Amazon river discharge. However the carbon sink in the Amazon river plume reported in Lefèvre et al. (2010) is not reproduced in our model. This discrepancy may be due to the modelled instantaneous remineralization of land-derived DOC or to shortcomings in the model representation of sedimentary processes.

A key finding of our model study is that the flux of anthropogenic CO_2 into the coastal ocean ($0.10\,\mathrm{Pg\,C\,yr^{-1}}$) is half the previous estimate (Wanninkhof et al., 2013). Unlike in that study, our specific flux of anthropogenic CO_2 is substantially lower for the global coastal ocean than for the global open ocean (i.e. -0.31 vs. $-0.54\,\mathrm{mol\,C\,m^{-2}\,yr^{-1}}$ for the 1993–2012 average). Although the coastal-ocean surface area is 7.5 % of the global ocean, it absorbs only 4.5 % of the globally integrated flux of anthropogenic carbon into the ocean.

Our estimate for coastal-ocean uptake of anthropogenic carbon is 10 times smaller than the $1\,\mathrm{Pg\,C\,yr^{-1}}$ estimate by Tsunogai et al. (1999) associated with their proposed continental shelf pump (CSP). However, Tsunogai's CSP is based on contemporary measurements and thus concerns total carbon, not the anthropogenic change. That nuance is critical because contemporary estimates of fluxes are not directly comparable to anthropogenic fluxes nor global budgets of carbon from the IPCC and the Global Carbon Project, both focused on the anthropogenic change. Unfortunately Tsunogai et al. (1999) prompted confusion by stating that their total carbon flux into the coastal ocean was equivalent to half of the global-ocean uptake of anthropogenic carbon. The same confusion prompted Thomas et al. (2004) to emphasize that the coastal ocean contributes more to the global carbon budget than expected from its surface area.

The lower specific flux of anthropogenic CO_2 into the global coastal ocean relative to the average for the open ocean could have two causes: (1) physical factors (e.g. if vertical mixing in the coastal ocean is relatively weak or if there is a bottleneck in the offshore transport carbon) and (2) chemical factors, if coastal waters have a lower chemical capacity to absorb anthropogenic carbon (lower carbonate ion concentration, higher Revelle factor R_f).

To assess how R_f differs between coastal- and open-ocean surface waters, we computed it using CO2SYS from simulated sea surface temperature, salinity, alkalinity, and DIC for the model years 1993–2012. Thus we computed mean Revelle factors of 12.5 for the global coastal ocean, 10.9 for the global ocean, 9.2 for the tropical oceans (30° S–30° N), and 12.8 for the Southern Ocean (90–30° S). These tendencies are persistent. During the period 1910–2012, the average coastal-ocean Revelle factor remains 15 % larger than for the open ocean. Hence average surface waters in the model's coastal ocean have a lower chemical capacity to take up anthropogenic carbon relative to average surface waters of the global ocean. That finding is consistent with the lower simulated specific fluxes of anthropogenic carbon into the coastal ocean. Yet it is not only the chemical capacity that matters. For example, despite similar chemical capacities, the specific flux of anthropogenic carbon into Southern Ocean is more than twice that of the global coastal ocean. Thus, we must turn to physical factors to help explain the lower efficiency of the coastal ocean to take up anthropogenic carbon.

Out of the $0.10\,\mathrm{Pg\,C\,yr^{-1}}$ absorbed by the coastal ocean, we find that only 70 % (i.e. $0.07\,\mathrm{Pg\,C\,yr^{-1}}$) is transferred to the open ocean (Fig. 9). Thus $0.03\,\mathrm{Pg\,C\,yr^{-1}}$ of anthropogenic carbon accumulates in the coastal-ocean water col-

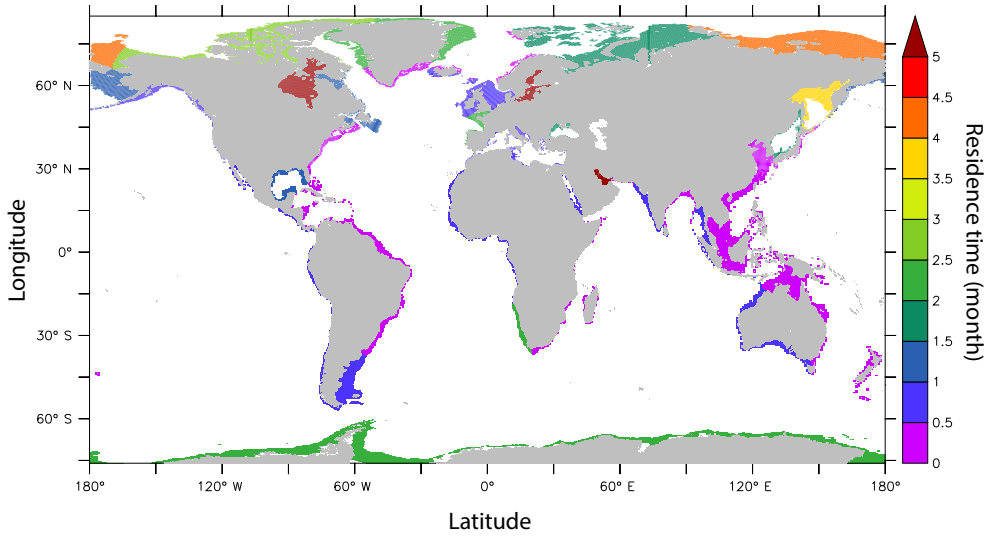

Figure 8. Global distribution of simulated residence time (month) for the global coastal ocean segmented following Laruelle et al. (2013).

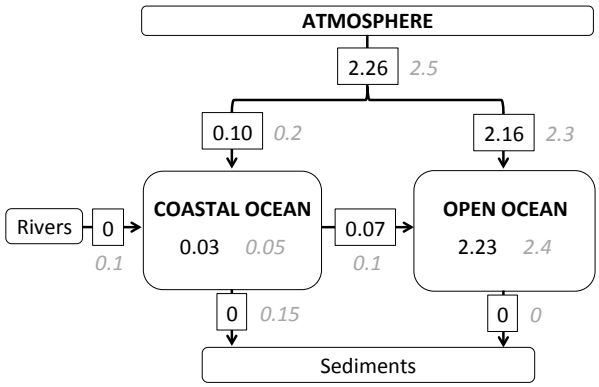

Figure 9. Transfer of anthropogenic carbon between the atmosphere, coastal ocean, and open ocean along with increases in the corresponding inventory in each reservoir, given as the average of simulated values over 1993–2012. All results are in $\mathrm{Pg\,C\,yr^{-1}}$. Simulated results are shown as dark numbers in boxes and adjacent numbers (grey italic) indicate data-based estimates for the 2000–2010 average (Regnier et al., 2013).

umn during the 1993–2012 period. That simulated accumulation is not significantly different from the estimate of $0.05 \pm 0.05\,\mathrm{Pg\,C\,yr^{-1}}$ from Regnier et al. (2013). The accumulation in the coastal ocean is effective over the entire period (1910–2012) as the uptake of anthropogenic carbon by the global coastal ocean is always inferior to its cross-shelf export (Fig. 10). To gain insight into this cross-shelf exchange, we computed the simulated mean water residence times for each MARCATS region (Fig. 8). Residence times for most coastal regions are of the order of a few months or less, except for Hudson Bay, the Baltic Sea, and the Persian Gulf. The latter three regions are generally more confined and we expect longer residence times, although our model simulations were never designed to simulate these regions accurately. Generally, our simulated residence times are shorter than what has been published for similarly defined coastal regions, although methods differ substantially (Jickells, 1998; Men and Liu, 2014; Delhez et al., 2004). Despite these short residence times, the cross-shelf export of anthropogenic carbon is unable to keep up with the increasing air–sea flux of anthropogenic carbon (Fig. 10). This may be explained by the open-ocean waters that are imported to the coastal ocean being already charged with anthropogenic carbon, thus limiting further uptake in the coastal zone. This accumulation rate of anthropogenic carbon in the coastal ocean contrasts with the lower simulated proportion that remains in the mixed layer of the global ocean. Using a coarse-resolution global model, Bopp et al. (2015) showed that on average for the global ocean, only ∼10 % of the anthropogenic carbon that crosses the air–sea interface accumulates in the seasonally-varying mixed layer. The CSP hypothesis from Tsunogai et al. (1999) assumes that much of the $1\,\mathrm{Pg\,C\,yr^{-1}}$ of total carbon absorbed by the coastal ocean is exported to the deep ocean. Also assuming that the CSP operates equally in all shelf regions across the world, Yool and Fasham (2001) used a coarse- resolution global model to estimate that 53 % of the coastal uptake is exported to the open ocean. Yet they considered only natural carbon. Conversely, we focus purely on anthropogenic carbon. Our simulations suggest that 70 % of the anthropogenic carbon absorbed by the coastal ocean over 1993 to 2012 is transported offshore to the deeper open ocean.

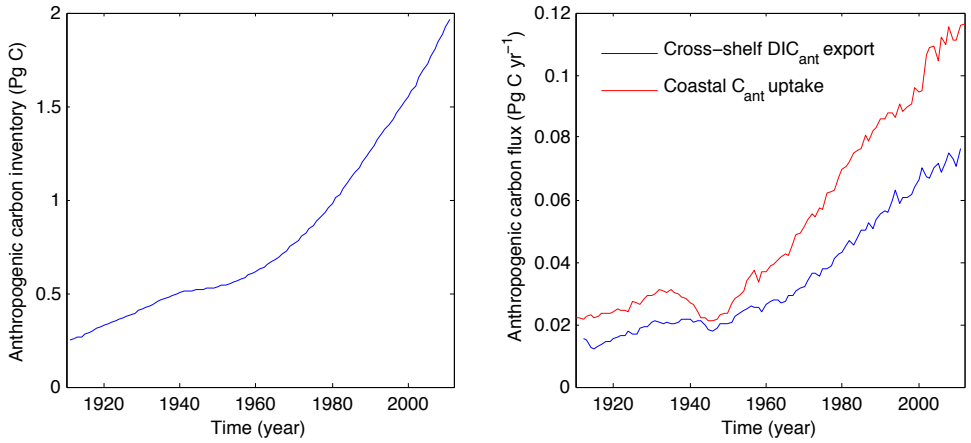

Figure 10. Simulated temporal evolution of **(a)** coastal-ocean inventory of anthropogenic carbon given in Pg C and **(b)** anthropogenic CO_2 (C_{ant}) uptake by the global coastal ocean and global cross-shelf export of anthropogenic carbon (DIC_{ant}) given in Pg C yr^{-1}.

5 Conclusions

The goal of this study was to estimate the anthropogenic CO_2 flux from the atmosphere to the coastal ocean, both globally and regionally, using an eddying global-ocean model, making 143-year simulations forced by atmospheric reanalysis data and atmospheric CO_2. We first evaluated the simulated air–sea fluxes of total CO_2 for 45 coastal regions and found a correlation coefficient R of 0.8 when compared to observation-based estimates. Then we estimated the average simulated anthropogenic carbon uptake by the global coastal ocean over 1993–2012 to be 0.10 ± 0.01 Pg C yr^{-1}, equivalent to 4.5 % of global-ocean uptake of anthropogenic CO_2, an amount less than expected based on the surface area of the global coastal ocean (7.5 % of the global ocean). Furthermore, our estimate is only about half of that estimated by Wanninkhof et al. (2013), whose budget was based on extrapolating adjacent open-ocean data-based estimates of the specific flux into the coastal ocean. We attribute our lower specific flux of anthropogenic carbon into the global coastal ocean mainly to the model's associated offshore carbon transport, which is not strong enough to reduce surface levels of anthropogenic DIC (and thus anthropogenic pCO_2) to levels that are as low as those in the open ocean (on average). Whether or not our model provides a realistic estimate of offshore transport at the global scale is a critical question that demands further investigation.

Clearly, our approach is limited by the extent to which the coastal ocean is resolved. Our model's horizontal resolution does not allow it to fully resolve some fine-scale coastal processes such as tides, which affect F_{CO_2} at tidal fronts (Bianchi et al., 2005). Model resolution is also inadequate to fully resolve mesoscale and submesoscale eddies and associated upwelling. Moreover, in the midlatitudes with a water depth of 80 m, the first baroclinic Rossby radius (the dominant scale affecting coastal processes) is around 200 km, but the latter falls below 10 km on Arctic shelves (Holt et al., 2014; Nurser and Bacon, 2014). Thus the higher latitudes need much finer resolution (Holt et al., 2009).

Yet all model studies must weigh the costs and benefits of pushing the limits toward improved realism. Our approach has been to use a model that takes only a first step into the eddying regime in order to be able to achieve long physical-biogeochemical simulations with atmospheric CO_2 increasing from preindustrial levels to today. It represents a step forward relative to previous studies with typical coarse-resolution ocean models (around 2° horizontal resolution), which may be considered to be designed exclusively for the open ocean. In the coming years, increasing computational resources will allow further increases in spatial resolution and a better representation of the coastal ocean in global ocean carbon cycle models.

Improvements will also be needed in terms of the modelled biogeochemistry of the coastal zone. Most global-scale biogeochemical models neglect river input of nutrients and carbon. Although that is taken into account in our simulations, the river input forcing is constant in time (Aumont et al., 2015). Seasonal and higher frequency variability in carbon and nutrient river input (e.g. from floods and droughts) is substantial as are typical anthropogenic trends. For simplicity, virtually all global-scale models neglect sediment resuspension and early diagenesis in the coastal zone. Those processes in some coastal areas may well alter nutrient availability, surface DIC, and total alkalinity, which would affect F_{CO_2}. In addition, in the coastal zone, one must eventually go beyond the classic definition of anthropogenic carbon, i.e. the change due only to the direct influence of the anthropogenic increase in atmospheric CO_2 on the F_{CO_2} and ocean carbonate chemistry. Changes in other human-induced perturbations may be substantial. For example, future research should better assess potential changes in sediment burial of carbon in the coastal zone during the industrial era, estimated

at up to $0.15\,\mathrm{Pg\,C\,yr^{-1}}$ but with large uncertainty (Regnier et al., 2013).

To improve understanding of the critical land–ocean connection and its role in carbon and nutrient exchange, we call for a long-term effort to exploit the latest, global-scale, high-resolution, ocean general circulation models, adding ocean biogeochemistry, and improving them to better represent the coastal and open oceans together as one seamless system.

6 Code availability

The code of the NEMO ocean model version 3.2 is available under CeCILL license at http://www.nemo-ocean.eu.

7 Data availability

As a supplementary material, we provide the simulated air-sea total and natural CO_2 fluxes over the 1993–2012 period (bg-2016-57-Cflux.nc), model grid parameters (bg-2016-57-grid.nc), and times series for area-integrated CO_2 fluxes (bg-2016-57-timeseries.txt).

Acknowledgements. We are grateful to the associate editor J. Middelburg for managing the peer-reviewing process and to two referees, N. Gruber and P. Regnier, for their helpful comments. We thank G. G. Laruelle for providing the raw data version of the Laruelle et al. (2014) database, and we are grateful to C. Nangini and P. Brockmann for their help with the GIS analysis, data treatment, and data visualization. We also thank J. Simeon for the first implementation of the ORCA05-PISCES model. The research leading to these results was supported through the EU FP7 project CARBOCHANGE (grant 264879), the EU H2020 project CRESCENDO (grant 641816), and the EU H2020 project C-CASCADES (Marie Sklodowska-Curie grant 643052). Simulations were made using HPC resources from GENCI-IDRIS (grant x2015010040). Timothée Bourgeois was funded through a scholarship cosupported by DGA-MRIS and CEA scholarship.

Edited by: J. Middelburg
Reviewed by: N. Gruber and P. Regnier

References

Allen, J. I., Blackford, J., Holt, J., Proctor, R., Ashworth, M., and Siddorn, J.: A highly spatially resolved ecosystem model for the North West European Continental Shelf, Sarsia, 86, 423–440, 2001.

Andersson, A. J. and Mackenzie, F. T.: Shallow-water oceans: a source or sink of atmospheric CO_2?, Front. Ecol. Environ., 2, 348–353, 2004.

Artioli, Y., Blackford, J. C., Nondal, G., Bellerby, R. G. J., Wakelin, S. L., Holt, J. T., Butenschön, M., and Allen, J. I.: Heterogeneity of impacts of high CO_2 on the North Western European Shelf, Biogeosciences, 11, 601–612, doi:10.5194/bg-11-601-2014, 2014.

Astor, Y. M., Lorenzoni, L., Thunell, R., Varela, R., Muller-Karger, F., Troccoli, L., Taylor, G. T., Scranton, M. I., Tappa, E., and Rueda, D.: Interannual variability in sea surface temperature and F_{CO_2} changes in the Cariaco Basin, Deep-Sea Res. Pt. II, 93, 33–43, 2013.

Atlas, R., Hoffman, R. N., Ardizzone, J., Leidner, S. M., Jusem, J. C., Smith, D. K., and Gombos, D.: A Cross-calibrated, Multiplatform Ocean Surface Wind Velocity Product for Meteorological and Oceanographic Applications, Bull. Am. Meteorol. Soc., 92, 157–174, 2011.

Aumont, O. and Bopp, L.: Globalizing results from ocean in situ iron fertilization studies, Global Biogeochem. Cy., 20, GB2017, doi:10.1029/2005GB002591, 2006.

Aumont, O., Ethé, C., Tagliabue, A., Bopp, L., and Gehlen, M.: PISCES-v2: an ocean biogeochemical model for carbon and ecosystem studies, Geosci. Model Dev., 8, 2465–2513, doi:10.5194/gmd-8-2465-2015, 2015.

Bakker, D. C. E., Pfeil, B., Smith, K., Hankin, S., Olsen, A., Alin, S. R., Cosca, C., Harasawa, S., Kozyr, A., Nojiri, Y., O'Brien, K. M., Schuster, U., Telszewski, M., Tilbrook, B., Wada, C., Akl, J., Barbero, L., Bates, N. R., Boutin, J., Bozec, Y., Cai, W.-J., Castle, R. D., Chavez, F. P., Chen, L., Chierici, M., Currie, K., de Baar, H. J. W., Evans, W., Feely, R. A., Fransson, A., Gao, Z., Hales, B., Hardman-Mountford, N. J., Hoppema, M., Huang, W.-J., Hunt, C. W., Huss, B., Ichikawa, T., Johannessen, T., Jones, E. M., Jones, S. D., Jutterström, S., Kitidis, V., Körtzinger, A., Landschützer, P., Lauvset, S. K., Lefèvre, N., Manke, A. B., Mathis, J. T., Merlivat, L., Metzl, N., Murata, A., Newberger, T., Omar, A. M., Ono, T., Park, G.-H., Paterson, K., Pierrot, D., Ríos, A. F., Sabine, C. L., Saito, S., Salisbury, J., Sarma, V. V. S. S., Schlitzer, R., Sieger, R., Skjelvan, I., Steinhoff, T., Sullivan, K. F., Sun, H., Sutton, A. J., Suzuki, T., Sweeney, C., Takahashi, T., Tjiputra, J., Tsurushima, N., van Heuven, S. M. A. C., Vandemark, D., Vlahos, P., Wallace, D. W. R., Wanninkhof, R., and Watson, A. J.: An update to the Surface Ocean CO2 Atlas (SOCAT version 2), Earth Syst. Sci. Data, 6, 69–90, doi:10.5194/essd-6-69-2014, 2014.

Barnier, B., Madec, G., Penduff, T., Molines, J. M., Treguier, A. M., Le Sommer, J., Beckmann, A., Biastoch, A., Böning, C., Dengg, J., Derval, C., Durand, E., Gulev, S., Remy, E., Talandier, C., Theetten, S., Maltrud, M., McClean, J., and De Cuevas, B.: Impact of partial steps and momentum advection schemes in a global ocean circulation model at eddy-permitting resolution, Ocean Dynam., 56, 543–567, 2006.

Bauer, J. E., Cai, W.-J., Raymond, P. A., Bianchi, T. S., Hopkinson, C. S., and Regnier, P.: The changing carbon cycle of the coastal ocean, Nature, 504, 61–70, 2013.

Bianchi, A. A., Bianucci, L., Piola, A. R., Pino, D. R., Schloss, I., Poisson, A., and Balestrini, C. F.: Vertical stratification and air-sea CO_2 fluxes in the Patagonian shelf, J. Geophys. Res.-Ocean., 110, 1–10, 2005.

Bopp, L., Lévy, M., Resplandy, L., and Sallée, J. B.: Pathways of anthropogenic carbon subduction in the global ocean, Geophys. Res. Lett., 42, 6416–6423, 2015.

Borges, A. V.: Do we have enough pieces of the jigsaw to integrate CO_2 fluxes in the coastal ocean?, Estuaries, 28, 3–27, 2005.

Borges, A. V., Delille, B., and Frankignoulle, M.: Budgeting sinks and sources of CO_2 in the coastal ocean: Diver-

sity of ecosystems counts, Geophys. Res. Lett., 32, L14601, doi:10.1029/2005GL023053, 2005.

Brodeau, L., Barnier, B., Treguier, A.-M., Penduff, T., and Gulev, S.: An ERA40-based atmospheric forcing for global ocean circulation models, Ocean Model., 31, 88–104, 2010.

Cai, W.-J.: Estuarine and coastal ocean carbon paradox: CO_2 sinks or sites of terrestrial carbon incineration?, Ann. Rev. Mar. Sci., 3, 123–45, 2011.

Cai, W.-J., Dai, M., and Wang, Y.: Air-sea exchange of carbon dioxide in ocean margins: A province-based synthesis, Geophys. Res. Lett., 33, L12603, doi:10.1029/2006GL026219, 2006.

Capet, X. J.: Upwelling response to coastal wind profiles, Geophys. Res. Lett., 31, L13311, doi:10.1029/2004GL020123, 2004.

Chen, C.-T. A.: Shelf-vs. dissolution-generated alkalinity above the chemical lysocline, Deep-Sea Res. Pt. II, 49, 5365–5375, 2002.

Chen, C.-T. A. and Borges, A. V.: Reconciling opposing views on carbon cycling in the coastal ocean: Continental shelves as sinks and near-shore ecosystems as sources of atmospheric CO_2, Deep-Sea Res. Pt. II, 56, 578–590, 2009.

Chen, C.-T. A., Huang, T. H., Chen, Y. C., Bai, Y., He, X., and Kang, Y.: Air-sea exchanges of CO_2 in the world's coastal seas, Biogeosciences, 10, 6509–6544, doi:10.5194/bg-10-6509-2013, 2013.

Ciais, P., Sabine, C., Bala, G., Bopp, L., Brovkin, V., Canadell, J., Chhabra, a., DeFries, R., Galloway, J., Heimann, M., Jones, C., Quéré, C. L., Myneni, R., Piao, S., Thornton, P., France, P. C., Willem, J., Friedlingstein, P., and Munhoven, G.: 2013: Carbon and Other Biogeochemical Cycles, Climate Change 2013: The Physical Science Basis. Contribution of Working Group I to the Fifth Assessment Report of the Intergovernmental Panel on Climate Change, 465–570, doi:10.1017/CBO9781107415324.015, 2013.

Conkright, M. E., Locarnini, R. A., Garcia, H. E., O'Brien, T. D., Boyer, T. P., Stephens, C., and Antonov, J. I.: World Ocean Database 2001: Objective analyses, data statistics and figures, 2002.

Cossarini, G., Querin, S., and Solidoro, C.: The continental shelf carbon pump in the northern Adriatic Sea (Mediterranean Sea): Influence of wintertime variability, Ecol. Model., 314, 118–134, 2015.

Cotrim da Cunha, L., Buitenhuis, E. T., Le Quéré, C., Giraud, X., and Ludwig, W.: Potential impact of changes in river nutrient supply on global ocean biogeochemistry, Global Biogeochem. Cy., 21, GB4007, doi:10.1029/2006GB002718, 2007.

de Baar, H. J. W. and de Jong, J. T. M.: Distributions, sources and sinks of iron in seawater, The Biogeochemistry of Iron in Seawater, IUPAC Series on Analytical and Physical Chemistry of Environmental Systems, 123–253, 2001.

Delhez, É. J., Heemink, A. W., and Deleersnijder, É.: Residence time in a semi-enclosed domain from the solution of an adjoint problem, Estuarine, Coast. Shelf Sci., 61, 691–702, 2004.

Dickson, A. G.: Standard potential of the reaction: $AgCl(s) + 12H_2(g) = Ag(s) + HCl(aq)$, and the standard acidity constant of the ion HSO_4^- in synthetic sea water from 273.15 to 318.15 K, The Journal of Chemical Thermodynamics, 22, 113–127, 1990.

Fennel, K.: The role of continental shelves in nitrogen and carbon cycling: Northwestern North Atlantic case study, Ocean Sci., 6, 539–548, doi:10.5194/os-6-539-2010, 2010.

Fennel, K., Wilkin, J., Previdi, M., and Najjar, R.: Denitrification effects on air-sea CO_2 flux in the coastal ocean: Simulations for the northwest North Atlantic, Geophys. Res. Lett., 35, L24608, doi:10.1029/2008GL036147, 2008.

Fichefet, T. and Morales Maqueda, M. A. M.: Sensitivity of a global sea ice model to the treatment of ice thermodynamics and dynamics, J. Geophys. Res., 102, 12609, doi:10.1029/97JC00480, 1997.

Fiechter, J., Curchitser, E. N., Edwards, C. A., Chai, F., Goebel, N. L., and Chavez, F. P.: Air-sea CO_2 fluxes in the California Current: Impacts of model resolution and coastal topography, Global Biogeochem. Cy., 28, 371–385, 2014.

Gattuso, J. P., Frankignoulle, M., and Wollast, R.: Carbon and carbonate metabolism in coastal aquatic ecosystems, Ann. Rev. Ecol. Syst., 29, 405–434, 1998.

Geider, R. J., MacIntyre, H. L., and Kana, T. M.: A dynamic regulatory model of phytoplanktonic acclimation to light, nutrients, and temperature, Limnol. Oceanogr., 43, 679–694, 1998.

Gent, P. R. and McWilliams, J. C.: Isopycnal Mixing in Ocean Circulation Models, J. Phys. Oceanogr., 20, 150–155, 1990.

GLOBALVIEW-CO2: Cooperative Global Atmospheric Data Integration Project Carbon Dioxide, Multi-laboratory compilation of synchronized and gap-filled atmospheric carbon dioxide records for the period 1979–2012, Compiled by NOAA Global Monitoring Division, Boulder, Colorado, doi:10.3334/OBSPACK/1002, 2012.

Griffies, S.: Problems and Prospects in Large-Scale Ocean Circulation Models, in: Proceedings of OceanObs'09, Sustained Ocean Observations and Information for Society, 1, European Space Agency, Venice, Italy, 410–431, 2010.

Gruber, N.: Ocean biogeochemistry: Carbon at the coastal interface, Nature, 517, 148–149, 2014.

Ho, D. T., Law, C. S., Smith, M. J., Schlosser, P., Harvey, M., and Hill, P.: Measurements of air-sea gas exchange at high wind speeds in the Southern Ocean: Implications for global parameterizations, Geophys. Res. Lett., 33, 1–6, 2006.

Hofmann, E. E., Cahill, B., Fennel, K., Friedrichs, M. A. M., Hyde, K., Lee, C., Mannino, A., Najjar, R. G., O'Reilly, J. E., Wilkin, J., and Xue, J.: Modeling the dynamics of continental shelf carbon, Ann. Rev. Mar. Sci., 3, 93–122, 2011.

Holt, J., Harle, J., Proctor, R., Michel, S., Ashworth, M., Batstone, C., Allen, I., Holmes, R., Smyth, T., Haines, K., Bretherton, D., and Smith, G.: Modelling the global coastal ocean, Philos. Trans. Ser. A, 367, 939–51, 2009.

Holt, J., Icarus Allen, J., Anderson, T. R., Brewin, R., Butenschön, M., Harle, J., Huse, G., Lehodey, P., Lindemann, C., Memery, L., Salihoglu, B., Senina, I., and Yool, A.: Challenges in integrative approaches to modelling the marine ecosystems of the North Atlantic: Physics to fish and coasts to ocean, Prog. Oceanogr., 129, 285–313, 2014.

Hu, X. and Cai, W.-J.: An assessment of ocean margin anaerobic processes on oceanic alkalinity budget, Global Biogeochem. Cy., 25, GB3003, doi:10.1029/2010GB003859, 2011.

Ishii, M., Kosugi, N., Sasano, D., Saito, S., Midorikawa, T., and Inoue, H. Y.: Ocean acidification off the south coast of Japan: A result from time series observations of CO_2 parameters from 1994 to 2008, J. Geophys. Res.-Ocean., 116, 1–9, 2011.

Jacobson, A. R., Fletcher, S. E. M., Gruber, N., Sarmiento, J. L., and Gloor, M.: A joint atmosphere-ocean inversion for surface fluxes

of carbon dioxide: 1. Methods and global-scale fluxes, Global Biogeochem. Cy., 21, GB1019, doi:10.1029/2005GB002556, 2007.

Jickells, T. D.: Nutrient Biogeochemistry of the Coastal Zone, Science, 281, 217–222, 1998.

Kelley, J. J., Longerich, L. L., and Hood, D. W.: Effect of upwelling, mixing, and high primary productivity on CO_2 concentrations in surface waters of the Bering Sea, J. Geophys. Res., 76, 8687–8693, 1971.

Key, R. M., Kozyr, A., Sabine, C. L., Lee, K., Wanninkhof, R., Bullister, J. L., Feely, R. A., Millero, F. J., Mordy, C., and Peng, T.-H.: A global ocean carbon climatology: Results from Global Data Analysis Project (GLODAP), Global Biogeochem. Cy., 18, GB4031, doi:10.1029/2004GB002247, 2004.

Krumins, V., Gehlen, M., Arndt, S., Van Cappellen, P., and Regnier, P.: Dissolved inorganic carbon and alkalinity fluxes from coastal marine sediments: model estimates for different shelf environments and sensitivity to global change, Biogeosciences, 10, 371–398, doi:10.5194/bg-10-371-2013, 2013.

Lachkar, Z. and Gruber, N.: Response of biological production and air-sea CO_2 fluxes to upwelling intensification in the California and Canary Current Systems, J. Mar. Syst., 109/110, 149–160, 2013.

Lachkar, Z., Orr, J. C., Dutay, J. C., and Delecluse, P.: Effects of mesoscale eddies on global ocean distributions of CFC-11, CO_2, and $\Delta^{14}C$, Ocean Sci., 3, 461–482, doi:10.5194/os-3-461-2007, 2007.

Landschützer, P., Gruber, N., Bakker, D. C. E., and Schuster, U.: Recent variability of the global ocean carbon sink, Global Biogeochem. Cy., 28, 927–949, 2014.

Laruelle, G. G., Dürr, H. H., Slomp, C. P., and Borges, A. V.: Evaluation of sinks and sources of CO2 in the global coastal ocean using a spatially-explicit typology of estuaries and continental shelves, Geophys. Res. Lett., 37, L15607, doi:10.1029/2010GL043691, 2010.

Laruelle, G. G., Dürr, H. H., Lauerwald, R., Hartmann, J., Slomp, C. P., Goossens, N., and Regnier, P.: Global multi-scale segmentation of continental and coastal waters from the watersheds to the continental margins, Hydrol. Earth Syst. Sci., 17, 2029–2051, doi:10.5194/hess-17-2029-2013, 2013.

Laruelle, G. G., Lauerwald, R., Pfeil, B., and Regnier, P.: Regionalized global budget of the CO_2 exchange at the air-water interface in continental shelf seas, Global Biogeochem. Cy., 28, 1199–1214, doi:10.1002/2014GB004832, 2014.

Le Quéré, C., Peters, G. P., Andres, R. J., Andrew, R. M., Boden, T. A., Ciais, P., Friedlingstein, P., Houghton, R. A., Marland, G., Moriarty, R., Sitch, S., Tans, P., Arneth, A., Arvanitis, A., Bakker, D. C. E., Bopp, L., Canadell, J. G., Chini, L. P., Doney, S. C., Harper, A., Harris, I., House, J. I., Jain, A. K., Jones, S. D., Kato, E., Keeling, R. F., Klein Goldewijk, K., Körtzinger, A., Koven, C., Lefèvre, N., Maignan, F., Omar, A., Ono, T., Park, G.-H., Pfeil, B., Poulter, B., Raupach, M. R., Regnier, P., Rödenbeck, C., Saito, S., Schwinger, J., Segschneider, J., Stocker, B. D., Takahashi, T., Tilbrook, B., van Heuven, S., Viovy, N., Wanninkhof, R., Wiltshire, A., and Zaehle, S.: Global carbon budget 2013, Earth Syst. Sci. Data, 6, 235–263, doi:10.5194/essd-6-235-2014, 2014.

Le Quéré, C., Moriarty, R., Andrew, R. M., Peters, G. P., Ciais, P., Friedlingstein, P., Jones, S. D., Sitch, S., Tans, P., Arneth, A., Boden, T. A., Bopp, L., Bozec, Y., Canadell, J. G., Chini, L. P., Chevallier, F., Cosca, C. E., Harris, I., Hoppema, M., Houghton, R. A., House, J. I., Jain, A. K., Johannessen, T., Kato, E., Keeling, R. F., Kitidis, V., Klein Goldewijk, K., Koven, C., Landa, C. S., Landschützer, P., Lenton, A., Lima, I. D., Marland, G., Mathis, J. T., Metzl, N., Nojiri, Y., Olsen, A., Ono, T., Peng, S., Peters, W., Pfeil, B., Poulter, B., Raupach, M. R., Regnier, P., Rödenbeck, C., Saito, S., Salisbury, J. E., Schuster, U., Schwinger, J., Séférian, R., Segschneider, J., Steinhoff, T., Stocker, B. D., Sutton, A. J., Takahashi, T., Tilbrook, B., van der Werf, G. R., Viovy, N., Wang, Y.-P., Wanninkhof, R., Wiltshire, A., and Zeng, N.: Global carbon budget 2014, Earth Syst. Sci. Data, 7, 47–85, doi:10.5194/essd-7-47-2015, 2015.

Lefèvre, N., Diverrès, D., and Gallois, F.: Origin of CO_2 undersaturation in the western tropical Atlantic, Tellus B, 62, 595–607, 2010.

Liu, K.-K., Atkinson, L., Quiñones, R., and Talaue-McManus, L., (Eds.): Carbon and Nutrient Fluxes in Continental Margins, Global Change – The IGBP Series, Springer Berlin Heidelberg, Berlin, Heidelberg, doi:10.1007/978-3-540-92735-8, 2010.

Longhurst, A., Sathyendranath, S., Platt, T., and Caverhill, C.: An estimate of global primary production in the ocean from satellite radiometer data, J. Plank. Res., 17, 1245–1271, 1995.

Ludwig, W., Probst, J.-L., and Kempe, S.: Predicting the oceanic input of organic carbon by continental erosion, Global Biogeochem. Cy., 10, 23, doi:10.1029/95GB02925, 1996.

Lueker, T. J., Dickson, A. G., and Keeling, C. D.: Ocean pCO_2 calculated from dissolved inorganic carbon, alkalinity, and equations for K1 and K2: validation based on laboratory measurements of CO_2 in gas and seawater at equilibrium, Mar. Chem., 70, 105–119, 2000.

Mackenzie, F. T., Lerman, A., and Andersson, A. J.: Past and present of sediment and carbon biogeochemical cycling models, Biogeosciences, 1, 11–32, doi:10.5194/bg-1-11-2004, 2004.

Madec, G.: NEMO ocean engine, Note du Pole de modélisation de l'Institut Pierre-Simon Laplace, 27, 250 pp., 2008.

McKiver, W. J., Vichi, M., Lovato, T., Storto, A., and Masina, S.: Impact of increased grid resolution on global marine biogeochemistry, J. Mar. Syst., 147, 153–158, doi:10.1016/j.jmarsys.2014.10.003, 2015.

Men, W. and Liu, G.: Distribution of ^{226}Ra and the residence time of the shelf water in the Yellow Sea and the East China Sea, J. Radioanal. Nucl. Chem., 303, 2333–2344, 2014.

Meybeck, M.: Carbon, nitrogen, and phosphorus transport by world rivers, Am. J. Sci., 282, 401–450, 1982.

Monod, J.: The Growth of Bacterial Cultures, Annu. Rev. Microbiol., 3, 371–394, 1949.

Najjar, R. G. and Orr, J. C.: Biotic-HOWTO, Internal OCMIP Report, LSCE/CEA Saclay, Gif-sur-Yvette, France, 1–15, 1999.

Nurser, A. J. G. and Bacon, S.: The Rossby radius in the Arctic Ocean, Ocean Sci., 10, 967–975, doi:10.5194/os-10-967-2014, 2014.

Pfeil, B., Olsen, A., Bakker, D. C. E., Hankin, S., Koyuk, H., Kozyr, A., Malczyk, J., Manke, A., Metzl, N., Sabine, C. L., Akl, J., Alin, S. R., Bates, N., Bellerby, R. G. J., Borges, A., Boutin, J., Brown, P. J., Cai, W. J., Chavez, F. P., Chen, A., Cosca, C., Fassbender, A. J., Feely, R. A., González-Dávila, M., Goyet, C., Hales, B., Hardman-Mountford, N., Heinze, C., Hood, M., Hoppema, M., Hunt, C. W., Hydes, D., Ishii, M., Johannessen,

T., Jones, S. D., Key, R. M., Körtzinger, A., Landschützer, P., Lauvset, S. K., Lefèvre, N., Lenton, A., Lourantou, A., Merlivat, L., Midorikawa, T., Mintrop, L., Miyazaki, C., Murata, A., Nakadate, A., Nakano, Y., Nakaoka, S., Nojiri, Y., Omar, A. M., Padin, X. A., Park, G. H., Paterson, K., Perez, F. F., Pierrot, D., Poisson, A., Ríos, A. F., Santana-Casiano, J. M., Salisbury, J., Sarma, V. V. S. S., Schlitzer, R., Schneider, B., Schuster, U., Sieger, R., Skjelvan, I., Steinhoff, T., Suzuki, T., Takahashi, T., Tedesco, K., Telszewski, M., Thomas, H., Tilbrook, B., Tjiputra, J., Vandemark, D., Veness, T., Wanninkhof, R., Watson, A. J., Weiss, R., Wong, C. S., and Yoshikawa-Inoue, H.: A uniform, quality controlled Surface Ocean CO_2 Atlas (SOCAT), Earth Syst. Sci. Data, 5, 125–143, doi:10.5194/essd-5-125-2013, 2013.

Phelps, J. J. C., Blackford, J. C., Holt, J. T., and Polton, J. A.: Modelling large-scale CO_2 leakages in the North Sea, Int. J. Greenh. Gas Con., 38, 210–220, doi:10.1016/j.ijggc.2014.10.013, 2014.

Prowe, A. E. F., Thomas, H., Pätsch, J., Kühn, W., Bozec, Y., Schiettecatte, L.-S., Borges, A. V., and de Baar, H. J. W.: Mechanisms controlling the air-sea flux in the North Sea, Cont. Shelf Res., 29, 1801–1808, 2009.

QGIS Development Team: QGIS Geographic Information System, 2015.

Rabouille, C., Mackenzie, F. T., and Ver, L. M.: Influence of the human perturbation on carbon, nitrogen, and oxygen biogeochemical cycles in the global coastal ocean, Geochim. Cosmochim. Ac., 65, 3615–3641, 2001.

Regnier, P., Friedlingstein, P., Ciais, P., Mackenzie, F. T., Gruber, N., Janssens, I. A., Laruelle, G. G., Lauerwald, R., Luyssaert, S., Andersson, A. J., Arndt, S., Arnosti, C., Borges, A. V., Dale, A. W., Gallego-Sala, A., Goddéris, Y., Goossens, N., Hartmann, J., Heinze, C., Ilyina, T., Joos, F., LaRowe, D. E., Leifeld, J., Meysman, F. J. R., Munhoven, G., Raymond, P. A., Spahni, R., Suntharalingam, P., and Thullner, M.: Anthropogenic perturbation of the carbon fluxes from land to ocean, Nat. Geosci., 6, 597–607, doi:10.1038/ngeo1830, 2013.

Soetaert, K., Middelburg, J. J., Herman, P. M., and Buis, K.: On the coupling of benthic and pelagic biogeochemical models, Earth-Sci. Rev., 51, 173–201, 2000.

Sundquist, E. T., Plummer, L. N., and Wigley, T. M. L.: Carbon Dioxide in the Ocean Surface: The Homogeneous Buffer Factor, Science, 204, 1203–1205, 1979.

Takahashi, T., Broecker, W. S., and Langer, S.: Redfield ratio based on chemical data from isopycnal surfaces, J. Geophys. Res., 90, 6907, doi:10.1029/JC090iC04p06907, 1985.

Takahashi, T., Sutherland, S. C., Wanninkhof, R., Sweeney, C., Feely, R. A., Chipman, D. W., Hales, B., Friederich, G., Chavez, F., Sabine, C., Watson, A., Bakker, D. C. E., Schuster, U., Metzl, N., Yoshikawa-Inoue, H., Ishii, M., Midorikawa, T., Nojiri, Y., Körtzinger, A., Steinhoff, T., Hoppema, M., Olafsson, J., Arnarson, T. S., Tilbrook, B., Johannessen, T., Olsen, A., Bellerby, R., Wong, C. S., Delille, B., Bates, N. R., and de Baar, H. J. W.: Climatological mean and decadal change in surface ocean pCO_2, and net sea-air CO_2 flux over the global oceans, Deep-Sea Res. Pt. II, 56, 554–577, 2009.

Tegen, I. and Fung, I.: Contribution to the atmospheric mineral aerosol load from land surface modification, J. Geophys. Res., 100, 18707, doi:10.1029/95JD02051, 1995.

Thomas, H., Bozec, Y., Elkalay, K., and de Baar, H. J. W.: Enhanced open ocean storage of CO_2 from shelf sea pumping, Science (New York, NY), 304, 1005–1008, doi:10.1126/science.1103193, 2004.

Thomas, H., Schiettecatte, L.-S., Suykens, K., Koné, Y. J. M., Shadwick, E. H., Prowe, A. E. F., Bozec, Y., de Baar, H. J. W., and Borges, A. V.: Enhanced ocean carbon storage from anaerobic alkalinity generation in coastal sediments, Biogeosciences, 6, 267–274, doi:10.5194/bg-6-267-2009, 2009.

Timmermann, R., Goosse, H., Madec, G., Fichefet, T., Ethe, C., and Dulière, V.: On the representation of high latitude processes in the ORCA-LIM global coupled sea ice-ocean model, Ocean Model., 8, 175–201, 2005.

Treguer, P., Nelson, D. M., Van Bennekom, A. J., DeMaster, D. J., Leynaert, A., and Queguiner, B.: The Silica Balance in the World Ocean: A Reestimate, Science, 268, 375–379, 1995.

Tsunogai, S., Watanabe, S., and Sato, T.: Is there a "continental shelf pump" for the absorption of atmospheric CO_2?, Tellus B, 51, 701–712, 1999.

Turi, G., Lachkar, Z., and Gruber, N.: Spatiotemporal variability and drivers of pCO_2 and air-sea CO_2 fluxes in the California Current System: an eddy-resolving modeling study, Biogeosciences, 11, 671–690, doi:10.5194/bg-11-671-2014, 2014.

Uppström, L. R.: The boron/chlorinity ratio of deep-sea water from the Pacific Ocean, Deep-Sea Res. Oceanogr. Abstracts, 21, 161–162, 1974.

Van Heuven, S., Pierrot, D., Rae, J., Lewis, E., and Wallace, D.: CO2SYS v1.1, MATLAB program developed for CO_2 system calculations., in: ORNL/CDIAC-105b. Carbon Dioxide Information Analysis Center, Oak Ridge National Laboratory, US DoE, Oak Ridge, TN., doi:10.3334/CDIAC/otg.CO2SYS_MATLAB_v1.1, 2011.

Wakelin, S. L., Holt, J. T., Blackford, J. C., Allen, J. I., Butenschön, M., and Artioli, Y.: Modeling the carbon fluxes of the northwest European continental shelf: Validation and budgets, J. Geophys. Res., 117, C05020, doi:10.1029/2011JC007402, 2012.

Walsh, J. J.: Importance of continental margins in the marine biogeochemical cycling of carbon and nitrogen, Nature, 350, 53–55, 1991.

Wanninkhof, R.: Relationship between wind speed and gas exchange over the ocean, J. Geophys. Res., 97, 7373, doi:10.1029/92JC00188, 1992.

Wanninkhof, R., Park, G. H., Takahashi, T., Sweeney, C., Feely, R., Nojiri, Y., Gruber, N., Doney, S. C., McKinley, G. A., Lenton, A., Le Quéré, C., Heinze, C., Schwinger, J., Graven, H., and Khatiwala, S.: Global ocean carbon uptake: magnitude, variability and trends, Biogeosciences, 10, 1983–2000, doi:10.5194/bg-10-1983-2013, 2013.

Weiss, R.: Carbon dioxide in water and seawater: the solubility of a non-ideal gas, Mar. Chem., 2, 203–215, 1974.

Yool, A. and Fasham, M. J. R.: An Examination of the "Continental shelf pump" in an open ocean general circulation model, Global Biogeochem. Cy., 15, 831–844, 2001.